Rui César Vilão

Isolated hydrogen in II–VI zinc–chalcogenide widegap semiconductors modelled by the muon analogue

Faculdade de Ciências e Tecnologia
Universidade de Coimbra
Coimbra – 2007

Rui César Vilão

Isolated hydrogen in II–VI zinc–chalcogenide widegap semiconductors modelled by the muon analogue

[Hidrogénio isolado em calcógenos de zinco da família II-VI com propriedades semicondutoras e intervalo largo de energias proibidas, estudado através da analogia com o muão]

Dissertação de doutoramento em Física,
especialidade de Física Experimental,
submetida à Faculdade de Ciências e Tecnologia,
Universidade de Coimbra

Coimbra - 2007

Aos meus Pais

À Susana

Abstract

We have investigated the behaviour of isolated hydrogen in II–VI zinc chalcogenide widegap semiconductors, by means of the positive-muon analogue. A broad program of muon-spin rotation, relaxation and resonance measurements was undertaken for monocrystalline samples of ZnSe, upon adequate characterization (particularly on the electrical transport properties, by means of Hall-effect and resistivity measurements). Two compact paramagnetic muonium states Mu_I and Mu_{II} were identified and the interconversion process was characterized. Capture of a second electron by Mu_{II}, forming the negative ion Mu_{II}^- was observed as well. This charged state becomes thermally unstable above 60 K and we relate this to possible ionization to the conduction band and estimate the corresponding acceptor level. In adition to ZnSe, monocrystalline samples of ZnS and ZnTe were investigated. Only one paramagnetic state is observed in ZnS, whose behaviour is shown to be much similar to that of Mu_{II} in ZnSe. In ZnTe, only a diamagnetic state is observed, which we suggest corresponds to a deep donor in this material. Finally, a global configuration and energy level model is presented for muonium/hydrogen in II–VI semiconductors.

Resumo

Neste trabalho investigou-se o comportamento, através da analogia com o muão positivo, do hidrogénio isolado em materiais calcógenos de zinco com propriedades semicondutoras e intervalo largo de energias proibidas, da família II-VI. Foi realizado um programa amplo de medidas experimentais de rotação, relaxação e ressonância do spin do muão em amostras monocristalinas de ZnSe devidamente caracterizadas (particularmente do ponto de vista das propriedades de transporte eléctrico, através de medidas de efeito de Hall e resistividade eléctrica). Identificou-se dois estados paramagnéticos compactos de muónio, Mu_I e Mu_{II}, e caracterizou-se o processo de interconversão. Observou-se ainda a captura de um segundo electrão pelo estado Mu_{II}, formando o ião negativo Mu_{II}^-. Este estado negativamente carregado é instável para temperaturas superiores a 60 K, possivelmente ionizando para a banda de condução, tendo sido determinado o presumível nível aceitador correspondente. Para além de ZnSe, investigou-se também amostras monocristalinas de ZnS e ZnTe. Observa-se apenas um estado de muónio paramagnético em ZnS, cujo comportamento se verificou ser muito semelhante ao do estado Mu_{II} existente em ZnSe. Em ZnTe observa-se um estado diamagnético que sugerimos corresponder a um dador profundo neste material. Finalmente, apresenta-se um modelo global para as configurações e níveis de energia do muónio/hidrogénio nos semiconductores da família II-VI.

Acknowledgements

A work such as the one now presented is necessarily a team work. The input and collaboration of many people is present at all stages, from the initial ideas and proposals, through the beamline days and discussion at all levels of the experimental data and respective significance, up to the final redaction. It is to me a privilege to make part of a team such as the one which helped to complete this work. A scientific privilege, certainly, but a personal privilege as well. I am very happy to express now my public thanks:

- to Prof. Dr. João Campos Gil, whom I owe a most dedicated, friendly, present guidance, in the big lines as in the little details.

- to Prof. Dr. Nuno Ayres de Campos, whose counsel, encouragement and friendship helped me looking farther with confidence.

- to Prof. Dr. Alois Weidinger, whose profound physical insight, shared friendly and patiently in intense interaction and discussions, brought me immense benefits.

- to Dr. Helena Vieira Alberto, a quotidian source of science, humanism and friendship.

- to João Pedro Duarte, comrade of many scientific and non-scientific fights, always fought with wit and joy.

- to Prof. Dr. Stephen Cox, Prof. Dr. Roger Lichti and Dr. Kim Chow, who have contributed to this investigation with their eminent knowledge, as well as with many days of hard work.

I would also like to gratefully acknowledge the kind help, during this work, of Dr. Benilde Costa, Dr. Francisco Gil, Dr. D. Siche, Dr. K. Irmscher, Marco Peres, Prof. Dr. Teresa Monteiro, Prof. Dr. Ermelinda Eusébio, Dr. Manuela Silva, Victor Hugo Rodrigues, Prof. Dr. José António Paixão, Dr. Ana Maria Matos Beja, Dr. Bassam Hitti, Dr. Stephen Cottrell, Dr. James Lord, Dr. U. Zimmermann, Dr. Robert Scheuermann, Dr. Alex Amato, Dr. Hubertus Luetkens, Dr. Dierk Herlach, Dr. Philip King, as well of my colleagues at the Physics Department of the University of Coimbra.

Contents

Chapter 1

Hydrogen in semiconductors

Embarque vossa doçura
que cá nos entenderemos...
Tomareis um par de remos,
veremos como remais;
e, chegando ao nosso cais,
nós vos desembarcaremos.[1]

Gil Vicente
Auto da Barca do Inferno

1.1 Introduction

Impurities play an essential part in the physics of semiconductors. The extreme sensibility of the electrical and optical properties of the members of this class of materials with respect to the presence of impurity atoms may be regarded as one of its most defining characteristics [See82, Yu99]. Hydrogen occupies a special role among all impurities. As the simplest atom, one might expect hydrogen to have a specially simple behaviour in semiconductors, upon which generalizations to other impurities could be inferred. Notwithstanding the current state of hydrogen research in semiconductors depicts an extremely complex impurity which assumes a variety of forms, from several possible atomic configurations to molecular states

[1] Free translation: *"Climb your sweetness aboard and we shall go along... You shall take a pair of oars, we shall watch you rowing; and, when we arrive to our pier, we shall step you off."*

and complexation with other impurities and defects [Est95, Mye92, Nic98, Nic99a, Pan91, Pea94, VdW05, VdW06]. Much interest is deposited in the knowledge of the hydrogen impurity *per se*, due to its omnipresence in semiconducting materials science.

This interest extends also strongly to several technological applications of semiconductors. Hydrogen atoms are present either in the materials's growth, as part of the source materials or carrier gases, or in the processing itself. This pervasiveness urges the understanding of the consequences of hydrogen incorporation in the materials.

In this chapter we intend to concisely place the research directly associated with this work inside that broader context. After an inevitably very brief introduction to the hydrogen in semiconductors subject we bring into special prominence the contribution put forward by the muon spin techniques, characteristic of this work, to the study of isolated hydrogen in semiconductors. Reasons for the choice of II-VI semiconductors for the theme os this work are presented and are followed by an outline of the present state of the art of the research on isolated hydrogen in this class of semiconductors.

1.2 Hydrogen as a passivating/activating impurity

Hydrogen is extremely reactive inside materials, and is best known for its role in the passivation of defects or impurities in semiconductors, thus altering significatively its electrical and optical properties.

One of the most significant effects of hydrogen incorporation in semiconductor's properties (and also one of the examples known for a longer time) is the passivation of dangling bonds in amorphous silicon [Pan78, Pau76]. This passivation phenomenon removes the unwanted electron energy levels from the bandgap, thus increasing the carriers mobility and allowing amorphous-silicon-based technology such as solar cells or thin-film transistors [Nic99b].

Hydrogen was also found to activate impurities in semiconductors, namely the

formation of shallow-acceptor Si–H and C–H complexes in Ge, the isoelectronic Si and C impurities being otherwise electrically inactive [Hal80]. However, this effect is far less common than passivation.

The passivation of impurities is also known since the 1980's, when the boron acceptor in Si was found to be deactivated by hydrogen [Pan83, Sah83]. Since then, many more examples were found not only in the elemental semiconductors, but also in compound semiconductors, namely from the III–V and II–VI families. Detailed acounts up to 2003 can be found in a number of reviews [Est95, Mye92, Myn03, Nic98, Nic99a, Pan91, Pea94].

Among recent developments, hydrogen was found to passivate Mn acceptors in ferromagnetic GaMnAs, changing epilayers from metallic to semiconducting behaviour upon hydrogenation [Bra04].

It is important to stress the distinction between passivation and compensation: passivation implies the formation of a complex between two impurities/defects, thereby forming a new defect with electrical and optical properties distinct from the two originating defects. In compensation, the two defects keep their individuality and mutually cancel the respective contributions to the conductivity. In terms of electrical transport characteristics, the two situations may be distinguished by the charge–carrier mobilities, which are smaller in the case of compensation [VdW05].

Despite the importance of the passivation effects, the hydrogen impurity *per se* may also affect the host material properties, and much research effort has been dedicated in the past decades to clarify the role of isolated hydrogen.

1.3 Isolated hydrogen in semiconductors

Due to the high reactivity of hydrogen, the studies on isolated hydrogen are much more demanding for usual experimental techniques. The information obtained by experimental methods that are sensible to hydrogen itself is therefore much scarcer, usually painfully obtained, and limited to a reduced number of systems, notably silicon [Bon99, Bon02, Her01, Hit99] and, recently, zinc oxide [Cox01a, Hof02, Lav02, McC02]. In the last thirty years, the use of positive muons as a model for

protons, together with theoretical work, has immensely enlarged the perspectives in this relevant, albeit hard, field. We shall here concisely present some essential results of these investigations, which are essential guides in the work now presented: from the "usual" role of hydrogen as a compensating center and the vast amount of information for hydrogen in silicon, to the possibility that hydrogen be a source of conductivity in ZnO and other ionic semiconductors. The information obtained by the muon analogue has played a major part in these investigations.

1.3.1 Hydrogen as a compensating amphoteric centre

Silicon is the system where most intensive resarch on isolated hydrogen has been done. Two charged states have been identified: H^- at the interstitial tetrahedral position and H^+ at the bond-centre site, together with the respective neutrals [Hit99]. Unlike the tetrahedral site, the bond-centre position was completely unexpected: the associated neutral was first seen in μSR measurements [Bre73], and labelled "anomalous muonium", in contrast with the tetrahedral "normal muonium". The identification at the bond-centre site was proposed on the basis of chemical arguments [Cox86, Sym84] and confirmed by μSR [Kie88]. This centre was also seen in ^{1}H-EPR [Gor87] and by deep–level transient spectroscopy[2], in implanted proton experiments [Bon99], which confirmed the site and electronic structure assigned by μSR. The bond-centre neutral state is found to be more stable than the tetrahedral neutral state [Est95]. Muonium thus represents an example of interstitial metastability, i.e. coexistence of two distinct atomic arrangements for a single charge state of a defect [Bar85, Est87].

This system has now been exhaustively scrutinized by a number of experimental methods:

(i) after twenty years of investigations on dozens of samples from extreme p–

[2]The DLTS method, basically, relies on the dependence of the width, therefore of the capacitance, of the depletion layer in a junction diode with the doping concentrations. The injection of a short pulse in the forward direction injects carriers in the junction and floods the deep traps, changing the capacitance. The return to equilibrium is afterwards observed as the time evolution of the junction voltage. Cf. [See82], p. 129.

type to extreme n–type, a detailed model of the muonium states and dynamics in silicon has been put forward [Hit99], including the determination of the muonium levels in the bandgap: the Mu(0/+) donor level was placed 0.21 eV below the conduction band minimum and the Mu(-/0) acceptor level was estimated to lie approximately at 0.56 eV below the conduction band minimum;

(ii) the experimental investigations with protons have progressed much more slowly, due to the difficulties of observing isolated hydrogen and have followed two distinct paths: either using implanted protons [Bon99, Bon02] or finding ways to dissociate hydrogen–containing complexes and subsequently observing its behaviour [Her01]. The results from the latter method have the advantage of being free from the radiolysis problematics affecting both μSR and the techniques based on implanted protons.

The positions of the (bond-centre) donor (0/+) and (tetrahedral) acceptor (-/0) energy levels below the bottom of the conduction band, for isolated hydrogen in silicon, are summarized in table 1.1. The μSR slight differences are expected from differences in the proton and muon zero point motion. Similar differences, both in magnitude and trend, have been found from path-integral molecular dynamics simulations for hydrogen/muonium in diamond [Her06].

Method	E(0/+)	E(-/0)
Muon implantation	0.21 eV [Kre95]	$<$ 0.56 eV [Hit99]
Proton implantation	0.16 eV [Hol91]	0.65 eV [Bon02]
Dissociation of P-H complexes [Her01]	0.16 eV	0.67 eV
First-principles calculations [VdW89]	0.2 eV	0.6 eV

Table 1.1: Position of the (isolated) hydrogen donor (0/+) and acceptor (-/0) energy conversion level below the bottom of the conduction band, as determined by several experimental methods and by first-principles calculations.

These results, together with the associated theoretical work [Her01], allow a rather complete view on the fundamental characteristics of isolated hydrogen in silicon. An essential characteristic is that the acceptor level $-/0$, corresponding to the ionization of the doubly charged state H^-, is lower in the bandgap than the donor level $0/+$ (cf. Fig. 1.1). This apparently paradoxical result of the larger binding energy of the second electron, despite Coulombic repulsion effects, is explained attending to the implied change in configuration: BC for H^+ and T for H^-. The energy change associated with the lattice relaxation in the different configurations explains this otherwise odd behaviour [And75, Wei82].

The Anderson $U = E(0/-) - E(+/0)$ quantity, defined as the difference between the energy of the $0/-$ level, $E(0/-)$ and the energy of the $+/0$ level, $E(+/0)$, is therefore negative. The shortened expression *negative-U* is then frequently used to express this inverted ordering of the donor and acceptor level in the bandgap. In the *positive-U* or normal ordering, the energy required to ionize an electron from the singly occupied state is larger than that required to ionize an electron from the doubly occupied state, and therefore the donor level $0/+$ lies lower in the bandgap than the acceptor level $-/0$.

Another consequence from the negative-U situation is that, in thermodynamical equilibrium, the neutral states are not stable, their formation energies being always higher than one of the charged states. Depending on the position of the Fermi level in the bandgap, the formation energies of the neutral states H^0_{BC} and H^0_T are either higher than the formation energy of H^+_{BC} (for Fermi levels in the lower midgap), or higher than the formation energy of H^-_T (for Fermi levels in the upper midgap). This means that if the material is electron-defficient (p-type), hydrogen will tend to donate its electron to the conduction band, forming the H^+_{BC} species and consequently acting as a donor. If the material is electron rich (n-type), hydrogen will tend to capture and extra electron from the conduction band, forming the H^-_T species, and therefore behaving as an acceptor. In short, hydrogen will tend to always counteract the prevailing conductivity, and to act as an amphoteric impurity.

It should also be pointed that, at some value of the Fermi level in the bandgap,

the formation energies of the H^+_{BC} configuration and the H^-_T configuration are found to be equal. This defines a transition level, loosely designated $E(+/-)$, which is particularly popular among theorists, because it corresponds to a transition between ground state configurations, which are easily accessible via total energy calculations with conventional methods. Theoretical works therefore tend to overlook the experimentally accessible neutral states and the corresponding transition levels, by concentrating in the $+/-$ transition level and, at most, at the lowest formation energy neutral state. Also, it is even more difficult to address theoretically the metastability issue of the neutral species, which is nevertheless established experimentally in firm grounds for Si and other semiconductors [Bon02, Bon03, Est87, Hol91]. These difficulties do not facilitate the comparison of experimental information with theoretical calculations.

The amphoteric behaviour of hydrogen is not exclusive of Si, but is common to other technologically important semiconductors. Evidence for this, both theoretical and experimental, have been accumulated for Ge [Bud00, Dob04], diamond, GaAs [Lic03] and GaN [Neu95].

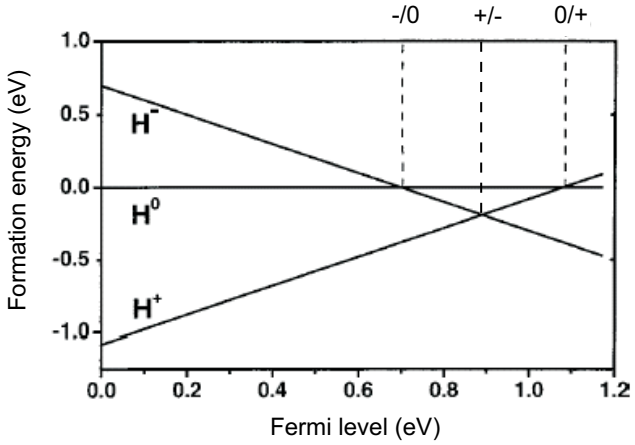

Figure 1.1: Formation energies of interstitial H^+_{BC}, H^0_{BC} and H^-_T in silicon, as a function of the position of the Fermi level in the bandgap [Her01]. The neutral state is never stable, for any position of the Fermi level, implying that the acceptor level $-/0$ lies lower than the donor level $0/+$. In this negative-U situation, the conversion level $+/-$ plays an important role in the theoretical conjectures.

1.3.2 Hydrogen as a source of conductivity

Amphoteric behaviour of hydrogen in semiconductors is, as pointed above, common to many of the most technologically relevant semiconductors. It implies that isolated hydrogen acts as a compensating centre, and not as an electrically active impurity.

The possibility that hydrogen behaved as a source of conductivity in materials had been raised as early as 1954 by E. Mollwo [Hei59, Mol54], who observed significant changes in the conductivity and luminescence of ZnO crystals upon heating in hydrogen atmosphere at high temperatures (above 500 ^{o}C). However, this subject only reappeared in 1999, with the discovery of a muonium state in CdS with a very small hyperfine interaction and an ionization energy of 26 meV [Gil99]. Parallel theoretical work predicted that hydrogen behaved as a shallow donor in ZnO as well [VdW00]. This prompted the finding in ZnO [Cox01a] of a muonium state similar to that found in CdS and the other cadmium chalcogenides CdSe and CdTe [Gil01].

This field has since then known intensive developments in many fronts:

(i) the shallow donor state in ZnO has been thoroughly scrutinized by many experimental methods and has been confirmed by EPR/ENDOR [Hof02] and IR measurements [Lav02, McC02].

(ii) μSR investigations in ZnO and the cadmium chalcogens have characterized exhaustively the shallow-donor muonium states [Alb01, Cox01a, Cox01b, Cox03b, Gil99, Gil00, Gil01] and suggested its location at an antibonding site [Gil01, Shi02]. The extended atomic orbital characteristic of the shallow donor wavefunction has also been investigated by probing the electron interaction with the nearest nuclei [Lor01]. Measurement of the g-value of the muonium electron were done and the results are consistent with known g-values for conduction electrons, which is a strong support for the shallow-donor model [Lor04]; this has prompted further technical developments in order to determine experimentally the sign of the g-factor as well [Lor06]. Experiments in p- and n-type CdTe have addressed the role of the interaction of the muonium states with impurities, and revealed the same electronic structure for the muonium centers, albeit with significantly different

formation probabilities [Cor04].

(iii) similar muonium states have been found or proposed in oxides (BaO, CdO, CeO_2, HfO_2, SnO_2, TiO_2, WO_3, Y_2O_3, ZrO_2) [Cox06a, Cox06b], nitrides [Dav03, Shi04] and chalcopyrites [Vil03b]. Such developments have been prompted by theoretical calculations suggesting that the $+/-$ conversion level might be located at a fixed value in an absolute energy scale [Kil02, Rob03, VdW03], for a wide range of semiconductors.

(iv) hydrogen-induced surface conductivity effects were also found in diamond [Mai00, Str04], and in ZnO [Wan05].

1.4 Isolated hydrogen in zinc II-VI compounds

1.4.1 Zinc II-VI compound semiconductors for optoelectronics

The zinc chalcogenides have been considered for long as potential candidates for use in optoelectronics applications in the blue/green region. However, progress was hampered by the common tendency of these materials (and of II–VI semiconductors in general) to unipolarity: ZnSe and ZnS are usually n–type and resist to p–type doping, and the inverse happens with ZnTe [Cha94, Des98, Zha02].

The interest in these materials, particularly in ZnSe, resurged in the 1990's, with the possibility of incorporating nitrogen acceptors above the equilibrium solubility, by beam doping during molecular beam epitaxial growth [Ohk91, Par90]. This allowed to produce reproducible p-type ZnSe films.

ZnSe has since then been thoroughly investigated, not only for the development of laser applications in the blue-green region [Gun97], but also for infrared optical applications [Gav03]. More recently, novel possible applications have been considered, such as using it as the photoconductive medium for the generation of terahertz radiation [Hol03, Kli05], or as the semiconductor layer in ferromagnetic/semiconductor heterostructures for spintronics applications [Edd06]. ZnTe has also appeared recently as a promising room-temperature ferromagnetic semi-

conductor, upon being doped with chromium [Oza06].

In the following paragraphs, we shall summarize the basic characteristics of the zinc chalcogenides, with a special emphasis on the doping problem in these materials.

Essential characteristics

The zinc chalcogenides ZnSe, ZnS and ZnTe all crystallize in the zinc blende structure[3], which has the translational symmetry of the face-centered cubic lattice. The conventional unit cell is depicted in Fig. 1.2. The most important interstitial positions can be seen there: the cation tetrahedral cage, surronded by four cations, the corresponding anion tetrahedral cage, and the bonding positions - bond-center, antibonding to the cation and antibonding to the anion. Some other positions are sometimes considered in the literature, but the above mentioned are the most important from both the theoretical and the experimental point of view.

The cation and anion cages are particularly important in the discussion of the interstitial hydrogen in its various charged states. Its is commonly anticipated that the negatively charged ion H^- is stabilized in the positively-charged environment of the cation cage and that the positively charged ion H^+ prefers negatively charged regions around the anion cage. Of course, this naïve view contains some heuristic value, but is found to be broken easily for the positive species (a proton) in highly covalent materials, where it easily forms chemical bonds within the material and may become stable at unexpected sites such as the bond-centre. In ionic compounds, it seems however that a more conventional location of H^+ in the anion cage is preferred, although the existence of chemical bonds with the anion may mean that the respective location is closer to the antibonding site than the actual center of the anion tetrahedron.

Table 1.2 summarizes the essential physical and electronical properties of these compounds. ZnS, ZnS and ZnTe all present a direct bandgap, whose minimum value in the reciprocal lattice is found at the Γ point in the centre of the Brillouin

[3]Actually, the prototypical compound of this crystallographical structure is ZnS, which is *the* zinc blende.

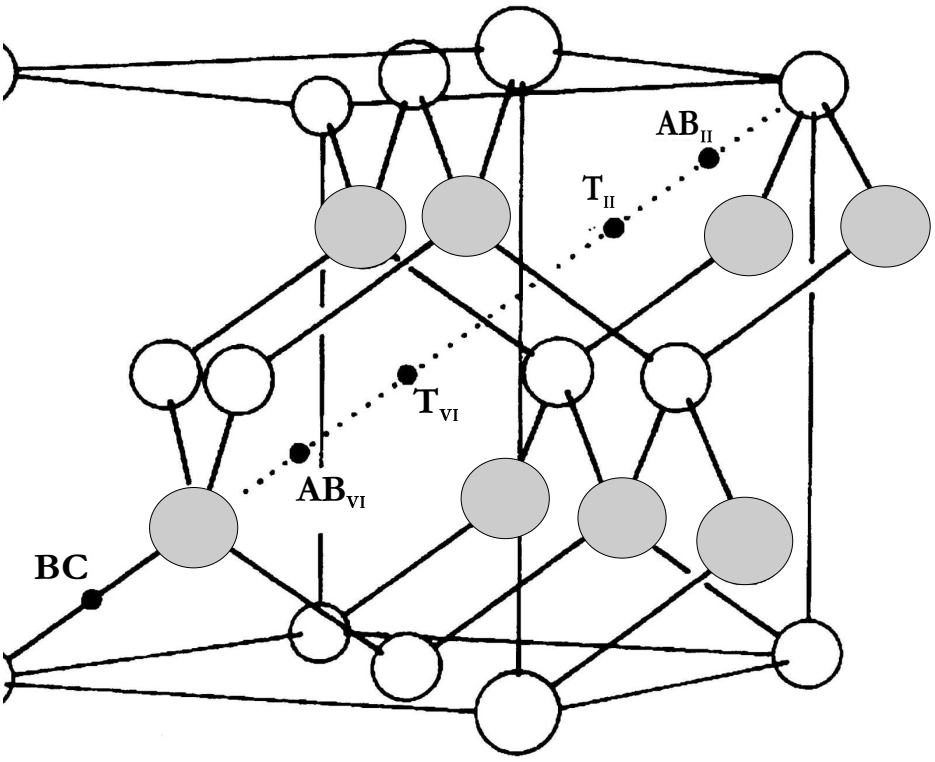

Figure 1.2: Conventional unit cell of the zinc blende structure: white circles indicate the group-II cation and grey circles denote the group-VI anion. The most important interstitial positions along the [111] direction are shown: bond-centre (BC), anion tetrahedral (T_{VI}), cation tetrahedral (T_{II}), anion antibonding (AB_{VI}) and cation antibonding (AB_{II}).

zone k=(0,0,0) [Ber87]. For ZnTe, the gap value corresponds to transition in the green/blue region, and in ZnSe and ZnS these lie already in the ultraviolet zone.

Material	a (Å)	E_g (eV)	χ	ϕ	m_e^0/m_0	m_h^0/m_0	ρ (g cm^{-3})	Θ_D (K)
ZnS	5.41	3.68	3.9	7.5	0.28	0.49	4.09	350
ZnSe	5.67	2.7	4.09*	6.82*	0.16	0.57	5.27	271
ZnTe	6.1	2.26	3.53*	5.76*	0.11	0.6	5.636	

Table 1.2: Essential properties of the zinc chalcogenides : a - lattice parameter at RT, E_g - bandgap at RT, χ - electron affinity, ϕ - photoelectric threshold ($\phi = E_g+\chi$), m_e^0 - electron effective mass at the bottom of the conduction band, m_h^0 - hole effective mass at the top of the valence band, ρ - density, Θ_D - Debye temperature. All values were obtained in Ref. [Mad82], except those marked with * which are from Ref. [Swa67].

The doping problem

As mentioned above, the zinc chalcogenides in particular and the II–VI materials in general present a strong tendency to unipolarity, and usually are easily doped in one of the types and resist being doped in the other type. ZnSe and ZnS are usually n–type and hard to obtain p–type; ZnTe is usually p–type, but resists to n–type doping [Cha94, Des98, Zha02].

A phenomenological "doping limit rule" has been proposed to explain these differences [Zha98], depending on the position of the valence band maximum and the conduction band minimum with respect to vacuum and to pinning levels. In this model, it is more probable not to achieve low-resistance p-type doping with a deep valence band maximum (e.g. ZnSe and ZnS). Also, a higher conduction band minimum turns it more difficult to obtain shallow donor levels (e.g. ZnTe).

A number of microscopic reasons have been raised to justify this behaviour. The compensation by native defects is a popular topic, but it seems not to be enough to justify the poor p–type doping in ZnSe [Lak91, Lak92], where the low solubility of the dopant appears as a much more important factor [Neu89, VdW93b]. The experimental success in achieving p–type doping in ZnSe has been obtained by increasing the solubility of the dopant beyond its equilibrium value, in the already mentioned N-doped MBE films [Ohk91, Par90]. Positive results have been achieved as well in bulk ZnSe:Sb samples, by forming quasi-stable non–equilibrium states *via* thermal treatments and subsequent quenching to RT [Pro02].

The passivation by formation of complexes with native defects and/or impurities seems to play an important role as well: the formation of DX centers hinders n–type doping in ZnTe [Cha94]. In ZnSe, complexes of donors with zinc vacancies have been reversibly formed by thermal annealing in different zinc atmospheres and identified *via* EPR and positron annihilation [Geb02, Irm01, Pro00]; these works clearly establish the possibility of controlling the conductivity of ZnSe by this method.

1.4.2 Hydrogen in zinc chalcogenides

Complexes of hydrogen

Very little is known about the complexes of hydrogen in II–VI semiconductors in general, and in the zinc chalcogenides in particular. Most of the information concentrates on the nitrogen acceptor in ZnSe, whose interaction with hydrogen has been thoroughly investigated, both experimentally [Ho95, Ho97, McC99, Tou00] and theoretically [Tor03]. These investigations established the role of hydrogen in the passivation of nitrogen in ZnSe:N. A similar role might be played regarding other impurities in ZnSe, namely the As and P acceptors [McC99, Tor03].

More recently, post-growth H irradiation was found to passivate oxygen impurity levels in ZnTe and Zn(Te,S), but not in Zn(Se,O) [Fel04, Pol04].

The research has also begun in ZnTe, where passivation of deep acceptors O_{Te} in bulk ZnTe [Bhu98, Bos99] and of nitrogen acceptors in MBE-grown ZnTe films

[Pel98] was found.

In the remainder II–VI's, CdTe has received particular attention [McC99]. In this compound, arsenic acceptors are found to be neutralized by hydrogen [Cle93].

Isolated hydrogen: *terra incognita*

The information about isolated hydrogen in the zinc chalcogenides up to now is even more limited than that regarding hydrogen complexes. Up to now, only limited exploratory work is available, both from theoretical and experimental point of view.

From the theoretical side, Kiliç and Zunger refer having calculated [Kil03] the equilibrium locations of H^+, H^0 and H^- in the zinc chalcogenides to be the bond-centre BC for the neutral and the positive species; the negative center prefers the cation tetrahedral cage T_{Zn}. However, the detailed calculations have not been published. These locations disagree with those presented by Van de Walle for ZnSe [VdW02], who finds the cation antibonding site AB_{Zn} as the most stable for the neutral and negative species. These results are summarized in Table 1.3.

Species	Location [Kil03]	Location [VdW02]
H^+	BC	BC
H^0	BC	AB_{Zn}
H^-	T_{Zn}	AB_{Zn}

Table 1.3: Equilibrium locations for the differently charged hydrogen states in ZnSe, according to Kiliç and Zunger [Kil03] and according to Van de Walle [VdW02]. Kiliç and Zunger refer having calculated the same sites also for ZnS and ZnTe. BC stands for the bond centre site and AB_{Zn} stands for the cation antibonding site.

In both references [Kil03] and [VdW02], the authors present results for the position of the acceptor level (-/0) and the donor level (+/0). For convenience in their calculations, Kiliç and Zunger adopt a definition of the values which maximizes its absolute value, namely referring the acceptor level with respect to the conduction band and the donor level with respect to the valence band. They thus define $\Gamma(-/0)$ as the position of the acceptor level below the conduction band minimum and $\Gamma(+/0)$ as the position of the donor level above the valence band maximum. No number is quoted in both references, but these levels are both shown in figures (Fig. 6 of ref. [Kil03] and Fig. 1 of ref. [VdW02]), from where they can be extracted.

The position of these levels is affected by the usual underestimation of the bandgap in the LDA approach, which is calculated for ZnSe to be 1.25 eV in ref. [Kil03] and 2.03 eV in ref. [VdW02]; the experimental value is 2.7 eV. Kiliç and Zunger propose correcting the levels with the following practical expressions:

$$\Gamma_{corr}(-/0) = \Gamma_{lda}(-/0) + 0.22\,\Delta E_g \tag{1.1}$$

$$\Gamma_{corr}(+/0) = \Gamma_{lda}(+/0) + 0.67\,\Delta E_g \tag{1.2}$$

where the subscript *corr* indicates corrected values and the subscript *lda* denotes the calculated LDA values. $\Delta E_g = E_g^{exp} - E_g^{lda}$ is the difference between the experimental bandgap E_g^{exp} and the calculated value E_g^{lda}. The LDA-calculated values of $\Gamma(+/0)$ and $\Gamma(-/0)$, for the three zinc chalcogenides ZnSe, ZnS and ZnTe, as well as the corresponding values corrected with eqs. 1.2, are summarized in table 1.4.

Van de Walle refers the problem as well, but indicates no correction. However, his Fig. 1 showing the levels plotted in a 2.7 eV bandgap (and not in a 2.03 eV one) suggest the existence of some unexplained correction.

The values of $\Gamma(-/0)$ and $\Gamma(+/0)$ for ZnSe, extracted from Fig. 6 in ref. [Kil03] and Fig. 1 in ref. [VdW02] are shown in table 1.5. Unsurprinsingly, attending to the referred divergence in the equilibrium locations, the values show very large differences. We also show the corresponding levels and bandgaps for ZnSe, ZnS and ZnTe, taken out from Fig. 6 in ref. [Kil03].

Material	$\Gamma_{lda}(-/0)$	$\Gamma_{corr}(-/0)$	$\Gamma_{lda}(+/0)$	$\Gamma_{corr}(+/0)$	Bandgap (LDA)
ZnS	1.4	1.9	2.6	4.1	1.3
ZnSe	0.8	1.12	2.1	3.1	1.25
ZnTe	1.2	1.24	1.3	1.4	2.1

Table 1.4: Position $\Gamma_{lda}(-/0)$ of the acceptor level below the conduction band minimum and position $\Gamma_{lda}(+/0)$ of the donor level above the valence band maximum in the zinc chalcogenides, as calculated with LDA in ref. [Kil03]. The corresponding values $\Gamma_{corr}(-/0)$ and $\Gamma_{corr}(+/0)$ resulting from the correction with expressions 1.2 are also shown, together with the LDA-bandgaps.

Reference	Method	$\Gamma(-/0)$	$\Gamma(+/0)$
[Kil03]	LDA	0.8	2.1
[Kil03]	LDA - corrected	1.12	3.1
[VdW02]	LDA - corrected?	2.0	2.1

Table 1.5: Position $\Gamma(-/0)$ of the acceptor level below the conduction band minimum and position $\Gamma(+/0)$ of the donor level above the valence band maximum in ZnSe.

Despite the large differences, both agree to place the acceptor level below the donor level in the bandgap, suggesting that hydrogen constitutes a negative–U centre in ZnSe.

Regarding the existing experimental information, it is limited to prospective μSR measurements done in the II–VI's in the middle 1980's by Schneider *et al.* [Sch86]. There the authors found evidence of Mu states with large hyperfine interaction in ZnSe and ZnS (respectively 3456.7 MHz and 3547.8 MHz). The value for ZnSe compares well with the calculated value (3333 MHz) for the muon at the cation tetrahedral site [VdW93a]. However, this investigation was not pursued.

The interest in a thorough investigation of the muonium states in the zinc chalcogenides gained a new impetus with the exciting developments in the respective cadmium counterparts, together with the progresses in the theoretical investigations of isolated hydrogen in wide bandgap compound semiconductors, as described above. This will be the arena of the work now presented.

Chapter 2

The μSR techniques

Ó rodas, ó engrenagens, r-r-r-r-r-r-r eterno!
Forte espasmo retido dos maquinismos em fúria!
Em fúria fora e dentro de mim,
Por todos os meus nervos dissecados fora,
Por todas as papilas fora de tudo com que eu sinto!
Tenho os lábios secos, ó grandes ruídos modernos,
De vos ouvir demasiadamente de perto,
E arde-me a cabeça de vos querer cantar com um excesso
De expressão de todas as minhas sensações,
Com um excesso contemporâneo de vós, ó máquinas![1]

Álvaro de Campos
Ode Triunfal

2.1 Introduction

The set of experimental techniques which use positive or negative muons as probes in condensed matter or gases is collectively known as μSR. This acronym was coined by Yamazaki, Nagamine, Crowe and Brewer in 1974 [Bre99]. In their own words: "*μSR stands for muon spin rotation, relaxation, resonance, research or what have you.*" .

[1] Free translation: *"O wheels, o gears, eternal r-r-r-r-r-r-r! Strong repressed spasm of infuriated mechanisms! Infuriated inside and outside me, outside by all my desiccated nerves, by all the taste buds outside everything which I feel with! My lips are dry, o great modern noises, of hearing you too closely, and my head fevers from wanting to sing you with an excess of expression of all my sensations, with an excess contemporary of you, o machines!"*

The muon (μ) and its respective muonic neutrino ν_μ constitute the second lepton family in particle physics standard model. The muon exists in two charge states, μ^+ and μ^-, which are antiparticles of each other. Negative muons are attracted by atomic nuclei upon implantation, rapidly cascading to $1s$ muonic orbitals with an extremely small radius ($\sim 250fm$) [Nag99]. Positive muons, being repelled by nuclei, occupy positions generally much farther apart and its subsequent behavior is essentially determined by the details of the material electronic structure. Consequently, the commonest muon techniques for condensed matter studies are based in the implantation of positive muons in matter, negative muon beams being of much more restricted use [Mam99, Mam06]. In this work, only positive-muon techniques have been used. In the remainder of this text, the shorter designation 'muon' will always mean 'positive muon'.

The systematic description of the μSR techniques much exceeds the objectives of this chapter. This can be found elsewhere [Bre94, Cho98, Cox87, Pat88, Sch85]. Here we shall limit ourselves to brief words on the fundamentals of the positive-muon-based techniques and to the essential features of the subtechniques used in this work.

2.2 μ^+ as a light pseudo-isotope of hydrogen

" *Who ordered that?*"[2]

In this work, we use the similarity between the proton and the muon, as expressed in table 2.1, which becomes more evident when considering the corresponding atoms, as summarized in table 2.2, where protium [p^+,e^-] and muonium [μ^+,e^-], corresponding to an electron bound to a positive muon[3], are compared.

[2]Comment of I. Rabi, when informed about the leptonic nature of the muon [Jun99].

[3]In particle physics, the designation *muonium* is reserved for the positive muon/negative muon $[\mu^+, \mu^-]$ bound system. However, in condensed matter physics and chemistry, the historically older designation *muonium*, due to Pontecorvo [Hug00, Pon58], has been kept, with no danger of confusion.

	muon	**proton**
charge/e	+1	+1
spin/$\hbar$	1/2	1/2
mass/m_{p}	0.1126	1
Gyromagnetic ratio (MHz T^{-1})	135.54	42.58
Lifetime/μs)	2.19703	stable

Table 2.1: Muon and proton properties compared. The muon's mass is approximately 1/9 of the the proton's mass m_{p} and its gyromagnetic ratio $\gamma_\mu = g_\mu \mu_\mu / h$ is larger than the proton's by approximately a factor of 3.

	Mu	**H**
Reduced mass (m_{e})	0.995187	0.999456
Binding energy in the ground state (eV)	13.54	13.60
Hyperfine parameter (MHz)	4463	1420.4
Gyromagnetic ratio/ (MHz T^{-1})	135.54	42.58
Atomic radius in the ground state (Å)	0.531736	0.529465

Table 2.2: Muonium (Mu) and hydrogen (H) properties compared. The factor of 3 between the hyperfine parameter of ground state muonium and ground state protium basically arises from the corresponding relation between the nuclei magnetic moments, the electron density at the nucleus being basically the same: when scaling the hyperfine parameter of Mu by the nuclei magnetic moment relation we obtain 1402 MHz.

Table 2.1 summarizes the physical properties of the muon, and compares it with the proton. The mass of the muon is only about 1/9 of the mass of the proton, but c. 206 times larger than the mass of the electron. The corresponding gyromagnetic ratio of the muon is therefore larger than the proton's. Of course, from the fundamental particle physics point of view, muons and protons are most different particles, muons being elementary leptons and protons compound hadrons. However, from the chemical point of view, the positive muon is far closer to the proton than to the positron, muon's lighter leptonic counterpart. This is eloquently expressed in table 2.2, where the two hydrogenic atoms protium and muonium are compared.

As expressed in tables 2.1 and 2.2, the positive muon can thus be seen, in the context of condensed matter physics, as a pseudo-isotope of hydrogen, with one ninth of its mass. The mass difference should of course be taken into account particularly when considering mass dependent properties, such as diffusion coefficients, but the electronics and chemistry are not expected to show much difference, except that arising from differences in zero-point energy, as we have already pointed out in the previous chapter [Cox03b, Her06]. For mass-dependent properties, the muon allows to extend isotopical studies into the lighter region.

2.3 Muonium

2.3.1 Preliminary remarks

As we shall see in section 2.4, the muon spin techniques rely on the possibility of following the evolution of the muon spin polarization upon implantation of nearly 100% spin-polarized muons in samples of the material under investigation. In the implantation process already, the possibility that the muon captures an electron, forming paramagnetic muonium, plays an important role in the final experimental outcome. We thus find it more adequate to begin by a summary of the essential physics of muonium in materials, relevant to this work, before discussing the details

of muon production, implantation in materials and subsequent thermalization.

Paramagnetic neutral muonium is easily distinguished due to the hyperfine interaction between the muon spin and the electron spin [Bra03][4]. This leads to characteristic precession frequencies of the muon spin in the presence of the hyperfine field. These precession frequencies of the muon present a distinctive behaviour with an applied magnetic field, as we move from the Zeeman *régime* where the hyperfine field dominates, to the Paschen-Back *régime* where the applied field is preponderant. Such studies, based upon the precession (or rotation) of the muon spin, are also designated muon spin rotation studies.

Despite the pure hyperfine frequency being observable in zero-field (the muonium "heartbeat" signal [Pat78]), the observation of the characteristic applied-field-dependence of the muonium precession frequencies requires that the applied field has a component perpendicular to the muon spin. Such spectroscopic studies are therefore best done in the transverse field geometry, where the external magnetic field is applied perpendicularly to the muon initial spin polarization. However, as shall be detailed below, the existence of muonium dynamical processes pre– or post–thermalization may lead to significant depolarization of the muon spin, thus preventing its study by the spectroscopic transverse-field method. In such cases, it is usually nevertheless possible to quench the muon polarization by application of an external magnetic field parallel to the initial muon spin. Such longitudinal field quenching experiments allow much insight into the strength of the depolarization mechanism. In these experiments, the polarization decay may be observed in the time spectrum as a polarization relaxation, thus providing access to the depolarization rates. Such longitudinal-field studies are therefore usually designated by muon-spin-relaxation studies.

The quenching of the polarization in a longitudinal field also opens the door to a further method of accessing the final muonium states formed upon depolarization: if the final state is thought to be diamagnetic or, being paramagnetic, its hyperfine interaction is presumably known, then it is possible to force transitions among the corresponding levels by means of resonant electromagnetic radiation. In longi-

[4]Cf., in the cited reference, its section 5.3.

tudinal field geometry, such induced transitions will in general further depolarize the muon spin. The presence of the muonium state under investigation will then be established through the comparison of the longitudinal field polarization with and without excitation by means of electromagnetic radiation. This method is far more useful for the investigation of final diamagnetic states, since the excitation frequency then simply corresponds to the well-known Larmor frequency. Suitable values of this frequency fall into the radio-frequency domain (50–200 MHz). This muon-spin-resonance subtechnique is then also usually known as radio-frequency-μSR (RF-μSR). In favourable cases where the hyperfine interaction of a paramagnetic muonium state is known, it is also possible to perform these studies, though then it may be preferable to use higher excitation frequencies, falling already in the microwave region (1–2 GHz) [Kre94].

In this section we will summarize some useful theoretical considerations on the hyperfine structure of the muonium atom and on the muonium dynamics. We leave for the next section a brief introduction to the basic μSR techniques.

2.3.2 Hyperfine structure of the muonium atom

The spectroscopy of muonium began [Hug60] in the domain of atomic and particle physics, where the hyperfine structure of this exotic atom has been (and still is) object of intense research [Bai71, Cle72, Hug00, Jun99, Liu99, Tho73] since it provides an ideal benchmark for extremely precise tests to quantum electrodynamical models, being an atom with a purely punctual and leptonic nucleus .

Inside solids, the positive muon may eventually capture and electron, which becomes bound by its attractive coulombian force. However, in such dense electronic media, the purely atomic description of muonium formed in vacuum or gases no longer applies. In the simplest cases, the electron wavefunction is still isotropic (i.e. spherically symmetric), but its density is changed with respect to the vacuum value. But other configurations are often found, most importantly the bond-centred configuration characterized by an axially symmetric wavefunction. When this Mu_{BC} configuration was first observed, it was labelled "anomalous" or "anisotropic" muonium, by contrast to the "normal", isotropic muonium. With

the development of the understanding of the muonium configurations in solids, "anomalous" muonium is now usually labelled Mu_{BC} and "normal" muonium is identified with the tetrahedral cage configuration, thus Mu_T.

Isotropic "normal" muonium

For $1s$ isotropic muonium, the relevant hyperfine hamiltonian simply corresponds to the well-known Fermi contact interaction [Bra03, Sch85] between the muon spin $\mathbf{S}_\mu$ and the electron spin $\mathbf{S}_e$:

$$H = hA\mathbf{S}_\mu \cdot \mathbf{S}_e \tag{2.1}$$

where the hyperfine interaction A is simply proportional to the electron density at the muon $|\Psi_{1s}(r=0)|^2 = 1/\pi a_0^3$:

$$A = \frac{\mu_0}{4\pi}\frac{8}{3}\frac{g_\mu \mu_\mu g_e \mu_B}{a_0^3} = \frac{\mu_0}{4\pi}\frac{8\pi}{3} g_\mu \mu_\mu g_e \mu_B \left|\Psi_{1s}(r=0)\right|^2 \tag{2.2}$$

where $g_\mu = 2$, $g_e = 2$, $\mu_\mu = e\hbar/2m_\mu$ and $\mu_B = e\hbar/2m_e$ are the muon gyromagnetic factor, electron gyromagnetic factor, muon magneton and Bohr magneton, respectively. μ_0 is the magnetic permeability of the free space and a_0 is the Bohr radius. The value of the hyperfine interaction in vacuum is $A = 4.463302765(53)$ GHz [Liu99]. As mentioned, in solids this value is in general smaller, due to admixture with the surrounding atomic wavefunctions, but there are also (much rarer) examples where the hyperfine interaction exceeds the vacuum value [Cox87].

μSR techniques being usually undertaken in the presence of an external applied magnetic field $\mathbf{B}$, the muon and electron Zeeman terms should be added to the hamiltonian 2.1:

$$H = hA\mathbf{S}_\mu \cdot \mathbf{S}_e - \mathcal{M}_\mu \cdot \mathbf{B} - \mathcal{M}_e \cdot \mathbf{B} \tag{2.3}$$

where the muon and electron magnetic moment operators $\mathcal{M}_\mu$ and $\mathcal{M}_e$ can be explicited in terms of the corresponding spin operators as:

$$\mathcal{M}_\mu = \frac{g_\mu \mu_\mu}{\hbar}\mathbf{S}_\mu \tag{2.4}$$

$$\mathcal{M}_e = -\frac{g_e \mu_B}{\hbar}\mathbf{S}_e \tag{2.5}$$

where the muon magneton μ_μ and the Bohr magneton μ_B are given, as usual, by:

$$\mu_\mu = \frac{e\hbar}{2m_\mu} \tag{2.6}$$

$$\mu_B = \frac{e\hbar}{2m_e} \tag{2.7}$$

Assuming, without loss of generality, that $\mathbf{B} = B\hat{\mathbf{k}}$, eq. 2.3 becomes:

$$H = hA\mathbf{S}_\mu \cdot \mathbf{S}_e - \frac{g_\mu \mu_\mu B}{\hbar}\hat{\mathbf{S}}_{\mu,z} + \frac{g_e \mu_B B}{\hbar}\hat{\mathbf{S}}_{e,z} = hA\mathbf{S}_\mu \cdot \mathbf{S}_e - \omega_\mu \hat{\mathbf{S}}_{\mu,z} + \omega_e \hat{\mathbf{S}}_{e,z} \tag{2.8}$$

where

$$\omega_e = 2\pi\gamma_e B \tag{2.9}$$

$$\omega_\mu = 2\pi\gamma_\mu B \tag{2.10}$$

and the muon and electron gyromagnetic ratios are, respectively,

$$\gamma_\mu = g_\mu\mu_\mu/h = 135.53\,\mathrm{MHz/T} \tag{2.11}$$

$$\gamma_e = g_e\mu_B/h = 28024.21\,\mathrm{MHz/T} \tag{2.12}$$

The eigenvectors and respective eigenvalues for hamiltonian 2.3 can be found in table 2.3, where the $|m_\mu\, m_e\rangle$ set has been used as a base of the spin space. A characteristic field B_0 ($B_0 = 0.1585$ T in vacuum) and a reduced field x are defined as:

$$B_0 = \frac{A}{\gamma_e + \gamma_\mu} \tag{2.13}$$

$$x = \frac{B}{B_0} \tag{2.14}$$

and the amplitudes of probability are:

$$\begin{aligned} \cos\zeta &= \left(\frac{1 + \frac{1}{2}\left(\frac{B_0}{B}\right)^2}{1 + \left(\frac{B_0}{B}\right)^2} \right)^{\frac{1}{2}} = \left(\frac{2x^2+1}{2(x^2+1)} \right)^{\frac{1}{2}} \\ \sin\zeta &= \left(\frac{\frac{1}{2}\left(\frac{B_0}{B}\right)^2}{1 + \left(\frac{B_0}{B}\right)^2} \right)^{\frac{1}{2}} = \left(\frac{1}{2(x^2+1)} \right)^{\frac{1}{2}} \end{aligned} \tag{2.15}$$

Eigenstate	Eigenvectors (base $\lvert m_\mu\, m_e\rangle$)	Eigenenergy
$\lvert 1\rangle$	$\lvert ++\rangle$	$\frac{h\,A}{4} + \frac{h(\gamma_e-\gamma_\mu)\,B}{2}$
$\lvert 2\rangle$	$\sin\zeta\lvert +-\rangle + \cos\zeta\lvert -+\rangle$	$-\frac{h\,A}{4} + \frac{h(\gamma_e+\gamma_\mu)\sqrt{B^2+B_0^2}}{2}$
$\lvert 3\rangle$	$\lvert --\rangle$	$\frac{h\,A}{4} - \frac{h(\gamma_e-\gamma_\mu)\,B}{2}$
$\lvert 4\rangle$	$\cos\zeta\lvert +-\rangle - \sin\zeta\lvert -+\rangle$	$-\frac{h\,A}{4} - \frac{h(\gamma_e+\gamma_\mu)\sqrt{B^2+B_0^2}}{2}$

Table 2.3: Isotropic muonium eigenvectors and eigenvalues corresponding to the Breit-Rabi hamiltonian 2.3. B_0 and the amplitudes of probability $\cos\zeta$ and $\sin\zeta$ are defined in equations 2.13 and 2.15.

The effect of an applied magnetic field on hyperfine levels was first considered by Breit and Rabi [Bre31]. The corresponding diagram of the hyperfine energy levels as a function of the applied magnetic field B is therefore usually known as the Breit-Rabi diagram. The essential physics contained in table 2.3 arises naturally through the consideration of the asymptotic limits $B = 0$ and $B \to \infty$. In the

asymptotic limit $B = 0$ (or in the limit of small magnetic fields $B << B_0$), the two spins add up to a total spin F=1, yielding a triplet $F = 1$ state with energy $h\,A/4$

$$|1\rangle = |++\rangle = |F = 1, m_F = +1\rangle \tag{2.16}$$
$$|2\rangle = \frac{\sqrt{2}}{2}|+-\rangle + \frac{\sqrt{2}}{2}|-+\rangle = |F = 1, m_F = 0\rangle \tag{2.17}$$
$$|3\rangle = |--\rangle = |F = 1, m_F = -1\rangle \tag{2.18}$$

and a singlet $F = 0$ state with energy $-3\,h\,A/4$

$$|4\rangle = \frac{\sqrt{2}}{2}|+-\rangle - \frac{\sqrt{2}}{2}|-+\rangle = |F = 0, m_F = 0\rangle \tag{2.19}$$

In the high magnetic field limit $B >> B_0$, the muon and the electron spins are decoupled and each then has the two Zeeman levels in the presence of the magnetic field B:

$$|1\rangle \rightarrow |++\rangle \tag{2.20}$$
$$|2\rangle \rightarrow |-+\rangle \tag{2.21}$$
$$|3\rangle \rightarrow |--\rangle \tag{2.22}$$
$$|4\rangle \rightarrow |+-\rangle \tag{2.23}$$

Of course, if $A = 0$ (or in the limit of $\mu_B\,B >> h\,A$), the two spins are free, and each then has two energy levels in the presence of the magnetic field B, separated by the Larmor energy $\mu_B\,B$.

The problem of muonium formation in matter being essentially one of statistical physics of quantum systems, it is best dealt with by the density-matrix, $\rho(t)$, formalism [Lan96, Tol79, Vil98]. The quantity of interest is essentially the polarization $\vec{p}_\mu(t)$ of the muon spin ensemble, which arises from the known result:

$$\vec{p}_\mu(t) = Tr[\rho(t)\vec{\sigma}_\mu] \tag{2.24}$$

where the density-matrix is defined as

$$\rho(t) = \frac{1}{4}\left[1 + \vec{p_\mu}(t)\cdot\vec{\sigma}_\mu + \vec{p_e}(t)\cdot\vec{\sigma}_e + \sum_{jk} P^{jk}(t)\sigma_\mu^j\sigma_e^k\right] \tag{2.25}$$

Attending to the usual initial condition arising from muonium being formed statistically with 50% electron spin up and 50% electron spin down:

$$\rho(0) = \frac{1}{4}\left[1 + \vec{p_\mu}(0)\cdot\vec{\sigma}_\mu\right] \tag{2.26}$$

The time dependent muon spin polarization projection in the muon incoming direction can then be proved to correspond to a sum of muonium frequencies

$$p_\mu(t) = \sum_{\mathrm{nm}} a_{\mathrm{nm}} \cos 2\pi\nu_{\mathrm{nm}} t \tag{2.27}$$

where the precession amplitudes a_{nm} and frequencies $\nu_{\mathrm{nm}} = (E_{\mathrm{n}} - E_{\mathrm{m}})/h$ are summarized in table 2.4. The $1-3$ and $2-4$ transitions correspond to forbidden transitions and are not observed [Sch85][5].

nm	a_{nm}	$\nu_{\mathrm{nm}} = \lvert E_{\mathrm{n}} - E_{\mathrm{m}}\rvert/h$
12	$(\cos\zeta)^2/2$	$\left\lvert \frac{A}{2} + \frac{(\gamma_e-\gamma_\mu)\,B}{2} - \frac{(\gamma_e+\gamma_\mu)\sqrt{B^2+B_0^2}}{2}\right\rvert$
34	$(\cos\zeta)^2/2$	$\left\lvert \frac{A}{2} - \frac{(\gamma_e-\gamma_\mu)\,B}{2} + \frac{(\gamma_e+\gamma_\mu)\sqrt{B^2+B_0^2}}{2}\right\rvert$
14	$(\sin\zeta)^2/2$	$\left\lvert \frac{A}{2} + \frac{(\gamma_e-\gamma_\mu)\,B}{2} + \frac{(\gamma_e+\gamma_\mu)\sqrt{B^2+B_0^2}}{2}\right\rvert$
23	$(\sin\zeta)^2/2$	$\left\lvert -\frac{A}{2} + \frac{(\gamma_e-\gamma_\mu)\,B}{2} + \frac{(\gamma_e+\gamma_\mu)\sqrt{B^2+B_0^2}}{2}\right\rvert$

Table 2.4: Isotropic muonium precession amplitudes and frequencies.

[5] Cf. p. 228 in the cited reference.

Again, much insight arises from inspection of the asymptotic limits. In the low-field limit ($B << B_0$), one has

$$\nu_{12} \rightarrow \frac{(\gamma_e - \gamma_\mu)\, B}{2} \tag{2.28}$$

$$\nu_{14} \rightarrow A \tag{2.29}$$

$$\nu_{23} \rightarrow \frac{(\gamma_e - \gamma_\mu)\, B}{2} \tag{2.30}$$

$$\nu_{34} \rightarrow A \tag{2.31}$$

The ν_{14} and ν_{34} are generally beyond the experimentally accessible range. Thus only half of the muonium precession is accessible experimentally. The ν_{12} and the ν_{23} coincide, but are here independent of the hyperfine interaction, simply corresponding to a gyromagnetic ration of 1.4 MHz/G. Measurements at low fields are therefore most useful to identify the presence of muonium, but nothing can be extracted about the hyperfine interaction.

In the high-field limit, we have

$$\nu_{12} \rightarrow \gamma_\mu\, B - \frac{A}{2} \tag{2.32}$$

$$\nu_{14} \rightarrow \gamma_e\, B + \frac{A}{2} \tag{2.33}$$

$$\nu_{23} \rightarrow \gamma_e\, B - \frac{A}{2} \tag{2.34}$$

$$\nu_{34} \rightarrow \gamma_\mu\, B + \frac{A}{2} \tag{2.35}$$

Now, the higher ν_{14} and the ν_{23} frequencies are generally unobservable, and the lower ν_{12} and the ν_{34} frequencies are symmetrically placed around the diamagnetic line at $\gamma_\mu\, B$, its difference being a direct measurement of the hyperfine interaction A.

In figure 2.1, we depict a Breit-Rabi diagram including a clear view of the crossing of the energies of the $|1\rangle$ and $|2\rangle$ eigenstates, which occurs at

$$B = \frac{\gamma_e - \gamma_\mu}{2\gamma_e\gamma_\mu} A \tag{2.36}$$

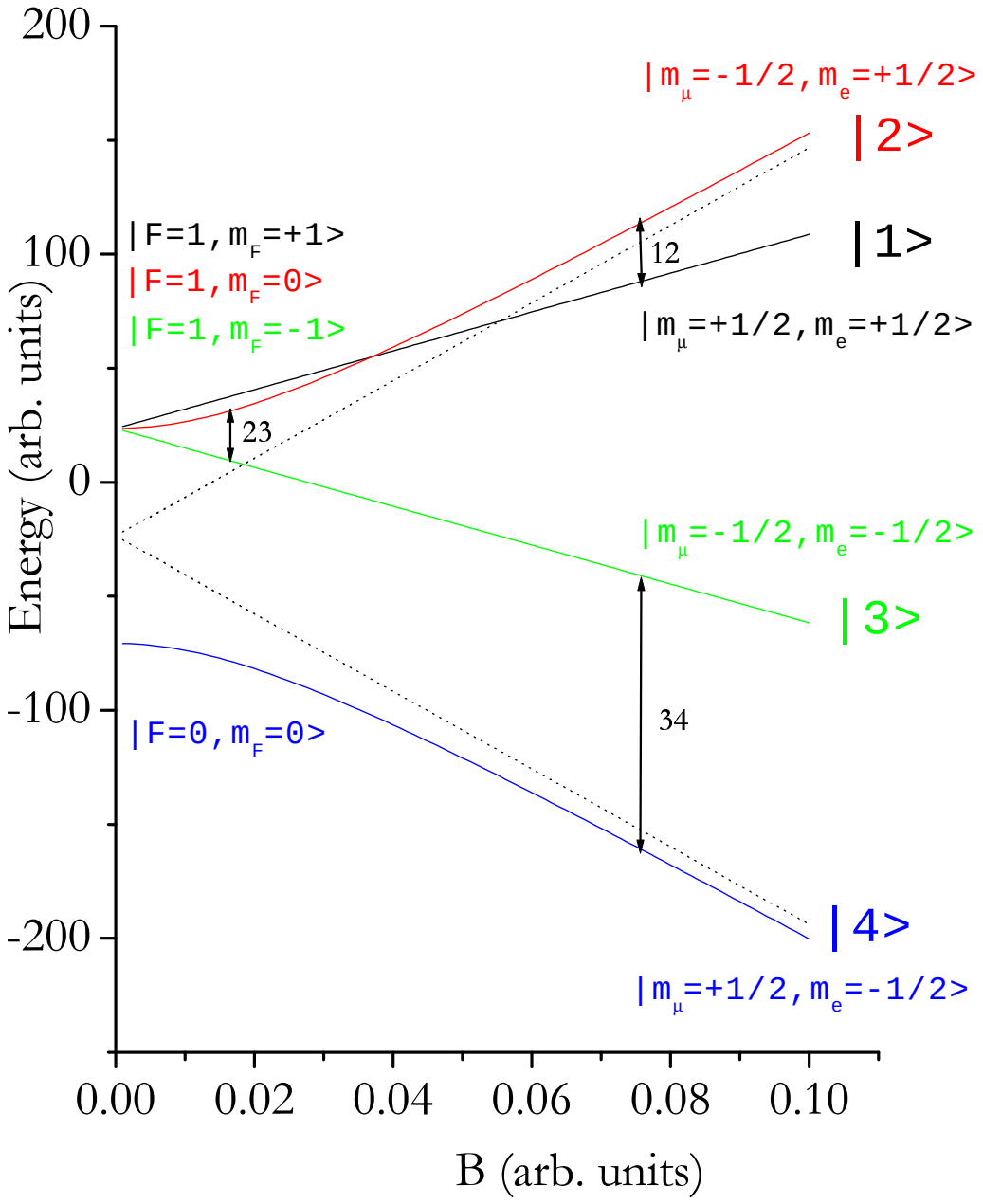

Figure 2.1: Energy eigenvalues of the isotropic muonium hyperfine hamiltonian 2.3, as a function of the applied magnetic field B. This diagram is usually known as the Breit-Rabi diagram. We have used a fictitious value of γ_e ($\gamma_e = 3\gamma_\mu$), in order to display more clearly the essential features of this diagram. We draw as well, as dashed lines, the asymptotes of the non-linear eigenenergies of the $|2\rangle$ and $|4\rangle$ eigenstates.

In order for this crossing to be clearly visible, a fictitious value of γ_e ($\gamma_e = 3\gamma_\mu$) was adopted in figure 2.1. A Breit-Rabi diagram with the real value of γ_e is shown in figure 2.2, for $A = 3454.26$ MHz, which, as we shall see in chapter 4, corresponds to the hyperfine parameter of the most stable muonium state in ZnSe. The transition frequencies corresponding to this value of A are shown in figure 2.3, where the level crossing corresponding between levels $|1\rangle$ and $|2\rangle$ is seen to occur at 12.7 T. The corresponding transition amplitudes are plotted in figure 2.4.

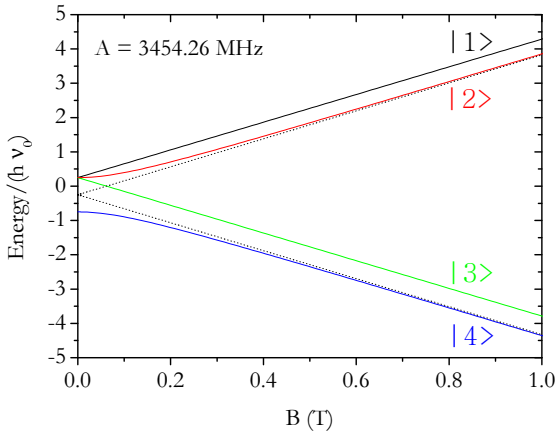

Figure 2.2: Low–field detail of the (non-fictitious) Breit-Rabi diagram for isotropic muonium with $A = 3454.26$ MHz. This value corresponds to the hyperfine interaction of the most stable muonium state in ZnSe, as we shall see in chapter 4. The dashed lines represent the high–field asymptotes of the $|2\rangle$ and $|4\rangle$ eigenstates.

Anisotropic "anomalous" muonium

The above formalism may be easily extended to the case where the electronic wavefunction is not isotropic, as in the bond-centred state found in silicon. The hyperfine interaction parameter now becomes a 2^{nd}–rank hyperfine tensor and the hamiltonian writes:

$$H = h\,\mathbf{S}_\mu \cdot \tilde{\mathbf{A}} \cdot \mathbf{S}_e - \mathcal{M}_\mu \cdot \mathbf{B} - \mathcal{M}_e \cdot \mathbf{B} \tag{2.37}$$

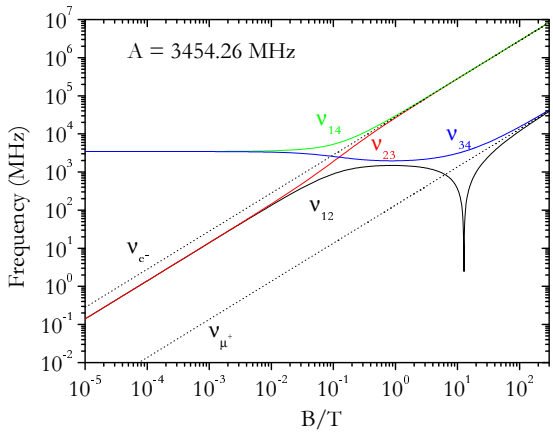

Figure 2.3: Hyperfine transition frequencies for an isotropic muonium state with $A = 3454.26$ MHz (as in fig. 2.2), as a function of the applied magnetic field B. The Larmor precession frequencies of the free muon and the free electron are drawn as dashed lines, clearly showing that for high fields the ν_{14} and the ν_{23} frequencies tend to $\nu_e \pm A/2$ and that the ν_{12} and the ν_{34} frequencies tend to $\nu_\mu \pm A/2$. The latter is preceded by the $1-2$ level crossing at 12.7 T.

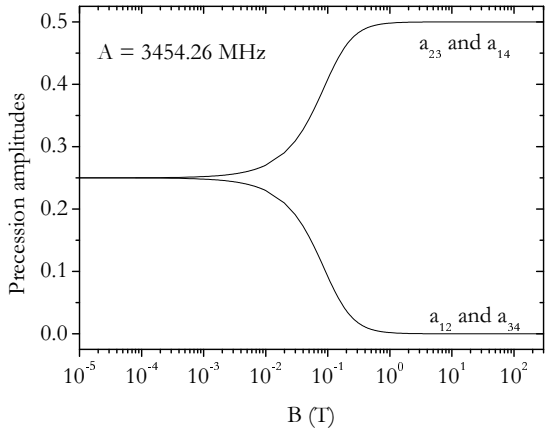

Figure 2.4: Amplitude of the permitted hyperfine transitions for isotropic muonium with $A = 3454.26$ MHz, as a function of the applied magnetic field B. The spectral weight is seen to be transferred at high fields from the $1-2$ and $3-4$ transitions to the $2-3$ and $1-4$ transitions.

In the bond-centred case, the hyperfine tensor is axially symmetric and can be written, in its proper coordinate system, as

$$\tilde{\mathbf{A}} = \begin{pmatrix} A_\perp & 0 & 0 \\ 0 & A_\perp & 0 \\ 0 & 0 & A_\parallel \end{pmatrix} \tag{2.38}$$

where the $A_\perp$ perpendicular and $A_\parallel$ parallel components of the tensor can be expressed in terms of an isotropic component A_{iso} and a dipolar component D as [Sch85]:

$$A_\perp = A_{\text{iso}} + D \tag{2.39}$$

$$A_\parallel = A_{\text{iso}} - 2\,D \tag{2.40}$$

Though it is possible to express analytically the eigenenergies and eigenvectors of the hamiltonian 2.37 for some important particular cases [Pat88], the general solution can only be obtained numerically. As can easily be anticipated, the precession amplitudes and frequencies are now dependent not only of the applied magnetic field $\boldsymbol{B}$, but also from the angle between $\boldsymbol{B}$ and the symmetry axis of the hyperfine center. We shall however go no further in the description of this particularly important model, since the experimental data obtained in this investigation seem to require no more than the isotropic muonium model. For further developments, see the "classical" references [Pat88, Sch85].

Quenching of isotropic muonium polarization in a magnetic field

As mentioned in this section's introduction, the quenching of the muon polarization in an applied field parallel to the muon initial spin polarization is a powerful tool when depolarizing mechanisms become important. Before moving on to the particulars of muonium dynamics, we present the theoretical framework for isotropic muonium subject to no dynamical depolarization process.

We begin by noting that, in the process of muonium formation, the muon captures an electron, forming, in the spin sub-space $|m_\mu, m_e\rangle$, one of the initial states $|+,+\rangle$, $|+,-\rangle$, $|-,+\rangle$ or $|-,-\rangle$. As can be seen in table 2.3, in the absence

of any applied field (i.e., in zero-field), the states $|+,+\rangle$ and $|-,-\rangle$ are eigenstates of the Breit-Rabi hamiltonian and therefore stationary, whereas the states $|-,+\rangle$ and $|+,-\rangle$ are superpositions of the $^1S_0$ and $^3S_1$, $m_F = 0$, $|2\rangle$ and $|4\rangle$ states. For the usual values of A, these muonium atoms formed in the latter non stationary states will therefore oscillate with the hyperfine frequency between the $|2\rangle$ and $|4\rangle$ states and depolarize too quickly to be observed. Thus the observable polarization is only 50%. In the high-field Paschen-Back *régime*, the initial states will all correspond to eigenstates, and therefore the polarization will be preserved.

The formation of muonium may be thus probed by means of the characteristic variation of the polarization with an applied longitudinal field. The correspondent time– and field–dependent polarization is found to be, for isotropic muonium [Pat88]:

$$p(t) = a_{\parallel} + \frac{(\sin 2\zeta)^2}{2} \cos 2\pi\nu_{24} t \tag{2.41}$$

where

$$a_{\parallel} = (\cos 2\zeta)^2 + \frac{(\sin 2\zeta)^2}{2} \tag{2.42}$$

and the frequency ν_{24} is, from the values of table 2.3.

$$\nu_{24} = (\gamma_\mu + \gamma_e)\sqrt{B^2 + B_0^2} \tag{2.43}$$

ν_{24} is in general too high to be experimentally visible and the corresponding parcel in equation 2.41 thus simply averages out to zero. The observed polarization then results

$$p = a_{\parallel} = \frac{1}{2} + \frac{x^2}{2\,(1+x^2)} \tag{2.44}$$

An example of this field-dependent polarization curve is shown in figure 2.5, where we have once again used the value $A = 3454.26$ MHz. This curve reflects once more the basic physics already discussed in the preceding section. for low fields half of the polarization is lost, and at high fields the muonium states formed correspond to eigenvectors and are therefore stationary, the muon spin polarization

being preserved. Such curve is therefore appropriately known as a repolarization curve.

Such characteristic variations of polarization with applied field constitute a very powerful tool to probe the formation of muonium, even in cases where it is subject to strong dynamical interactions that lead to the loss of muon spin polarization, thus preventing its direct spectroscopical identification. This loss in muon spin polarization is often designated "missing fraction". In such cases, as we shall see below, the repolarization curves can be distorted with respect to the shape of eq. 2.44.

The first identification of muonium formation in solids has actually been postulated based upon the existence of "missing fractions" and obtained by means of repolarization curves [Fer57, Fer60, Sen57], even before direct spectroscopic identification in transverse field was possible [Hug60].

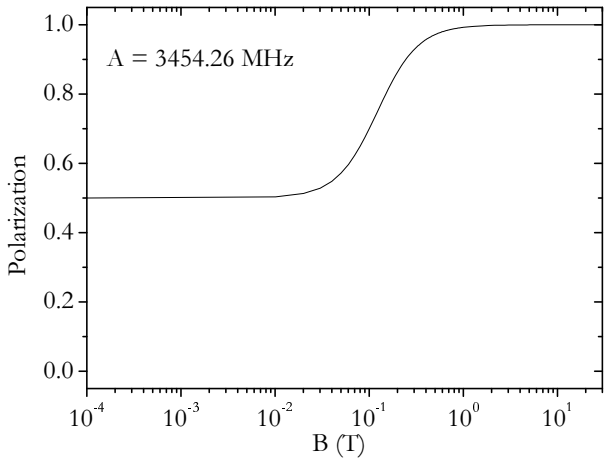

Figure 2.5: Dependence of the muon spin polarization with the applied longitudinal magnetic field B, for an isotropic muonium state with $A = 3454.26$ MHz. The spin polarization is shown to vary from 50% at zero-field up to 100% at high-fields. This curve is therefore known as a repolarization curve.

2.3.3 Muonium dynamics

If dynamical processes such as charge or spin–exchange exist, these will induce a depolarization of the muon spin. This simply arises from the finite lifetime of the converting state, as can be seen from the following very simple argument. If a state 1 is converting to a state 2 with a rate $\lambda = 1/\tau$, where τ is the lifetime of state 1:

$$Mu_1 \underset{\lambda}{\rightarrow} Mu_2 \tag{2.45}$$

then the polarization change dP_1 of state 1 in a time interval dt will be

$$dP_1 = -\lambda\, P_1\, dt \tag{2.46}$$

implying an exponential relaxation of the corresponding polarization

$$P_1(t) = P_1^0\, \exp(-\lambda\, t) \tag{2.47}$$

If λ is inside the experimental frequency window, it is possible to have access to these conversion and/or inter-conversion processes, which appear *via* relaxation of the corresponding states' polarization. If λ is too high, then the entire polarization of the converting state is lost before it can be observed and a "missing fraction" in the polarization is detected. In such conversion cases, the precession frequency of the final state can nevertheless be observed and the existence of a prior conversion process can be inferred from the shifting of the precession phase, as we shall see.

The general form of the polarization of muonium subject to interconversion dynamical processes can then be written as a sum of exponentially relaxing phase-shifted precession frequencies [Pat88]:

$$P(t) = \sum_{nm} a_{nm} \exp\left(-\lambda_{nm}\, t\right) \cos\left(2\pi\nu_{nm} t + \phi_{nm}\right) \tag{2.48}$$

Muonium dynamics has been the object of intensive theoretical treatment over the years [Cho94, Dua03, Pat88, Sch85, Smi94]. We shall not here delve it deep, but rather concentrate on two approaches with proved much useful in the course of this investigation: firstly presenting a simple approach to the problem of conversion

between two isotropic muonium states, as seen in transverse field, and then summarizing some essential results from the Nosov-Yakovleva theory for spin/charge-exchange muonium dynamics, as probed by longitudinal field methods. While these two selected examples are far from covering the entire spectrum of this ample field, they nevertheless contain most of the essential features common to all dynamical approaches, independently of their degree of sophistication.

Conversion between muonium states: a simple approach

The conversion of an initial state, after some lifetime, to a final state gives rise to a change in the precession frequency. If the initial state lives long compared to the observation time, only the spin precession of the initial state is observed. In the other extreme of a short lifetime, one sees only the precession of the final state, but some effects of the precursor state might still be detectable as a phase shift or a reduction in amplitude. Since the lifetime often depends on temperature, one may observe a transition from one extreme to the other as a function of temperature. A general treatment of the spin precession in the conversion region is given in Ref. [Mei82]. In the high-field case, the simple one-dimensional formula as given e.g. in Ref. [Mos83] and Ref. [Kie86] can be applied. The polarization of muons at state I, detected via frequency ω_{I} and with initial polarization P_I, converting at an instant t' to a state II, detected via frequency ω_{II}:

$$P'(t) = P_I \Theta(t' - t) \cos \omega_I \, t + P_1 \Theta(t - t') \cos \left[\omega_{II}(t - t') + \omega_I \, t'\right] \tag{2.49}$$

where $\Theta(x)$ represents the step function

$$\Theta(x) = \begin{cases} 1 & if \quad x > 0 \\ 0 & if \quad x \leq 0 \end{cases} \tag{2.50}$$

Assuming that the conversion time t' follows a Poisson distribution with mean conversion time τ, then the fraction df of muons converting from $\mathrm{Mu_I}$ to $\mathrm{Mu_{II}}$ in the infinitesimal time interval $[t', t' + dt'[$ is simply:

$$df = \frac{1}{\tau} \exp\left(-\frac{t'}{\tau}\right) dt' \tag{2.51}$$

The total polarization for the muon ensemble arises from the sum

$$P(t) = \int_0^\infty P'(t) df \tag{2.52}$$

and the result of the integration is:

$$\begin{aligned} \Delta P(t) &= P_{\mathrm{I}} \exp(-t/\tau) \cos(\omega_{\mathrm{I}}\, t) \\ &+ \frac{P_{\mathrm{I}}}{\sqrt{1+(\Delta\omega\,\tau)^2}} \cos(\omega_{\mathrm{II}}\, t - \tan^{-1}(\Delta\omega\,\tau)) \\ &- \frac{P_{\mathrm{I}} \exp(-t/\tau)}{\sqrt{1+(\Delta\omega\,\tau)^2}} \cos(\omega_{\mathrm{I}}\, t - \tan^{-1}(\Delta\omega\,\tau)) \end{aligned} \tag{2.53}$$

where $\Delta\omega = \omega_{\mathrm{II}} - \omega_{\mathrm{I}} > 0$. The first term in eq. 2.53 represents the relaxation of component I with the rate τ^{-1} corresponding to the lifetime of the state, the third term introducing as well a phase-shift and amplitude decrease of that component, at the the same relaxation rate τ^{-1}. The second term gives the increase of the amplitude of component II due to the conversion. The amplitude, if not relaxing otherwise, is constant and depends critically on the product $\Delta\omega\,\tau$. The conversion introduces a phase shift that also depends on $\Delta\omega\,\tau$.

Spin-charge exchange dynamics probed in longitudinal fields

Already in the very first muonium studies *via* the respective repolarization curves, it was found that the experimental curves deviated from the simple expression 2.44, full polarization not being attained as expected. This was interpreted as a sign of charge-exchange processes sufficiently slow to cause enough depolarization [Fer60]. Nosov and Yakovleva [Nos63] have developed subsequently a refined density-matrix approach assuming depolarization of the muon spin induced by electron spin-flips at a rate $2\,\nu$.

$$\left[\mu^+, e^{-,\uparrow}\right] \underset{2\nu}{\rightleftharpoons} \left[\mu^+, e^{-,\downarrow}\right] \tag{2.54}$$

They have further assumed this depolarization process to be still a consequence of the muon stopping mechanism, and thus to be over after a meantime τ.

Nosov and Yakovleva have explicitly considered the limiting cases of fast and slow electron spin relaxation. In the latter case (fast electron spin relaxation, $\nu >> \sqrt{\omega_0^2 + \omega_L^2}$, where $\omega_L = 2\pi\gamma_\mu B$ is the Larmor frequency), the muon spin polarization is simply found to relax exponentially with time:

$$P(t) = \exp\left(-\frac{\omega_0^2\, t}{4\nu}\right) \tag{2.55}$$

the average polarization resulting as a consequence of the dynamical process is:

$$\overline{P} = \int_0^\infty P(t) \exp\left(-\frac{t}{\tau}\right) \frac{dt}{\tau} = \frac{1}{1 + \omega_0^2\tau/4\nu} \tag{2.56}$$

In the case of slow electron spin relaxation ($\nu << \sqrt{\omega_0^2 + \omega_L^2}$), the authors find convenient to distinguish two situations :

i)in the case $\nu\tau << 1$ (i.e. meantime of the dynamical process much smaller than spin-flip period), the average polarization results

$$\overline{P} = \frac{1}{2(1+x^2)} \left\{ 1 + 2x^2 + \frac{1}{1 + (1+x^2)\omega_0^2\tau^2} \right\} \tag{2.57}$$

ii) in the case $\tau\sqrt{\omega_0^2 + \omega_L^2} >> 1$ (meantime of the dynamical process much larger than the muonium precession period), it is expressed as:

$$P = \frac{1 + 2x^2}{2(1 + x^2 + \nu\tau)} \tag{2.58}$$

Ivanter and Smilga [Iva68, Iva71] have subsequently extended the Nosov-Yakovleva theory for the entire range of electron spin depolarization and derived the following formula for the muon spin repolarization in a longitudinal field:

$$\overline{P} = \frac{\frac{1}{2}\,(1+\gamma\tau)^2 + 2\tau^2\,(x^2(1+\zeta)^2) + \frac{1}{2}}{\frac{1}{2}\,(1+\gamma\tau)^2 + 2\tau^2\,(x^2(1+\zeta)^2) + 1 + \frac{\gamma\tau}{2}} \tag{2.59}$$

where x represents the reduced field defined in eq. 2.14 and γ is a dimensionless electron spin flip rate defined from the electron spin flip rate ν and the hyperfine parameter $\omega_0 = 2\pi A$:

$$\gamma = \frac{4\nu}{\omega_0} \tag{2.60}$$

and ζ is the ratio of the magnetic moments of the muon and of the electron:

$$\zeta = \frac{\mu_\mu}{\mu_B} = \frac{m_e}{m_\mu} \tag{2.61}$$

The exponential decay of polarization with time in a longitudinal-field experiment, found in eq. 2.55, is a general characteristic of isotropic muonium undergoing cyclic charge exchange:

$$P(t) = P_0 \exp\left(-\frac{t}{T_1}\right) \tag{2.62}$$

A particularly useful analytical approximation for T_1 was derived by Chow [Cho94], for the case of different rates of electron capture and release by the muon:

$$Mu^0 \underset{\lambda_0}{\longrightarrow} Mu^\pm \tag{2.63}$$

$$Mu^\pm \underset{\lambda_\pm}{\longrightarrow} Mu^0 \tag{2.64}$$

the spin-lattice $1/T_1$ relaxation being found to be, in the limit $\tau >> \lambda_0^{-1}$:

$$\frac{1}{T_1} = \frac{1}{2}\left(\frac{\lambda_0\,\lambda_\pm}{\lambda_0 + \lambda_\pm}\right)\left(\frac{\omega_0^2}{\lambda_0^2 + \omega_{24}^2}\right) \tag{2.65}$$

Equation 2.65 gives back the result found by Nosov-Yakovleva (eq. 2.55) when $\lambda_0 = \lambda_\pm = \nu$ and $\nu >> \omega_{24}$.

Despite its intrinsic limitations and the subsequent work on muonium dynamics, the Nosov-Yakovleva simpler approach keeps its vitality and usefulness for the experimentalist [Pat88].

Further approaches to the mechanisms of the muon spin depolarization include the master-equation approach of Celio and Meier [Cel83] and the time-ordered stochastic method adopted by Senba [Sen90, Sen93, Sen00]. Reviews of these developments can be found, e.g., in refs. [Cho94, Dua03, Pat88, Sch85, Smi94].

2.4 Production of polarized muon beams

Positive muons are naturally produced in the high atmosphere by nuclear reactions of cosmic rays generating pions, such as:

$$p + p \rightarrow p + n + \pi^+ \tag{2.66}$$

The pions rapidly decay into muons and neutrinos (mean life is 26 ns):

$$\pi^+ \xrightarrow[26\,ns]{} \mu^+ + \nu_\mu \tag{2.67}$$

For laboratorial experimental research, the same principle is used to produce muons [Eat99]: protons are accelerated to high energies (typically 500 to 800 MeV) and afterwards directed towards a target made of a light element (usually graphite or beryllium), where the proton-nuclei reactions favour the production of pions as in eq. 2.66. The pion decay follows according to eq. 2.67. The resulting muons are collected, discriminated according to electric charge and directed to implantation into the sample.

2.4.1 Muon decay

Muons are radioactive particles, decaying *via* weak interaction with a meanlife of $2.2\,\mu$s, according to equation:

$$\mu^+ \xrightarrow[2.2\,\mu s]{} e^+ + \nu_e + \nu_\mu \tag{2.68}$$

The usefulness of the muon as a condensed matter probe comes from its decay reaction (eq. 2.68). In the muon's reference frame, the positron is emitted with a maximum kinetic energy $E_{\max} = 52.3$ MeV. Governed by the weak interaction, the muon decay does not follow parity conservation, and this shows up as an asymmetry in the positron emission direction. The probability dW for emission of a positron with energy in the interval $[E, E + dE]$, in the directions inside the cone with aperture angle between $[\theta, \theta + d\theta]$ (defined with respect to the direction of the muon's spin), is defined by the expression [Jun99, Sch85]:

$$dW = \frac{G^2 m_\mu^5}{192\pi^3} (3 - 2\varepsilon) \varepsilon^2 [1 + A(\varepsilon) \cos\theta] \, d\varepsilon \, d\cos\theta \tag{2.69}$$

where $G/\sqrt{2} = 1.01 \times 10^{-5} m_p^{-2}$ expresses the intensity of the weak interaction (m_p is the proton's mass), $\varepsilon = E/E_{\max}$ is the energy of the positron normalized to the maximum energy and $A(\varepsilon)$ is a factor governing the asymmetry in the angular distribution of the decay positrons.

$$A(\varepsilon) = \frac{2\varepsilon - 1}{3 - 2\varepsilon} \tag{2.70}$$

The energy spectrum of decay positrons (resulting from the integration over θ of eq. 2.69) is show in Fig. 2.6, together with the asymmetry factor $A(\varepsilon)$.

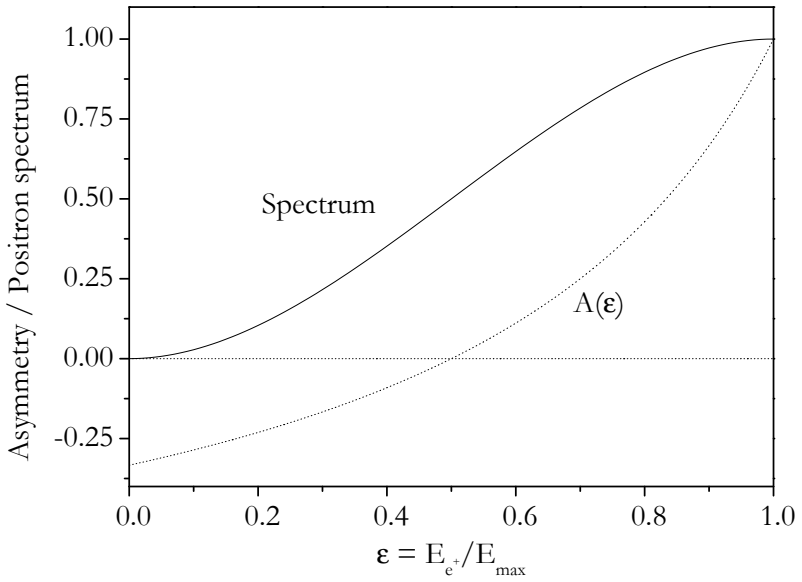

Figure 2.6: Normalized energy spectrum of decay positrons (solid line) and dependence of asymmetry with positron energy (dotted line).

The angular distribution of decay positrons is represented in Fig. 2.7 for some values of the asymmetry factor, as well as for the average asymmetry value, $\langle a \rangle$, for all energies $\left(\langle a \rangle = \frac{1}{3}\right)$.

These characteristics of the muon decay allow the monitoring of the muon spin direction, after implantation in a material, by measuring the time evolution of the asymmetry in the positron emission. Of course, a *sine qua non* condition for that is the presence of some degree of spin polarization of the ensemble of implanted muons (*i.e.*, a non-zero average component in some direction of the ensemble of muon spins).

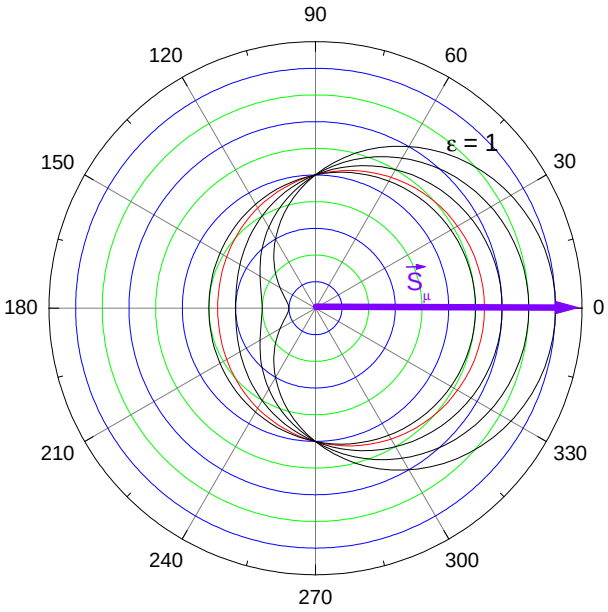

Figure 2.7: Angular distribution of decay positrons with relation to the muon spin direction (at 0 degrees). We represent the cases of maximum positron energy, as well as the result of integration over all energies (red line).

2.4.2 Polarized muon beams

Again, the physics of the particles involved gives the means to obtain not only partially polarized, but even *completely* polarized muon beams. As a matter of fact, the pion decays (eq. 2.67) into a muon and a muonic neutrino. But the neutrino, being a zero-mass particle, has negative helicity (*i.e.*, its linear momentum is necessarily antiparallel to its spin).[6] So, as the pion has zero spin, linear momentum and angular momentum conservation (cf. fig. 2.8) imply that, in the pion's reference frame, the muon helicity is negative as well. The muon resulting from the pion decay thus has its spin necessarily anti-parallel to its momentum, in the pion reference frame. It is therefore possible to produce an almost 100% spin-polarized muon beam by using the muons emitted in a small solid angle, by pions at rest. Usually, the small amount of muons escaping from the target's surface, emitted by pions thermalized in that location, are used [Pif76]. These muons have a kinetic energy of 4 MeV and are 100% spin-polarized in any emission direction. It is also possible to use muons emitted by pions in flight, albeit the polarization of such beams is smaller.

Figure 2.8: The decay of the positive pion. Conservation of linear and angular momentum imply that the muon's spin is antiparallel to its linear momentum.

[6] The superkamiokande experiment [Fuk98, Pas06] seems to indicate a non-zero mass for neutrinos. However, this crucial result does not affect the known experimental result that the neutrino helicity, and therefore the muon's, is sufficiently well defined.

2.5 Muon implantation and thermalization

The spin-polarized muon beam is directed to the sample, where the muon implantation occurs. The implantation and thermalization of 4–MeV muons in a solid is of course a violent process, its details remaining somewhat obscure, particularly at the final stages of thermalization, where the muon spin is often subject of powerful interactions which lead to the loss of spin polarization. Such polarization losses are often designated by "missing fraction(s)".

For the initial higher energies, the thermalization proceeds *via* usual "coulombian" collisions with electrons, which is adequately described by the Bethe-Bloch theory [Fle82, Leo94, Sch85]. These processes develop essentially *via* the electrostatic interaction and therefore the muon spin is not involved, leading to a conservation of the spin-polarization. After an extremely short time (which varies from 30 ns for a gas like He at 3 atm [Fle82] to only about 10 ps for a solid like silicon [Pat88]), the muon velocity approaches values close to the velocities of valence electrons in the material (c. 35 keV, [Fle82]), so that resonant charge-exchange processes set-in, further reducing the muon energy up to tens of eV. These charge-exchange processes consist of cyclic capture and release of electrons of the medium by the muon, in cyclic formation and dissociation of the muonium atom. In the gas phase, the ionization potential of the medium plays a decisive role in muonium formation at this stage, this being favoured on media with ionization potentials less than 13.6 eV (the ionization potential of Mu) [Ars84, Fle82, Hug70a, Hug70b]. This charge-exchange *régime* is found to be extremely fast in gases (for example, about 76 cycles occur in Ar at 1 atm, lasting about 14 ps [Fle82]). Since they strongly depend on the density, these charge-exchange processes are expected to be even faster in condensed matter, and thus no appreciable muon-spin-depolarization is expected (the lifetime of the neutral state in the process is much shorter than the inverse hyperfine interaction, whose influence on the muon spin thus becomes negligible) [Pat88, Sch85, Vaĭ60].

The most crucial stage, which has been continuously discussed over the years, is that of the chemical interactions of the resulting epithermal species (Mu^+, Mu^0 and, possibly, Mu^-), which may largely influence the final paramagnetic and dia-

magnetic fractions and lead to depolarization. This has been studied more deeply for the gas phase: here the stopping range of the implanted muons is quite long (about 40 cm for Ar in 1 atm [Fle82]), and the depolarization processes have been frequently explained in terms of "hot chemistry" models, implying reactions of the epithermal muon(ium) energetically unaccessible to the thermalized species [Wal83]. However, this model deals with difficulty with the large missing fractions observed in the condensed phase since it provides no sufficiently fast depolarizing mechanism. An alternative "spur model" has been proposed, by analogy to what is known of the positron thermalization from positron annihilation experiments, considering that the muon might interact with the products of its radiation track [Per78], particularly the radiolysis electrons, not only by charge-exchange, but also by spin-exchange processes [Per82]. The "spur" model for muonium formation in gases has been object of intense debate, since the long stopping range of muons in low-density matter seemed incompatible with significant interactions with radiolysis products [Wal83].

Due to the reduction of the stopping range, the interaction with the radiation track becomes more important for the condensed phase. In the liquid phase the relevance of "spur" processes over "hot chemistry" processes has been pointed out[Ars84]. Recent studies in supercritical CO_2 also suggest the predominance of radiolysis reactions over hot Mu reactions in this high-density fluid [Gha04]. Of course, the interaction with the track is expect to be even more important in solids, where the stopping range is much smaller (c. 700 μm, for a 4 MeV muon implanted in silicon [Pat88]).

Mu formation in semiconductors

Much less is known about the process of muonium formation in solids than in liquids and gases. It has been known for long that no muonium is formed in conductive materials [Swa58]. Here, fast charge exchange processes with conduction electrons remain even after thermalization, and basically the muon is not kept bound to any electron [Cha83, Vaĭ60].

In insulators and semiconductors, two basic models, inspired in the above men-

tioned "hot-model" and "spur-model", concur for the understanding of muonium formation [Sto99a]:

i) prompt (epithermal) muonium formation: the implanted muon suffers charge-exchange processes with the solid at the end of the thermalization process, the yield of Mu^+, Mu^0 and Mu^- being determined by the fraction of muons which, being at these charge states at some point of the thermalization process, do not have anymore enough energy either to ionize the lattice molecules, or to release the captured electrons;

ii) delayed muonium formation: the muon thermalizes at some charge state after the charge-exchange process described above, eventually capturing an electron from the radiolysis track left behind.

These two processes are generally intermixed and are not easily separable experimentally. A privileged access to delayed muonium formation is by application of electric fields in the kV/cm range, parallel to the muon linear momentum, during the μSR experiment. The electric-field either favors or hinders the capture of electrons from the track by the muon. Using this electric-field-μSR method, delayed muonium formation has been established for some insulators and cryocrystals [Sto97], notably solid nitrogen [Sto99a], as well as for GaAs [Sch05]. Delayed muonium formation is also a strong hypothesis for the electric-field-μSR dependence in CdS [Esh03] and GaP [Sto03].

An alternative explanation of the electric-field data without the need of considering delayed muonium formation considers capture at highly-excited (Rydberg) states, which is inhibited in the presence of the electric-field. This has been proposed upon observation of a feeble frequency shift in the shallow muonium ionization in CdS [Sto01], and the generalization to other systems was proposed as well [Sto04], in particular to GaAs [Sto05]. However, careful experiments revealed no phase shift of the observed Mu^0_{BC} state in GaAs, as expected if it proceeded from a precursor shallow state [Sch05]. The evidence from electron capture from the track and its suppression with electric fields must then find its root in alternative explanations, e. g. electron capture to the ground state, from an exciton [Sch05].

Recently, the use of pulsed radio-frequency techniques has arised as a possibility

to access directly the muonium formation [Cot03]. However, this technique fights with narrow time-windows, which make its use very limited up to now.

Mu^- formation

Of course, the same reasoning just presented for muonium formation can be applied to Mu^- formation. However, the problem of verifying Mu^- formation in μSR is preceded by the problem of its direct identification.

A fundamental problem in μSR studies is the extreme difficulty in discerning Mu^+ from Mu^- spectroscopically. In fact, as we have already pointed out above, the muon is essentially sensitive to the local magnetic field, which is of course very different in the case of the existence of a muon–electron hyperfine interaction (Mu^0) or in its absence (Mu^+). However, if the *1s* orbital is doubly occupied (Mu^-), then the electronic cloud magnetic moment is null and the total wavefunction is diamagnetic. So, the interaction of the muon spin with the electronic cloud for the Mu^- situation is therefore undistinguishable from Mu^+ by purely spectroscopic means. This problem has usually been circumvented in semiconductors either by doing experiments in highly doped samples, in order to force Mu^- or Mu^+ formation [Cho95, Cho96, Daw00], or by educated guess [Kre95, Hit99]. In the latter case, Mu^- formation, either prompt or delayed, has been proposed in the framework of an elaborate interpretation model.

However, the capture of two electrons by a muon thermalizing in a solid is by no means an uncommon or unobserved phenomenon. Mu^- formation has been directly observed by means of magnetic time-of-flight spectrometry after firing muons through thin metal foils [Kua87, Kua89].

The formation of H^- in solids is also a well-known phenomenon. Older measurements on hydrogen beams equilibrated in solid Be and Al foils show significant H^- formation [All58][7]. More recently, H^- formation has been observed by backscattering of 1-600 eV protons in dielectric surfaces [Bor00], and ionic compounds [Sou99], notably LiF [Ron99]. Significant differences have been found as well for the scattering in Al and AlF_3 surfaces, underlining the importance of the surface band

[7] Cf. section V. B, p. 1159.

structure [Lug05a, Lug05b]. This suggests that the capture of two electrons by the implanted muon may become more important with increasing ionic character of the host.

"Post-thermalization" processes

The question of whether the muon actually achieves thermal equilibrium with the lattice in its lifetime remains an open question, particularly for the delicate paramagnetic muonium fractions. For example, the paramagnetic muonium states are observed at low temperatures in silicon, albeit they correspond to no stable thermodynamical states of this negative-U system. The charged states corresponding to the thermodynamically stable states are nevertheless observed at higher temperatures, and the study of the temperature dependence of these states allows access to the conversion levels. Thus, the observation of the metastable neutral states, more than an hindrance, becomes a strength of the muon techniques.

After "thermalization", the muon may be involved in dynamical processes arising from its interaction with the material. For example, we have already mentioned the extremely fast charge-exchange processes in metals, where the muon captures and releases conduction electrons in such a fast way that the muonium bound state is unobservable, the process itself being too fast to cause any appreciable depolarization [Vaĭ60]. This charge– and/or spin–exchange processes may however become important depolarizing processes in undoped or lightly–doped semiconductors, when the charge/spin–exchange rates are sufficiently small so that the depolarization in the bound-muonium state is no longer negligible. Of course, such depolarizing mechanisms are both extremely dependent on the concentration of free carriers, hence on the doping and temperature.

Another important dynamical mechanism is that concerned with the muon's diffusion, which for sufficiently high temperatures and high concentrations of imperfections even allows the muon to be trapped at impurities and/or defects. For example, in the ternary chalcopyrite semiconductor $CuInSe_2$, diffusion data strongly suggest the muon to be trapped at copper vacancies [Vil02, Vil03a], whereas the muon analogue of the passivation of a zinc-acceptor in GaAs by hydrogen was

identified[Cho01]. Diffusion studies have thus played an important role in the modelling of hydrogen in semiconductors *via* μSR [Lic99a]. However, these studies rely on the interaction of the muon spin with nearby nuclei magnetic moments. The small density of nuclear magnetic moments in the zinc chalcogenides unfortunately prevents any useful research on this domain, justifying the absence of this important information in this work. It is possible to obtain information about paramagnetic Mu diffusion from motional narrowing behaviour in anisotropic states [Dua03, Dua06], but as we have already pointed out in section 2.3, only isotropic species are observed in this work.

2.6 Muon spin rotation, relaxation, resonance

2.6.1 Basic experimental setup

The basic experimental setup for muon experiments is drawn in Fig. 2.9. A spin-polarized muon beam is directed towards a sample of the material under scrutiny. A minimum of two positron detectors is adequately placed around the sample, usually in the forward (F) and backward (B) positions with respect to the upcoming beam. The basic sample environment includes adequate instruments for temperature dependence studies (cryostats, furnaces). External magnetic fields may be applied to the sample region, as will be detailed in the following sections.

In quasi-continuous muon sources such as PSI and TRIUMF, the start of the chronometer is set by an incoming muon crossing a thin cintilator placed before the sample. In pulsed sources such as ISIS, the approximation is assumed that the time zero coincides with the center of the muon pulse (which is 80 ns wide at ISIS); this approximation works well if the evolution of the implanted muon spin polarization takes place at a longer timescale than the muon pulse width [EMU04]. The stop of the chronometer is defined by the arrival of the corresponding decay positron at a given detector. A time histogram for each detector is henceforth accumulated. In some experiments, time-integral measurements may be enough, and the time histogram associated with time-differential measurements becomes unnecessary.

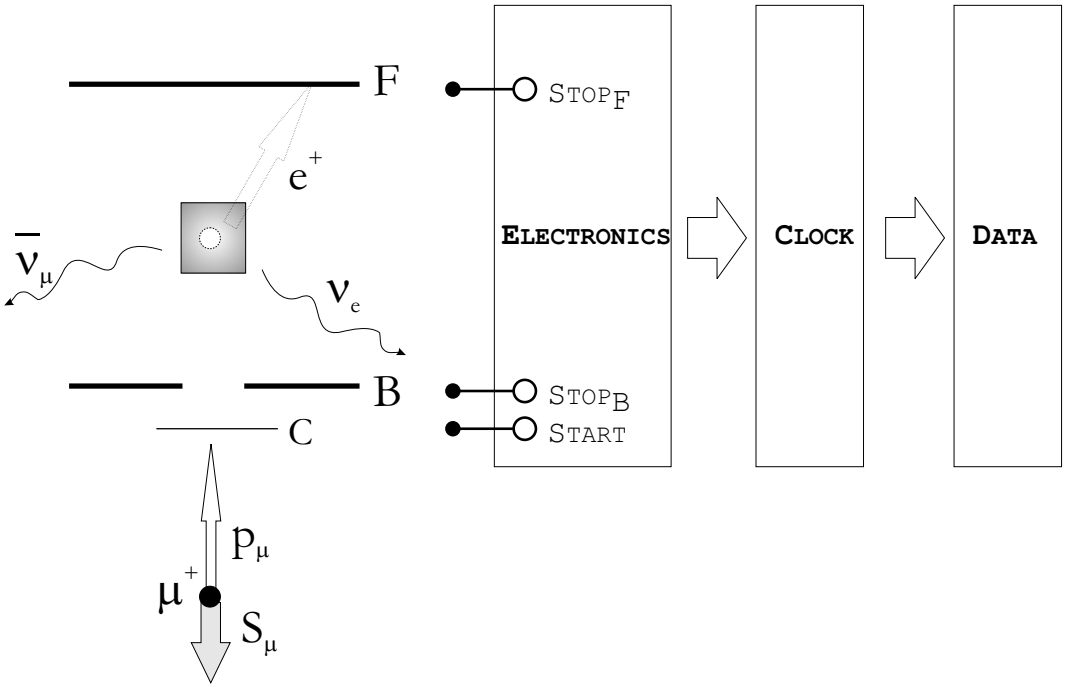

Figure 2.9: Basic setup of a muon experiment. Spin polarized muons are implanted in a sample and decay into detected positrons and undetected neutrinos. In the simplest arrangement, two positron detectors are placed in the forward and backward direction with respect to the incoming beam. The arrival of a single muon or muon pulse starts a chronometer, which is stopped upon detection of the corresponding decay positron. Time histograms for each detector are gathered.

The number of counts N_D in detector D may be described by the expression (see *e.g.* [Bre99])

$$N_D = B_D + N_0 \varepsilon_D \left[1 \pm A\, P_z\left(t\right)\right] \exp\left(-\frac{t}{\tau_\mu}\right) \tag{2.71}$$

where:

- B_D is a factor describing the spurious (background) counts in the detector, which in principle are time-independent;
- N_0, multiplied by the number of detectors, corresponds to the number of real events at time zero;
- ε_D is the detection efficiency, relating not only to the detector intrinsic efficiency, but also to the geometrical disposition (for example, a detector placed farther away detects less positrons, thus decreasing ε;
- A is the intrinsic asymmetry of the detector arrangement. For detector B, the count rate is proportional to $(1 + A)$, in the case of fully polarized muons with polarization in the detector's symmetry axis; in the same circumstances, the count rate is proportional to $(1 - A)$ for detector F;
- $P_z\left(t\right)$ is the time evolution of the z component of the muon spin polarization (where the z axis is defined by the incoming beam direction);
- τ_μ is the muon lifetime;

In a μSR experiment, we are interested in obtaining $P_z(t)$. This is usually done in two steps, by obtaining (i) the asymmetry $A\, P_z(t)$ in the experiment *proper* and (ii) the intrinsic detector asymmetry A in calibration measurements.

The intrinsic asymmetry A is in general less than the maximum theoretical value of 1/3 [Sch85]. It can be determined by calibration measurements on a sample where the muon spin polarization is known. Silver is usually used for this purpose, since 100% of the muons implanted on this metal are known to form an easily identifiable non-relaxing diamagnetic fraction. Low-transverse field (20 G) measurements on Ag are thus commonly used for these calibrations.

An experimental asymmetry is obtained through the difference between the number of counts in detectors F and B (after subtracting the background counts), normalized to the total number of counts (for more complex detector dispositions, simple generalizations apply):

$$A_{\text{exp}}(t) = \frac{[N_B(t) - B_B] - [N_F(t) - B_F]}{[N_B(t) - B_B] + [N_F(t) - B_F]} \tag{2.72}$$

However, due to different detector efficiencies, the expression 2.72 does not give us $A\,P_z(t)$ directly, but instead (after considering eq. 2.71):

$$A_{\text{exp}}(t) = \frac{(\alpha - 1) + (1 + \alpha)\,A\,P_z(t)}{(1 + \alpha) + (\alpha - 1)\,A\,P_z(t)} \tag{2.73}$$

where

$$\alpha = \frac{\varepsilon_B}{\varepsilon_F} \tag{2.74}$$

It is therefore necessary to correct the experimental asymmetry 2.72, which is usually done by computing:

$$A_{\text{corr}}(t) = \frac{N_B(t) - \alpha N_F(t)}{N_B(t) + \alpha N_F(t)} = A\,P_z(t) \tag{2.75}$$

The quantity α depends both on the intrinsic detection of the detectors and the geometrical details of the experimental setup, including positron absorption factors such as the sample thickness and the cryostat walls. α must therefore be determined for each case, usually together with the calibration measurements for the intrinsic (maximum) asymmetry A.

2.6.2 Muon spin rotation

The simplest experimental geometry corresponds to the case where an external magnetic field B is applied perpendicularly to the initial muon spin polarization, as depicted in Fig. 2.10. In this situation, and in the simplest situation where the muon spin is subject only to the Zeeman interaction with the applied magnetic field, a simple precession of the spin occurs around B, with the Larmor frequency ν_L:

$$\nu_L = \gamma_\mu B \tag{2.76}$$

In this case, the polarization component in the initial direction z has a sinusoidal temporal evolution:

$$P_z(t) = P_{\max} \cos(2\pi\nu_L t + \phi) \tag{2.77}$$

where the phase ϕ depends on the definition of time zero $t = 0$, and is trivially associated with precession frequencies high enough (compared with the experimental resolution) for a non-negligible rotation of the polarization to occur between the initial cintilator and the sample [Ama05]. These trivial phase shifts present no temperature dependence and are simply proportional to the applied field. More significantly, the existence of a temperature-dependent phase-shift is a clear sign of conversion between states, as discussed already in section 2.3.

This subtechnique based upon the muon spin precession is commonly designated *muon spin rotation* and, as mentioned in the beginning of section 2.3, is most adequate for muonium spectroscopy.

In Fig. 2.10 we show a particularly simple example, for calibration measurements on a silver sample. The individual time histograms for detectors F and B are shown, together with the corresponding asymmetry. The geometrical factor α can be extracted from these type of measurements as follows: the different detection efficiencies originating $\alpha \neq 1$ imply, in these TF measurements, that the experimental asymmetry oscilates with time around an average value different from zero. Fits to the time spectra are performed after correction of this offset by the fitting

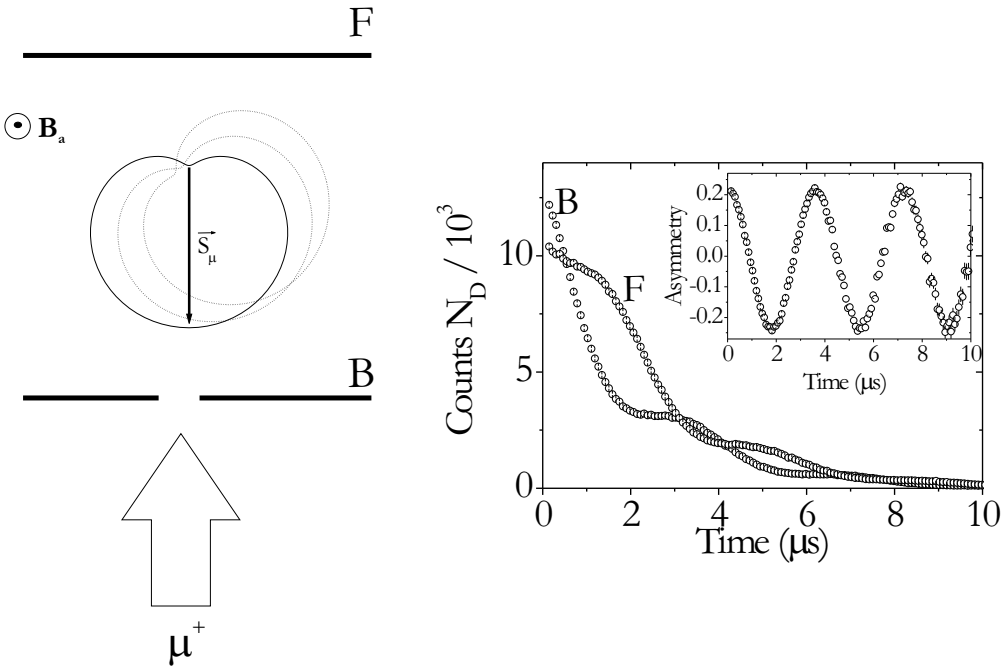

Figure 2.10: The basic muon spin rotation experiment. In the left side we sketch the basic setup: spin-polarized positive muons are implanted into a sample, in a region subjected to a magnetic field B_a perpendicular to the initial muon spin, surrounded by two positron detectors in the forward (F) and backward (B) direction. The asymmetric probability for positron emission rotates with the muon spin and is drawn for three different times. The positrons are detected by detectors F and B, forming histograms like those shown in the right side. The corrected asymmetry $A_{\rm corr}(t) = (N_B - \alpha N_F)/(N_B + \alpha N_F)$ is shown as an inset.

routine.

In muon spin rotation measurements, the presence of paramagnetic muonium is easily identified by its characteristics precession frequencies. A typical experimental test for the presence of paramagnetic muonium is done at low-field, where the characteristic $\nu_{12} = \nu_{23}$ precession at 1.4 MHz/G is observed. An example is shown in figure 2.11.

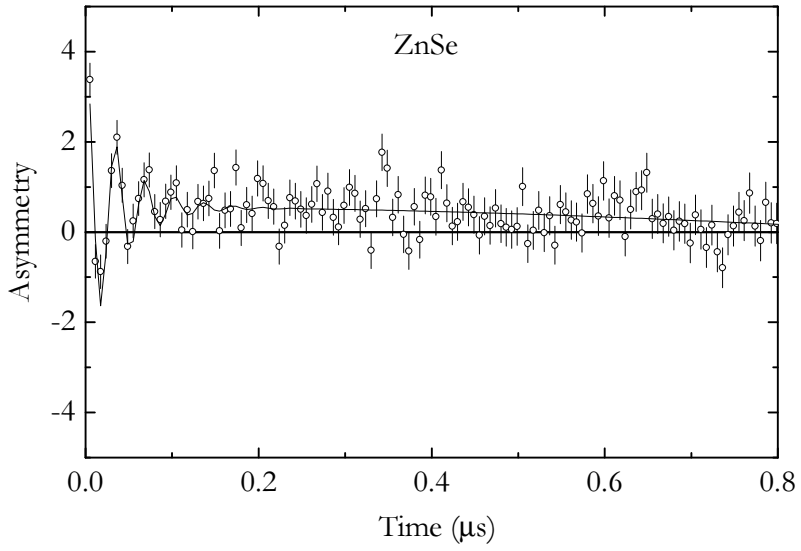

Figure 2.11: Time spectrum of a ZnSe sample at T=2 K and transverse field B=20 G. The characteristic muonium $\nu_{12} = \nu_{23}$ precession at 28.6 MHz is observed. This precession frequency allows verifying the presence of muonium, but it is not adequate for its characterization, since it is independent of the hyperfine interaction. In this particular example, the muonium precession is seen to be heavily damped, which is a clear sign of muonium dynamical behaviour.

2.6.3 Muon spin relaxation

Relaxation studies are best done at longitudinal geometry, by applying an external magnetic field parallel to initial polarization. In this case, the alterations to polarization arise from muon spin-flips in the presence of the magnetic field, by interactions with the lattice. Such spin-flipping motivate a gradual loss of polarization, generally visible via a relaxation in asymmetry, as was discussed in section 2.3.3; an example is shown in Fig. 2.12. In such longitudinal field measurements, the geometrical parameter α may eventually change with the magnitude of the applied field, due to the alteration of the positron trajectories, particularly for high-fields, where the charged particles trajectories may be significantly changed. In these cases, it may be necessary to perform a silver calibration in the entire field range.

As mentioned as well in section 2.3.3, and will be shown in the forthcoming chapters, such longitudinal field measurements also prove much useful for the investigation of the strength of depolarizing mechanisms *via* quenching of the muon spin polarization.

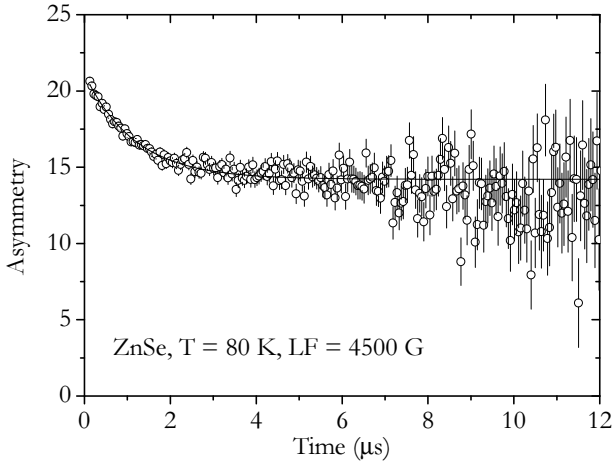

Figure 2.12: Time spectrum of a ZnSe sample at T=80 K, subject to a longitudinal field of B=4500 G. The appearance of a relaxation in this nuclear-magnetic-moment-free compound is a sign of dynamical processes envolving the muonium states.

2.6.4 Muon spin resonance

As we have pointed out in section 2.3.1, the occurrence of muon spin depolarization in the muon thermalization process and/or the existence of muon charge/spin dynamics may lead to a "missing fraction" in the polarization, as seen in transverse- or longitudinal-field measurements, thus hiding the nature of the final state. However, if a given state is present, albeit depolarized, its presence may be demonstrated by a change in the longitudinal field polarization induced by forcing transitions between the corresponding spin levels, by means of resonant electromagnetic radiation.

In this *muon-spin resonance* method, one basically begins with a longitudinal-field configuration, and then force the transitions between the spin energy-levels in the presence of the static longitudinal field, by means of electromagnetic radiation.

For the most common case where the final-state, analyzed through this method, is a diamagnetic state, the spin-level transitions are determined (as will be further detailed below) by the muon gyromagnetic ratio $\gamma_\mu = 135.5$ MHz/T and thus fall on the radio-frequency domain. This subtechnique is thus also commonly designated radio-frequency-μSR (RF-μSR). However, final-state analysis of paramagnetic states is also possible, despite being harder and less common, in which case the much higher energy differences between hyperfine levels for a given field are best dealt with microwave radiation [Kre94]. The principle is nevertheless the same and the acronym RF-μSR will be often used throughout this work even for the microwave case.

As we shall see, this method allows the extraction of quantitative information about the state under investigation. In this work, we shall concentrate on the usual RF in diamagnetic or deep paramagnetic states. The details for the novel shallow muonium states found in the cadmium chalcogenides may be somewhat different, in spite the principles being the same. However, the extreme low values of the hyperfine interaction in these materials scale down the corresponding Breit-Rabi diagram several orders of magnitude, and reveal some subtleties unknown to the usual studies, such as excitation of the ESR levels and the corresponding RF-induced repolarization features [Cox03b, Lor04]. Usually, though, the forced transitions in muon-spin-resonance methods further depolarize the muon spin.

Basic principle

The basics of the RF technique are more easily explained in a (pseudo)-classical precession model in a rotating reference frame [Kre90].

As known, a magnetic moment $\vec{\mu} = \gamma \vec{J}$ subject to a static magnetic field $\vec{B} = B\hat{\mathbf{k}}$ precesses around the field due to the torque $d\vec{J}/dt = \vec{\mu} \times \vec{B}$, with the Larmor frequency $\omega_0 = \gamma B$. The magnetic moment precesses in a constant-energy conical surface with constant angle with the applied field, so that its component in the $\hat{\mathbf{k}}$ direction remains constant. When applying a circularly polarized radio-frequency field $\vec{B}_{rf}$ perpendicularly to the static field

$$\vec{B}_{\text{rf}}(t) = B_1 \left[\cos(\omega t + \phi)\, \hat{\imath} + \sin(\omega t + \phi)\, \hat{\jmath}\right] \tag{2.78}$$

the effective field becomes, in a reference frame $\{\hat{\imath}_R, \hat{\jmath}_R, \hat{\mathbf{k}}\}$ rotating with the rf-field frequency ω around $\hat{\mathbf{k}}$,

$$\vec{B}_{\text{eff}} = \frac{\omega_0 - \omega}{\gamma}\, \hat{\mathbf{k}} + B_1\, \hat{\mathbf{p}} \tag{2.79}$$

where $\hat{\mathbf{p}} = p(\phi) = \cos\phi\, \hat{\imath}_R + \sin\phi\, \hat{\jmath}_R$.

From eq. 2.79, we regain the trivial Larmor precession in the trivial case where no rf-field is applied, $B_1 = 0$, so that the muon spin precesses with frequency $\omega_0 - \omega$ in the frame rotating with frequency ω. This implies the spin is static when $\omega = \omega_0$, which corresponds to precession at the Larmor frequency ω_0 in the laboratory frame.

If the rf-field is at resonance with the magnetic moment precession (i.e., $\omega = \omega_0 = \gamma B$), then

$$\mathbf{B}_{\text{eff}} = B_1 \hat{\mathbf{p}} \tag{2.80}$$

and the spin precesses, in the rotating reference frame, around the $\hat{\mathbf{p}}$ direction with frequency $\omega_1 = \gamma B_1$.

In the general off-resonance case, the effective field in the rotating reference makes an angle θ with the $\hat{\mathbf{k}}$ direction, defined by:

$$\tan\theta = \frac{\omega_1}{\omega_0 - \omega} \tag{2.81}$$

so that

$$\mathbf{B}_{\text{eff}} = \cos\theta\hat{\mathbf{k}} + \sin\theta\hat{\mathbf{p}} \tag{2.82}$$

Considering the longitudinal field configuration, where the initial spin polarization $\hat{\mathbf{P}} = P\hat{\mathbf{k}}$ is parallel to $\hat{\mathbf{k}}$, we have, in the general off-resonance case as seen through the rotating reference frame (please refer to fig. 2.13), a polarization component $P_{\parallel} = P\cos\theta$ parallel to the effective-field which is kept constant. The polarization component $P_{\perp} = P\sin\theta$ perpendicular to the effective-field precesses around $\mathbf{B}_{\text{eff}}$, with the effective frequency ω_{eff}:

$$\omega_{\text{eff}} = \sqrt{(\omega_0 - \omega)^2 + \omega_1^2} \tag{2.83}$$

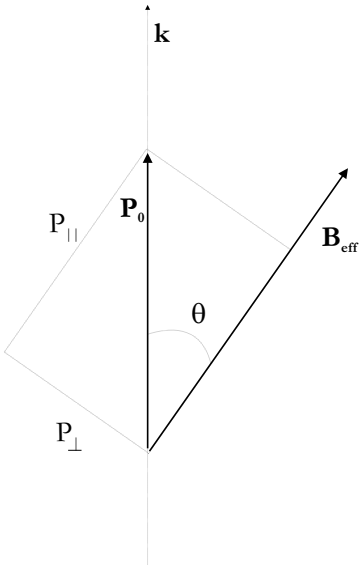

Figure 2.13: Polarization considered on a rotating reference frame: the polarization component $P_{\perp}$ precesses around the effective-field B_{eff}, whereas the parallel component $P_{\parallel}$ is locked. The final polarization z component in the laboratory reference frame is composed of the corresponding projections of $P_{\perp}$ and $P_{\parallel}$.

So, the component P_k of the polarization in the $\hat{\mathbf{k}}$ direction becomes:

$$\begin{aligned} P_k &= P_{\parallel}\cos\theta + P_{\perp}\cos(\omega_{\text{eff}}t)\sin\theta \\ &= P_0\left(\cos^2\theta + \sin^2\theta\cos(\omega_{\text{eff}}\,t)\right) \end{aligned} \tag{2.84}$$

Generally, radio-frequency measurements are done in time-integral mode:

$$\begin{aligned} \overline{P_k} &= \nu_\mu \int_0^\infty P_0\left(\cos^2\theta + \sin^2\theta\cos(\omega_{\text{eff}}\,t)\right)\, e^{-\nu_\mu\, t}\, dt \\ &= P_0\cos^2\theta + P_0\sin^2\theta\frac{\nu_\mu^2}{\nu_\mu^2+\omega_{\text{eff}}^2} \end{aligned} \tag{2.85}$$

So, the difference between the polarization when the radio-frequency is applied (RF-on), P_{on}, and the polarization when the radio-frequency is off (RF-off), P_{off}, becomes:

$$\begin{aligned} \overline{P_{\text{off}}} - \overline{P_{\text{on}}} &= P_0 - P_0\cos^2\theta - P_0\sin^2\theta\frac{\nu_\mu^2}{\nu_\mu^2+\omega_{\text{eff}}^2} \\ &= P_0\sin^2\theta\frac{\omega_{\text{eff}}^2}{\nu_\mu^2+\omega_{\text{eff}}^2} \end{aligned} \tag{2.86}$$

and, attending to eq. 2.81 (implying that $\sin^2\theta = \omega_1^2/\omega_{\text{eff}}^2$), we obtain

$$\overline{P_{\text{off}}} - \overline{P_{\text{on}}} = P_0\frac{\omega_1^2}{\nu_\mu^2+\omega_1^2+(\omega_0-\omega)^2} \tag{2.87}$$

This represents a lorentzian-shaped curve centered in the resonance frequency. At resonance ($\omega = \omega_0$), for $\omega_1 >> \nu_\mu$, the initial polarization P_0 arises directly. This implies $B_1 >> 33$ G, which is however usually not the case.

An alternative way to the simple computation of the difference between the RF-on and RF-off situations, is to define a RF-asymmetry as follows [Kre90, Kre95]:

$$A_{rf} = \frac{N_F^{on} - N_F^{off}}{N_F^{on} - N_F^{off}} - \frac{N_B^{on} - N_B^{off}}{N_B^{on} - N_B^{off}} \tag{2.88}$$

The RF-asymmetry in eq. 2.88 is most commonly used and can be demonstrated [Kre90, Kre95] to have the same lorentzian dependence shown for the polarization difference 2.87.

Experimental praxis

Detailed descriptions of the radio-frequency setup at the ISIS Facility and of the microwave setup at TRIUMF, which were both used in this work, can be found in references [Jon04] and [Kre94]. Here we shall limit to some essential points in the conduction of a typical RF experiment. Pulsed muon sources provide here less problems due to RF-heating, since the RF excitation may be turned on and off synchronically with the beam pulses [Cot00].

A specific RF cavity is needed for these experiments, where the sample is placed inside a non-ferromagnetic non-conducting target cell. There, the sample (itself non-ferromagnetic and non-conducting) is surrounded by a coil (usually designed as a solenoid) which produces the B_1 field created by the RF current delivered by an appropriately matched RF signal generator and amplifier. The sample holder itself should be non-conducting non-ferromagnetic. For the experiments at ISIS, mylar sample holders specifically cut for each sample were used. The sample was glued at the sample holder with varnish, after being involved in (insulating) kapton tape, and subsequently in adhesive copper tape, used as the solenoid coil. This copper tape was further connected to the RF circuit.

In order to obtain calibration of the intrinsic asymmetry o the setup, a non-conducting calibration material must be used. Polyethene is a usual choice, with a polarization from a diamagnetic state of about 66%. The calibration measurements for each sample are performed in two steps: (i) measurement of the diamagnetic TF polarization of a polyethene sample cutted with the same shape of the sample under research, by comparison with a silver sample; (ii) measurement of the maximum RF asymmetry for the polyethene sample, by means of a resonance curve.

We present in figure 2.14 an example of a lorentzian resonance observed for polyethene. The usual experimental procedure is to fix the excitation frequency and vary the amplitude of the static field. This turns out to be simpler and more

reliable than changing ω_1. Thus, after fixing the excitation radio-frequency ω_1 and the corresponding excitation power at some adequate value in order to be able to appropriately define a resonance curve within the values of the static field accessible experimentally. The static field is thus varied around the resonance field (ω_1/γ_μ, for RF-μSR studies of diamagnetic states). In the course of the experiment, different histograms are accumulated for the RF-on and the RF-off situations. An example is shown in figure 2.15.

Usually, the information is extracted from the time-integrated RF asymmetry A_{RF}. However, as can be seen from fig. 2.15, the weak precession about the B_1 field can nevertheless be observed in the RF-on time spectrum. Some authors have therefore dedicated some effort to the interpretation of the time-differential RF-μSR data, particularly regarding the determination of parameters of muonium conversion [Cot03, Mor86, Nis85]. However, such studies are seldom used, due to its extreme statistics-accumulation demands in order to clearly define the precessions around the B_1 field.

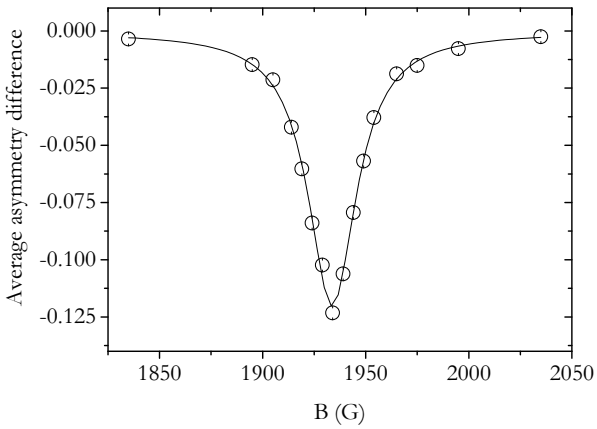

Figure 2.14: A lorentzian resonance curve obtained for polyethene at T=290 K. The excitation frequency is 26.2 MHz.

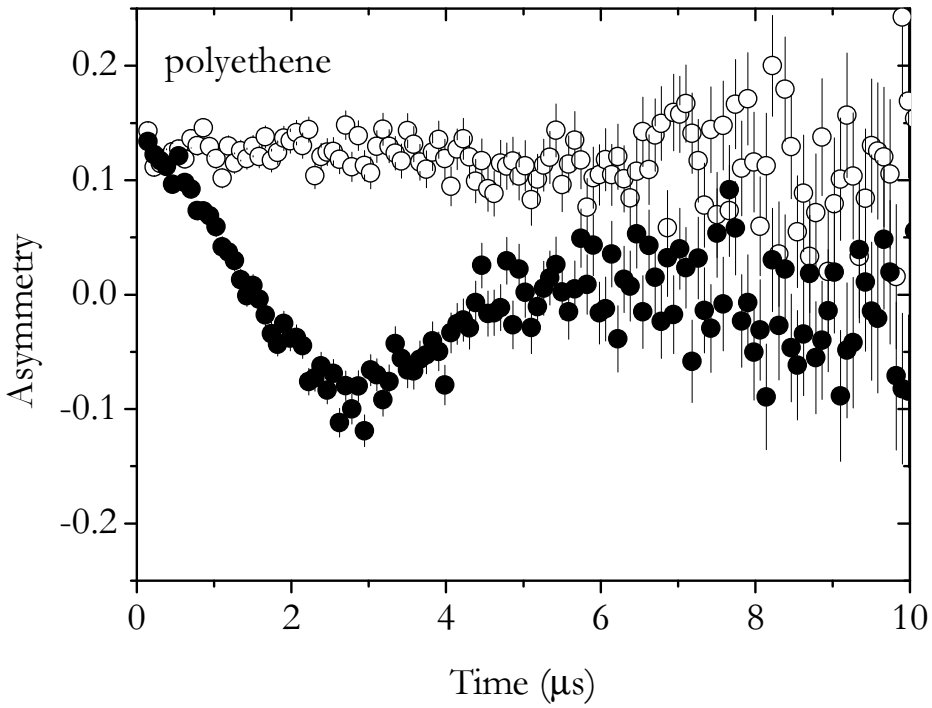

Figure 2.15: Radio-frequency μSR time spectrum for polyethene at T=290K. Black circles denote "RF-on" and white circles represent "RF-off". The static field is B=1934 G, corresponding to the lorentzian's peak in fig. 2.14, matching the resonance condition $2\pi\gamma_\mu B = 26.2$ MHz for the applied RF excitation frequency.

2.6.5 User facilities and spectrometers

The muon production process requires a proton accelerator capable of reaching hundreds of MeVs. Such accelerators exist only in large-scale installations. Currently, the following muon user facilities exist in four laboratories around the world:

- ISIS pulsed muon facility [ISI07] at the Rutherford Appleton Laboratory, in the United Kingdom;
- Laboratory for muon spin spectroscopy [PSI07] at the Paul Scherrer Institut, in Switzerland;
- Centre for molecular and materials science [TRI07] at the Tri-University Meson Facility (TRIUMF), in Canada;
- Meson science laboratory [KEK07] at KEK, in Japan. This muon facility has been shut down on March 31, 2006 [Kad07], and a new facility (J-PARC Muon Facility) is currently under construction, muon beam delivery to users being planned to 2009 [Miy06].

In this work, we have used the spectrometers EMU [ISI04] at ISIS, HELIOS and HITIME at TRIUMF, and GPS [Ama05] and DOLLY at PSI. Each has particular characteristics and capabilities. We shall describe them briefly now and point the specific use of each facility in this work.

ISIS

The ISIS facility at the Rutherford–Appleton Laboratory, in the United Kingdom, has a pulsed 800 MeV proton beam. The simple pulse has a full width at half-maximum of 80 ns; such width limits the maximum observable frequency to about 10 MHz. Muons are produced by proton collisions on a few-millimeters graphite target, placed at 45^o with the proton beam. Surface muons with momentum 26.5 MeV/c and c. 3.2 MeV are extracted, corresponding to a stopping power of about 100 mg/cm^2. The muon beam intensity is about 4×10^5 muons/s, which is divided among the three experimental areas EMU, MuSR and DEVA, allowing typical accumulation rates of 10–20 millions of events per hour.

EMU The EMU instrument is optimized for measurements in zero field and longitudinal field. The positron detectors are basically 32 cintillating segments placed in two circular rows of 16 detectors each. The rows are placed so that the incoming beam coincides with the symmetry axis. The detectors signal is transferred by light guides to nearby photomultipliers, so that local magnetic fields do not affect the electronics.

It is possible to apply longitudinal fields up to 4000 G (0.4 T) with a set of Helmholtz coils. A set of ancillary coils allows transverse-field measurements up to 100 G (0.01 T). A further set of ancillary coils does the automatic compensation of the Earth's magnetic field with a precision better than 30 mG.

A wide range of temperatures is accessible with the available cryostats and furnaces. A simple closed-cycle cryostat allows measurements in the 2 K - 360 K range. Two other cryostats allow reaching temperatures as low as 350 mK. A furnace allows extending the temperature range from room temperature up to 1000 K.

A fly-past method has been developed at EMU in order to allow measurements almost with no background, even in the smallest samples: this flypast method simply consists of a long tube placed longitudinally after the sample, so that muons which do not hit the sample fly to the tube and decay there, therefore minimizing as much as possible its contribution to the background. This implies a sample holder specifically designed to be as thin as possible and be entirely covered by even the smallest samples, so that muon stopping in the holder is prevented.

In recent years, radio-frequency facilities have been developed at ISIS, taking advantage of the pulsed nature of the beam, which prevents the heat-up problems found at continuous sources [Cot00, Cot03]. An optical reflector furnace has most recently been developed that allows measurements above room temperature, up to 1300 K. This was used for muon-spin resonance measurements in the course of this work, and the experimental data acquired with this new capability count among the very first results obtained with it.

PSI

The Paul Scherrer Institut, in Switzerland, has a quasi-continuous beam of 590 MeV protons. 28 MeV/c muons are gathered in a beam with polarization greater than 95%. Before arriving to the sample, the muon beam is directed through a spin-rotator, which turns the muon spin–polarization with respect to the linear momentum from an angle variable between 6 and 60^o.

Unlike ISIS, the proton beam at PSI is continuous, so that the time resolution is limited essentially by the resolution of the positron detectors, thus allowing access to much higher frequencies (typically hundreds of MHz).

General Purpose Instrument (GPS) and its clone DOLLY The GPS spectrometer, and its clone DOLLY, are optimized for transverse-field experiments. They have 5 positron detectors, placed in the forward (F), backward (B), up (U), down (D), and right (R) positions (all the positions are referred to the incoming beam direction). The setup also includes a muon detector before the sample (which starts the clock) and two *veto* detectors (*veto*-B and *veto*-F). The *veto*-B detector is a pyramidal cintilator with a small 7×7 mm hole in front of the muon detector. This detector serves for collimating the muon beam, and rejects the muons (and the corresponding positrons) missing the hole. The *veto*-F detector rejects the muon (and respective positron) signal for muons that do not stop in the sample, and is particularly useful for investigations on small samples. For samples large enough, this detector can be coupled to the F detector, and used to enlarge the solid angle for detection.

In order to deal with the high beam-borne background typical of a high repetition rate quasi-continuous source, a "Muons-On-REquest" setup is available, which reduces the background by at least a factor of 100 [Ama05].

The experimental setup includes a continuous He-flow cryostat, for the 2 to 300 K range, and a set of coils for magnetic fields up to 6000 G (0.6 T) in the direction of the incoming beam. Compensation of the Earth's magnetic field is usually better than 0.1 G in every direction. A furnace is also available, allowing to extend the temperature range up to 800 K.

TRIUMF

Similarly to PSI, TRIUMF has a quasi-continuous muon beam. Two dedicated beamlines, M15 and M20, are used for positive-muon spin investigations. We have used the HITIME spectrometer in the M15 line and the HELIOS spectrometer in the M20 line.

HITIME at the M15 beamline. The M15 beamline is dedicated to surface μ^+ from a 1cm graphite or beryllium proton target. The muon's momentum range goes from about 19 MeV/c to 40 MeV/c. Dual spin-rotators in the M15 line both separate positrons from the beam and rotate the muon spin to be perpendicular to the beam direction.

The High-Time spectrometer is based on a superconducting magnet dedicated to studies with high transverse fields and high frequencies. The magnet is a superconducting split solenoid delivering 7.5 T at its maximum current of 100 A. The cryostat is a hybrid between a gas flow and cold finger cryostat as the helium flow is through a ring around the sample area - the sample is cooled by helium exchange gas surrounding it. The counters are small size cintilators, adequate for high-time resolution at high transverse fields. Spin rotated muons are used. The HITIME spectrometer has been designed so that a 8×8 mm sample is enclosed inside the cintilators. This ingenious design, together with the extremely high field attainable, transform this spectrometer into an extremely powerful tool for high-resolution spectroscopic measurements.

HELIOS, in the M20 beamline Although it can be used as a (high momentum) decay muon beamline, M20 is, effectively, a dedicated (low momentum: 29 MeV/c) surface-muon channel. It takes muons from a 10-cm Be target. Its spin rotator can provide clean beam with longitudinal or transverse (spin-rotated) polarization.

Helios is a superconducting magnet, which provides 6.7 T at its maximum current of 70 A. The main counter array is for solid state work in narrow cryostats, and there is another set of counters for larger samples such as gas cells. Both sets

have long light guides and poor timing resolution ($\geq$ 1 ns). All access is axial, but the large bore makes this a versatile magnet, allowing experiments in longitudinal field and transverse field. A microwave setup has been developed for using with this spectrometer. This setup pioneered muon spin resonance measurements in paramagnetic states [Kre94] and keeps its status as the best instrument for such investigations.

Final remarks

In short, the specific advantages of each facility may be summarized as follows: high resolution, low background, spectroscopic measurements are possible at TRIUMF with its high magnetic field capabilities. The extension to high-temperatures is however only possible at PSI, which, despite lower fields, has a versatile furnace setup. ISIS, as a pulsed source, can not compete with such high resolutions, but the existence of pulsed radio-frequency capabilities from liquid-helium temperatures up to much above room temperature (c. 1300 K), allows deeper research by RF-μSR final-state analysis of diamagnetic states.

Chapter 3

Sample characterization

Contar-te longamente as perigosas
Cousas do mar, que os homens não entendem,
Súbitas trovoadas temerosas,
Relâmpagos que o ar em fogo acendem,
Negros chuveiros, noites tenebrosas,
Bramidos de trovões que o mundo fendem.
Não menos é trabalho que grande erro,
Ainda que tivesse a voz de ferro.[1]

Luís Vaz de Camões
Os Lusíadas, V, 16

3.1 Introduction

The samples used in this work were obtained either commercially or from other investigation groups which had previously done research on these materials. Not much information was available about the samples, particularly for the ones obtained commercially, except for very general descriptions such as "nominally undoped".

[1]Free translation: *"Tell you extensively the dangerous things of the sea, that men do not understand, sudden frightening storms, lightnings firing the air, dark rains, tenebrous nights, the roar of thunders breaking the world. It is no less effort than big mistake, even if I had an iron voice."*

In the course of this investigation, an urgency for sample characterization grew immensely with the accumulation of μSR experimental data on different samples of the same material (especially ZnSe), which showed different features related to the interaction of the muon with electrons in the material, as will be described in detail in Chapter 4. The need was particularly felt to have basic transport measurements (resistivity and Hall-effect) which might give some information regarding the concentration of conduction electrons. Conscious of the many experimental difficulties associated with this kind of measurements, particularly those related to establishing ohmic contacts in highly-resistive samples, the first efforts were directed to find other research groups specialized in these measurements, in order to establish some colaboration. However, establishing ohmic contacts in bulk ZnSe seems to be a rare and disappearing art.

Already at the final stages of this work, and attending to the simplicity of the basic experimental physics involved in doing Hall-effect and resistivity measurements, the decision was taken of trying to establish a modest Hall-effect and resistivity setup in Coimbra and thus try to obtain at least order-of-magnitude values for the resistivity of our ZnSe samples. Despite the difficulties and the limited results obtained up to now, this setup allowed to estimate the resistivity of our samples, and may thus be considered as a declaration of capability, to improve in the future. The obtained results, although minimal, already shine much light on the observed sample differences.

3.2 Samples

3.2.1 ZnSe

In the beginning of this work, the samples were simply acquired commercially from usual suppliers, such as Crystec and Alpha-Aesar. The initial μSR measurements were performed in two nominally undoped single crystals from these two companies, labeled "*AA*" and "*Ctec*". In order to have the possibility of investigating anisotropy effects, oriented single crystals from the same batch, cutted along different crystallographic orientations, were bought as well. The crystallo-

graphic orientations were checked by X-ray diffraction with the help of the physical crystallography group at Coimbra. All these samples are nominally undoped.

Later on, we established a contact with the team of K. Irmscher and D. Siche at the Institut für Krystal-Forschung Berlin (IKF-Berlin), who had done some work on the growth of ZnSe in the 90's. Though the research topic of this team has meanwhile moved towards other interests, they have kindly gave us three ZnSe samples: two samples grown by chemical vapour transport (CVT) and one grown by the Bridgmann method. The chemical agent used in the CVT growth is I_2 [Bot01], which implies always a doping, even if unwanted, with the iodine donor [Chi83]. Thus the two CVT samples (labelled "*CVTu*" and "*CVT:I*") are doped: *CVTu* undeliberately and *CVT:I* deliberately.

We should emphasize that, in spite of the absence of intentional doping in all the samples except *CVT:I*, we expect all the samples to be *n*-type, as known for ZnSe and discussed in chapter 1. Of course, different concentrations of free carriers are expected, according to the different concentration of electrically active impurities and defects, whose presence is evidenced by photoluminescence measurements to be presented, and according to the degree of compensation. Among the compensating centres, the zinc vacancy V_{Zn} plays a special role in ZnSe, as mentioned in chapter 1: it has been shown to form complexes with donors, and this process can be reversibly controlled by thermal annealing in zinc atmosphere [Geb02, Irm01, Pro00], thus allowing to control the concentration of conduction electrons and therefore the conductivity. This has prompted us to try to change the concentration of conduction electrons of one of the samples, in order to change the formation probability of the muonium states observed. In this context, we have annealed a piece of the [100] *Ctec* sample in zinc atmosphere, for 100 hours at 900^oC. For the annealing, the sample was sealed in primary vacuum, together with 2 mg of zinc (99.9998% purity) in a 6-mm diameter quartz tube with about 8 cm length. The resulting sample was labelled *Ctec:Zn* and the degree of compensation by zinc vacancies is expected to be less than in the original *Ctec* sample, thus presenting a smaller resistivity and a higher "net" concentration of free carriers.

A *résumé* of the used ZnSe samples can be found in table 3.1.

Name	Company/Laboratory	Doping	Other information
AA	Alpha-Aesar	undoped	-
Ctec	Crystec	undoped	[100], [110] and [111] orientations
Ctec:Zn	Crystec	undoped	*Ctec* [100] annealed in Zn atmosphere
CVTu	IKF-Berlin	"undoped"	CVT grown
CVT:I	IKF-Berlin	Iodine doped	CVT grown
B	IKF-Berlin	undoped	Bridgmann-grown

Table 3.1: Monocrystalline ZnSe samples used in this investigation. Though all the samples, except *CVT:I* are nominally undoped, ZnSe presents n-type conductivity, as mentioned in chapter 1. In the case of the *CVTu* sample, the CVT growth implies unintentional doping with the shallow donor iodine.

Basic photoluminescence characterization

A very basic characterization by photoluminescence was done with the photoluminescence apparatus at the Physics Department of the University of Aveiro. All the samples in table 3.1 were checked, except the *Ctec:Zn* piece resulting from annealing the *Ctec* sample in zinc atmosphere. The measurements were done inside a closed-cycle cryostat at 15 K. The 325 nm ultraviolet line of He-Cd laser was used for the optical excitation. The study of the dependence of the intensity of the luminescence light was done as usually [Mon05] by means of a photomultiplier attached to a monochromator.

The results for the near band edge photoluminescence are shown, for samples *AA*, *Ctec*, *CVTu*, *CVT:I* and *B*, in Figs. 3.1, 3.2, 3.3, 3.4 and 3.5, respectively.

The essential features of the spectra can be readily interpreted, with the help of the vast amount of photoluminescence literature on ZnSe.

The F_x peak is associated with the free exciton and is an intrinsic property of the samples, usually associated with crystalline perfection [Su01, Tri96]. We find it at 2.8038 eV for the *AA* and *Ctec* samples and at 2.8013 eV for the *CVTu* sample.

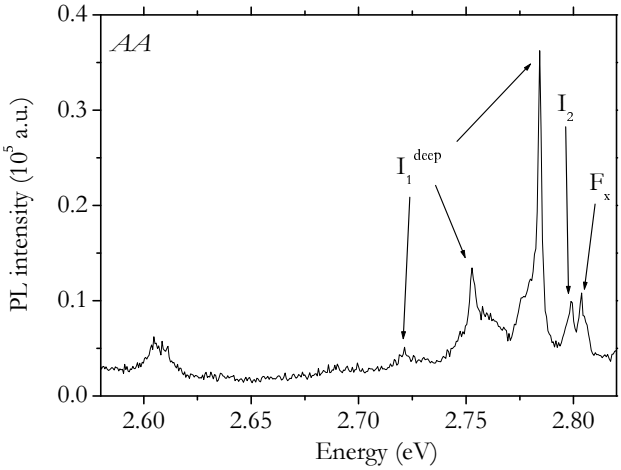

Figure 3.1: Near-band-edge photoluminescence spectrum of the undoped ZnSe single crystal from Alfa Aesar (AA sample), at 15 K. The free-exciton F_x line, the donor-bound exciton I_2 line, and the deep-acceptor-bound exciton I_1 line (with its phonon replicas), may be readily identified with the existing literature support.

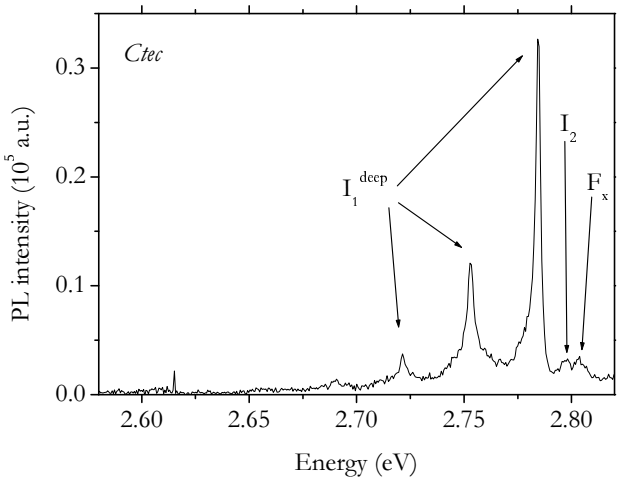

Figure 3.2: Near-band-edge photoluminescence spectrum of the undoped ZnSe single crystal from Crystec (*Ctec* sample), at 15 K. The same basic features present in the AA sample (see Fig. 3.1) are visible.

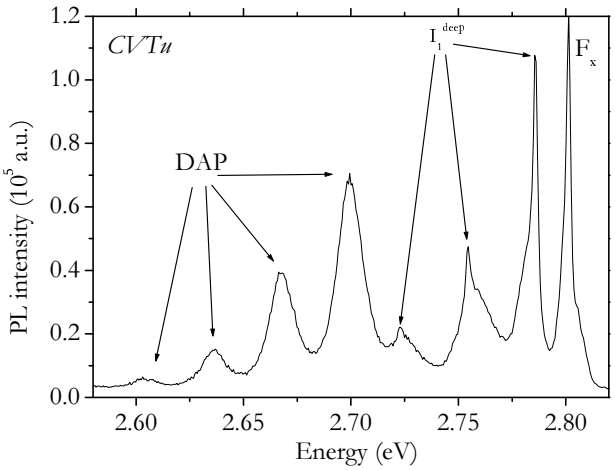

Figure 3.3: Near-band-edge photoluminescence spectrum of the "undoped" (i.e., undeliberately doped with iodine) ZnSe single crystal grown by CVT and obtained from the IKF-Berlin group (*CVTu* sample). The spectrum was obtained at a temperature of 15 K. Aditionally to that observed in the *AA* (Fig. 3.1) and in the *Ctec* (Fig. 3.2) samples, a strong donor-acceptor pair (DAP) line and its phonon replica is observed. Of note, the strong intensity of the free-exciton F_x line, a sign of crystalline perfection. It probably overwhelms the weaker I_2 line.

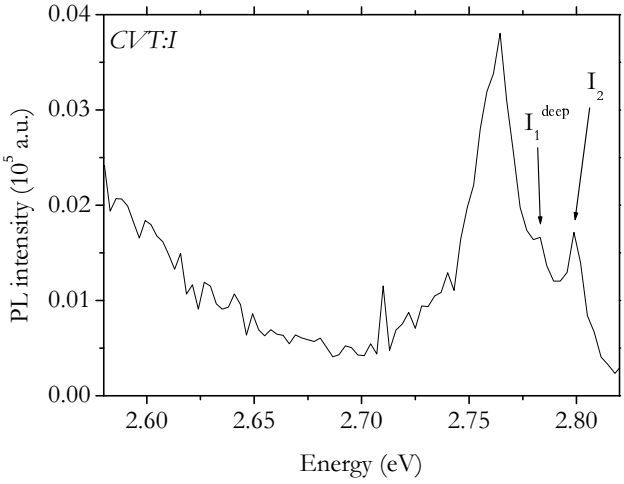

Figure 3.4: Near-band-edge photoluminescence spectrum of the (deliberately) iodine-doped ZnSe single crystal grown by CVT and obtained from the IKF-Berlin group (*CVT:I* sample). The spectrum was obtained at a temperature of 15 K. The luminescence of this sample is very weak, but I_1 and I_2 emission seem to be present. A peak of unknown origin is observed at 2.764 eV.

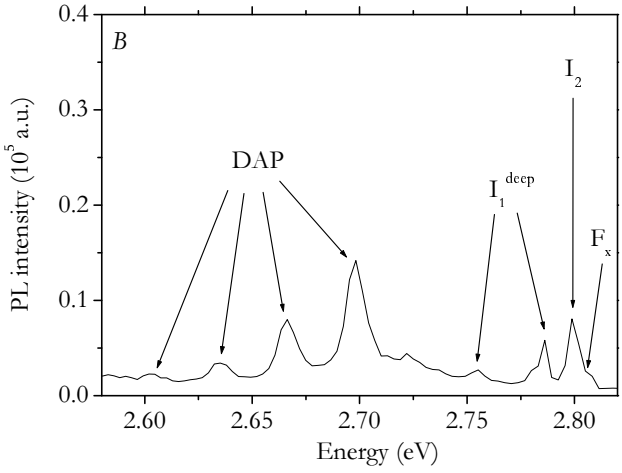

Figure 3.5: Near-band-edge photoluminescence spectrum of the undoped ZnSe single crystal grown by the Bridgmann method and obtained from the IKF-Berlin group (*B* sample). The spectrum was obtained at a temperature of 15 K. F_x, I_2, I_1 (with replica) and DAP (with replica) lines, as in the previous samples, are observed.

Such small variations between samples are also found in the cited literature. This emission is also visible in the B sample as a "shoulder" in the I_2 emission.

The I_1^{deep} emission is followed by longitudinal-optical-phonon (LO) replica at intervals of 31 meV. We observe it at 2.786 eV for the B sample, at 2.785 eV for the *CVTu* sample, at 2.784 eV for the *AA* and *Ctec* and, possibly, at 2.783 eV for the *CVT:I* sample. Two origins seem to coexist for this emission: an exciton bound to a deep Zn vacancy (V_{Zn}) acceptor or to a copper impurity substituting at a zinc site Cu_{Zn} [Iss88].

I_2 emission is found at 2.798 eV in the *Ctec* sample and at 2.799 eV in the *AA*, *B* and *CVT:I* samples. It *"has been attributed to the exciton bound to a substitutional neutral donor, such as Al, Ga, In on the Zn site or Cl and F on the Se site"* [Su01].

In the *CVTu* and *B* samples, donor-acceptor pair(DAP) emission is also present (at 2.699 eV in the *CVTu* and at 2.698 eV in the *B*), together with the respective LO replica with 31 meV intervals. Su *et al.* identify it with the DAP associated with the Li or Na acceptor [Su01].

In these brief photoluminescence measurements, we have observed intense deep-level emission as well, visible in the lower energy region of the photoluminescence spectra. These are depicted in Figs. 3.6, 3.7, 3.8, 3.9 and 3.10, for samples *AA*, *Ctec*, *CVTu*, *CVT:I* and *B*, respectively. Please note that the band-edge emission part (2.57 - 2.82 eV) of these figures has already been represented in figs. 3.1, 3.2, 3.3, 3.4 and 3.5.

Three main bands appear, usually known in the literature as the "red band" (c. 1.94 eV), the "yellow" band (c. 2.17 eV) and the "green" band (c. 2.34 eV) [Mal88, Par72, Pla00, Pla03, Str68].

The "red" band arises from a superposition of luminescence with two different origins [Pla03]. One contribution is from self–activated luminescence arising from a complex involving a zinc vacancy and a group-III or group-VII donor: such complex behaves as an acceptor and the luminescence arises from recombination of donor electrons with the acceptor holes [Bou75, Pla03]. The other contribution is from the well-known transitions either from the conduction band or from shallow–

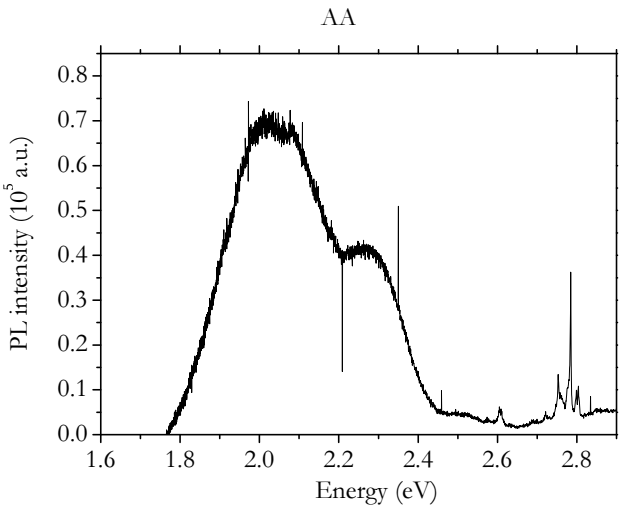

Figure 3.6: Deep-level photoluminescence emission for the ZnSe *AA* sample, at 15 K. "Red" (c. 2.0 eV) and "green" (c. 2.3 eV) bands are observed and, possibly, also an "yellow" (c. 2.1 eV) band.

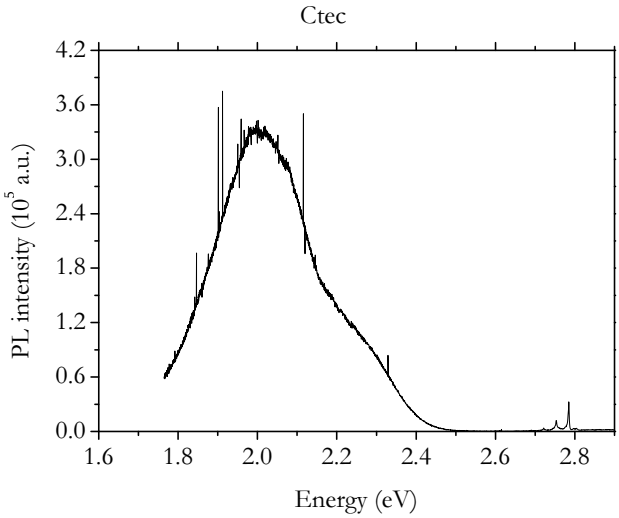

Figure 3.7: Deep-level photoluminescence emission for the ZnSe *Ctec* sample, at 15 K. A strong "red" (c. 2.0 eV) and a weaker "green" (c. 2.3 eV) bands are clearly distinguishable.

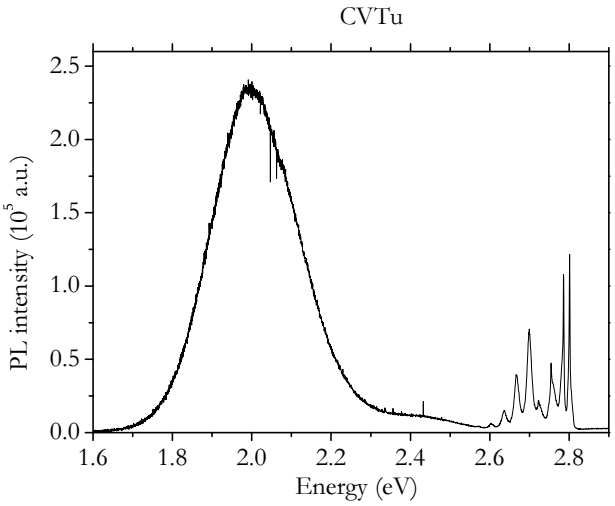

Figure 3.8: Deep-level photoluminescence emission for the ZnSe *CVTu* sample, at 15 K. As in the *Ctec* sample (Fig. 3.7), the "red" band is the strongest. The "green" band is barely present.

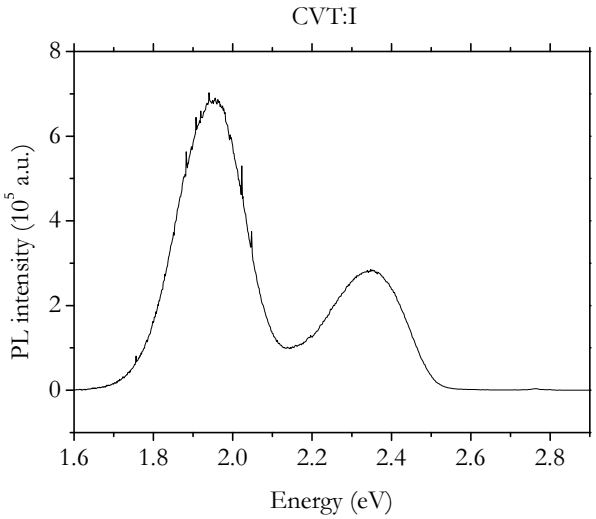

Figure 3.9: Deep-level photoluminescence emission for the ZnSe *CVT:I* sample, at 15 K, with the characteristic "red" and "green" bands.

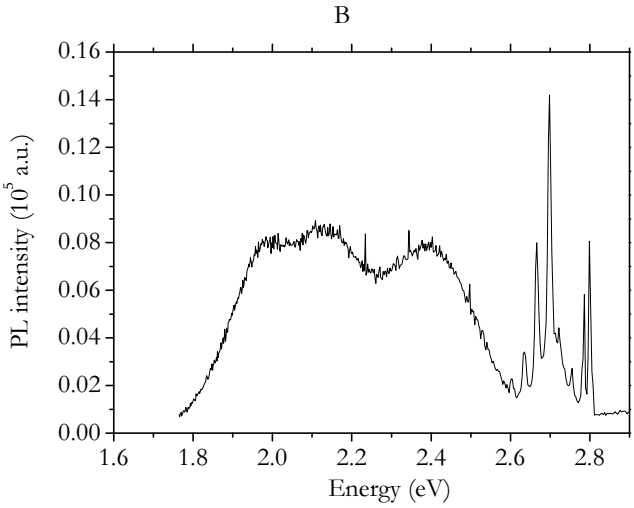

Figure 3.10: Deep-level photoluminescence emission for the ZnSe *B* sample, at 15 K. Of note, the similar intensities of the "red", "yellow" and "green" bands.

donor levels to the empty Cu_{Zn} center [Str68]. We observe this "red" band in all samples, with peak energies ranging from 1.946 eV to 2.01 eV. Again, we find similar differences in the literature. The adopted analysis may also shift slightly the position of the peaks, depending on the number of contributions considered.

The "green" band is associated with an acceptor defect that contains a zinc vacancy [Heu92, Pla03]. Again, it is present in all samples, with peak energies ranging from 2.281 eV to 2.396 eV.

Finally, the "yellow" band is ocasionally observed [Bou75, Mal88, Par72] and has been attributed to a defect involving aluminum and an alkaline impurity [Bou75]. We observe it for the *B* sample at 2.139 eV and, eventually, also for the *AA* sample at 2.1 eV.

These brief photoluminescence measurements already provide some insight into the samples properties. Particularly, they clearly display the extremely rich interplay between defects and impurities in this material, where the same basic features seem to be present in all samples (eventually with the exception of the doped *CVT:I* sample), with small diferences arising from the incorporation of impurities at the growth process.

3.2.2 ZnS and ZnTe

We have also investigated monocrystalline samples of the two other zinc chalcogenides, ZnS and ZnTe. As mentioned in Chapter 1, these play nowadays a lesser role in the technological applications, but its study imposes itself by fundamental reasons and also in a systematic approach.

Two factors conjugate in the slighter weight of ZnS and ZnTe in this investigation. The first arises from the μSR data itself: as will be shown in Chapters 4 and 5, we find in ZnSe a wealth of phenomena requiring deeper research. Secondly, the research focus on ZnSe over the recent past has provided a vast amount of information on this compound which allows more significant insight.

The ZnS and ZnTe samples investigated were all from commercial origin and are compiled in table 3.2. Again, we should stress that, despite the samples are nominally undoped, the already mentioned tendency of the II–VI semiconductors to one type of conductivity is also present in ZnS, tipically n–type, and in ZnTe, tipically p–type.

Name	Company/Laboratory	Doping	Other information
ZnS	Crystec	undoped	[110] and [111] orientations
ZnTe	Crystec	undoped	[100],[110] and [111] orientations

Table 3.2: ZnS and ZnTe samples used in this investigation. Albeit they are nominally undoped, ZnS is known to be n-type and ZnTe is known to be p-type.

3.3 Resistivity and Hall effect in ZnSe

As mentioned in this chapter's introduction, the most delicate issue regarding the aimed resistivity/Hall-effect measurements, is the establishing of ohmic contacts in the material. We first discuss this point, before presenting the measurement apparatus *proper* and discussing the obtained results.

3.3.1 Ohmic contacts

The electronics at a metal-semiconductor interface can be described in a simple way by the simple Schottky model [Mil72, Nea97, Sze81]. For the case of a metal with a work function ϕ_m larger than the work function ϕ_S of a n–type semiconductor, $\phi_m > \phi_S$ (Cf. Fig. 3.11 (a)), the thermal equilibrium condition (same chemical potential E_F over the metal-semiconductor system) implies a flow of electrons from the semiconductor to the metal, leaving a depletion region of positively–charged donors at the interface. As illustrated in Fig. 3.11 (b), this gives rise to a barrier $\phi_m - \chi_S$ for electrons flowing from the metal to the semiconductor and to a barrier $\phi_m - \phi_S$ for electrons flowing from the semiconductor to the metal, χ_S being the electron affinity of the semiconductor. Whereas the metal–to–semiconductor barrier $\phi_m - \chi_S$ is insensitive, in idealized conditions, to a potential difference across the metal–semiconductor interface, this is not the case for the semiconductor–to–metal barrier $\phi_m - \phi_S$, which is reduced if a positive potential is applied to the metal with respect to the semiconductor (*forward bias*), and is increased in the opposite situation (*reverse bias*) [Nea97][2]. Such metal-semiconductor contact is therefore a rectifying contact, and this junction acts as a metal–semiconductor diode, which happens to be one of the oldest known semiconductor applications, dating from 1904 [Sze81][3].

If the metal work function ϕ_m is smaller than the semiconductor work function ϕ_S, as depicted in Fig. 3.11 (c), we will now have a flow of electrons from the metal to the semiconductor, creating a negatively–charged layer at the semiconductor

[2]Cf. pp. 308–312 of the cited reference.
[3]Cf. p. 245 of the cited reference.

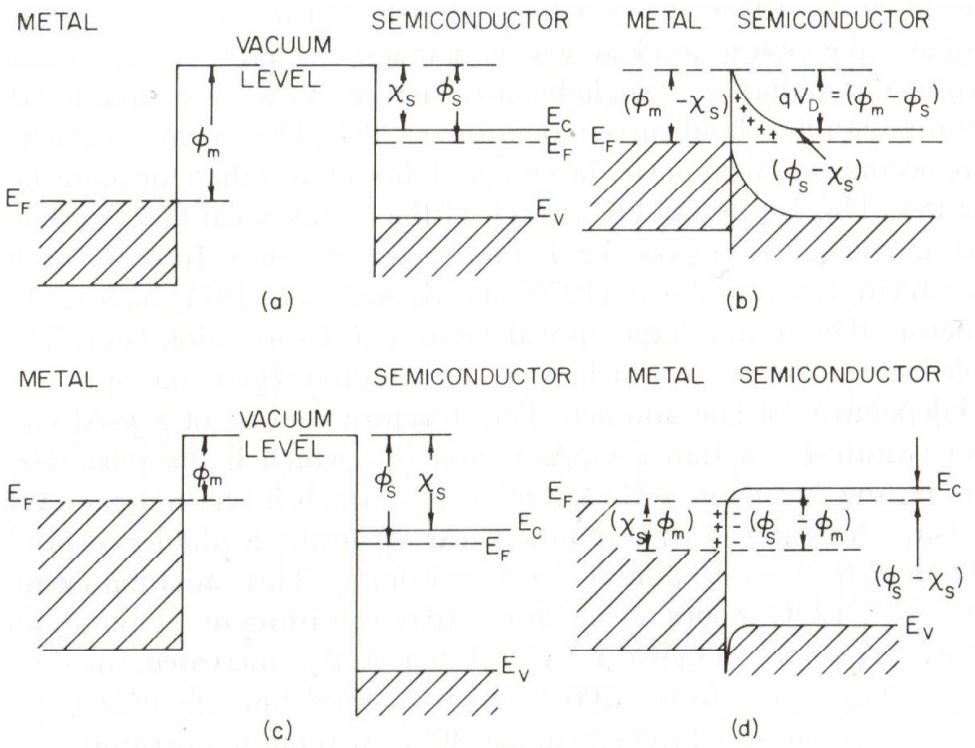

Figure 3.11: Energy level diagrams for a metal–semiconductor (type n) interface, as in ref. [Mil72]. In the top, the situation for the case where the metal's work function ϕ_m is larger than the semiconductor's work function ϕ_S (and the semiconductor electron affinity χ_S) (a). After establishing the contact (b), conduction electrons face barriers $\phi_m - \chi_S$ from the metal to the semiconductor and $\phi_m - \phi_S$ from the semiconductor to the metal, and the junction is rectifying. Below, the corresponding situation for the case where $\phi_m < \phi_S$ (c): no significant barriers exist (d) and the contact is ohmic.

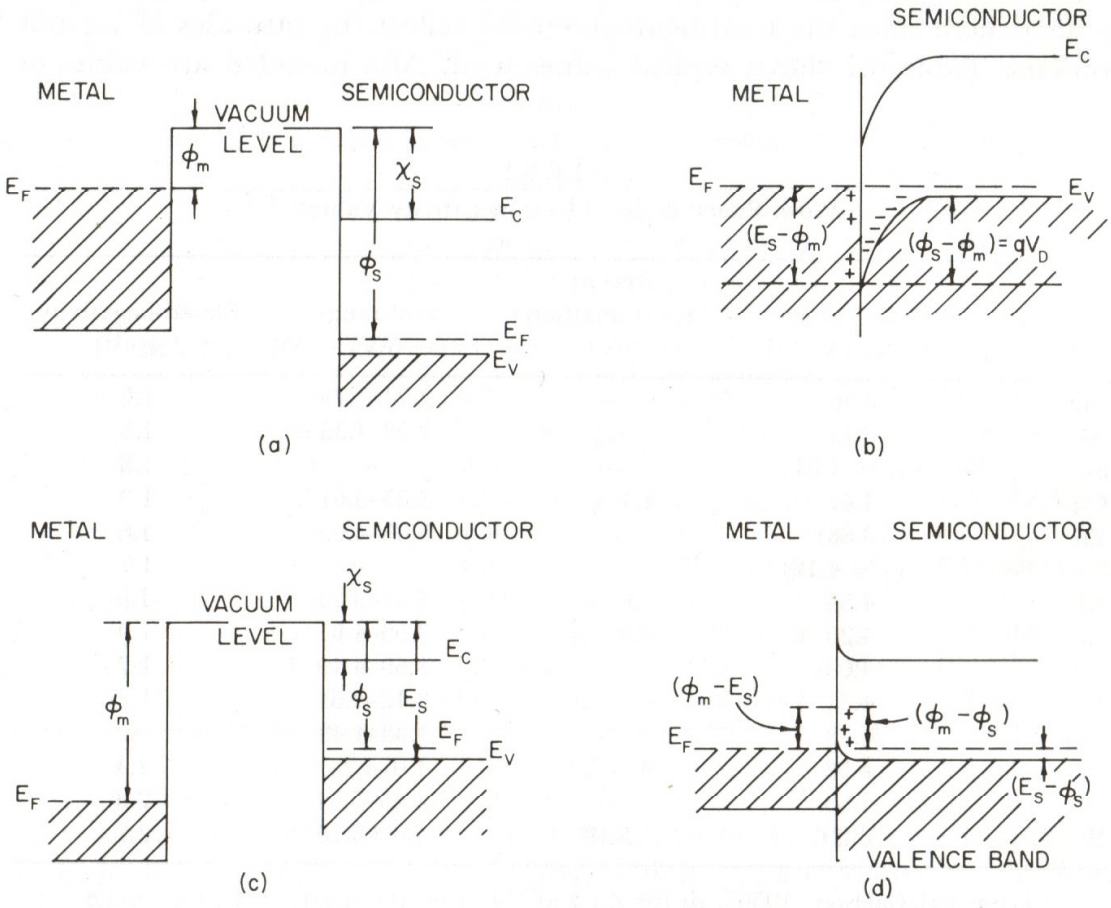

Figure 3.12: Energy level diagrams for a metal–semiconductor (type p) interface, as in ref. [Mil72]. In the top, the situation for the case where the metal's work function ϕ_m is smaller than the semiconductor's work function ϕ_S (and the semiconductor electron affinity χ_S) (a). After establishing the contact (b), holes face barriers $\chi_S - \phi_m$ from the metal to the semiconductor and $\phi_S - \phi_m$ from the semiconductor to the metal, and the junction is rectifying. Below, the corresponding situation for the case where $\phi_m > \phi_S$ (c): no significant barriers exist (d) and the contact is ohmic.

interface, affecting the band levels as in Fig. 3.11 (d). In this situation, electrons can flow easily in each direction when a voltage (either positive or negative) is applied to the metal with respect to the semiconductor. This junction is therefore an ohmic contact.

The discussion above can easily be reproduced, *mutatis mutandis*, for a junction between a metal and a p–type semiconductor. The corresponding energy diagrams are shown in Fig. 3.12.

In order to access the electrical transport characteristics of a semiconductor, electrical metal contacts with ohmic behaviour are required. At such contacts, and for a not too small voltage range, the threshold voltage for zero current is negligible with respect to the applied voltage and the proportionality between current and voltage does not vary measurably with voltage [Krö56].

However, as pointed out by Sze, "*it is difficult to make ohmic contacts in wide-gap semiconductors. A metal does not generally exist with a low-enough work function to yield a low barrier. In such cases the general technique for making an ohmic contact involves the establishment of a heavily doped surface layer such as metal-n^+-n or metal-p^+-p contact by various methods, such as shallow diffusion, alloy regrowth, in-diffusion of a dopant contained in the contact material, double epitaxy, and ion implantation*" [Sze81][4].

The investigation and development of ohmic contacts is therefore a task specific to each semiconductor and which, despite the overall principles being basically understood for long [Krö56, Smi55], still occupies a considerable amount of research effort, particularly in the wide–gap materials such as ZnSe, CdS and CdTe [Dar98], and focusing recently in ZnO [Che06, Hu06, Kan06]. Of course, such investigations are far off the main trend of this work, where we aimed at achieving but reasonable ohmic contacts to ZnSe, in order to have some basic characterization of the transport properties of our samples.

[4]Cf. p. 306 of the cited reference.

3.3.2 Ohmic contacts to ZnSe

The basic mechanism of formation of ohmic contacts to ZnSe has been investigated by Kaufman and Dowbor [Kau74] and, despite recent improvements [Par99], it can be taken as a guide for our objective. These authors build upon an already quite established practice of obtaining ohmic contacts in ZnSe and other II-VI semiconductors by means of contacting with In metal [Ave63, Ave65, Dub70, Swa69], either pure or alloyed with other elements. They suggest that, upon heating, In dissolves ZnSe, forming a liquid-phase epitaxial layer which provides the ohmic contact after cooling.

For the formation of such layer, Kaufmann and Dowbor emphasize the absolute necessity of the In wetting the crystal, as evidenced by experiment. Therefore, the optimum conditions for the formation of the contact include a clean surface and the fusion of the In at the surface at a low temperature (around 300^{o}C). The presence of an inert atmosphere prevents the oxidation of the surface, hydrogen being a usual choice (as it may act as an oxygen getter): Aven and Segall [Ave63] electrode ZnSe with "*In dots fused-in under H_2 atmosphere at 300^oC*", Dubenskii *et al.* refer that the "*In alloying was carried out in an atmosphere of purified H_2 with rapid heating and cooling*" [Dub70], Swank *et al.* inform that their samples "*were provided with ohmic contacts of indium, fired in hydrogen at 300^oC for 30 s*" [Swa69], Ray and Kröger acknowledge having heated the crystals "*for 2-3 min to 300^oC and then cooled to room temperature*" [Ray78]. Introduction of hydrogen into the sample (thereby affecting the electrical properties) is not expected to occur for low temperatures and reduced annealing times [Hei59, Mol54].

Etching

Prior to applying the indium, the surface of the ZnSe crystals must be appropriately cleaned. Again, many recipes are available in the literature, also due to the importance of having appropriate surfaces for optical studies. Though the earlier studies only mention "simple" procedures such as chemical polishing in hot concentrated NaOH [Ave63], more recently many workers find adequate a multi-stepped etching, in order to remove different kinds of surface imperfections [Nak97, Wen99]. We

adopted the following procedure: after degreasing the samples with standard solvents (ethanol, acetone), we submitted them firstly to a chemical etching step in a $K_2Cr_2O_7/H_2SO_4/H_2O$ solution [Pro02, Sch94, Wen99]. Afterwards, the reduction of the oxide layer was taken by etching in a HCl-H_2O 1:1 solution and subsequently in a 1:3 NH_4OH(29%)-methanol solution [Chi83, Nak97]. The former is thought to dissolve SeO_x, and the latter ZnO_x [Kim93]. The mentioned etching times vary between 3 minutes [Pro02, Sch94] and 10 minutes [Chi83]. We adopted the latter value for all steps.

After the etching, indium metal contacts (purity 99.998%) were placed, whenever possible, in the corners of the sample, as illustrated in Fig. 3.13. The samples were then immediately placed in a quartz tube, in a H_2 atmosphere.

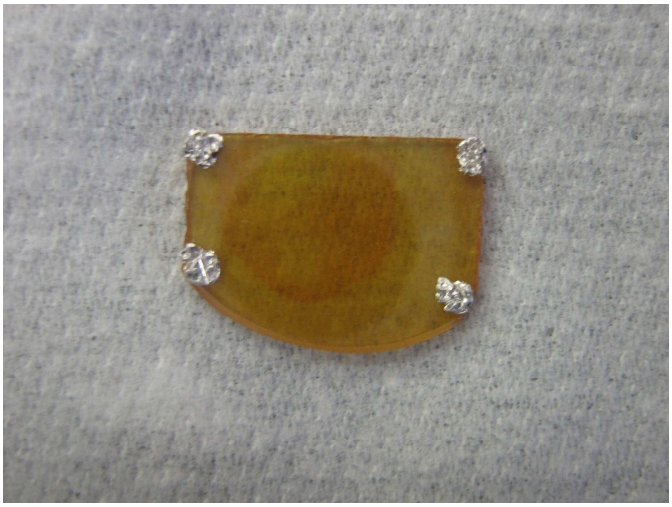

Figure 3.13: Indium contacts on a ZnSe sample, placed at the four corners in order to allow Hall-effect/resistivity measurements using the van der Pauw method. The sample is shown before the thermal treatment applied in order to provide the ohmic contacts.

Heat treatments

We have thus tried to obtain ohmic contacts by annealing the samples, prepared as described previously, for some minutes at 300^{o}C. A high-impedance electrometer, for resistance measurements up to 210 TΩ (as well as corresponding DC current and voltage measurements), was used to inspect the contacts electric behaviour: the electrometer was used in current mode in order to measure the current through the sample and contacts by applying a fixed dc voltage.

Rather unexpectedly, we found no linear behaviour, even for a sample annealed for 30 minutes at 300^{o}C (Fig. 3.14), but rather a non-ohmic I–V curve similar to that obtained for a sample where the In contacts were simply soldered to the sample.

However, we did find ohmic behaviour when annealing at 400^{o}C for 30 minutes, as shown in Fig. 3.15.

At 400^{o}C, there should be no alteration of the conductivity of ZnSe due to diffusion effects. The diffusion of In for the effect of doping is reported to occur only at 900^{o}C [Chi83]. Takenoshita *et al.* have measured the diffusion depth for this impurity and indicate only 10 μm, after a diffusion time of 10 hours at 600^{o}C [Tak86]. Regarding self-diffusion in ZnSe, the respective coefficients have been measured by Henneberg and Stevenson [Hen71] to be $D_{Zn} = 9.8\,\exp(-3.0\,eV/kT)\,cm^2s^{-1}$ and $D_{Se} = 0.13\,\exp(-2.6\,eV/kT)\,cm^2s^{-1}$. For estimating the corresponding diffusion depth , we may use the simple relation between the diffusion coeficient D, the diffusion depth X and the diffusion time t [Cra86, Jon94]

$$D = \frac{1}{4t}\left(\frac{X}{0.81}\right)^2 \tag{3.1}$$

From equation 3.1, the self-diffusion depth in ZnSe at 400^{o}C, after annealing for 30 minutes, also corresponds to only some micrometers.

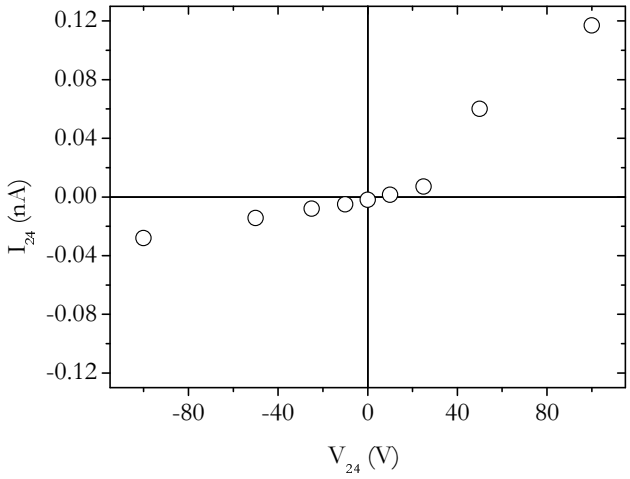

Figure 3.14: I–V curve obtained for a pair of contacts at a ZnSe sample annealed for 30 minutes at 300^{o}C. An unexpected non-linear behaviour shows up.

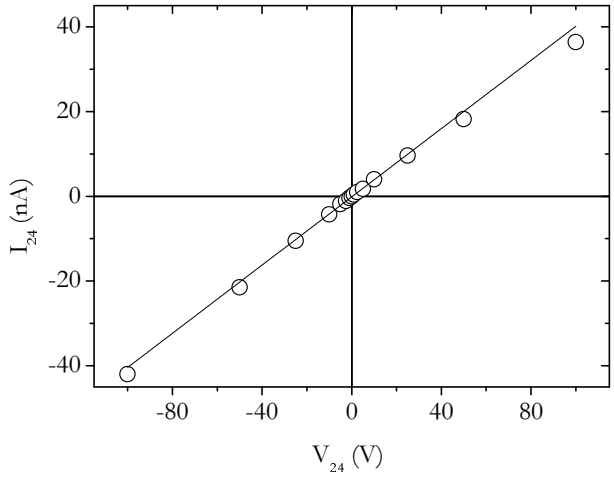

Figure 3.15: I–V curve obtained for a pair of contacts at a ZnSe sample annealed for 30 minutes at 400^{o}C. A piece of the same sample as that shown in Fig. 3.14 was used.

Conclusion: adopted procedure

We have thus adopted the following procedure for obtaining ohmic contacts to ZnSe:

- degrease the sample in acetone;
- chemical etching in $K_2Cr_2O_7/H_2SO_4/H_2O$ solution for 10 minutes;
- etching in HCl-H_2O 1:1 solution for 10 minutes;
- etching in 1:3 NH_4OH(29%)-methanol solution for 10 minutes;
- immediately applying In contacts at the surface (as in Fig. 3.13) and placing sample in a quartz tube at H_2 atmosphere;
- heating in H_2 atmosphere for 30 minutes at 400^oC.

3.3.3 Resistivity and Hall effect measurements

We shall here briefly describe the basic principles and method used for the resistivity and Hall-effect measurements. These are standard techniques, and an essential part of any semiconductor textbook, at all levels [Ash76, See82, Yu99]. Here, we closely followed the procedure recommended by the US National Institute of Standards and Technology (NIST) [Ast00, Nis06], which is based upon the van der Pauw four-point method [vdP58a, vdP58b].

Basic Hall effect

The basic Hall effect was first observed by E. H. Hall in 1879, while in a research program to find magnetoresistive effects [Ash76][5]. The Hall effect has since then played a major role in the development of solid state physics, becoming a standard technique for obtaining basic transport parameters, and being simultaneously at the forefront of research, as is eloquently expressed by the unveiling of phenomena as the quantum Hall effect (K. v. Klitzing, Nobel prize 1985) and the fractional

[5]Cf. pp. 11 and 12 of the cited reference.

quantum Hall effect (D. C. Tsui, H. L. Störmer and R. B. Laughlin, Nobel prize 1998) [Kli86, Lau99, Sto99b, Tsu99].

The basic Hall-effect measurement is depicted in Fig. 3.16. A magnetic field $\mathbf{B}=B_z\ \hat{\mathbf{k}}$ is applied perpendicularly to the face of a flat sample, subject to an electric current due to an applied electric field $\mathbf{E}=E_x\ \hat{\mathbf{i}}$. The charge-carriers in the sample will be deflected in the y direction due to the Lorentz force

$$\mathbf{F_L} = q\,\mathbf{v}\times\mathbf{B} \tag{3.2}$$

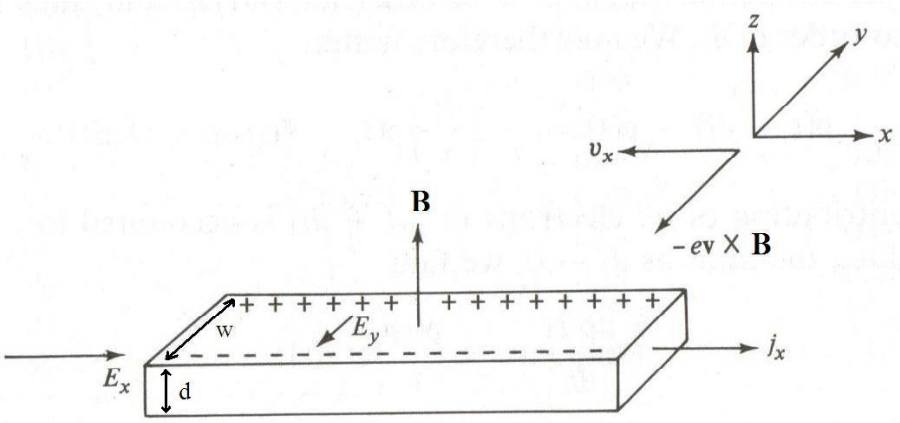

Figure 3.16: Schema of the basic Hall effect: a current $\mathbf{j}=j_x\ \hat{\mathbf{i}}$ flows due to the application of an electric field $\mathbf{E}=E_x\ \hat{\mathbf{i}}$, while the material is subject to an external magnetic field $\mathbf{B}=B_z\ \hat{\mathbf{k}}$. The negative-charge carriers situation is depicted, where the Lorentz force and the Hall electric field, in the reference frame of the figure, point in the negative y direction. The width w and depth d of the sample are also indicated.

The charge therefore accumulates in one of the y faces of the sample, thus creating a y-component of the electric field against the Lorentz force. A potential between the two y faces arises, named Hall potential. In the steady state, these two forces in the y direction mutually cancel. The velocity of the charge carriers, in this situation, is $\mathbf{v}=v_x\,\hat{\mathbf{i}}$. The current density, in the steady state, is also only in the x direction, according to

$$\mathbf{j} = n\,q\,\mathbf{v} \tag{3.3}$$

The sign of the final Hall potential depends on the sign of the charge carriers. As a matter of fact, for positive charge carriers such as holes, we have (see the referential in Fig. 3.16) $v_x > 0$, $(q\,\mathbf{v}\times\mathbf{B})_y < 0$ and therefore $E_y > 0$; for negative charge carriers such as as electrons, it is $v_x < 0$, $(q\,\mathbf{v}\times\mathbf{B})_y < 0$ and therefore $E_y < 0$; this last case is illustrated in Fig. 3.16.

In the classical relaxation time approximation (Drude model) [Ash76], the dynamics of negative charge carriers is described by (similarly to positive charge carriers):

$$\frac{d\mathbf{p}}{dt} = -e\,\mathbf{E} - \frac{e}{m}\mathbf{p}\times\mathbf{B} - \frac{\mathbf{p}}{\tau} \tag{3.4}$$

where $\mathbf{p}/\tau$ is a friction term and τ is the mean collision time. In the steady-state, $d\mathbf{p}/dt = 0$ and $v_y = 0$. Eq. 3.4 becomes

$$-e\,E_x = \frac{p_x}{\tau} \tag{3.5}$$

$$e\,E_y = \frac{e}{m}\,p_x\,B \tag{3.6}$$

and, attending to eq. 3.3, we finally get:

$$j_x = \frac{n\,e^2\,\tau}{m}\,E_x \tag{3.7}$$

$$E_y = -\frac{1}{n\,e}\,B\,j_x \tag{3.8}$$

The same result for j_x and E_y is obtained if positive charge carriers are considered.

The conductivity[6] σ becomes:

$$\sigma = \frac{n\, e^2\, \tau}{m} \tag{3.9}$$

and the Hall coefficient, defined as $R_H = E_y/(B\, j_x)$, is

$$R_H = -\frac{1}{n\, e} \tag{3.10}$$

Unlike the metal case, where n is temperature independent, for semiconductors the temperature dependence of the conductivity arises both from the increase of the carrier concentration with temperature (increasing σ) and from the decrease of the collision time with temperature (decreasing σ). It is therefore customary to separate these two contributions by defining the mobility μ as the proportionality factor between the drift velocity and the applied electric field:

$$v_x = \mu\, E_x \tag{3.11}$$

The conductivity thus becomes:

$$\sigma = -n\, e\, \mu \tag{3.12}$$

and, from eqs. 3.10 and 3.12 the relation of the mobility to the conductivity and the Hall coefficient is simply expressed by

$$\mu = R_H\, \sigma \tag{3.13}$$

The Hall mobility μ_H given by eq. 3.13 may not correspond exactly to the mobility μ defined by eq. 3.11, when the assumption that all charge carriers have the same energy is no longer valid. In that case, the relation between the two is adequately described by [Yu99][7]:

$$\mu_H = \frac{\overline{\tau^2}}{\overline{\tau}^2}\, \mu \tag{3.14}$$

[6] $\sigma = 1/\rho$, where ρ is the resistivity.

[7] Cf. pp. 226 and 227 of the cited reference.

van der Pauw method

The most common method for measuring the resistivity and the Hall coefficient of a material "*is based upon a theorem which holds for a flat sample of arbitrary shape if the contacts are sufficiently small and located at the circumference of the sample*" [vdP58a]. The sample must be singly connected (no geometrical holes). Two "resistances" are defined as (see Fig. 3.17):

$$R_{MN,OP} = \frac{V_P - V_O}{i_{MN}} \tag{3.15}$$

$$R_{NO,PM} = \frac{V_M - V_P}{i_{NO}} \tag{3.16}$$

where $V_j - V_k$ is the potential difference between contact j and contact k and i_{lm} is the intensity going from contact l to contact m.

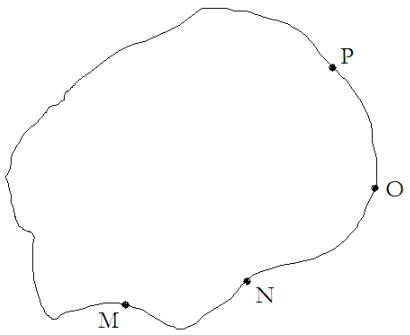

Figure 3.17: Essential features for the application of the van der Pauw theorem: a flat sample with no (geometrical) holes, in which border four electrical contacts M, N, O and P are established.

This theorem, named after van der Pauw, states that the resistivity ρ of the sample, assumed to have thickness d, relates to the resistances defined in eq. 3.16 by the expression:

$$\exp\Big(-\frac{\pi\, d}{\rho}\, R_{MN,OP}\Big) + \exp\Big(-\frac{\pi\, d}{\rho}\, R_{NO,PM}\Big) = 1 \tag{3.17}$$

Thus, by measuring $R_{MN,OP}$ and $R_{NO,PM}$ one immediately obtains ρ by solving equation 3.17. This has to be done numerically, as it is not possible to express ρ analitically from eq. 3.17. An algorithm for the corresponding computation may be found in appendix **??**.

In his seminal paper [vdP58a], van der Pauw showed as well that the Hall mobility μ_H of the sample can be determined by measuring the resistance change $\Delta R_{MN,OP}$ when applying a magnetic field B perpendicularly to the sample:

$$\mu_H = \frac{d}{B}\,\frac{\Delta R_{MN,OP}}{\rho} \tag{3.18}$$

From eqs. 3.13 and 3.10, the density of carriers is thus given by:

$$n = \frac{1}{q\rho\mu_H} \tag{3.19}$$

Resistivity measurements and apparatus

In order to proceed with the aimed measurements, we began by soldering metal wires to the contacts with indium. The contacts were labelled 1 to 4, in the direct rotation order, as shown in Fig. 3.18. Such ordering is important in order to clearly define the sign of the Hall voltage and therefore that of the charge carriers. The sample was subsequently placed inside an improvised metal Faraday cage, on top of a dielectric polystirene sheet. The cage was thin enough in order to be placed between the poles of the electromagnet to be used in the subsequent Hall-effect measurements. It was provided as well with holes, in order to allow the wires to be connected to the remainder apparatus.

For each measured sample, we verified the linear dependence for the pairs $1-3$ and $2-4$, as in Fig. 3.15.

The resistivity measurements were done according to the procedure recommended by the U.S. National Institute of Standards and Technology [Nis06]. This procedure recommends using a stabilized current source to set a current I_{jk}, entering the sample in contact j and leaving through contact k, and measuring simultaneously the potential difference $V_{lm} = V_l - V_m$ between contact l and contact m, by means of a sensitive electrometer. However, we did not have access to such a current source and used another high-impedance electrometer instead: this brings an operational difference, since the current I_{jk} is not set but measured. For highly resistive samples such as ours', this constitutes an important source of experimental error.

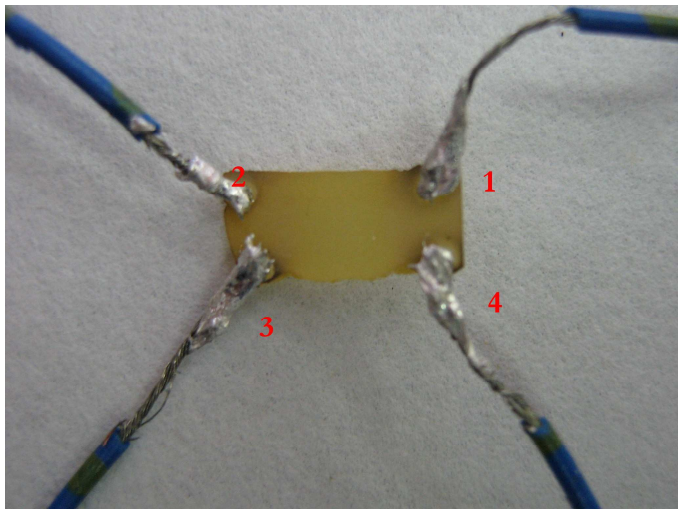

Figure 3.18: Metal wires soldered with indium to the In ohmic contacts on a ZnSe sample. The contacts are labelled 1-4 in the direct order.

For the resistivity measurements, we proceeded as follows: for each pair of adjacent contacts we established a tension V_{jk} with electrometer A and measured the corresponding current I_{jk}. The tension V_{lm} between the remaining two contacts was simultaneously measured. A resistance associated with this measurement was computed:

$$R_{jk,lm} = \frac{V_{lm}}{i_{jk}} \tag{3.20}$$

We have also determined R_{kjml} from an independent measurement of V_{ml} and i_{kj}, as recommended in order to check systematic errors. We have thus obtained the four resistances $R_{12,43}$, $R_{23,14}$, $R_{34,21}$, and $R_{41,32}$, together with its respective reverse order counterparts $R_{21,34}$, $R_{32,41}$, $R_{43,21}$, and $R_{14,23}$.

As a result of the reciprocity theorem, well-known from elementary circuit theory [Mit49], we have

$$R_{jk,lm} = R_{lm,jk} \tag{3.21}$$

and, it follows immediately that

$$R_{21,34} + R_{12,43} = R_{43,12} + R_{34,21} \tag{3.22}$$

$$R_{32,41} + R_{23,14} = R_{14,23} + R_{41,32} \tag{3.23}$$

Two characteristic resistances to be used within the van der Pauw theorem can then be estimated experimentally from the average of each quartet expected equal resistances in eqs. 3.22 and 3.23:

$$R_A = \frac{R_{21,34} + R_{12,43} + R_{43,12} + R_{34,21}}{4} \tag{3.24}$$

$$R_B = \frac{R_{32,41} + R_{23,14} + R_{14,23} + R_{41,32}}{4} \tag{3.25}$$

The resistivity follows immediately from eq. 3.17.

Hall effect measurements and apparatus

For the Hall-effect measurements, the Faraday cage described above was placed in the uniform field region between the poles of a Helmholtz-coils electromagnet. This device can provide a maximum field of 1 T (10000 G), though this extreme can be maintained only for a few seconds due to extreme heating. However, few thousand Gauss offer no difficulties and we decided to use the compromise value of 0.6 T (6000 G). It is possible as well to reverse the direction of the field by reversing the direction of the input current. The calibration of the direction dial was done by simple checking of the deviation, in the presence of the magnetic field, of a thin aluminum-foil band subject to a known current.

The magnetic field in the sample location was measured by a gauss-meter, previously placed inside the cage and next to the sample.

The measurements now imply establishing a known current i_{jk} from contact j to contact k and measuring the voltage $V_{lm} = V_l - V_m$ in the other pair of opposite contacts, in the presence of a magnetic field perpendicular to the sample face. As in the resistivity measurements, it is also advisable to measure i_{kj} and V_{ml} as well. Again, we used a high-impedance electrometer to measure i_{jk} due to an established voltage V_{jk}.

For non-symmetrical contacts placed in samples with odd geometries, the voltage V_{lm} has in general two contributions: the Hall-voltage *proper* and an offset voltage arising from the non-symmetry, and which is generally much larger than the Hall voltage. The accuracy of the measurements is usually improved by measuring V_{lm} for both possible directions of the magnetic field, denoted **P** and **N**, as sketched in Fig. 3.19. We denote the corresponding tensions V_{lmP} and V_{lmN}.

We have thus measured the following pairs:

- (i_{13},V_{24P}) and, correspondingly, (i_{31},V_{42P});
- (i_{24},V_{31P}) and, correspondingly, (i_{42},V_{13P});
- (i_{13},V_{24N}) and, correspondingly, (i_{31},V_{42N});
- (i_{24},V_{31N}) and, correspondingly, (i_{42},V_{13N}).

Here, due to the hindrance arising from using an electrometer instead of a current source, we took particular care to ensure that all the currents were measured to be equal, within a minimum dispersion of current values, in order for the concentration of carriers be more easily determined afterwards (see eq. 3.30 below).

The offset voltage can be removed by computing the following differences:

$$V_C = V_{24P} - V_{24N} \tag{3.26}$$

$$V_D = V_{42P} - V_{42N} \tag{3.27}$$

$$V_E = V_{13P} - V_{13N} \tag{3.28}$$

$$V_F = V_{31P} - V_{31N} \tag{3.29}$$

The sum $\mathcal{V} = V_C + V_D + V_E + V_F$ directly gives the sample type, determined to be p-type if $\mathcal{V} > 0$ and n-type if $\mathcal{V} < 0$. Each of the parcels in the sum $\mathcal{V}$ corresponds to twice the Hall potential V_H, so that $\mathcal{V} = 8\,V_H$.

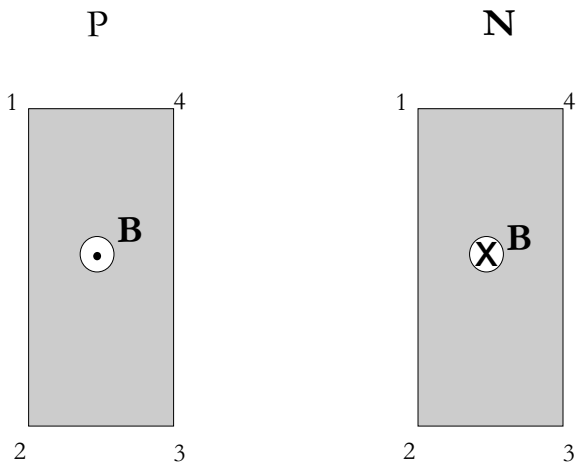

Figure 3.19: Sketch of **P** and **N** directions of magnetic field in Hall-effect measurements.

The concentration of carriers n (or p, for p-type samples), in SI units, can also be obtained immediately from eq. 3.10 and the definition of the Hall coefficient, :

$$n = \frac{8\,I\,B}{q\,d\,\mathcal{V}} \tag{3.30}$$

where we used $j_x = I/(w\,d)$ and $V_y = E_y\,w$ (see Fig.3.16).

From eqs. 3.30 and 3.18, the Hall mobility follows as well.

3.3.4 Results

We present in table 3.3 the obtained results for the resistivity, free-carrier concentration and mobility, where possible, for the six ZnSe samples we presented in the begining of this chapter.

Sample	ρ ($\Omega.cm$)	n (cm^{-3})	μ_H ($cm^2\,V^{-1}\,s^{-1}$)
AA	$\geq 10^{11}$	-	-
Ctec	7×10^9	-	-
B	9×10^8	2×10^{10}	0.33
Ctec:Zn	7×10^8	3×10^{10}	0.27
CVTu	1×10^5	3×10^{12}	0.02
CVT:I	1×10^4	1×10^{13}	0.06

Table 3.3: Resistivity ρ, free-carrier concentration n and Hall mobility μ_H for the ZnSe samples presented in the beginning of the chapter.

The first remark regarding the results of table 3.3 respects to the extremely high-values of the sample resistivities. This is not a surprise, since similar values are presented in the literature for as–grown ZnSe crystals. Hartmann and Siche quote typical high resistivities for ZnSe as $10^{11} - 10^{12}\,\Omega.cm$ [Har94]. ZnSe has even been used as a test sample for demonstrating the performance of apparatus

for high-resistivity measurements [Hem73]. Correspondingly small values for the free-carrier concentration appear, consistent with similar measurements for high-resistivity samples [Col68, Hem73].

Here, we should point the high experimental difficulties arising from trying to measure such extreme values with our improvised apparatus. The essential sources of error, both random and systematic, relate to the long transients associated with the involved high resistances and to the deficient electrical isolation from external sources, which become a hindrance when measuring nA and pA currents. All this adds up to underline the due caution at looking at the values, which should not be taken to contain more information than the order-of-magnitude. However, even this may be considered to be successfull enough and even beyond expectation: for example, Gebauer *et al.* [Geb02] mention that the detection limit of their setup is $10^9\,\Omega$.cm.

The above-mentioned experimental difficulties prevented the Hall-effect measurements for the highest-resistive samples, for which we therefore do not have an estimation for the charge-carrier concentration. This is nevertheless expected to be $\leq 10^{10}\,cm^{-3}$. Also, from the differences in the measured resistivities of the AA and the *Ctec* samples, we expect the charge carrier concentration of the AA sample to be significantly smaller than that of the *Ctec* sample. For all the other samples, the corresponding sign of the carrier confirms, as expected, n–type, and we expect nothing but that for the AA and *Ctec* samples, given the known difficulty of obtaining p–type ZnSe, mentioned in Chapter 1.

The high-resistivity of our samples may be the key to understand the procedure differences we had to adopt, with respect to the older literature on the subject, in order to obtain ohmic contacts in ZnSe. Particularly, we were unable to obtain ohmic contacts by simply annealing at 300^{o}C for a short time, as was done by Swank [Swa69] and by Ray and Kröger [Ray78]. However, most of the samples used in these older researches were previously subject to a "purification" treatment by annealing in liquid Zn at 1000–1050^{o}C for one to two days [Ave62]. This treatment basically removes the compensating zinc vacancies and reduces the resistivity to values as small $10^{-1}\,\Omega.cm$ [Har94]. One may speculate that the liquid-phase epi-

taxial layer formed by In dissolving ZnSe, as proposed by Kaufmann and Dowbor [Kau74], and which is essential to attain ohmic contact, is more easily formed for lesser concentrations of zinc vacancies.

A final word on the mobility values, which are all quite small compared with the maximum values found in the literature, where numbers between 500 $cm^{-2}\,V^{-1}\,s^{-1}$ and 600 $cm^{-2}\,V^{-1}\,s^{-1}$ are accessible, close to the theoretical limit [Pro00]. This points to the presence of electron scattering at impurities and/or defects. The above mentioned zinc vacancies are obvious candidates, and its role is stressed by the differences observed between the *Ctec* sample and the *Ctec:Zn* sample.

Conclusive remarks

As mentioned in chapter 2, the concentration of conduction electrons plays a role in the formation probability of the neutral muonium state or even of the doubly charged state Mu^-. The electrical transport information now obtained, in spite of its unsophisticated nature, will prove to be essential in the reasoning and interpretation of the μSR measurements on ZnSe that constitute the core of this investigation and that will be presented in the next chapter. The brief photoluminescence characterization adds finer microscopic information from the viewpoint of the type and nature of the impurities and defects present, adding important qualitative information for the discussion of the data.

Chapter 4

Experimental results and discussion I: ZnSe

Há-de tomar o pregador uma só matéria, há-de defini-la para que se conheça; há-de dividi-la para que se distinga; há-de prová-la com a Escritura, há-de declará-la com a razão, há-de confirmá-la com o exemplo, há-de amplificá-la com as causas, com os efeitos, com as circunstâncias, com as conveniências que se hão-de seguir, com os inconvenientes que se devem evitar.[1]

Pe. António Vieira
Sermão da Sexagésima

4.1 Introduction

We will now present and discuss the experimental information obtained about the muonium states in ZnSe, by means of the μSR techniques. As we shall see, the physics of muonium in ZnSe is very rich, and a vast amount of different phenomena and interactions is unveiled in temperature-dependent studies. This doesn't ease the experimentalist's work and, in order to disentangle the physics, it is sometimes

[1] Free translation: *"The preacher shall take a single subject, he shall define it so that it is known; he shall divide it so that it is distinguishable; he shall prove it with Scripture, he shall declare it with reason, he shall confirm it with example, he shall amplify it with the causes, with the effects, with the circumstances, with the conveniences that shall be followed, with the inconveniences that should be avoided."*

necessary to focus in specific parts of the experimental data, which more clearly display the particularities of a given phenomenon. In the following, we have chosen to present the experimental data in comprehensive sets grouped essentially according to the experimental subtechnique used. This has the advantage of allowing a broader view first, before moving to particular details, thus facilitating the interpretation path. Of course, there is physical thought before and after experimental data, and the disadvantage of this presentation scheme is that the identified processes become somewhat scattered across the chapter. A final synthesis is then needed and this will be tried in the end of the chapter.

In the course of this work, the samples *AA* and *Ctec* have been the most intensively investigated. As seen in the previous chapter, these are the most intrinsic samples, and so they prove the most adequate for access the "basic" physics of muonium/hydrogen in ZnSe. However, even these samples show already some significant differences, thus pointing clearly the importance of the interactions with charge carriers even at this lower extreme doping limit.

We start by presenting high-transverse field (7 T), high time resolution experiences at TRIUMF for the *AA* and *Ctec* samples, which allowed the discovery of a novel muonium state in ZnSe, as well as deep insight into the paramagnetic muonium conversion at low temperatures. Low-transverse field ($5-10$ G) experiments at PSI, presented subsequently, revealed additional dynamics of the diamagnetic components at about 60 K, which was further explored *via* final-state analysis with RF-μSR. These two sets of data, together with the respective interpretation, constitute the core of this chapter.

We present also additional experimental information, which further supports the interpretation of the above mentioned data, and whose associated work was only begun: the spectroscopy at high-temperatures (above room temperature), the further insight into muonium dynamics by longitudinal field techniques, and the low-transverse field investigations of the other ZnSe samples, which constitute the beginning of doping-dependent studies in this material.

4.2 High-transverse field spectroscopy

4.2.1 Novel deep muonium center in ZnSe

High-field, high time resolution muon spin rotation experiments were performed using the HITIME spectrometer in the M15 beam-line at TRIUMF, in Vancouver, Canada. The *AA* and *Ctec* samples were investigated. The positron counts in the four detectors, arranged in a box-like configuration around the sample, were analysed in a rotating reference frame. A typical time-spectrum (for the *AA* sample, T=2 K, at B=7 T) is shown in Fig. 4.1, for a reference frame rotating at 670 MHz. The superposition of two precession frequencies (692.1 MHz and 776.8 MHz, in the case of figure 4.1), is clearly visible in the time spectrum. The corresponding Fourier spectrum is shown in Fig. 4.2, where the lower frequency line is seen to be significantly broader than the upper line.

Each frequency signal was analysed using an exponentially-damped cosine function of the form $A\,\exp(-\lambda\,t)\,\cos(\omega\,t+\phi)$. The fractions of the two states compared to all muons were calculated from the measured μSR amplitudes assuming that only half of the weight is expected in the observed ν_{12} transition, the second half being contained in the unobserved higher-frequency ν_{34} transition (please refer to section 2.3). Instrumental effects that lead to a decrease in the amplitude of the signals at high-fields are corrected by comparing with the muon precession signal in silver at the same frequency.

Only the ν_{12} transition in muonium being observable at high fields, in the experimentally accessible range, the observation of the two lines indicates either two distinct muonium centers with different isotropic hyperfine interactions or a single muonium center with an anisotropic hyperfine interaction. In the latter situation, the two lines could arise from different angles between the applied field and the symmetry axis of the hyperfine interaction. We have thus undertaken an orientation dependence study of these lines, in order to check the anisotropy hypothesis.

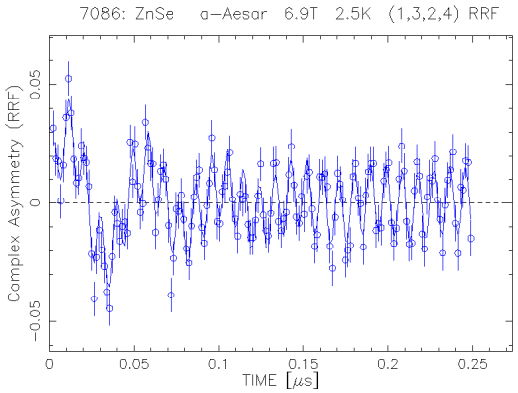

Figure 4.1: Time spectrum obtained for ZnSe at T=2.5 K, B=6.9 T. In order to facilitate the visual inspection, the data are plotted in a rotating reference frame at 670 MHz. The superposition of the 692.1MHz and 776.8 MHz frequencies is seen. Note the higher relaxation of the lower frequency. The line is a fit with a sum of two exponentially-damped cosine functions, as described in the text.

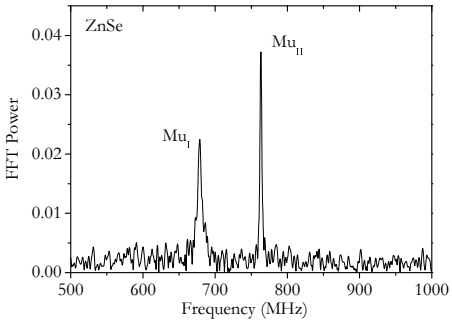

Figure 4.2: Fourier transform μSR spectrum of ZnSe (*AA sample*) at B = 7 T and T = 2.07 K. Two different states, Mu_I and Mu_{II} are observed. The two lines correspond to two different isotropic hyperfine interactions, as discussed in the text.

Orientation dependence study

In order to check the orientation dependence of the muonia precession lines, we have used three oriented ZnSe single crystals from the same *Ctec* batch, cut on the main crystallographic orientations. In these experiments, the magnetic field was applied parallel to the [100], [110] and [111] crystallographic orientations, respectively. The precession frequencies at high-fields for these three samples, together with those for the *AA* sample, are summarized in table 4.1. The frequencies are either equal, at the same applied field, or shift with the characteristic 135.5 MHz/T ratio expected for purely isotropic centers, for different fields. We thus find that the hyperfine frequencies are independent, within experimental errors, of the direction between the applied field and the three major crystallographic directions [100], [110] and [111].

Sample	T (K)	TF (T)	f_I (MHz)	f_{II} (MHz)	A_I (MHz)	A_{II} (MHz)
AA	1.9(6)	6.899968	692.1(2)	776.80(8)	3454.6(2)	3282.2(4)
Ctec [111]	5.1(9)	6.899968	692.1(2)	776.82(7)	3454.7(1)	3282.2(4)
Ctec [110]	4.8(12)	6.77999	707.96(19)	792.60(8)	3454.2(2)	3281.9(4)
Ctec [110]	4.86(3)	5.999996	811.9(3)	896.31(8)	3454.3(2)	3282.0(1)
Ctec [100]	2.8(2)	6	812.5	896.25	3454.2(2)	3283.3(4)

Table 4.1: Orientation dependence of the muonium precession frequencies. The corresponding isotropic part of the hyperfine interaction, as obtained from equation 4.1, is also included.

We therefore conclude that two distinct Mu centers, Mu_I and Mu_{II}, with different isotropic hyperfine interactions are responsible for the observed spectra.

We include in table 4.1 the corresponding hyperfine interactions, obtained from the following expression, easily derived from table 2.4:

$$A = \frac{2\gamma_e\gamma_\mu B^2 - 2\nu_{12}^2 + 2\nu_{12}(\gamma_e - \gamma_\mu)B}{(\gamma_e - \gamma_\mu)B - 2\nu_{12}} \tag{4.1}$$

where the corresponding error σ_A is given by:

$$\sigma_A = 2 \left| \frac{A}{(\gamma_e - \gamma_\mu)B - 2\nu_{12}} + 1 \right| \sigma_{\nu_{12}} \tag{4.2}$$

From the average value of the hyperfine parameters in table 4.1, we estimate the corresponding values of the hyperfine interactions to be $A_I = 3282.1(1)$ MHz and $A_{II} = 3454.4(1)$ MHz at the lowest measured temperature. These values correspond to 73.5 % and 77.4 % of the vacuum value, respectively.

From the maximum observed difference of the hyperfine interaction values in table 4.1 and eqs. 2.40 and 2.39, we may obtain a maximum limit for the value of a presumed dipolar component D in the hyperfine interaction, obtaining $D_I < 0.5$ MHz and $D_{II} < 1.4$ MHz.

4.2.2 Temperature dependence of the paramagnetic states: *AA* sample

We now address the temperature dependence of the paramagnetic lines, as observed in these high-field muon spin rotation experiments. We present firstly, in this section, the results for the AA sample, which allow deeper insight, and leave for the next section the corresponding results for the *Ctec* sample.

Figure 4.3 shows the fractions of the two muonium states in the AA sample, as a function of temperature. Up to 40 K, both states coexist, Mu_I being nearly twice as intense as Mu_{II}, and the total muonium fraction being 79±1%. Above 40 K, Mu_I disappears and the fraction of Mu_{II} increases strongly in a narrow temperature interval. This indicates a conversion of Mu_I to Mu_{II}, the latter being the only state visible at higher temperatures. The total intensity of visible muonium signals decreases strongly above the conversion region. This probably is an effect of muon spin depolarization during the time between implantation and formation of the final state, since no appreciable change in the diamagnetic signal is observed in the entire temperature range. The diamagnetic signal strength is extremely small and consistent with zero diamagnetic fraction arising from the ZnSe sample. This signal can probably be entirely accounted for by muons stopping outside the sample, at

all temperatures below 300 K. We shall come back to this point.

The temperature dependence of the depolarization rates λ of the two states can be seen in Fig. 4.4. The most obvious feature is the strong increase of λ for Mu_I between 10 and 40 K. This is attributed to the temperature activated conversion of state I to state II. The relaxation of Mu_I is also rather large (about 14 $\mu\, s^{-1}$) before the onset of the conversion process perhaps due to a rapid spin fluctuation of Mu_I. The relaxation of state Mu_{II} is very low and does not change up to approximately 200 K, which includes the region of the conversion of state I to state II. Above 200 K an increase of the depolarization of Mu_{II} is seen.

The phases of the signals in each detector are governed by the detector geometry with respect to the muon spin polarization prior to implantation. However, as was discussed in chapter 2, additional phase shifts are introduced if the muon exists for some time in a precursor state before it forms the final configuration. Such phase shift effects are seen in Fig. 4.5 for Mu_{II} as a dip around 50 K and as the gradual decrease above 100 K.

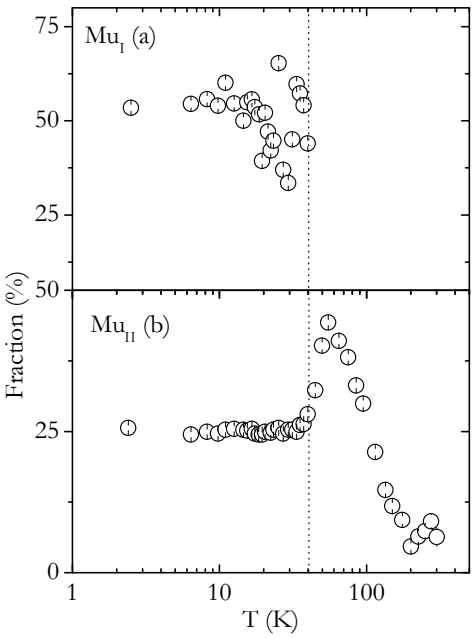

Figure 4.3: Fractions of the two muonium states, Mu_I (a) and Mu_{II} (b), observed for the AA sample at TF 7 T, as a function of temperature. Mu_I is seen only up to approximately 40 K.

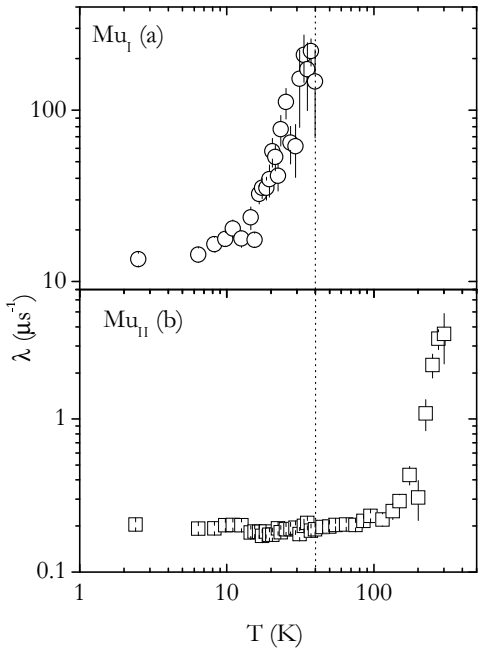

Figure 4.4: Depolarisation rates of the two muonium states, observed for the AA sample at TF 7 T, as a function of temperature.

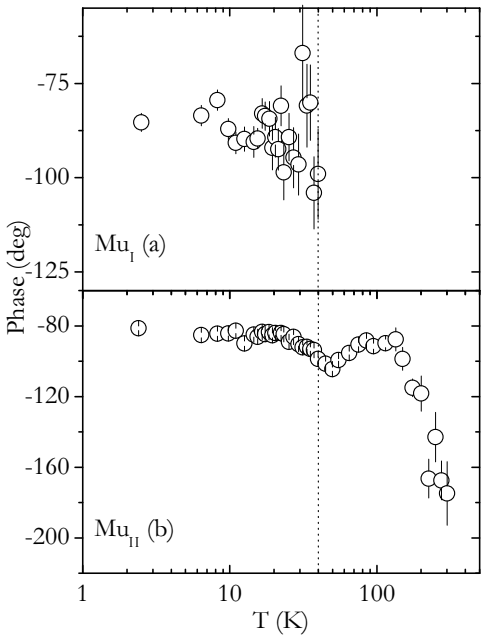

Figure 4.5: Phases of the two muonium states, observed for the AA sample at TF 7 T, as a function of temperature.

Temperature dependence of the hyperfine interaction

Before discussing the above-mentioned results in more detail, we begin by addressing the temperature dependence of the hyperfine interaction A_{iso} for Mu_{II}, as shown in Fig. 4.6. Such data are often modelled assuming an interaction with long-wavelength phonons which are treated within the Debye model [Pat88].

In this model, the decrease with temperature of the hyperfine interaction is usually explained by admitting that the atom ground state configuration is mixed *via* orbit-lattice interaction with excited configurations of the form ns by a dynamic phonon-induced field [Šim66], where the lattice vibrations are treated within a Debye model. The temperature dependence of the hyperfine interaction is proved to be, in this description:

$$A = A_0 \left[1 - C\,T^4 \int_0^{\theta_D/T} \frac{x^3}{e^x - 1} dx \right] \tag{4.3}$$

where A_0 is the hyperfine interaction at $T = 0\ K$, T is the absolute temperature, θ_D is the Debye temperature of the material and C is a temperature-independent parameter.

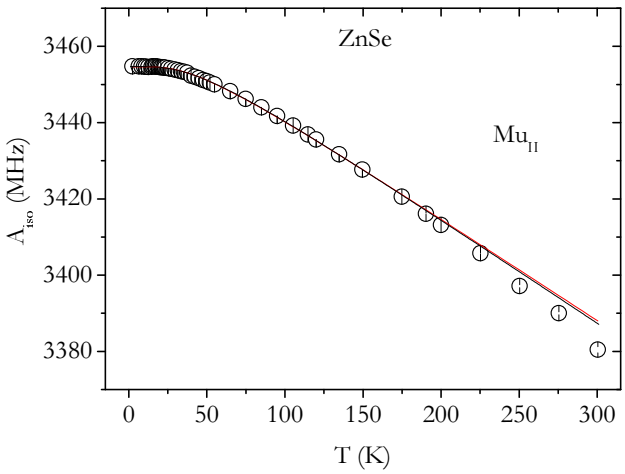

Figure 4.6: Temperature dependence of A_{iso} of state Mu_{II}, observed for the AA sample at TF 7 T. The red solid line is a fit with a (first-order) Einstein model. The black line is a fit with a Debye model.

In the present case the fit to this model, which is shown in figure 4.6, gives a Debye temperature of $T_D = 160$ K. The Debye temperature for the ZnSe matrix from the literature is 275 K [Bir75]. Similar discrepancies in a ratio of roughly 2 to 3, were also found for several other semiconductors [Lic04, Pat88]. However, the fit with the Debye model is rather poor for the high temperature points in the current case.

We should note that this model was developped by Šimanék and Orbach specifically to explain the temperature dependence of the hyperfine interaction in $3d^5$, ^6S paramagnetic ions such as Mn^{2+}. In the case of muonium, we have a $1s^1$ ground state configuration, which is admitted to be mixed, in the framework of this model, with $2s^1$, $3s^1$, etc configurations. Perhaps part of the explanation of the failure lies in the possible mixture with $2p$ configurations. Or else, the underlying Debye model does not apply entirely.

A different approach to the problem is to assign the temperature dependence to a local vibrational mode (e.g. the oscillation of muonium in the potential provided by the matrix) and assume that the change of the hyperfine interaction is adequately described by a series on the mean square displacement $< u^2 >$:

$$A(T) = a_0 + a_2 < u^2 > + a_4 < u^4 > + ... \tag{4.4}$$

Within this harmonic oscillator model, the temperature dependence can be obtained from a Boltzmann distribution. Admitting, for simplicity, a single vibrational frequency ν (Einstein model), one arrives at the following formula for the temperature dependent isotropic hyperfine interaction $A(T)$:

$$A(T) = A_0 + \frac{C_1}{\exp(h\nu/kT)} + \frac{C_2}{(\exp(h\nu/kT))^2} \tag{4.5}$$

where A_0 is the hyperfine interaction at $T = 0\,K$ and ν is the single vibration frequency in an Einstein model. The coupling constants C_1 and C_2 are assumed temperature-independent. Eq. 4.5 corresponds to the first three terms of the formula given in reference [Rod95] and reference [Mor94]. Without the second order term, a fit with this model, shown in figure 4.6, did not describe well the

data points at the higher temperatures, indicating a deviation from the simple proportionality between A and $< u^2 >$.

The fit (solid line in Fig. 4.7) gives an energy $h\nu = 8.0 \pm 0.1$ meV. Such a low vibrational energy, if attributed to the oscillation of muonium in the cage, would correspond to an extremely flat potential.

The limited temperature range for observation of Mu_I does not allow any detailed determination of the temperature dependence of the respective hyperfine interaction.

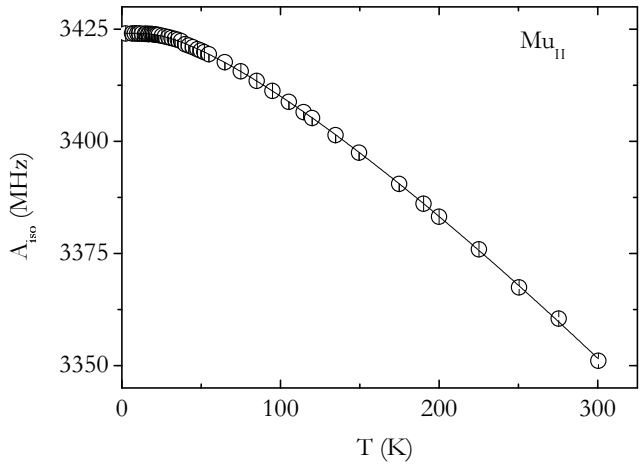

Figure 4.7: Temperature dependence of A_{iso} of state Mu_{II}, observed for the AA sample at TF 7 T. The solid line is a fit with an Einstein model, as described in the text.

Mu_I to Mu_{II} conversion

A second important aspect in these high-field experimental data relates to the conversion of Mu_I to Mu_{II}. We have analysed this aspect with the simple conversion model presented in chapter 2. There, we found the following expression for the polarization change $\Delta P(t)$, in the case where state I, detected via frequency ω_I, converts to a state II, which is detected via frequency ω_{II}:

$$\begin{aligned} \Delta P(t) &= A_I \exp(-t/\tau)\cos(\omega_I\, t + \phi_I) \\ &+ \frac{A_I}{\sqrt{1+(\Delta\omega\,\tau)^2}}\cos(\omega_{II}\, t + \phi_I - \tan^{-1}(\Delta\omega\,\tau)) \\ &- \frac{A_I \exp(-t/\tau)}{\sqrt{1+(\Delta\omega\,\tau)^2}}\cos(\omega_I\, t + \phi_I - \tan^{-1}(\Delta\omega\,\tau)) \end{aligned} \tag{4.6}$$

where τ is the mean lifetime of the initial state and $\Delta\omega = \omega_{II} - \omega_I > 0$. For τ an Arrhenius ansatz $\tau = \tau_{inf}\exp(E_a/kT)$ was used, with E_a the activation energy. An acceptable global fit of all data using a unique set of parameters for the conversion could not be obtained. The increase of the relaxation of Mu_I and the rise of the fraction of Mu_{II} (Fig. 4.8) are too far separated in temperature to be fitted with a single activated conversion process. A similar discrepancy was observed for the conversion of Mu_I to Mu_{II} in CuCl and CuBr [Kie86]. The reason is probably that in the stage before the actual conversion, local motion of muonium and of the lattice atoms change dramatically and result in an increase of the spin relaxation.

In Fig. 4.8(b) and Fig. 4.8(c), the solid lines show the fit to the amplitude and phase of Mu_{II}. In the fit we assumed that the amplitudes of Mu_I and Mu_{II} do not change in the conversion temperature range and that their values are the same as at low temperatures. This, however, is not completely correct and leads to the overestimation of the Mu_{II} fraction above 60 K in Fig. 4.8(c). From this fit, we obtain $E_a = 17$ meV and $\tau_{inf} = 1.1 \times 10^{-4}$ μs. These values should be considered as a first approximation for the Mu_I to Mu_{II} transition, since any other dynamic process involving either state has been left out of this simple model. With the same fitted parameters as in Fig. 4.8(b) and (c), the solid line in Fig. 4.8(a) is calculated. The discrepancy indicates again that the conversion process is more intrincate than assumed in our model. The possible existence of a pre-conversion dynamics, as discussed above, may justify the difference.

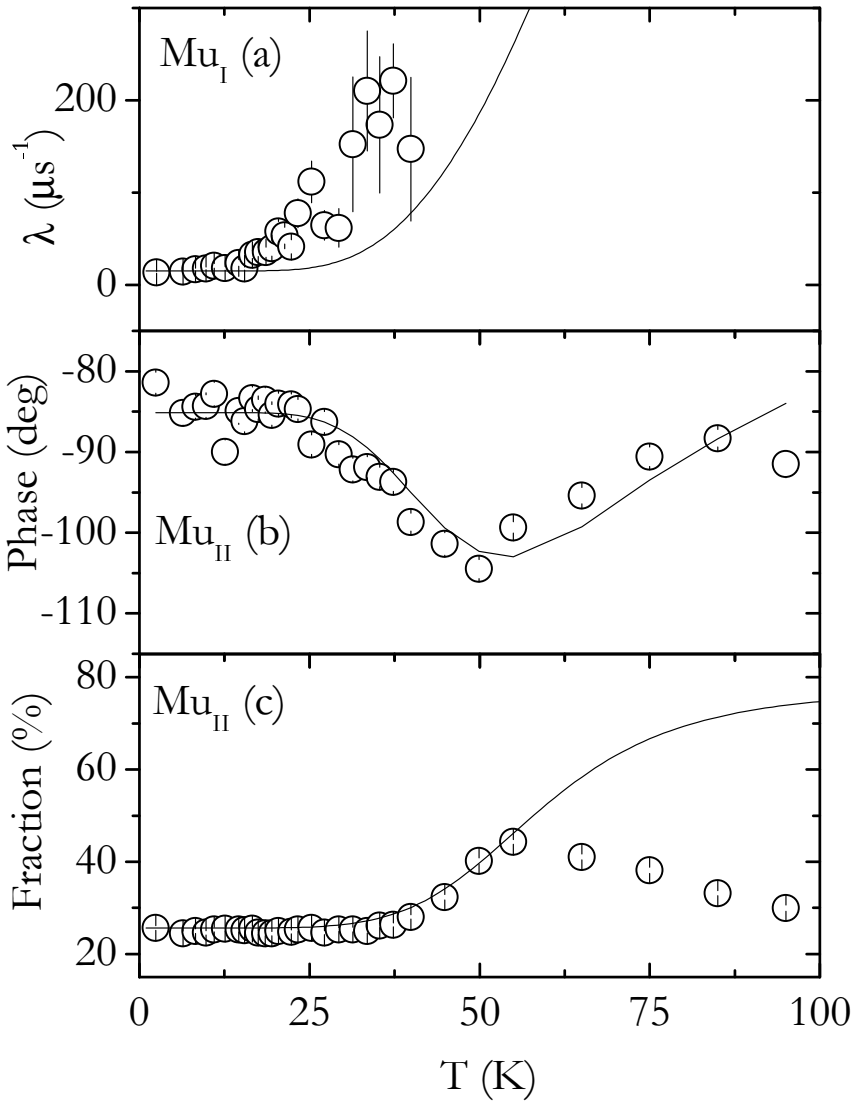

Figure 4.8: Relaxation rate of Mu_I, phase shift of Mu_{II}, and fraction of Mu_{II}, observed for the *AA* sample at TF 7 T, as a function of temperature. The solid lines are fit curves assuming activated conversion of Mu_I into Mu_{II}, as described in the text.

"Missing fraction"

At low temperatures, $\sim 21\%$ of the muons are not observed in high transverse-field. Figures 4.3 and 4.8 show that the total muonium fraction, above 60 K represented by the fraction Mu_{II}, decreases with temperature. As pointed out above, no corresponding change is observed in the diamagnetic fraction. A possible explanation for the "missing fraction" is that the donor electrons of ZnSe, which become activated [Dev67] at around 60 K, cause a depolarization of the muon spin in a precursor stage during the thermalization process, i.e. in the time between the implantation and the formation of the final state.

As indicated in Fig. 4.4 and Fig. 4.5, there is a dramatic change in the relaxation and phase of the Mu_{II} signal above about 200 K. Aditionally, in the same temperature range, up to room temperature, the muonium fraction becomes temperature independent (fig. 4.3). Above 200 K, donor ionization is essentially complete and any process that depends critically on conduction electron concentration begins to saturate. We note that a conversion from a precursor stage can not lead to an increase in the relaxation of the final state. Therefore, the increase of the depolarization of Mu_{II} above 200 K (Fig. 4.4) must be due to a process acting on Mu_{II} directly.

It is also unlikely that the increase of the relaxation is due to the onset of a conversion of this state to another state since, as we shall see in section 4.5.3, Mu_{II} is observed up to 550 K. This observation is not consistent with an activated conversion setting in already at 200 K.

Additionally, the observed change in the phase of Mu_{II} above 150 K (Fig.4.5) is not related to the Mu_I to Mu_{II} conversion since that transition has already become very rapid well below that temperature. These features imply that additional dynamics are present for both Mu_{II} and a precursor state which is not necessarily Mu_I. Thus an interaction with conduction electrons might be the cause of the relaxation and the phase shift must be caused by some process in the precursor stage. We shall come back to this in section 4.4.

4.2.3 Temperature dependence of the paramagnetic states: *Ctec* sample

We show in figures 4.9 to 4.12 the result of similar temperature dependence studies in high-field muon-spin rotation experiments, undertaken with the *Ctec* [100] sample.

Though the basic characteristics of the two muonium states are the same, as was already pointed out in table 4.1, these data nevertheless show some enlightening differences:

(i) as show in figure 4.9, the total muonium fractions observed at the lowest temperature is now 91(1)% (79(1)% for the *AA* sample), and the additional fraction is essentially due to Mu_I;

(ii) above 25 K, the Mu_{II} state is now seen to broaden (fig. 4.10) and its amplitude to decrease to zero at 60 K (fig. 4.9), whereas the Mu_I state is no longer observable due to extreme broadening, as seen in figure 4.10;

(iii) the two states cease to be observed before any significant phase shift appears, as seen in fig. 4.11.

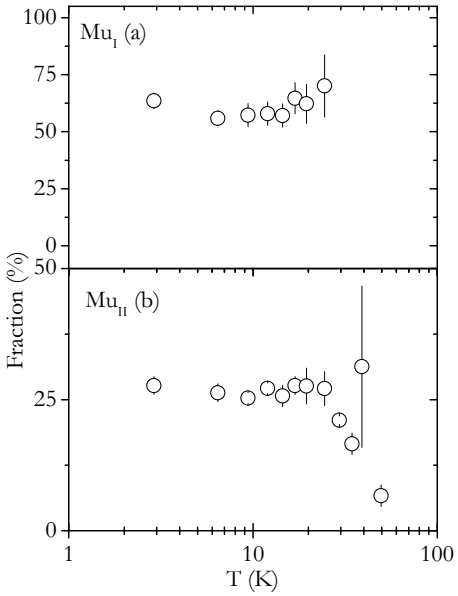

Figure 4.9: Fractions of the two muonium states, Mu_I (a) and Mu_{II} (b), observed for the *Ctec* sample at TF 7 T, as a function of temperature. Mu_I is seen only up to approximately 20 K and Mu_{II} up to 50 K.

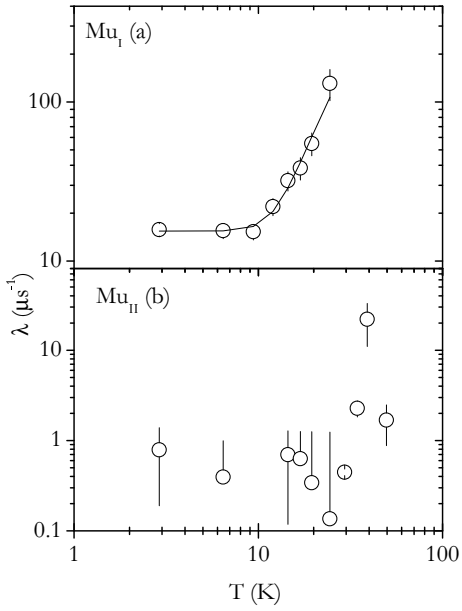

Figure 4.10: Depolarisation rates of the two muonium states, observed for the *Ctec* sample at TF 7 T, as a function of temperature. The line in (a) is a fit with an Arrhenius activated function, yielding an activation energy of 6(1) meV.

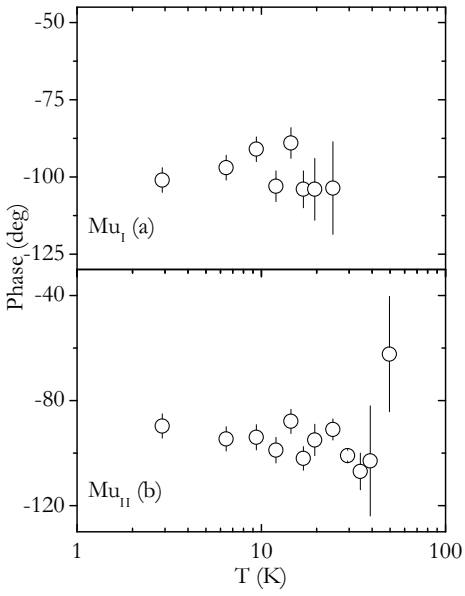

Figure 4.11: Phases of the two muonium states, observed for the *Ctec* sample at TF 7 T, as a function of temperature.

These features point to the presence of an additional process besides $Mu_I \rightarrow Mu_{II}$ conversion. This conversion is still present, and is signed only *via* the broadening of the Mu_I state seen in fig. 4.10, similarly to that observed for the *AA* sample 4.4. However, the onset at 25 K of the new process involving Mu_{II} and leading to its disappearance already above 50 K prevents the observation of the characteristic phase shift in the Mu_{II} precession frequency. Also, as seen in fig. 4.12, only a hint of the the temperature dependence of the hyperfine interaction A_{II} is seen. Thus, only the increase of the relaxation rate remains as sign of conversion, which has been fitted to a simple Arrhenius activation, yielding an activation energy of 6(1) meV. This should be compared to the value obtained when fitting the same process to the corresponding increase in the *AA* sample (fig. 4.4), where we obtain an energy of 7(1) meV, much smaller than the 17 meV obtained in the global fit of fig. 4.8.

From these data, not much can be extracted about the nature of this process, except that it is related to the greater abundance of charge carriers in the *Ctec* sample (please refer to table 3.3 and subsequent comments). This larger concentration of charge carriers in the *Ctec* sample is apparent in the larger fraction of muons that capture an electron at low temperatures, as expressed in the total muonium fraction. The reason why only the formation probability of Mu_I is affected is however not clear.

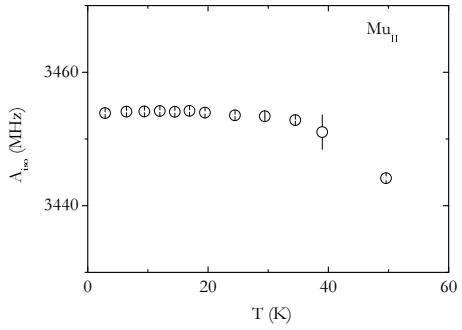

Figure 4.12: Temperature dependence of A_{iso} of state Mu_{II}, observed for the *Ctec* sample at TF 7 T. Only a hint of the corresponding decreasewith temperature is present, before the disappearance of the Mu_{II} frequency.

4.2.4 Discussion

The high-field muon spin rotation experiments have revealed a new muonium state in ZnSe at low temperatures, the presence of which accounts for a large portion of the muon fraction that was missing in previous experiments. The detection of this state was made possible only in a high time resolution setup, by the application of a high magnetic field in which the depolarization of the state is sufficiently slow to allow for its observation. The two states observed here have characteristics very similar to those reported[Kie86, Sch90, Sch92] for CuCl. In these publications, after a detailed characterization of the local surroundings of muonium, definite site assignments were determined *via* interaction with the abundant nuclear moments, placing both Mu centers in the tetrahedral cage with Cu nearest neighbors but with different lattice relaxations and different specific locations and motional properties for Mu.

A similar situation may exist for both Mu_I and Mu_{II} in ZnSe. By analogy, we expect both centers to reside in the same region, i.e. in the tetrahedral interstitial cage surrounded by four nearest neighbor Zn ions. In this case, Mu_I corresponds to muonium embedded in the not yet relaxed lattice. It finds potential minima slightly off the center position and tunnels among the different sites. A muonium impurity at an off-center location within the tetrahedral cage should have some anisotropy in its hyperfine interaction. The dynamical effect of tunneling would average out this anisotropy and could explain the rather large depolarization of Mu_I discussed above. In the CuCl analogy, Mu_{II} can be assigned to muonium in the center of the Zn cage after lattice relaxation has occurred in reaction to the presence of the muon. There is apparently a barrier between the two configurations which is overcome thermally in the range where the conversion from Mu_I to Mu_{II} is observed. A separation of singlet and triplet tunneling states for muonium delocalized over four cation-related sites has also been proposed as an explanation for such a barrier [Cox87].

Another interpretation of the two signals could be that they correspond to two different sites, one to muonium in the anion tetrahedral cage and the other to muonium in the cation tetrahedral cage of ZnSe. In a theoretical paper [VdW93a],

isotropic hyperfine interactions of 3333 MHz for Mu in the Zn cage (T_{Zn}) and of 3248 MHz for Mu in the Se cage (T_{Se}) were predicted, which are remarkably close to our experimental values. In this second interpretation, Mu_I would correspond to a deep-donor state at T_{Se}, where a neutral and a positively charged muonium center can be located. Mu_{II} corresponds in this interpretation to a deep acceptor state at the T_{Zn} site, where a neutral and a negatively charged center can be located.

In the zincblende structured II-VI materials, which have considerable ionic character in the bonding, the anion cage becomes competitive with the bond-centered location for both the neutral and positively charged donor states. The strong evidence here for conversion from Mu_I to Mu_{II} would then imply that the T_{Zn} acceptor site is the more stable location for Mu in ZnSe. This experimental evidence also implies that, in the two-site model, the site-change transition is faster than Mu_I ionization below roughly 50 K. However, if the Mu_I deep-donor ionization rate were competitive and increasing rapidly with temperature, then ionization of Mu_I prior to conversion to Mu_{II} could provide an explanation for the decrease in Mu_{II} amplitude that is observed between 60 and 150 K (Fig.4.3). This is also consistent with a second exit route from Mu_I as inferred from the mismatch of the Mu_I relaxation results when compared to the fits to the data of Fig. 4.8.

The present experiment confirms that normal muonium at an acceptor site, here called Mu_{II}, is the stable muon configuration in ZnSe. The only other neutral signal in ZnSe is Mu_I which converts to Mu_{II}. Here, no sign of the shallow effective-mass donor has been found. Thus ZnSe belongs to the class of semiconductors in which the shallow donor is absent and instead one or more deep muonium centers are observed, as is the case for Si or for GaAs [Cho98, Pat88]. These high-field data provide no clear experimental evidence for ZnSe, as there was for CuCl, on which to base an independent choice between the two-site and single-site models; thus, it is not definite at this juncture whether or not a deep donor state is also observed in addition to the deep acceptor ground state. However, several arguments favour the single-site model: the Mu_I relaxation rates, the very close resemblance of ZnSe to the CuCl system (both from the crystallographical and the ionic character point of view), as well as the similarity of the respective muonium experimental

data, together with the definite assignment of the two Mu signals to the same T-site cage in CuCl. All these advocate rather strongly in favour of the single-site interpretation.

4.3 Low-transverse field spectroscopy

The investigation of the above-noted difference among the *AA* and *Ctec* samples was continued at low-transverse-fields at PSI. The *AA* sample was investigated at the GPS instrument, with a transverse field of 5 G, and the *Ctec* [111] sample was investigated at the DOLLY instrument, with a transverse field of 10 G. Both samples were implanted with muons polarized in the backward (B) direction, and the transverse field was applied in the left-right (L-R) direction. As usual, all directions are referred with respect to the incoming muon momentum. Time histograms were accumulated in the detectors placed in the forward (F), backward (B), up (U) and down (D) positions. Again, each histogram was fitted with one or two exponentially damped sinusoidal function with the form $A\exp(-\lambda t)\cos(2\pi\nu t + \phi)$. Silver calibration measurements were used to obtain the instrument maximum asymmetry. Typical spectrums for the *AA* and *Ctec* samples are shown in figs. 4.13 and 4.14.

4.3.1 *AA* sample

As is eloquently expressed by fig. 4.13, in the *AA* sample we observe essentially a paramagnetic fraction, although a marginal diamagnetic fraction is present as well in the spectra.

We present in figures 4.15 and 4.16 the results for the paramagnetic and diamagnetic fractions and relaxations. A very small diamagnetic fraction is observed, presenting no temperature dependence, and which may be attributed to background.

At these low-fields, the muonium ν_{12} and ν_{23} precession frequencies are independent of the hyperfine interaction, and it is therefore not possible to distinguish the paramagnetic Mu states spectroscopically. However, the observed state is iden-

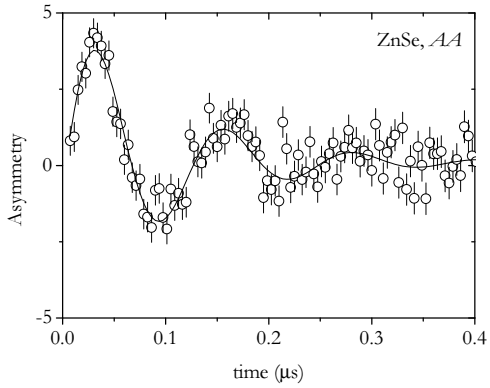

Figure 4.13: Time spectrum obtained for the AA sample, at T=55 K and TF=5 G. Only the first 400 ns are shown, where a 8 MHz oscilation, due to muonium, is visible. The line is a fit with a lorentzian damped 8 MHz oscillation.

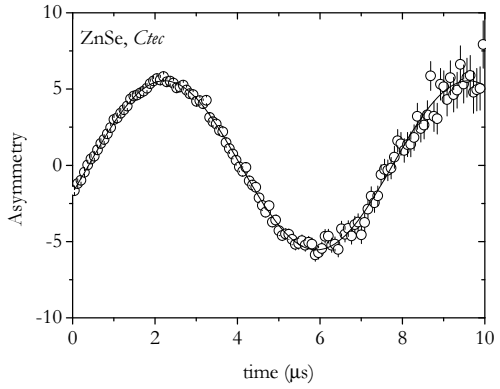

Figure 4.14: Time spectrum obtained for the *Ctec* sample, at T=55 K and TF=10 G. Unlike what is observed for the AA sample (fig. 4.13), the muonium oscillation is no longer visible at this temperature, instead a significant 0.14 MHz diamagnetic frequency is seen. The line is a fit with an unrelaxed 0.14 MHz oscillation.

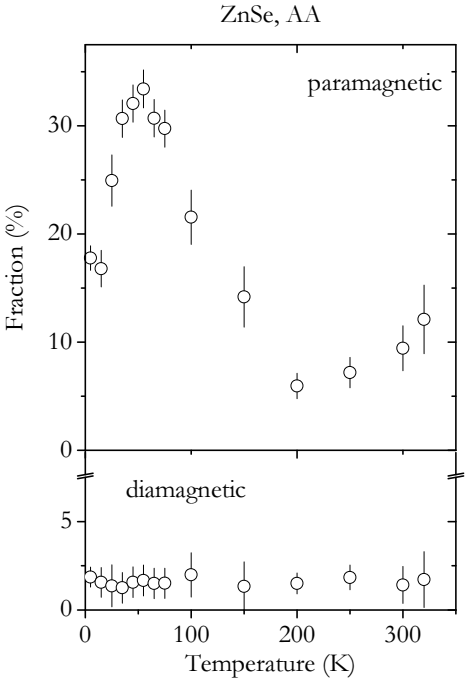

Figure 4.15: Paramagnetic (Mu_{II}) and diamagnetic fractions, observed for the AA sample at TF 5 G = 0.5 mT, as a function of temperature.

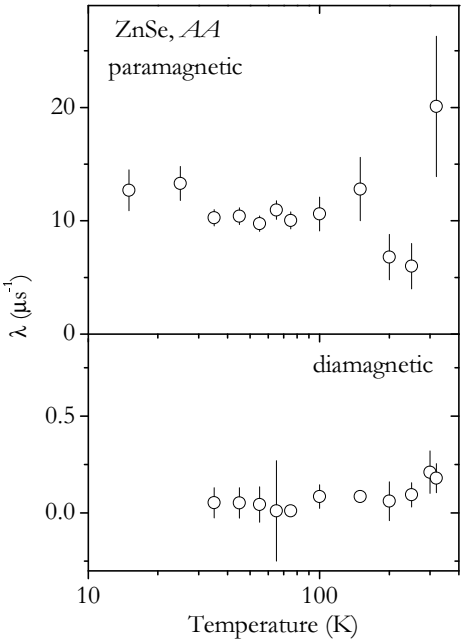

Figure 4.16: Depolarisation rates of the paramagnetic (Mu_{II}) and diamagnetic fractions, observed for the AA sample at TF 5 G = 0.5 mT, as a function of temperature.

tified with Mu_{II}, since the high relaxation of the Mu_I state, as seen under the 7 T field, does not allow its direct observation in the lower resolution setup at PSI. Also, the experimentally observed Mu precession frequency presents no temperature dependence, as expected at low fields where the ν_{12} and ν_{23} frequencies are independent of the hyperfine interaction, as discussed in section 2.3.

We note, in fig. 4.15, the difference in the paramagnetic Mu_{II} fraction at the lowest temperature (17%, vs. 25% at 7 T, see fig. 4.3). This may be due to the repolarization of part of the missing fraction. We note that this can not be attributed to the field dependence of the converted asymmetry, since we expect it to be smaller in high fields.

The 50 K peak observed in the high transverse field data (fig. 4.3), is here observed at the same temperature and is again identified with $Mu_I \rightarrow Mu_{II}$ conversion. The decrease of the Mu_{II} fraction above 50 K is also present, with no apparent impact in the diamagnetic fraction. The corresponding relaxations are shown in fig. 4.16. Despite no significant changes are observed in the respective temperature dependence, a quite broad relaxation of the Mu_{II} state is observed.

Again, the dynamical process above 200 K makes itself visible *via* a slight reincrease of the Mu_{II} fraction, which amounts to c. 12% of the total muon spin polarization at 300 K.

It looks therefore that these low-field data bring no new information with respect to the high-field data at TRIUMF and are, in some sense, redundant. However, three types of reasons impose the need to consider them here:

(i) the contrast with the *Ctec* low-field TF data, shown in the next section, and which have, unlike these data, new information;

(ii) the spectroscopical investigations of the processes undergoing at higher temperatures (above room temperature) can only be done at PSI; these data thus provide us with a coherent set of data from liquid-He temperature, to the highest temperature attainable at PSI; we leave the presentation of these high temperature investigations to a later moment;

(iii) finally, these data confirm our previous high-field data and interpretation.

4.3.2 *Ctec* sample

We present in figures 4.17, 4.18, 4.19 and 4.20 the results for the corresponding low field (TF10G) muon spin rotation measurements of the *Ctec* sample, undertaken at the DOLLY instrument at PSI. Unlike the case for the *AA* sample, we now observe a significant diamagnetic fraction (see fig. 4.14), peaking at about 60 K (fig. 4.17). This had not been observed in the 7 T measurements, which stopped, for this sample, at 45 K. The diamagnetic fraction is seen to increase with temperature from 3% at 30 K up to 25% at 65 K. This increase matches the corresponding decrease in the paramagnetic fraction, identified once again with Mu_{II}. Of note, the low-temperature Mu_{II} fraction now observed is equal to the one seen in the high-field experiments (cf. fig. 4.9), indicating that the low-temperature dynamical process leading to the missing fraction in the *AA* sample is now absent.

Other signatures of conversion from Mu_{II} to the diamagnetic fraction, in the 30 - 60 K region, include the relaxation increase in the Mu_{II} signal (figure 4.18) and the pronounced phase-shift in the diamagnetic signal (figure 4.19).

Above 60 K, another process sets in, leading to the disappearance of the diamagnetic fraction, and an increase of the diamagnetic relaxation is observed (fig. 4.20), though it is obscured by the almost complete disappearance of this fraction above 100 K.

Discussion

The data just presented for the *Ctec* sample at TF 10 G clearly display signs of conversion of the paramagnetic fraction (presumably, and most reasonably, Mu_{II}) to a diamagnetic fraction. This occurs as a thermally activated process from about 30 K to 60 K and, as the difference among the two samples indiciates, is observed mostly in the sample with higher concentration of conduction electrons.

As in the conversion of Mu_I to Mu_{II}, discussed in the previous section, the conversion of the paramagnetic fraction to the diamagnetic fraction is visible through the increase of relaxation of the converting state, and as an asymmetry increase and phase-shift of the converted state.

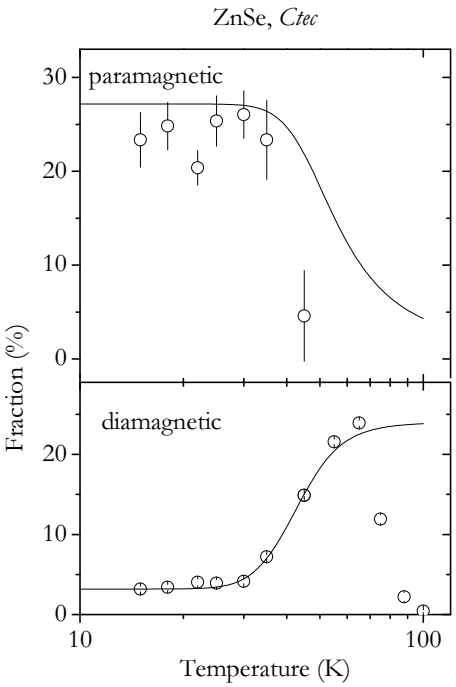

Figure 4.17: Paramagnetic (Mu_{II}) and diamagnetic fractions, observed for the *Ctec* sample at TF 10 G = 1 mT, as a function of temperature. The line in the diamagnetic fraction graph is a fit assuming an activated electron capture, as discussed in the text. The line in the paramagnetic fraction graph is a simulation for the corresponding variation of the paramagnetic fraction.

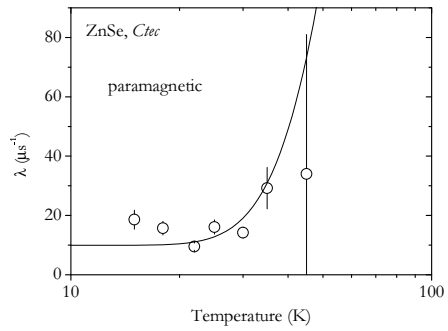

Figure 4.18: Paramagnetic relaxation, observed for the *Ctec* sample at TF 10 G = 1 mT, as a function of temperature. The line is a fit assuming an activated electron capture, as discussed in the text.

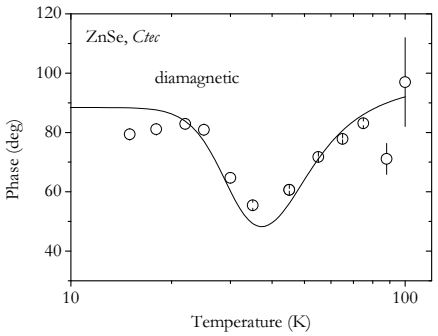

Figure 4.19: Phase of the diamagnetic component, observed for the *Ctec* sample at TF 10 G = 1 mT, as a function of temperature. The line is a fit assuming an activated electron capture, as discussed in the text.

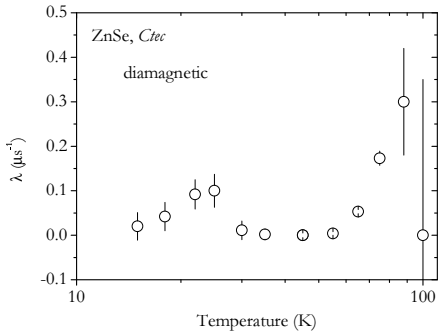

Figure 4.20: Relaxation of the diamagnetic component, observed for the *Ctec* sample at TF 10 G = 1 mT, as a function of temperature. The increase at c. 60 K is a sign of the onset of a second process, leading to the decrease of the diamagnetic fraction.

At first sight, three processes may be considered as candidates to supply an interpretation of these conversion data:

- simple electron ionization: $\mathrm{Mu}^0_{\mathrm{II}} \rightarrow \mathrm{Mu}^+ + e^-$. However, this activated ionization of the Mu electron should not differ among samples; also, such a fundamental process is also expected to occur at much higher temperatures for such compact centers;

- hole ionization $\mathrm{Mu}^0_{\mathrm{II}} \rightarrow \mathrm{Mu}^- + h^+$: this case corresponds to an activated electron promotion from the valence band (or hole ionization). Again, such activated process is expected to be the same for the two samples, except that it implies a previous hole capture, at possibly different cross-sections. However, the hole capture is roughly proportional to hole concentration [h], which is a negligible quantity at these temperatures. Nevertheless, from the law of mass-action, the concentration of holes is related to the intrinsic concentration of conduction electrons, n_i, and to the actual concentration of electrons, n, by $[h] = n_i^2/n$. So, $[h]$ is expected to be larger for the AA sample, again in apparent contradiction with the data.

- second electron capture $Mu^0_{II} + e^- \rightarrow Mu^-$, which seems to be the most physically sensible process and which readily makes the data understandable:
  - this implies the capture of a second electron occurring after the ionization of the donors of the material, possibly after the muon thermalization;
  - it seems likely that this delayed capture may be even more delayed if the concentration of donors is smaller, and this might explain why the diamagnetic fraction is not observed in the *AA* sample; the second electron takes too long, and/or this capture is preceded by spin fluctuations that depolarize the muon spin and lead to a (much smaller) decrease of the paramagnetic amplitude, without the corresponding increase of the diamagnetic amplitude.
  - at the lowest temperatures, as pointed out in the preceding section, only a small percentage of the muons implanted in the *Ctec* sample manage to capture the second electron; the process becomes more important as donors are ionized and more conduction electrons become available.

Analysis of second electron capture by Mu_{II}

We have analysed the relevant parameters (paramagnetic relaxation, diamagnetic fraction, diamagnetic phase) with the same model applied to the Mu_I to Mu_{II} conversion (eq. 4.6).

In the $Mu^0_{II} + e^- \rightarrow Mu^-$ model, the lifetime τ of the Mu_{II} state is the inverse of the capture rate ν_c of the second electron. In the simplest approach, ν_c is expected to be proportional to the concentration n of conduction electrons and to the respective velocity v_e:

$$\nu_c = \sigma_c \, v_e \, n \tag{4.7}$$

where σ is the cross section for the capture and the mean thermal velocity is given by [Rei65][2]:

[2] Cf. eq. 7.10.16 of the cited reference.

$$v_e = \sqrt{\frac{3kT}{m_e^*}} \tag{4.8}$$

The temperature dependence of the concentration of conduction electrons in the conduction band, for a compensated n-type semiconductor with N_a compensating acceptors and N_d donors with spin degeneracy β (usually taken to be $\beta = 1/2$) at the single donor ionization energy E_d, is given by [Bla62][3]:

$$\frac{n(n+N_a)}{N_d - N_a - n} = \beta\, N_c \exp\left(-\frac{E_d}{kT}\right) \tag{4.9}$$

where N_c is the effective density of states in the conduction band and is given by[Bla62][4]:

$$N_c = 2\left(\frac{m_e^* kT}{2\pi\hbar^2}\right)^{3/2} \tag{4.10}$$

and $m_e^* = 0.16\, m_0$ is the electron effective mass in this compound [Mad82].

This formula can be further simplified at low temperatures, assuming $N_d >> n >> N_a$:

$$n = n_\infty \exp\left(-\frac{E_d}{2kT}\right) \tag{4.11}$$

where

$$n_\infty = \sqrt{\beta\, N_c\, N_d} \tag{4.12}$$

An exponential, Arrhenius-like, dependence for the capture rate 4.7 is therefore expected in this approximation, with an activation energy which is about half of the donor energy E_d:

$$\nu_c = \sigma_c\, v_e\, n_\infty \exp\left(-\frac{E_d}{2kT}\right) = \nu_c^\infty \exp\left(-\frac{E_d}{2kT}\right) \tag{4.13}$$

In the final analysis, we have used this exponential approximation, and fixed the donor energy to 30 meV (i.e., the Arrhenius activation energy to 15 meV),

[3]Cf. p. 138, in the cited reference.

[4]Cf. p. 80, in the cited reference.

which is a usual value for donors in ZnSe [Mad82]. Thus, the only free parameter is the pre-exponential factor ν_c^∞, which results $\nu_c^\infty \sim 3$ GHz. This points to capture cross-sections of about 10^5 Å^2. The common fit to the diamagnetic fraction and phase, as well as to the paramagnetic relaxation, is shown in figs. 4.17, 4.18 and 4.19, respectively. In fig. 4.21 we represent together the diamagnetic fraction and phase, in order to more clearly display their inter-relation.

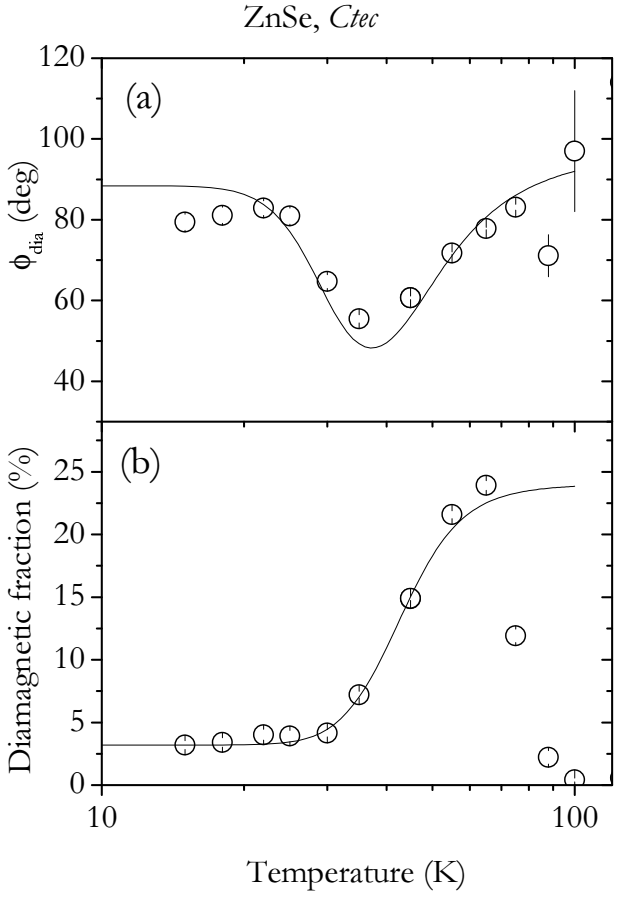

Figure 4.21: Diamagnetic phase and asymmetry, fitted with a function assuming an activated electron capture, as discussed in the text.

4.4 Final-state analysis experiments

The low-field experiments presented above prompted us to investigate more thoroughly the diamagnetic fraction in ZnSe. From eq. 4.6, it is clear that the amplitude of the diamagnetic final fraction is expected to vary with $1/\sqrt{1+(\Delta\omega\,\tau)^2}$, from which we may expect a rough variation with the inverse of the applied magnetic field. This effect, which corresponds to the dephasing of the converted state, explains why the diamagnetic fraction is seen only in low applied fields.

The final state can be best investigated by means of the muon spin resonance technique presented in Chapter 2, which, being in its essence a longitudinal field technique, is free from the dephasing problems.

We have thus undertaken final state analysis of the diamagnetic fraction in the *Ctec* and the *AA* samples, by means of RF-μSR measurements. These measurements were performed at ISIS, with the RF setup. The flypast setup was used in order to reduce background. Polyethene calibration measurements were done in order to obtain the maximum experimental asymmetry, thus allowing to obtain the fraction of muons thermalizing in the diamagnetic state in the sample under investigation. The corresponding temperature dependences of the measured diamagentic fractions are represented in figs. 4.22 and 4.23, respectively.

These measurements were further complemented in the same sample with muon spin resonance measurements of the paramagnetic Mu_{II} fractions state, performed by Prof. Roger Lichti and Dr. Kim Chow with the microwave setup at TRIUMF. In these microwave measurements, no calibration of the maximum asymmetry was done, which prevents to determine the observed muonium fractions. However, at the lowest temperature, the fraction of the Mu_{II} state observed in the muon spin resonance measurements should not be inferior to the fraction observed in high-transverse field (unlike the situation at temperatures above the conversion to diamagnetic, where the relaxation of Mu_{II} may disguise the total integral asymmetry). We have thus taken the asymmetry of the lowest temperature point in the microwave measurements to correspond to the Mu_{II} fraction observed at the lowest temperature in TF 7T. This has been used as our "calibration" and we have thus estimated the corresponding Mu_{II} fractions. It should be stressed that

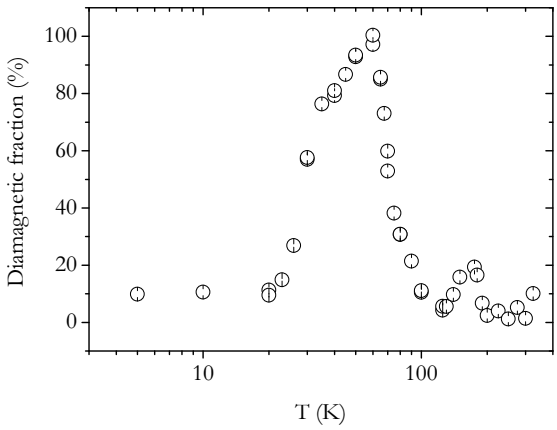

Figure 4.22: Temperature dependence of the diamagnetic fraction in the *Ctec* sample, as measured by muon spin resonance methods at ISIS.

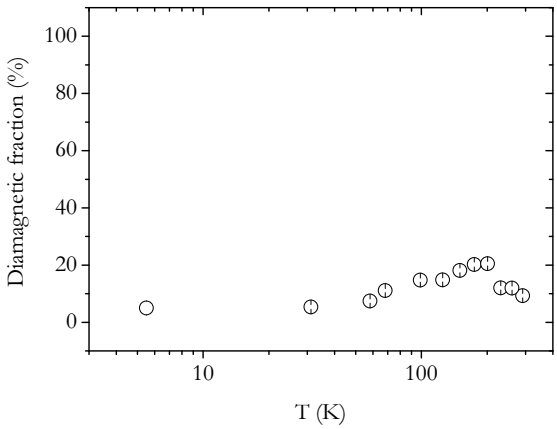

Figure 4.23: Temperature dependence of the diamagnetic fraction in the *AA* sample, as measured by muon spin resonance methods at ISIS.

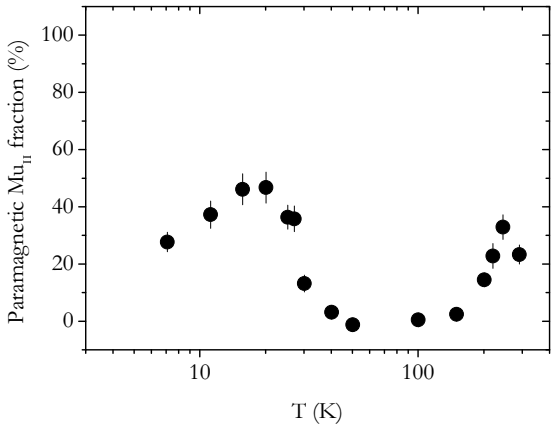

Figure 4.24: Temperature dependence of the paramagnetic Mu_{II} fraction in the *Ctec* sample, as measured by muon spin resonance methods at TRIUMF.

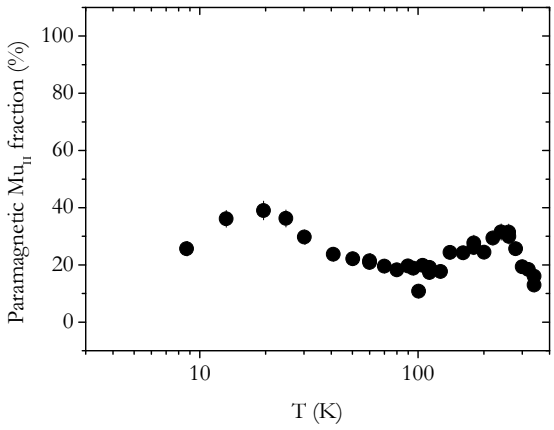

Figure 4.25: Temperature dependence of the paramagnetic Mu_{II} fraction in the *AA* sample, as measured by the muon spin resonance method at TRIUMF.

these correspond to a lower limit, admitting the entire Mu_{II} asymmetry is observed in the resonance measurements at the lowest temperature (8 K). The estimated paramagnetic Mu_{II} fractions, are represented in figs. 4.24 and 4.25 for the *Ctec* and the *AA* sample, respectively.

4.4.1 Discussion

We start the discussion of these results by the most informative data of the *Ctec* sample, and afterwards reason about the data of the *AA* sample.

For the *Ctec* sample, the diamagnetic RF experiments proved most successfull and full diamagnetic fraction is observed at 60 K, soon followed by a rapid decay up to 100 K. This increase of the diamagnetic fraction appears in relation to the observed decrease of the paramagnetic Mu_{II} fraction, which is observed in the microwave experiments. Also, it correlates with the relaxation of the Mu_{II} fraction, observed in the spectroscopic studies (cf. figs. 4.10 and 4.18).

All this is readily understood if we admit that the growth of the diamagnetic fraction is due to the delayed capture of a second electron, available *via* ionization of the donors in the material, as discussed for the low-transverse field data.

Regarding the low temperature diamagnetic fraction (9.9%), which is not observed in the spectroscopic 7 T data, it may be argued that it too corresponds to slowly-formed Mu^-, unobserved at high-fields due to dephasing. If it corresponded to muons thermalizing directly as Mu^+, there seems not to be any reason for it being invisible at 7 T.

In the *AA* sample, with its lower concentration of conduction electrons, this delayed capture of a second electron by Mu_{II} is almost suppressed, and instead the effect of the ionization of donors and subsequent increase of conduction electrons is a depolarization of the muon spin, eventually by spin-exchange dynamics before thermalization. This causes a decrease of the observed Mu_{II} fraction both by purely spectroscopic means (as was already pointed out in the discussion of the missing fraction of the 7 T data) and by muon-spin-resonance methods.

These muon spin resonance experiments allow us to clearly establish a third process in the *Ctec* sample, corresponding to the disappearance of the diamag-

netic fraction in the 60-100 K region which, as we shall see below, may be related to the increase of the paramagnetic Mu_{II} fraction, observed at somewhat higher temperatures in the microwave experiments.

The disappearance of the diamagnetic fraction above 60 K, together with the late reappearance of the paramagnetic fraction can be thought of as either:

(a) hole capture: $Mu^- + h^+ \rightarrow Mu^0$

(b) (second) electron ionization: $Mu^- \rightarrow Mu^0 + e^-$

Regarding (a), this process is again dependent on the hole concentration, presumably negligible at these temperatures. Also, it is reasonable that the second electron may be somewhat loosely bound, meaning a not very intense potential well at the muon site. We therefore prefer the second electron ionization as the best candidate model to explain the decrease of the diamagnetic fraction observed in the RF experiments at the *Ctec* sample, although we have no clear experimental evidence in favour of process (b), or against process (a).

Capture and Release model for T≥60K

We now present a very simple model that tries to describe the essential features in figs. 4.22 and 4.24, while trying to extract some essential quantitative information, particularly the most relevant ionization energy. We start with a capture and ionization model trying to grasp the details in the T≥60 K region.

We therefore assume that, above T≥60 K, both capture and release of a second electron occur:

$$Mu^0_{II} + e^- \underset{\nu_c}{\longrightarrow} Mu^-_{II} \tag{4.14}$$

$$Mu^-_{II} \underset{\nu_i}{\longrightarrow} Mu^0_{II} + e^- \tag{4.15}$$

where the capture rate ν_c and the ionization rate ν_i are assumed to be given by:

$$\nu_c = n_e v_e \sigma_c \tag{4.16}$$

$$\nu_i = \nu_i^0 \exp\left(-\frac{E_i}{kT}\right) \tag{4.17}$$

As done previously, when the expression 4.16 was first presented (eq. 4.7), we have used its simpler form 4.13:

$$\nu_c = \sigma_c \, v_e \, n_\infty \exp\left(-\frac{E_d}{2kT}\right) = \nu_c^\infty \exp\left(-\frac{E_d}{2kT}\right) \tag{4.18}$$

where σ_c is the cross-section for electron capture and the mean thermal velocity of conduction electrons is given by

$$v_e = \sqrt{\frac{3kT}{m_e^*}} = 16\,857.69 \left[\frac{m\,s^{-1}}{\sqrt{K}}\right] \sqrt{T} \tag{4.19}$$

the electron effective mass in the bottom of the conduction band of ZnSe being $m_e^* = 0.16\, m_0$.

Regarding the ionization rate 4.17, we assume it to be essentially a thermally activated process, governed by the activation energy E_i. In our interpretation, this corresponds to the energy required to promote an electron from the doubly occupied $\mathrm{Mu_{II}}$ $1s$ orbital to the bottom of the conduction band. This parameter is thus identified, in this interpretation, with the depth of the $(-/0)_T$ conversion level below the conduction band.

From equations 4.14 and 4.15, the paramagnetic and diamagnetic fractions f_p and f_d may be derived, taking into account that a fraction converting at rate ν decreases exponentially with $\exp(-\nu t)$. The following set of coupled equations can therefore be written:

$$f_p(t) = f_p^0 \, e^{-\nu_c \, t} + \nu_i \int_0^\infty f_d(\tau) \, e^{-\nu_c \, (t-\tau)} \, d\tau \tag{4.20}$$

$$f_d(t) = f_d^0 \, e^{-\nu_i t} + \nu_c \int_0^\infty f_p(\tau) \, e^{-\nu_i (t-\tau)} \, d\tau \tag{4.21}$$

where f_p^0 and f_d^0 are the initial paramagnetic and diamagnetic fractions, respectively.

In a muon spin resonance experiment, the time-averaged fractions are bound to be observed. The time average $\overline{f}$ of a fraction $f(t)$ is:

$$\overline{f} = \nu_\mu \int_0^\infty f(t)\, e^{-\nu_\mu t} dt \tag{4.22}$$

However, the observation of the fractions in a muon spin resonance experiment may be obscured in the presence of dynamical phenomena leading to further depolarization of the states under research, such as those discussed in chapter 2.

Unlike the capture stage, evidence for the existence of such aditional dynamical phenomena is abundant for the ionization stage:

(i) the reincrease of the paramagnetic fraction in the *Ctec* sample occurs higher in temperature than the concomitant decrease in the diamagnetic fraction;

(ii) in the *AA* sample, the corresponding variations occur primarily in the paramagnetic fraction; as pointed out before already, this is taken as a sign of spin dynamics taking place in the presence of a concentration of conduction electrons small enough to almost completely suppress electron capture;

We have included these dynamical phenomena assuming it leads to further depolarization of the states. This has been included as an *ad hoc* depolarization rate ν_1 in eq. 4.22:

$$\overline{f} = \nu_\mu \int_0^\infty f(t)\, e^{-(\nu_\mu + \nu_1) t} dt \tag{4.23}$$

Furthermore, we have taken ν_1 with a Chow's dependence (cf. eq. 2.65):

$$\nu_1 = \frac{\nu_c\, \nu_i\, \omega_0^2}{2(\nu_c + \nu_i)(\nu_c^2 + \omega_0^2 + (2\pi(\gamma_e + \gamma_\mu)B))^2} \tag{4.24}$$

where $(\gamma_e + \gamma_\mu) = 28127.873\, MHz\, T^{-1}$, $\omega_0 = 2\pi \times 3454.26\, Mrad\, s^{-1}$ and $B = 0.1955$ T for the diamagnetic data and $B = 0.8746$ T for the paramagnetic data.

The resulting average fractions become:

$$\overline{f_p} = f_p^0\, \frac{\nu_\mu}{\nu_c + \nu_\mu + \nu_1} + \overline{f_d}\, \frac{\nu_i}{\nu_c + \nu_1 + \nu_\mu} \tag{4.25}$$

$$\overline{f_d} = f_d^0 \frac{\nu_\mu}{\nu_i + \nu_\mu + \nu_1} + \overline{f_p} \frac{\nu_c}{\nu_i + \nu_\mu + \nu_1} \tag{4.26}$$

and, after solving this linear system of two equations and two unknowns, we get:

$$\overline{f_p} = \frac{\nu_\mu}{\nu_\mu + \nu_1} \frac{f_p^0 (\nu_i + \nu_\mu + \nu_1) + f_d^0 \nu_i}{\nu_\mu + \nu_i + \nu_1 + \nu_c} \tag{4.27}$$

$$\overline{f_d} = \frac{\nu_\mu}{\nu_\mu + \nu_1} \frac{f_d^0 (\nu_c + \nu_\mu + \nu_1) + f_p^0 \nu_c}{\nu_\mu + \nu_i + \nu_1 + \nu_c} \tag{4.28}$$

Capture model including $\mathrm{Mu_I}$

The above model may be further improved by including the third known process involving the muonium states in ZnSe, which is the conversion between the paramagnetic states $\mathrm{Mu_I}$ and $\mathrm{Mu_{II}}$:

$$Mu_I^0 \xrightarrow[\nu_{I/II}]{} Mu_{II}^0 \tag{4.29}$$

where the conversion rate $\nu_{I/II}$ is again taken as

$$\nu_{I/II} = \nu_{I/II}^0 \exp\left(-\frac{E_{I/II}}{kT}\right) \tag{4.30}$$

The time-dependent fractions of the paramagnetic and diamagnetic states now become:

$$f_I(t) = f_I^0 \, e^{-\nu_{I/II} t} \tag{4.31}$$

$$f_{II}(t) = f_{II}^0 \, e^{-\nu_c t} + \nu_{I/II} \int_0^\infty f_I(\tau) \, e^{-\nu_c (t-\tau)} \, d\tau + \nu_i \int_0^\infty f_d(\tau) \, e^{-\nu_c (t-\tau)} \, d\tau \tag{4.32}$$

$$f_d(t) = f_d^0 + \nu_c \int_0^\infty f_{II}(\tau) \, d\tau \tag{4.33}$$

We note that the conversion from Mu_I to Mu_{II} is already finished by 40 K, well before the ionization of Mu_{II}^- sets in, so that these two extreme processes may be thought not to coexist. During the conversion of Mu_I to Mu_{II}, we may thus set $\nu_i = 0$. Consequently the relaxation arising from the ionization/capture process is negligible, and $\nu_1 = 0$ as well. The average fraction is given by the simpler eq. 4.22.

The average fractions, with the assumptions above, become:

$$\overline{f_I} = f_I^0 \frac{\nu_\mu}{\nu_{I/II} + \nu_\mu} \tag{4.34}$$

$$\overline{f_{II}} = f_{II}^0 \frac{\nu_\mu}{\nu_c + \nu_\mu} + \overline{f_I} \frac{\nu_{I/II}}{\nu_c + \nu_\mu} \tag{4.35}$$

$$\overline{f_d} = f_d^0 + \overline{f_{II}} \frac{\nu_c}{\nu_\mu} \tag{4.36}$$

and, after the solution of the above system of three coupled equations is:

$$\overline{f_I} = f_I^0 \frac{\nu_\mu}{\nu_{I/II} + \nu_\mu} \tag{4.37}$$

$$\overline{f_{II}} = f_{II}^0 \frac{\nu_\mu}{\nu_\mu + \nu_c} + f_I^0 \frac{\nu_\mu \nu_{I/II}}{(\nu_{I/II} + \nu_\mu)(\nu_\mu + \nu_c)} \tag{4.38}$$

$$\overline{f_d} = f_{II}^0 \frac{\nu_c}{\nu_c + \nu_\mu} + f_I^0 \frac{\nu_c \nu_{I/II}}{(\nu_{I/II} + \nu_\mu)(\nu_\mu + \nu_c)} + f_d^0 \tag{4.39}$$

Analysis with the model

We have used the above models for the analysis of muon spin resonance data of the *Ctec* sample. We started by the low-temperature (up to 60 K) data shown in figs. 4.22 and 4.24, which were analysed with eqs. 4.39 and 4.38, respectively. Despite the success of the fit to the diamagnetic data, the model does not describe accurately the paramagnetic data, as can be seen in fig. 4.26, where total paramagnetic

fraction observed in the high-transverse (7 T) field is also shown for comparison. In the fit, we allowed the Mu_I to Mu_{II} conversion parameters to vary with respect to the previous parameters obtained from the high-transverse field data and obtained $E_{I/II} = 13(1)$ meV and $\rho_{I/II} = 0.09(5) \times 10^3$ MHz. Regarding the capture parameters, the fit to the diamagnetic fraction improves very much if we allow the capture energy to vary. We obtain $\nu_c^\infty = 2.6(3)$ GHz and $E_c = 20.8(4)$ meV, slightly below the expected value for the donor energies in ZnSe, which are measured between 26 and 30 meV [Mad82].

We have fitted the high-temperature part separately with eqs. 4.28 and 4.27. We obtained, for the ionization parameters, $\nu_i^0 = 5(2) \times 10^{13}$ MHz and $E_i = 178(2)$ meV. Though the fit to the diamagnetic fraction works well by fixing the capture parameters from the low-temperature part, yielding similar values, the fit to the paramagnetic fraction works better by allowing the capture parameters to be let free, converging to new values ($\nu_c^\infty = 5.4(9) \times 10^9$ MHz, $E_c = 69(1)$ meV). We take this as a sign of the frailty of the model, more than of any substantial evidence for an actual change of the capture process. The result of the corresponding fit is shown in fig. 4.27.

A visual summary of the overall analysis is shown in fig. 4.28.

AA sample

It is clear from the discussion above that the model we used for analysing the muon spin resonance data of the *Ctec* sample is not expected to describe adequately the corresponding *AA* data. Here, the capture of the second electron is strongly suppressed due to the lower concentration of conduction electrons, and this seems to be substituted by temperature-dependent spin-dynamics. We have nevertheless used eq. 4.39 to fit the muon spin resonance data for the diamagnetic fraction, by fixing the parameters obtained for the *Ctec* sample, except the concentration dependent parameter ν_c^∞. We obtained $\nu_c^\infty = 0.45(2)$ MHz (to be compared with $\nu_c^\infty = 2.6(3)$ GHz for the *Ctec* sample), which is a very sensible lower value. The resulting fit is shown in fig. 4.29.

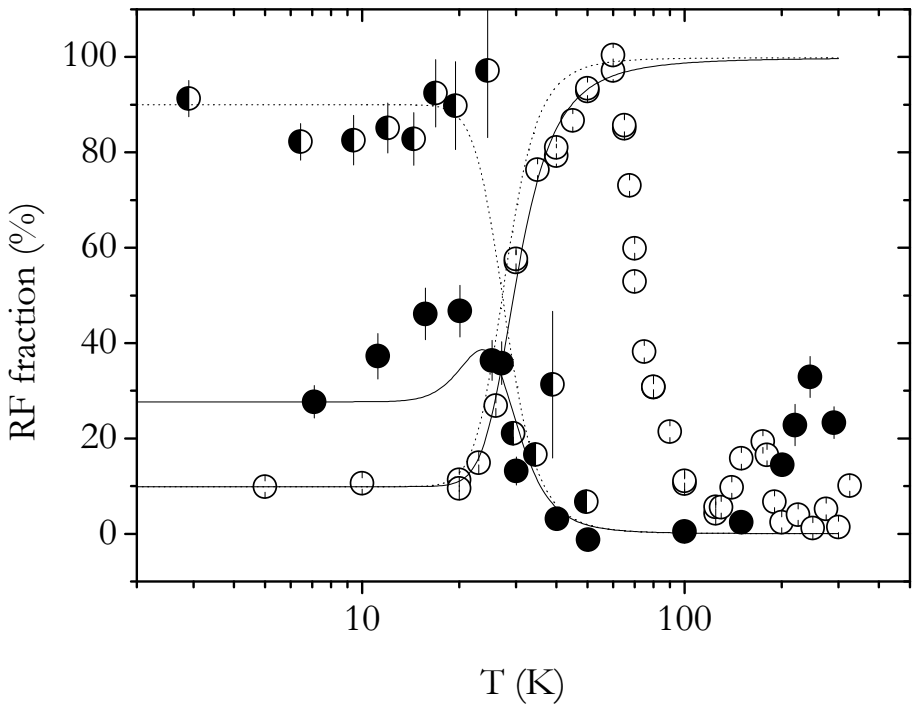

Figure 4.26: Diamagnetic (white circles) fraction and paramagnetic Mu_{II} (black circles) for the *Ctec* sample, as obtained by muon-spin-resonance methods. The half-black circles represent the total paramagnetic fraction observed in the spectroscopic 7 T experiments. Solid lines are fits with eqs. 4.39 and 4.38, respectively, using common parameters for the muonium interconversion and second electron capture. Dashed lines are simulations with the same capture parameters, but assuming the entire paramagnetic fraction is due to Mu_{II}, which allows to evidence the contribution of each process.

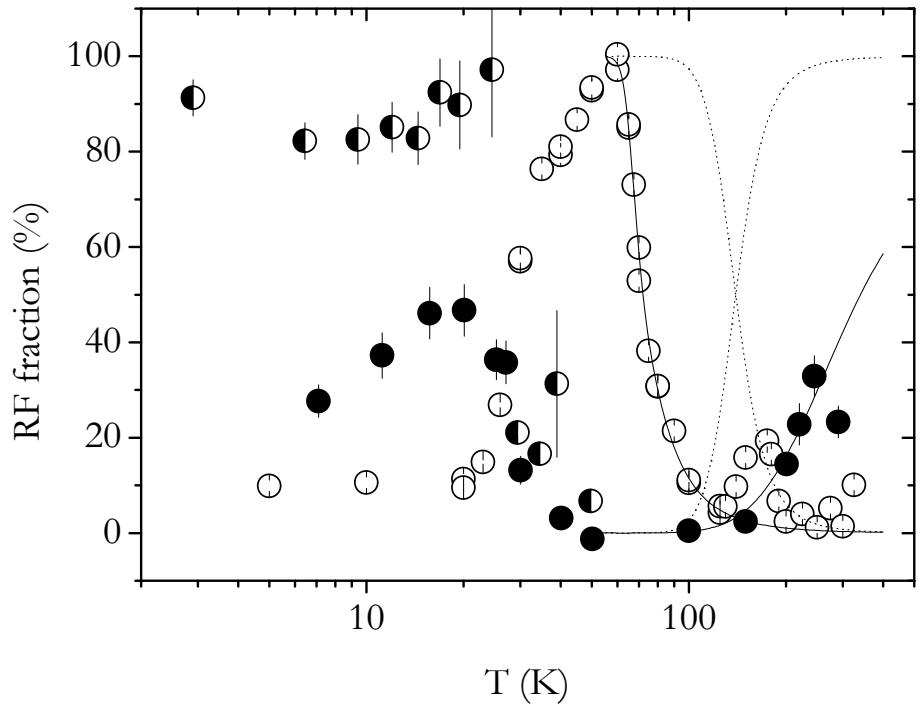

Figure 4.27: Diamagnetic (white circles) fraction and paramagnetic Mu_{II} (black circles) for the *Ctec* sample, as obtained by muon-spin-resonance methods. The half-black circles represent the total paramagnetic fraction observed in the spectroscopic 7 T experiments. Solid lines are fits with eqs. 4.28 and 4.27, respectively, using common parameters for the muonium ionization and second electron capture. Dashed lines are simulations with the same capture and ionization parameters, but seting the *ad hoc* relaxation ν_1 (eq. 4.24) to zero.

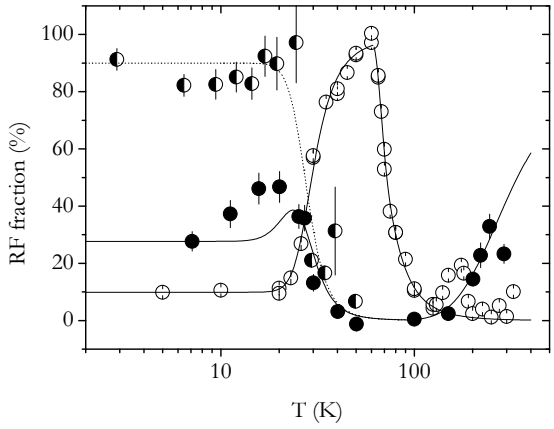

Figure 4.28: Diamagnetic (white circles) fraction and paramagnetic Mu_{II} (black circles) for the *Ctec* sample, as obtained by muon-spin-resonance methods. The half-black circles represent the total paramagnetic fraction observed in the spectroscopic 7 T experiments. Solid and dashed lines are the superposition of the corresponding fits and simulations presented in figs. 4.26 and 4.27.

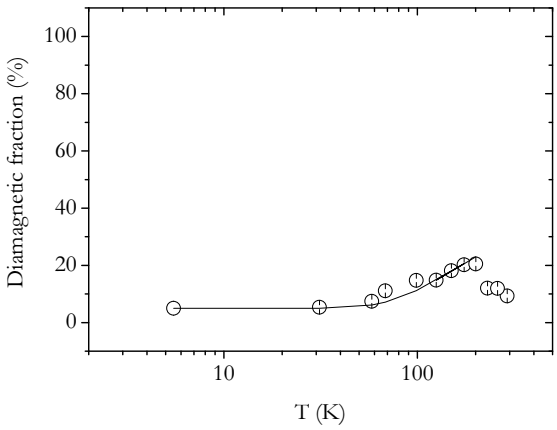

Figure 4.29: Diamagnetic fraction for the AA sample, as obtained by muon-spin-resonance methods. The line is a fit with eq. 4.39, as explained in the text.

4.5 Further experimental information

We now present additional experimental information gathered in the course of this work and which, despite its somewhat fragmentary nature, allows further significant insight either into the processes already discussed in the previous sections, or into new processes.

4.5.1 Probing Mu dynamics with LF

From the discussion of the muon spin resonance data, it is clear that our model, despite describing already the essential features of the muon spin resonance data for the *Ctec* sample, requires further refining in order to allow a confident and accurate determination of the relevant energy levels, which correspond o a major objective in this investigation, as discussed in chapter 1. A problem which was already partially adressed is that of the muonium spin dynamics in the course of the relevant electronic processes. As mentioned in chapter 2, a way of probing this spin dynamics is by verifying the field dependence of the average polarization and of the muon spin relaxation in longitudinal field geometry.

We have only begun to adress this question experimentally, by investigating the *Ctec* sample longitudinal fields at ISIS (EMU), in the temperature interval between 60 K and 100 K (corresponding to the range where the process we identify with ionization occurs). As usual in these measurements, a silver calibration was done in the entire field range (up to 4500 G), in order to obtain the (field-dependent) maximum asymmetry A_{max}.

A typical time spectrum is shown in fig. 4.30, where a relaxation is observed in the initial instants of the asymmetry. The time-averaged polarization $\tau_\mu^{-1} \int_0^{t_{max}} A(t) \exp(-t/\tau_\mu) dt / A_{max}$, as a function of applied longitudinal field, is shown for four temperatures in fig. 4.31. In fig. 4.32, we depict the corresponding relaxations, obtained by fitting a two-component function $A_1 + A_2 \exp(-\lambda t)$.

As expected, we observe in fig. 4.31 the typical field-dependent polarization behaviour in the presence of dynamical phenomena (as discussed in the context of eq. 2.59). However, the average polarization is seen to decrease pronouncedly with

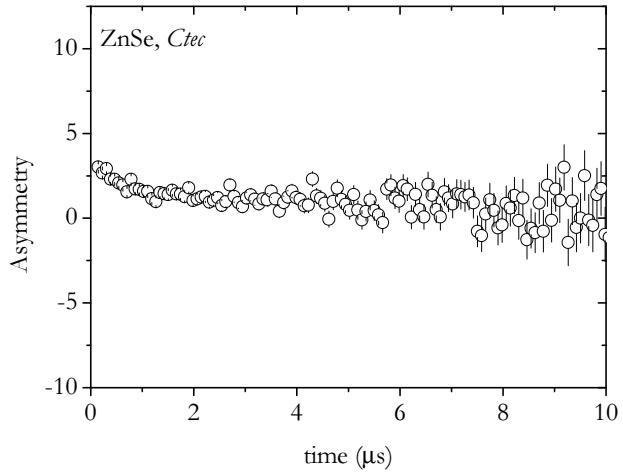

Figure 4.30: Muon spin relaxation time spectrum, obtained for the *Ctec* sample, at T=80 K, under an applied longitudinal field LF=10 G

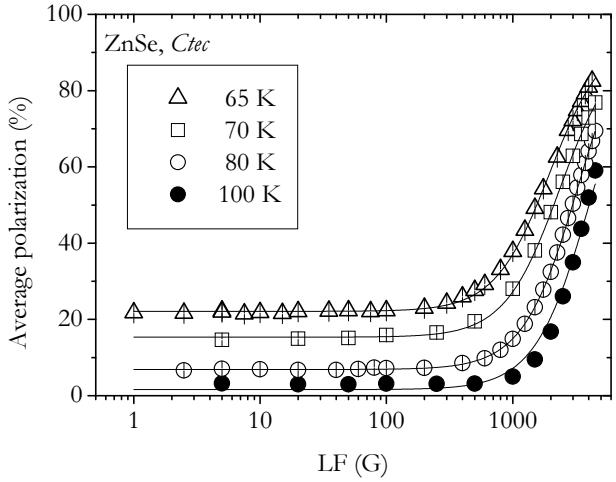

Figure 4.31: Longitudinal-field-quenching (repolarization) curves, obtained for the *Ctec* sample, for four distinct temperatures. Solid lines are fits with eq. 2.59.

increasing temperature, relating to the increasing relaxation. The repolarization curves are adequately fit with eq. 2.59: values for the charge-exchange rate ν about 10^7 MHz and for the duration of the charge-exchange cycle τ in the microsecond range are obtained, with a large error.

Fits to the relaxation data in fig. 4.32, with the refined Chow's model for the $1/T_1$ relaxation (eq. 2.65), allow to further extract the paramagnetic to diamagnetic conversion rate λ_{0d} and its converse λ_{d0}. In the interpretation used for the muon spin resonance data in the previous section, λ_{0d} corresponds to the capture rate ν_c and λ_{d0} corresponds to the ionization rate ν_i. The results of these fits are shown in fig. 4.33, together with the corresponding values predicted by the parameters obtained by fitting eq. 4.13 to the RF data. The obtained correlation is quite sucessfull. These data therefore suggest that a thorough longitudinal field study may allow to improve the estimation of the conversion levels, by using direct information about the temperature dependent conversion rates.

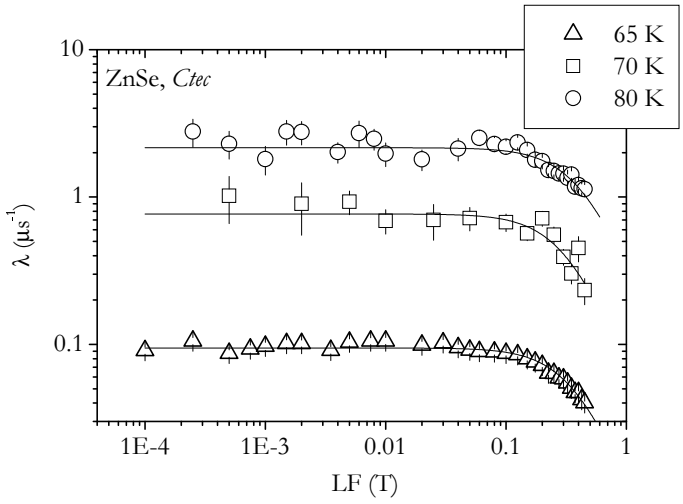

Figure 4.32: Relaxation rates corresponding to the repolarization curves in fig. 4.31. For 100 K, the relaxations are much close to the high limit of the experimentally accessible range and are not included in the plot. Solid lines are fits with eq. 2.65.

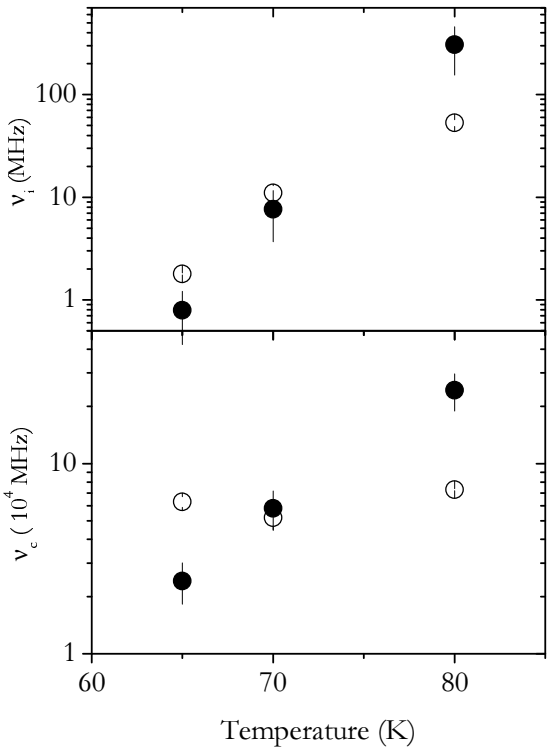

Figure 4.33: Ionization rate ν_i and capture rate ν_c, obtained from longitudinal-field (LF) measurements and from RF-μSR measurements. Black circles represent the values resulting from eqs. 4.13 and 4.17, with the parameters extracted with the analysis to the muon-spin resonance (RF) data. White circles represent the values extracted from the muon spin relaxation (LF) measurements (fig. 4.32), by fitting with the Chow's formula (eq. 2.65).

4.5.2 Development of doping-dependent studies

We extended the previous spectroscopical studies to the more strongly doped samples presented in Chapter 3: the chemical-vapour-grown (CVT) samples, deliberately or undeliberately doped with iodine (*CVT:I* and *CVTu*, respectively), as well as a *Ctec* sample annealed in Zn vapour, in order to reduce compensation by vacancies (*Ctec:Zn*). These studies, which still have a preliminary character, have been done at low transverse fields (10 G), at PSI.

We depict the temperature dependence of the diamagnetic fraction observed in all samples in fig. 4.34. For clarity, the *AA* sample is excluded, the corresponding diamagnetic fraction being residual (see fig. 4.15).

We note that, for the *Ctec:Zn* sample, the peak in the diamagnetic fraction attributed to delayed capture of a second electron is slightly higher both in height (26% vs. previous 23%) and in temperature (75 K vs. 65 K). We take this fraction increase as a sign of the expected larger capture rate. As mentioned in chapter 3, this sample was annealed in zinc, which reduces the concentration of zinc vacancies and the compensation associated with these defects. The concentration of free electrons is thus expected to increase, favouring the capture of a second electron by muonium and therefore increasing the diamagnetic fraction.

However, the most remarkable effect is observed for the low-temperature diamagnetic fraction observed in the CVT-grown samples, which is already much larger from the lowest temperatures, without even peaking. This is expected, in our interpretation, for these higher concentrations of conduction electrons, which correspondingly increase the capture rate.

Such high concentrations of free carriers and of impurities/defects, eventually leading even to impurity-band conduction, trigger or enhance processes whose presence is just unveiled by the current experiments. Particularly, it should be noted that no paramagnetic fraction is observed for the CVT-grown samples, in these TF 10 G experiments. A paramagnetic fraction (amounting to 30% at 45 K) is observed in the *Ctec:Zn* sample (not in the CVT-grown samples), representing already a significant difference with respect to what was observed before the annealing (cf. fig. 4.17). Even more strikingly, the diamagnetic fraction of the *CVT:I*

sample is observed to grow above 100 K to nearly 100%, and a similar trend is observed in the *CVTu* sample. These two samples also present an increasing relaxation of the diamagnetic fraction above 250 K (fig. 4.35). The presence of a second relaxing diamagnetic component in the *CVT:I* sample seems to occur (amounting to 4% at room temperature, with a relaxation rate around 7 μs^{-1}). No relaxation is observed in the *Ctec:Zn* sample.

It is possible that the above mentioned features above 200 K correspond to the high-free-carrier-concentration limit of the corresponding dynamical features observed for the more intrinsic samples, as discussed in the previous sections. Or they may be the sign of entirely new processes setting in only at high concentrations of conduction electrons. Processes such as muon and muonium diffusion, trapping at impurities/defects can not neither easily be ruled out or confirmed, attending to the low-density of nuclear moments in ZnSe, as discussed in section 2.5.

An adequate modelling for these phenomena is still lacking, and its interrelation is poorly understood. These data therefore constitute more a departure than an arrival point.

Most significantly, we take the mentioned correlation of the observed diamagnetic fraction at the lowest temperatures with the concentration of free carriers as a very positive qualitative confirmation of the delayed second capture model.

Aditionally, we should mention that we also undertook very brief measurements at an hydrogenated piece of a *Ctec* sample from the same batch. This piece was annealed in H_2 atmosphere (16 atm, 500^o C, for 22 h, Cf. [Hei59, Mol54]), and no mass difference was found before and after the treatment, thus giving a maximum introduced concentration of $[H] < 5 \times 10^{19}$ cm^{-3}). Hydrogen being amphoteric in ZnSe, it is expected to decrease the concentration of conduction electrons, and thus also decreasing the delayed formation of Mu^-. In the three experimental points obtained (5 K, 55 K and 300 K, at low-transverse field - 10 G - in the GPS instrument, PSI), the diamagnetic fraction was observed to drop below 6%, which we again take as further confirmation of our interpretation.

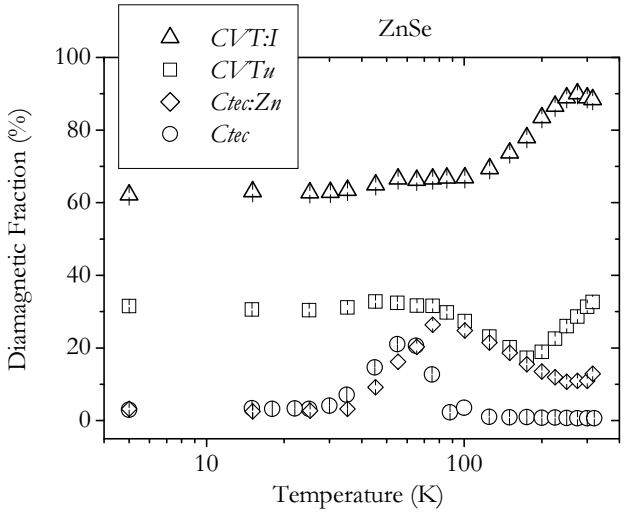

Figure 4.34: Temperature dependence of the diamagnetic fraction observed by muon spin rotation measurements (TF=10 G) for the *Ctec*, *Ctec:Zn*, *CVTu* and *CVT:I* samples (see chapter 3 for sample reference).

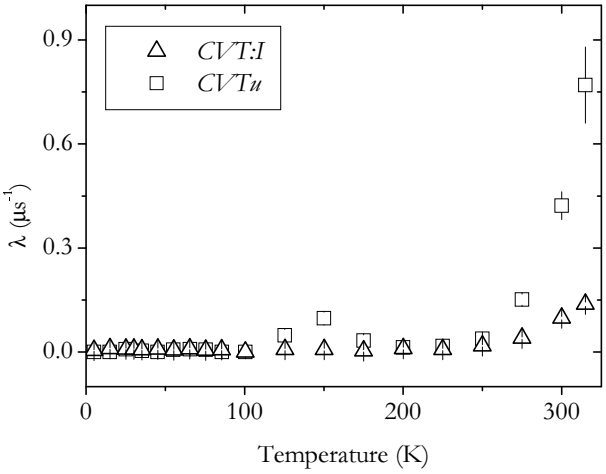

Figure 4.35: Temperature dependence of the diamagnetic relaxation observed by muon spin rotation measurements (TF=10 G) for the *CVTu* and *CVT:I* samples. No significant relaxation is observed for the *Ctec* and *Ctec:Zn* samples (see chapter 3 for sample reference).

4.5.3 High temperature investigations

As we have seen, the paramagnetic fraction is observed by muon-spin resonance methods in the *Ctec* and *AA* samples and is observed spectroscopically in the *AA* sample up to room temperature. The question of its thermal stability is a most relevant one with respect to the determination of the hydrogen levels in the band gap of this material.

However, as is abundantly expressed in the previous section, this determination is hindered by the coexistence of a profusion of phenomena affecting the muon spin. We have nevertheless started investigations above room temperature in the *Ctec* and *AA* samples, in the two possible experimental directions:

(i) probing spectroscopically the thermal stability of the paramagnetic fraction which is observed at room temperature in the *AA* sample; this requires the investigation at low transverse fields at PSI, where it is possible to extend spectroscopic studies up to 700 K;

(ii) final state analysis, by the muon spin resonance technique, of the diamagnetic fraction observed in the *Ctec* and *AA* samples; this is possible at ISIS, where a high-temperature RF setup has been recently developped.

Low transverse field spectroscopy

We have therefore extended the previous low-transverse field (5 G) investigations of the paramagnetic fraction of the *AA* sample up to 700 K. This is observed to disappear completely at 600 K, a concomitant reappearance of the diamagnetic fraction being observed as well (fig. 4.36). These data suggest that the Mu_{II} state might not be at all stable above 600 K.

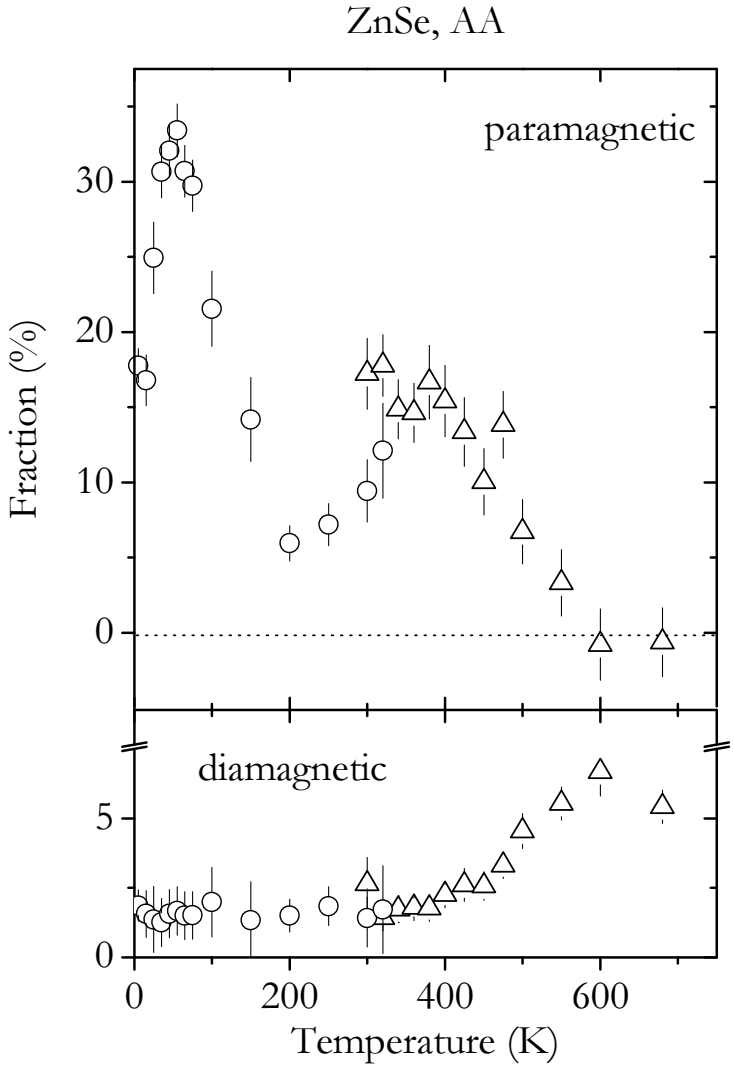

Figure 4.36: Temperature dependence of the paramagnetic and diamagnetic fractions observed by muon spin rotation measurements (TF=5 G), at PSI. White circles denote cryostat measurements and white triangles denote furnace measurements.

Final state analysis

The temperature dependence of the diamagnetic fraction was further detailed by the muon spin resonance technique, using the high-temperature RF setup at ISIS. Both RF measurements and usual TF20G measurements were done. We present the corresponding results for the *Ctec* sample and the *AA* sample in figs. 4.37 and 4.38, respectively.

The most simple process able to explain these data, at the light of the previous interpretation, is of course muonium ionization by promotion of the muonium electron to the conduction band:

$$Mu^0 \rightarrow Mu^+ + e^- \tag{4.40}$$

These data, together with the current state of the interpretation, are not enough to clearly establish process 4.40. Another simple process that might explain the increase of the diamagnetic fraction at these temperatures is hole ionization:

$$Mu^0 \rightarrow Mu^- + h^+ \tag{4.41}$$

However, this seems less reasonable, as it implies formation again at high temperatures of the Mu^- state, which is most likely to become thermally unstable already at 60 K. Nevertheless, the possibility that muonium behaves as a recombination centre, as is the case if process 4.41 occurs, has been considered in order to explain high-temperature data for GaAs [Cho96] and, more recently, for InSb [Sto06].

Despite the case for muonium ionization (process 4.40) still needing further experimental work in order to be established in more firm grounds, we have nevertheless tried to analyse the RF data with an electron capture and release model similar to the one used for the low temperature data.

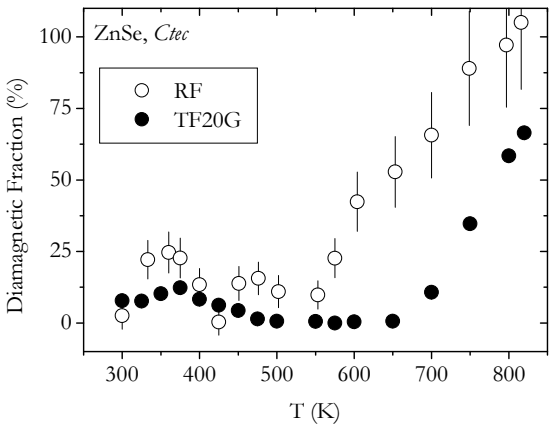

Figure 4.37: Diamagnetic fraction, observed for the *Ctec* sample above room temperature, at ISIS, by muon spin rotation measurements (black circles) and by muon spin resonance measurements (white circles).

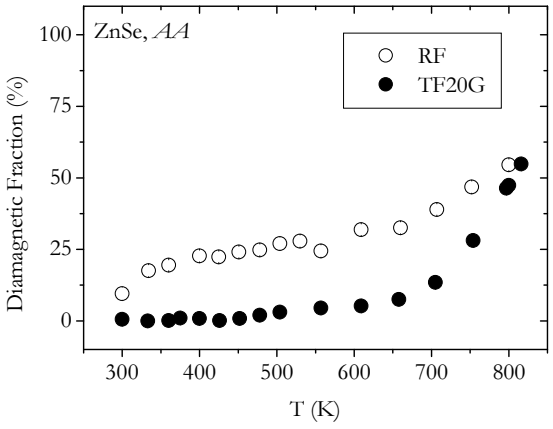

Figure 4.38: Diamagnetic fraction, observed for the *Ctec* sample above room temperature, at ISIS, by muon spin rotation measurements (black circles) and by muon spin resonance measurements (white circles).

We therefore assume that the increase of the diamagnetic fraction is essentially due to electron loss to the conduction band at a rate ν_i, with possible recapture at rate ν_c, *i.e.*:

$$Mu_{II}^{+} + e^{-} \underset{\nu_c}{\longrightarrow} Mu_{II}^{0} \tag{4.42}$$

$$Mu_{II}^{0} \underset{\nu_i}{\longrightarrow} Mu_{II}^{+} + e^{-} \tag{4.43}$$

where the corresponding rates are simply taken to have an Arrhenius-type temperature dependence:

$$\nu_i = \nu_i^0 exp\left(-\frac{E_i}{kT}\right) \tag{4.44}$$

$$\nu_c = \nu_c^0 exp\left(-\frac{E_c}{kT}\right) \tag{4.45}$$

Similarly to eqs. 4.28 and 4.27, the paramagnetic and diamagnetic fractions f_p and f_d can be expressed as:

$$f_p(t) = f_p^0\, e^{-\nu_i t} + \nu_c \int_0^\infty f_d(\tau)\, e^{-\nu_i(t-\tau)}\, d\tau \tag{4.46}$$

$$f_d(t) = f_d^0\, e^{-\nu_c t} + \nu_i \int_0^\infty f_p(\tau)\, e^{-\nu_c(t-\tau)}\, d\tau \tag{4.47}$$

The corresponding average fraction $\overline{f}$, relevant in muon spin resonance measurements, is once more given by:

$$\overline{f} = \nu_\mu \int_0^\infty f(t)\, e^{-(\nu_\mu+\nu_1)\, t} dt \tag{4.48}$$

where we have introduced again an *ad hoc* relaxation ν_1 given by eq. 4.24. We thus obtain:

$$\overline{f_p} = f_p^0\, \frac{\nu_\mu}{\nu_i + \nu_\mu + \nu_1} \; + \; \overline{f_d}\, \frac{\nu_c}{\nu_i + \nu_\mu + \nu_1} \tag{4.49}$$

$$\overline{f_d} = f_d^0 \frac{\nu_\mu}{\nu_c + \nu_\mu + \nu_1} + \overline{f_p} \frac{\nu_i}{\nu_c + \nu_\mu + \nu_1} \tag{4.50}$$

and the solution of the above system of equations is:

$$\overline{f_p} = \frac{\nu_\mu}{\nu_\mu + \nu_1} \frac{f_p^0 (\nu_c + \nu_\mu + \nu_1) + f_d^0 \nu_c}{\nu_\mu + \nu_c + \nu_i + \nu_1} \tag{4.51}$$

$$\overline{f_d} = \frac{\nu_\mu}{\nu_\mu + \nu_1} \frac{f_d^0 (\nu_i + \nu_\mu + \nu_1) + f_p^0 \nu_i}{\nu_\mu + \nu_c + \nu_i + \nu_1} \tag{4.52}$$

We have fitted both RF data-sets with this model, imposing the same value for the "ionization" energy E_i and fixing the capture energy to the value obtained in section 4.4.1 ($E_c = 69$ meV). We obtain values in the order of $n_i^0 = 1 \times 10^{30}$ MHz and $E_i = 1$ eV. For the capture prefactors, which were let free, we obtain $n_c^0 = 6 \times 10^{21}$ MHz for the *Ctec* sample and $n_c^0 = 1 \times 10^{10}$ MHz for the *AA* sample. The resulting fit is shown in fig. 4.39.

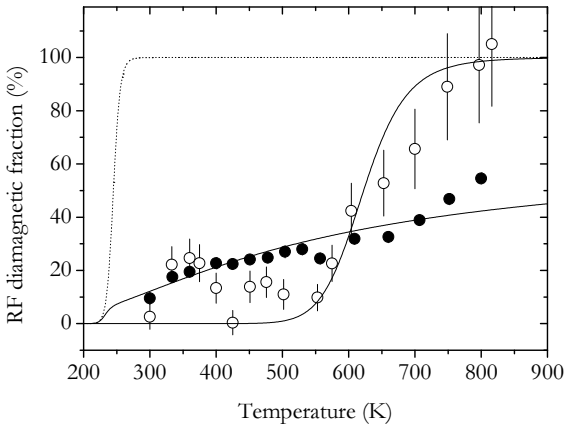

Figure 4.39: High-temperature diamagnetic fractions observed in the *Ctec* and *AA* samples by muon spin resonance. Solid lines are a fit as described in the text. The dashed line is a simulation of the diamagnetic fraction for the *AA* sample setting the *ad hoc* relaxation ν_1 to zero (no significant difference is found when doing the same for the *Ctec* fraction).

4.6 Conclusive remarks

We now summarize the essential results obtained for ZnSe in the course of this investigation. Some of these results have already been included in a number of publications, either dedicated specifically to ZnSe [Vil05b], either dedicated to the more general context of muonium/hydrogen in II-VI semiconductors [Cox03a, Lic06, Vil06, Vil07a, Wei03a, Wei03b]. Other aspects are presented here for the first time, the respective publication in peer-reviewed journals being currently (January/2007) in preparation [Vil07b].

At low temperatures, in high-precision transverse-field measurements, two muonium states Mu_I and Mu_{II} are observed with isotropic hyperfine parameters of A_I = 3282.63±0.51 MHz and A_{II} = 3454.26±0.02 MHz (74 % and 77 % of the vacuum value, respectively). State I is thermally unstable and converts to state II at approximately 40 K. State II is stable up to 600 K. We assign Mu_{II} to the cation interstitial tetrahedral site and discuss the possibility that Mu_I may correspond either to muonium at the same site but in the unrelaxed lattice or to the anion interstitial tetrahedral site. The temperature dependence of the hyperfine interaction of Mu_{II} was fitted with a local vibrational model giving an oscillator energy of approximately 8 meV.

Low-transverse field measurements, performed in a sample with a slightly higher concentration of free-electrons allowed to identify a conversion of the Mu_{II} state to a diamagnetic fraction, in the temperature range 20-60 K, which we assign to delayed capture of a second electron forming Mu_{II}^-. Mu_{II} is thus acting as a trapping center, although this designation should be taken with care, given the thermodynamical instability of this center.

This diamagnetic fraction was further investigated by muon-spin-resonance, and it was shown to become thermally unstable above 60 K, and a recovery of the paramagnetic Mu_{II} fraction was observed as well in related muon-spin-resonance measurements. We identify this process with ionization of the second electron of Mu_{II}^- to the conduction band. Analysis with a simple model yields an ionization energy of 178 meV, which in this interpretation corresponds to the distance of the acceptor level -/0 to the bottom of the conduction band. However, this process is

obscured by the existence of dynamical processes of the muon spin, which remain largely unexplored and poorly understood. Thus, alternative interpretations to ionization to the conduction band (such as hole capture) can not be entirely ruled out.

Muon spin relaxation methods, together with the extension to the investigation of doped samples, may allow deeper insight to these dynamical phenomena, thus providing more firm grounds to the level -/0 acceptor level assignment.

Muon spin spectroscopy and resonance measurements above room temperature unveil the thermal instability of the paramagnetic fraction above 400 K, together with a concomitant increase of the diamagnetic fraction. We tentatively assign this process to Mu_{II} ionization to the conduction band, in which case the +/0 level should lie c. 1 eV below the conduction band bottom. As the caveats expressed above clarify, this should be understood as a new resarch route to be pursued in the future.

Chapter 5

Experimental results and discussion II: ZnS and ZnTe

Nem sempre sou igual no que digo e escrevo.
Mudo, mas não mudo muito.
A cor das flores não é a mesma ao sol
De que quando uma nuvem passa
Ou quando entra a noite
E as flores são cor da sombra.
Mas quem olha bem vê que são as mesmas flores.[1]

Alberto Caeiro
O guardador de rebanhos, XXIX

We now present the experimental data obtained for the other two II-VI zinc chalcogenides ZnS and ZnTe. As discussed in Chapter 1, these two compounds also present the characteristic doping unipolarity, ZnS growing as n-type and ZnTe growing as p-type. At the light of what we learned already of the role of charge carriers in ZnSe, we thus expect to observe identical phenomena in ZnS to those of ZnSe, but not in ZnTe. This is effectively the case, as we shall now see.

[1]Free translation: *"I'm not always the same in what I say and write. I change, but I do not change much. The colour of the flowers is not the same under the sun than when a cloud is going by or when the night sets in and the flowers have the colour of the shadow. But he who looks attentively sees the same flowers."*

5.1 ZnS

For presenting the ZnS data, we follow the same scheme adopted for the ZnSe data in Chapter 4: we begin by the transverse field spectroscopy, both at high and low fields, and then move to the muon spin resonance information. Complementary experimental information (muon spin resonance, muon spin relaxation) is left to the end and followed by overall conclusive remarks.

5.1.1 High transverse field spectroscopy

High-transverse field (7 T) spectroscopic measurements have been performed on the [111] sample, at the HITIME instrument at TRIUMF. In this experiment, the magnetic field was applied parallel to the [111] crystallographic orientation. A typical time spectrum is shown in fig. 5.1 and the corresponding fast-Fourier frequency transform is depicted in fig. 5.2. These should be compared with the respective correspondent for ZnSe (figs. 4.1 and 4.2, respectively). In ZnS, a single frequency line (at 808 MHz) is seen at 2 K, corresponding to a deep isotropic muonium state with a hyperfine interaction $A = 3545(1)$ MHz. Similarly to the high-field data for ZnSe, no diamagnetic component is observed in these experiments.

The frequency signal was analysed, as before, using an exponentially-damped cosine function of the form $A\,\exp(-\lambda\,t)\,\cos(\omega\,t+\phi)$. We estimated the muonium fraction by using the same silver calibration used for the ZnSe measurements, since the sample geometrical parameters and the spectrometer are the same. We thus estimated the muonium fraction at 2 K to be 20%. A very large fraction of the muon spin polarization is therefore missing at low temperatures. The observed value of the paramagnetic fraction in ZnS is curiously similar to that of the $\mathrm{Mu_{II}}$ state in ZnSe, so that it is sensible reasoning to assume that the missing fraction may correspond to a depolarized $\mathrm{Mu_{I}}$ state in ZnS.

The temperature dependence of the (estimated) muonium fraction is shown in fig. 5.3, where it can be seen that it decreases sharply above 50 K. These high-field measurements were not pursued above 160 K.

The temperature dependence of the relaxation of the paramagnetic line is depicted, up to 80 K, in fig. 5.4, showing no appreciable change. At the higher

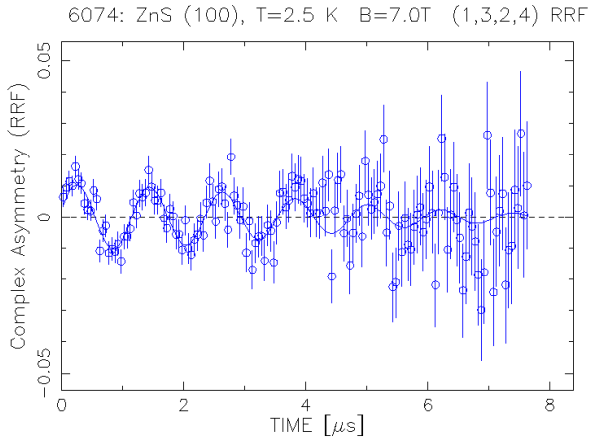

Figure 5.1: Time spectrum obtained for ZnS at T=3 K, B=7 T. In order to facilitate the visual inspection, the data are plotted in a rotating reference frame at 807 MHz. A single precession line at 808 MHz is seen.

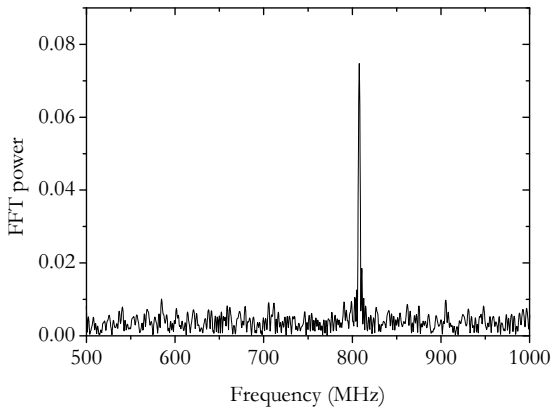

Figure 5.2: Fourier transform μSR spectrum of ZnS, at B=7 T and T=2 K. Only one line at 808 MHz, corresponding to a single isotropic Mu state, is observed.

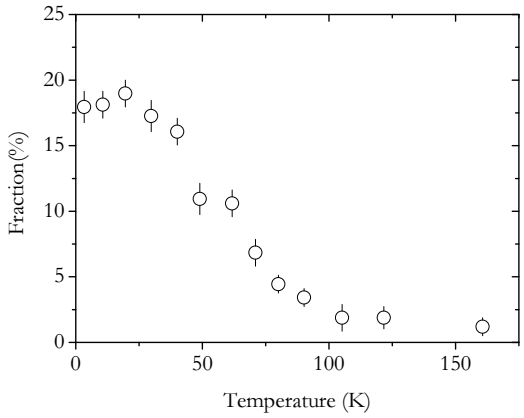

Figure 5.3: Temperature dependence of the (estimated) paramagnetic fraction in ZnS, at TF=7 T. The paramagnetic state becomes negligible above 100 K.

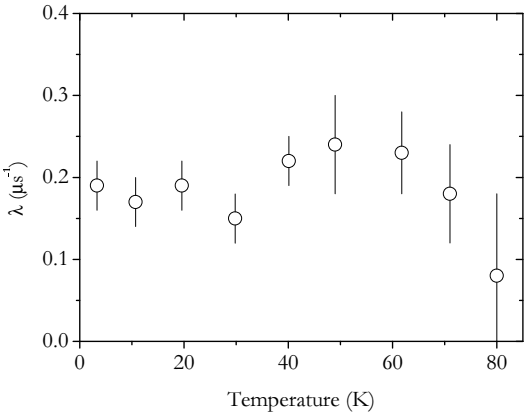

Figure 5.4: Temperature dependence of the relaxation of the paramagnetic component, observed in transverse field 7 T experiments. No significant variation is observed.

measured temperatures, due to the low asymmetry, it is impossible to extract sensible values for the relaxation λ and the frequency ω. We can not therefore establish any eventual increase of the relaxation above 80 K, due to the low value of the paramagnetic asymmetry.

A temperature decrease of the paramagnetic frequency with temperature, as noted for the Mu_{II} state in ZnSe (fig. 4.6), is observed here as well. In fig. 5.5 we plot the corresponding temperature dependence of the isotropic hyperfine interaction A_{iso} (obtained with eq. 4.1). This has been analysed with both models presented in chapter 4. Assuming an interaction with long-wavelength phonons, treated within the Debye model [Pat88] (eq. 4.3), we obtain a Debye temperature of 225 K, again in a rough 2 to 3 ratio to the known Debye temperature in ZnS (350 K, as quoted in ref. [Bir75]). If we instead assume the temperature dependence to arise from a local vibrational mode, treated within an Einstein model (eq. 4.5), we obtain for the vibrational energy $h\nu = 13.3 \pm 0.1$ meV, where it is sufficient to use eq. 4.5 up to first order. The obtained vibrational energy, similarly to the result obtained for the Debye temperature, is correspondingly larger than the 8 meV obtained for the ZnSe case. Unlike the ZnSe case, both models adequately describe the experimental data in the entire measured temperature range.

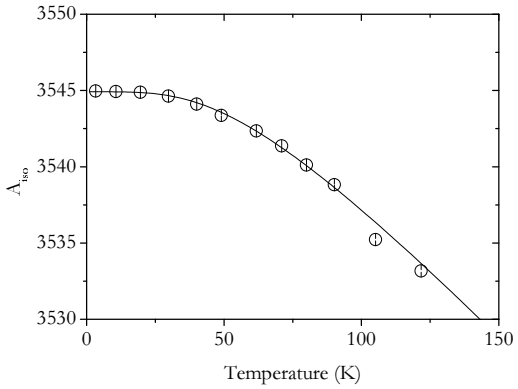

Figure 5.5: Temperature dependence of the isotropic hyperfine interaction A_{iso} in ZnS, observed in TF=7 T. The line is a fit with a model assuming interaction of the muonium atom with long-wavelength phonons treated within a Debye model, as described in the text. A fit with an Einstein model looks similar and is equally successful in describing these data.

5.1.2 Low transverse field spectroscopy

We have investigated the same sample at low transverse fields (15 G), at the DOLLY instrument at PSI. The temperature dependence from liquid-helium temperature up to room temperature was investigated. The same basic features found for the ZnSe samples are visible, as we will now present and discuss.

A paramagnetic fraction is observed, amounting to c. 29% at 2 K, and the diamagnetic fraction at the same temperature is 3%. These two fractions are observed up to room temperature, with varying amplitude, relaxation (for the paramagnetic fraction only) and phase (for the diamagnetic fraction only).

In fig. 5.6 we present the temperature dependence of the diamagnetic and paramagnetic fractions. The paramagnetic fraction is depicted only up to 80 K, where it is seen to decrease to c. 22%. Above this temperature, the paramagnetic fraction seems to remain constant at least up to 210 K, and was fixed, in this temperature range, to a constant value in the analysis in order to reduce the uncertainty of the correlated parameters.

Similarly to what was observed for the ZnSe *Ctec* sample, we observe for ZnS a modest increase of the diamagnetic fraction with increasing temperature from 40 K to 70 K (fig. 5.6), a significant phase-shift of this fraction being observed as well (fig. 5.7). A concomitant increase of the relaxation of the paramagnetic fraction is also present (fig. 5.8). Above 200 K, the diamagnetic fraction is found to decrease again, and this is possibly followed by an increase of the paramagnetic fraction (not represented in fig. 5.6, due to very significant uncertainty) and the respective relaxation.

The above-cited features somehow mimic those seen in ZnSe (figs. 4.17, 4.19 and 4.18), and we therefore make use of the same interpretation scheme developped in chapter 4, taking the under-100 K phenomena to correspond to the capture of a second electron by the paramagnetic Mu state and the above-200 K features to correspond to the ionization of this second electron to the conduction band. We leave a more quantitative analysis to the next section.

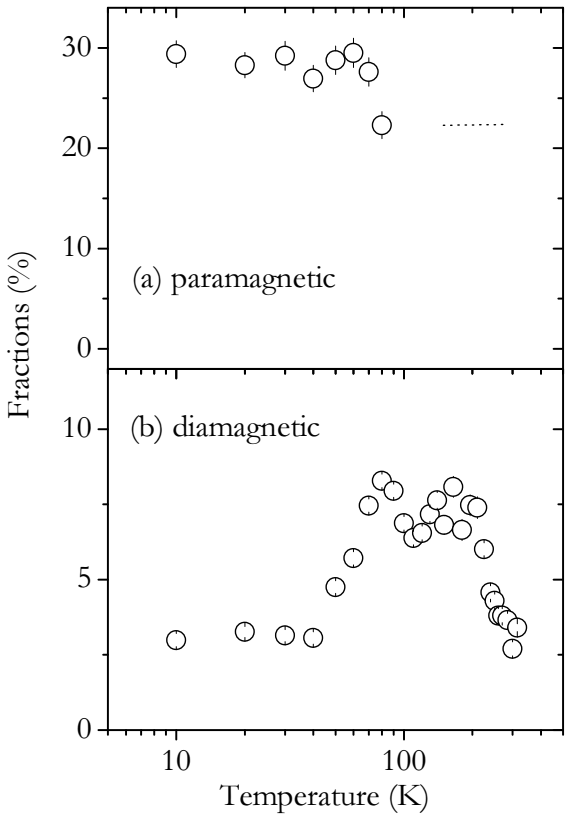

Figure 5.6: Temperature dependence of the paramagnetic (a) and diamagnetic (b) fraction in ZnS, as seen in TF 15 G experiments. The paramagnetic fraction is observed up to room temperature; its value on the fits to the time spectra was fixed up to 210 K, and is represented by a dashed line.

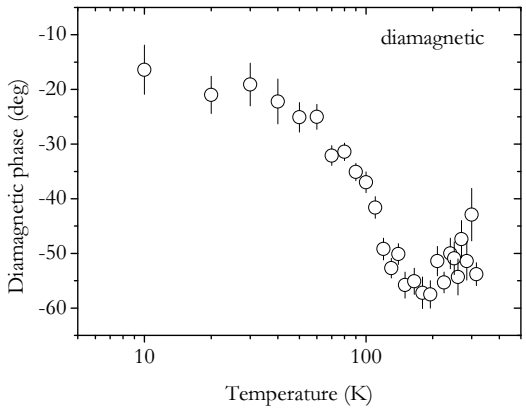

Figure 5.7: Phase of the diamagnetic fraction, as observed in temperature dependent studies under an applied transverse field of 15 G.

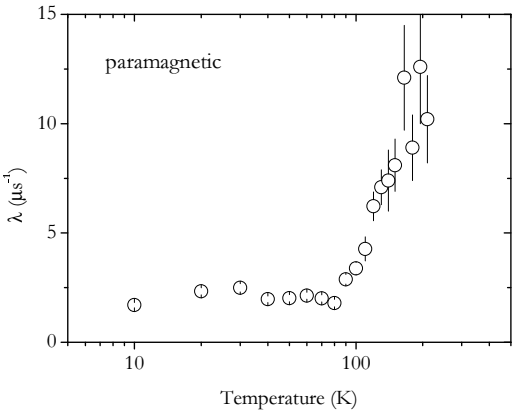

Figure 5.8: Temperature dependence of the relaxation of the paramagnetic component, observed at TF=15 G.

5.1.3 Final-state analysis of the diamagnetic fraction

The product of a conversion reaction such as $Mu^0 + e^- \rightarrow Mu^-$ is affected by dephasing in usual transverse-field measurements, as discussed in chapter 4, and the analysis of the final-state is best done by muon-spin resonance experiments.

We have undertaken, as for ZnSe, muon spin resonance experiments on the diamagnetic fraction of ZnS. These were done with the RF setup with flypast at ISIS, and complemented with calibration measurements on polyethene. The temperature dependence of the resulting diamagnetic fraction is depicted in fig. 5.9, where again a clear recovery up to nearly 100% is observed at c. 90 K. This has been analysed with the following equation, which results directly from eq. 4.39 in the case of the capture of the second electron occuring for a single paramagnetic species:

$$\overline{f_d} = f_p^0 \frac{\nu_c}{\nu_c + \nu_\mu} + f_d^0 \tag{5.1}$$

The limiting equation 5.1 follows directly from eq. 4.39 with the trivial limit $f_I^0 = 0$ (and the total identification $f_p = f_{II}$). However, it follows as well as the limiting case for extremely fast conversion from $\mathrm{Mu_I}$ to $\mathrm{Mu_{II}}$ (i.e. $\nu_{I/II} >> \nu_c$), in which case we have $f_p^0 = f_I^0 + f_{II}^0$ instead. We find the latter a more convincing description of the underlying physics. The resulting fit with eq. 5.1 to the data of fig. 5.9 yields $\nu_c^\infty = 19(3)$ MHz and $E_c = 17(1)$ meV (where f_p^0 was fixed to 79%, corresponding to the complement to 100% of the low temperature value of the diamagnetic fraction). The activation energy compares favourably with known donor energies in ZnS (c. 14 meV [Mad82]) and the pre-exponential factor is intermediate between the values found for the ZnSe *AA* and *Ctec* samples.

In fig. 5.9, a significant decrease of the diamagnetic fraction is observed only above 180 K. This was analysed with eq. 4.28, assuming it corresponds to the ionization of the muonium's second electron to the conduction band, as discussed in chapter 4. The capture parameters were fixed to the values obtained in the previous fit to the low temperature capture. We obtain, for the ionization parameters, $\nu_i^0 = 8(6) \times 10^5$ MHz and $E_i = 249(17)$ meV. The resulting fit is shown in fig. 5.10, where it can be seen to describe the experimental data only in the interval $180 - 280$ K, besides the fixed capture part in the range $30 - 70$ K.

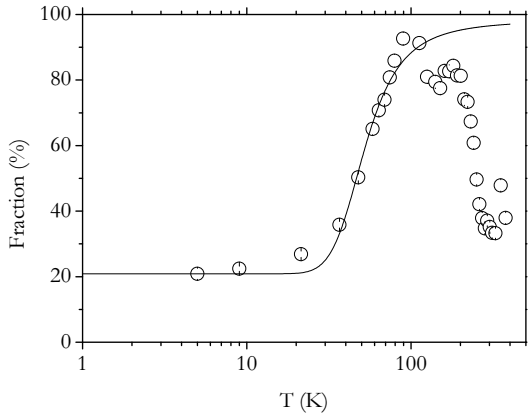

Figure 5.9: Temperature dependence of the diamagnetic fraction in ZnS, as measured by muon spin resonance methods at ISIS. The line is a fit with eq. 5.1.

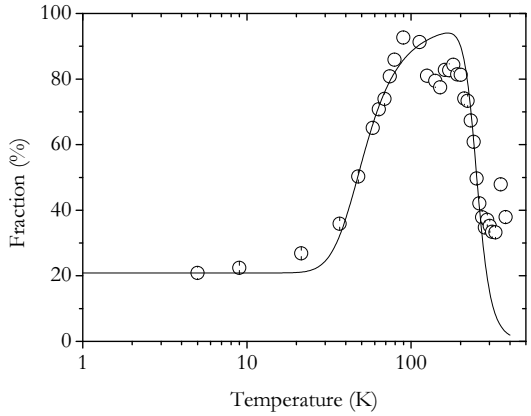

Figure 5.10: Temperature dependence of the diamagnetic fraction in ZnS, as measured by muon spin resonance methods at ISIS. The line is a fit with eq. 4.28, as described in the text.

5.1.4 Probing Mu dynamics with LF

As mentioned previously, measurements in longitudinal field geometry may provide further insight into the muon-spin dynamics, either by the longitudinal field quenching repolarization curves, either by the field dependence of the asymmetry relaxation. We have only begun these studies at ZnS, obtaining the field dependence of the average polarization and of the asymmetry relaxation at 13 K, in measurements performed at ISIS. These are represented, respectively, in figs. 5.11 and 5.12. In fig. 5.11 we include as well a tentative fit with equation 2.59 (yielding $\nu = 1.22(1) \times 10^7$ MHz and $\tau = 0.331(3)$ μs^{-1}). Of course, at this low temperature, this model is not expected to be adequate to describe the expected Mu_I to Mu_{II} conversion. Most likely, the apparent step in the low-field points of fig. 5.11 is now associated with the corresponding decrease observed for the relaxation in fig. 5.12. In this last figure, we include as well a fit with equation 2.65 (where we find $\lambda_{0d} = 2.2(3) \times 10^6$ MHz and $\lambda_{d0} = 8(2) \times 10^3$ MHz), where the above caveats equally apply. These data can nevertheless provide useful hints for the pursuit of this research path.

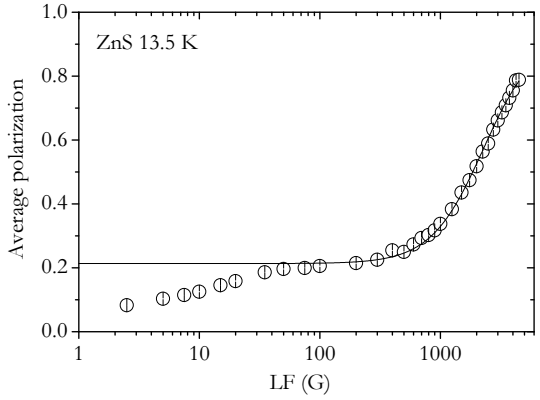

Figure 5.11: Longitudinal-field-quenching (repolarization) curve, obtained for ZnS at 13 K. The line is a fit with eq. 2.59 to the points above 80 G.

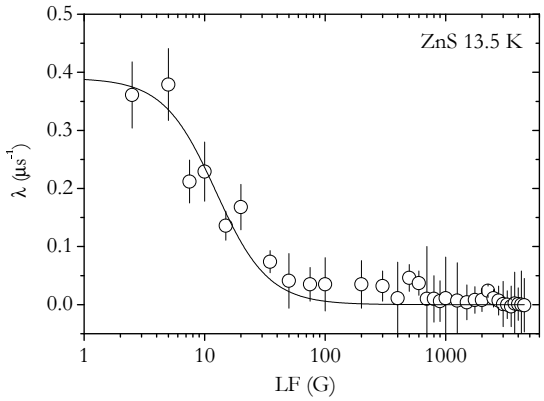

Figure 5.12: Relaxation rate corresponding to the repolarization curve in fig. 5.11. The line is a fit with equation 2.65.

5.2 ZnTe

In chapter 1, we have seen that ZnTe contrasts with ZnSe and ZnS, growing naturally p-type and being difficult to dope n-type. Such fundamental difference is bound to provide substantial differences in the muonium experimental data and interpretation. In this compound no neutral muonium state was observed to date [Pat88].

5.2.1 Spectroscopic measurements

Search for spectroscopic evidence of muonium

ZnTe was investigated at TRIUMF using the high-magnetic field capabilities. Both a high-purity powder and a monocrystalline sample ([110] orientation) were investigated: two high-statistics points (2.5 K and 100 K) were taken for the powder sample at a transverse field of 5 T; five high-statistics points were taken at selected temperatures from 5 K to room temperature for the single crystal, at 7 T. In all cases, the only spectroscopic is that of a diamagnetic component,

with temperature-dependent amplitude. Still searching for paramagnetic muonium signs, high-statistics measurements were taken as well at PSI (2 K, 50 K and 100 K), with low-transverse fields (20 G), again revealing nothing but a diamagnetic component. This diamagnetic component was subsequently investigated at the GPS instrument at PSI, for the [110] crystal, in the $2 - 300$ K range.

Temperature dependence of the diamagnetic fraction

A typical asymmetry time spectrum for ZnTe is shown in Fig. 5.13. Maximum obtainable asymmetry is, for this instrument, $A_{max} = 23.1\%$, as determined by measurements on silver. Figure 5.13 informs us that most of the asymmetry is not seen in ZnTe, constituting a missing fraction.

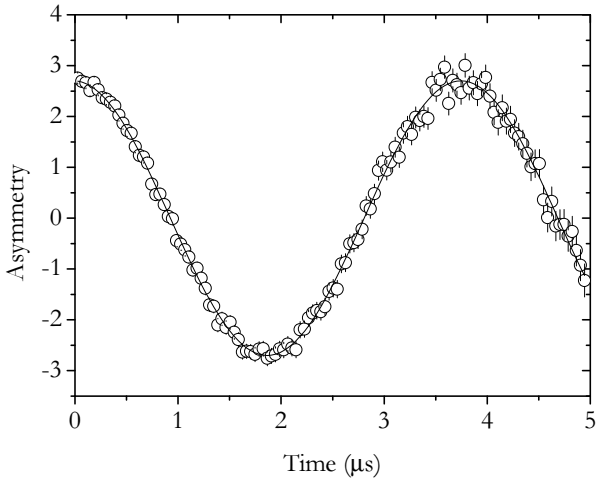

Figure 5.13: Asymmetry time spectrum obtained for a monocrystalline ZnTe sample on an applied transverse field TF=20 G, at T=2 K, TF=20 G. Only a diamagnetic precession is observed.

The observed asymmetry oscillations correspond to the Larmor precession of the muon spin at the given applied field, with a gyromagnetic ratio corresponding to diamagnetic muonium. These spectra were fitted with a simple cosine function, for all temperatures, since no relaxation was observed:

$$A(t) = A_0 \cos(2\pi f_L + \phi_0) \tag{5.2}$$

where A_0 is the asymmetry, f_L the Larmor frequency and ϕ_0 the phase parameter. The temperature dependence of this diamagnetic fraction was followed from 2 K to 300K under a transverse field of 20 G. The observed diamagnetic fraction, as obtained from fits after normalizing to the maximum asymmetry, is depicted in Fig. 5.14. The diamagnetic fraction is seen to decrease from the lowest temperature to 50 K, and afterwards increasing from 100 K up, not reaching yet a plateau at room temperature, keeping to values less than 22%. Thus, even at 300 K, c. 80% of the muons polarization is not seen, constituting a missing fraction. We also observe variations of the phase of the asymmetry oscillations above 50 K, which are plotted in Fig. 5.15.

Discussion

We first concentrate on the rise of the diamagnetic fraction from 100 K up to room temperature. The existence of a phase shift of the diamagnetic asymmetry oscillations denotes that this fraction is not formed promptly, and that between the time of muon implantation and the diamagnetic fraction formation, the muon spin is subject to interactions which are strong enough to induce the spin rotation, causing the observed angular shift. These interactions do not destroy completely the muon polarization, which is afterwards detected, suggesting that the delay should not exceed the nanosecond range. From the value of the shift, one may therefore estimate the strength of the interaction, which points to a gyromagnetic ratio of the order of GHz/T.[2] Deep muonium states present gyromagnetic ratia with this order of magnitude, which suggests that a rather strong interaction is

[2]An angular shift of $\phi = 60^o = \pi/3$ rad, occurring within $\Delta t = 1$ ns, in the presence of a magnetic field of $B = 20$ G corresponds to a gyromagnetic ratio $\gamma = \phi/(2\pi\Delta t B) = 83$ GHz/T.

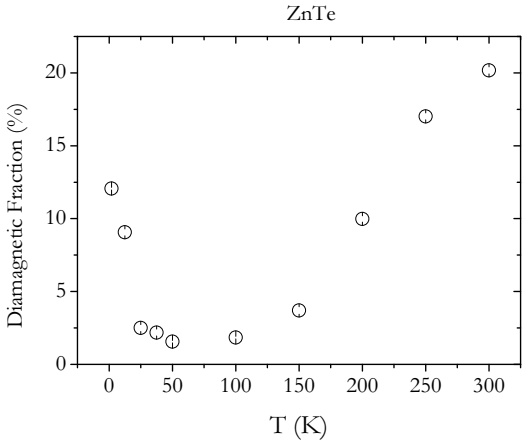

Figure 5.14: Temperature dependence of the diamagnetic fraction on ZnTe, observed under an applied transverse magnetic field of 20 G.

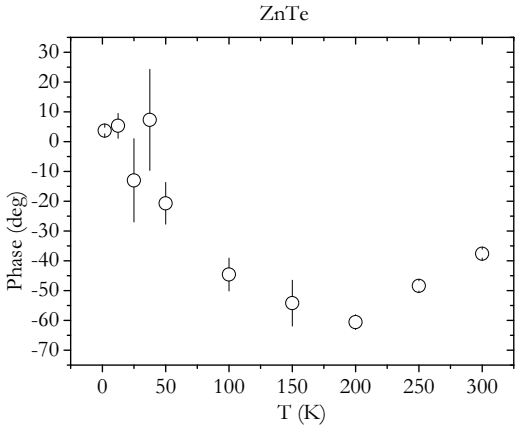

Figure 5.15: Phase of the diamagnetic asymmetry oscillations, as a function of temperature. The applied transverse magnetic field is 20 G.

involved in this case as well. Evidence of such deep state is bound to show up in longitudinal field repolarization measurements, as will be seen below.

One must also consider that the phase shift appears already above 50 K, at a temperature below the associated rise of the diamagnetic fraction at 100 K. This is also a sign of delayed formation. The diamagnetic fraction is hence expected to be growing before 100 K, the result of the growth not being visible in transverse field geometry due to dephasing of the muon's polarization. If this is the case, such diamagnetic fraction shall appear in RF-μSR measurements, and this is effectively the case, as we shall see.

Thus, the rise of the diamagnetic fraction from 100 K up, being the result of delayed formation, is observed only at temperatures high enough for the muon-polarisation dephasing to be negligible. The actual rise of the fraction occurs already at somewhat lower temperatures. Holes becoming mobile at about 100 K in ZnTe, suggests that as the paramagnetic muonium atom has a chance of meeting a hole, recombination occurs, by occupation of the non-occupied valence band state by the muonium electron. This process can not occur before acceptors ionization, since the muonium atom is expected to thermalize at an intrinsic environment, and the probability to be stopped near a localized hole is negligible. In this model, the muonium atom is behaving as a compensating (deep) donor.

The behaviour of the diamagnetic fraction below 50 K is most probably related to muon spin interactions in the precursor stage before thermalization. These processes, which lead to the missing fraction as well, are still not clearly identified.

5.2.2 Final-state analysis of the diamagnetic fraction

The above results prompted us to investigate the diamagnetic fraction by means of the final-state analysis allowed by RF-μSR (see section 2.6.4). The RF-μSR capabilities at ISIS were used. The same Crystec [110] sample used at PSI was investigated with this technique. The sample was mounted on a mylar flypast sample holder. The RF frequency was set to 23 MHz (resonance expected at LF = 1697 G, for the diamagnetic state) and the power to 114W, and a temperature scan was carried out from 2 K to 300 K. A polyethene sample with the same shape

of the ZnTe single crystal was used for calibration of the maximum RF average asymmetry at resonance.

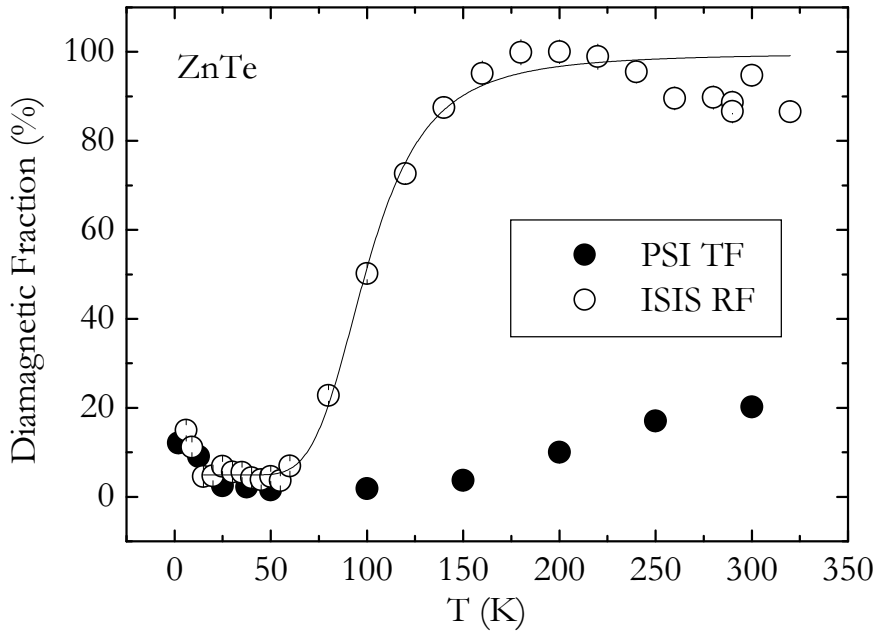

Figure 5.16: Diamagnetic fraction in ZnTe as seen by RF-μSR (open circles) and usual TF-μSR (closed circles). The line is a fit with the model described in the text, with $E_a = 89 \pm 9$ meV, $N_a = (8 \pm 83) \times 10^{17}$ cm^{-3}, $\sigma = (90 \pm 5) \times 10^{-7}$ Å^2, $p_0^d = 4.9 \pm 0.4\%$. The donor concentration parameter was fixed to $N_d = 2.8 \times 10^{13}$ cm^{-3}, and the initial paramagnetic fraction p_0^0 was forced to be $p_0^0 = 100\% - p_0^d$.

Discussion

The diamagnetic fraction in ZnTe, as determined from the RF temperature scan is depicted in Fig. 5.16, together with the corresponding diamagnetic fraction observed in the TF studies performed at PSI. The RF data clearly demonstrate that the missing fraction in ZnTe is completely recovered at 150 K.

In the interpretation suggested by the transverse-field data shown in the previous section, the muon is thought to try to form the deep muonium state at the tetrahedral interstitial site but, this configuration being unstable in this p-type material, it converts to the stable configuration at the anion-bonded location. The present RF data demonstrate that the suggested anion-bonded configuration gives a full account of the muon fraction. In this interpretation, the growth of the diamagnetic fraction in ZnTe (fig. 5.16) is related to the concentration of holes in the valence band. As the acceptors in the material ionize, holes become increasingly mobile, and the probability of meeting the muon increases, thus favouring electron recombination at the muon, in the process

$$Mu^0 + h^+ \underset{\nu_c}{\longrightarrow} Mu^+ \tag{5.3}$$

The hole capture rate ν_c (i.e., the recombination of the muonium electron with the empty state in the valence band) is assumed to be proportional to the hole concentration n_h, the hole velocity v_h, σ being the cross-section of the process:

$$\nu_c = n_h v_h \sigma \tag{5.4}$$

The temperature dependence of the concentration of holes in the valence band, for a compensated p-type semiconductor with N_d compensating donors and N_a acceptors with spin degeneracy β (usually taken $\beta = 2$) at the single acceptor ionization energy E_a, is given by [Bla62][3]:

$$\frac{n_h(n_h + N_d)}{N_a - N_d - n_h} = \frac{N_v}{\beta} \exp\left(-\frac{E_a}{kT}\right) \tag{5.5}$$

[3]Cf. p. 139, in the cited reference.

where N_v is the effective density of states in the valence band and is given by[Bla62][4]:

$$N_v = 2\left(\frac{m_v^* kT}{2\pi\hbar^2}\right)^{3/2} \tag{5.6}$$

and $m_v^* = 0.6\, m_0$ is the hole effective mass in this compound [Mad82]. Solving eq. 5.5 as a function of n_h, we obtain:

$$n_h = \frac{N_d + f}{2}\left(-1 + \sqrt{1 + \frac{4(N_a - N_d)f}{(N_a + f)^2}}\right) \tag{5.7}$$

where

$$f = CT^{3/2}\exp\left(-\frac{E_a}{kT}\right) \tag{5.8}$$

and

$$C = \frac{2}{\beta}\left(\frac{m_v^* k}{2\pi\hbar^2}\right)^{3/2} \tag{5.9}$$

The mean-square velocity is given by [Rei65][5]:

$$v_h = \sqrt{\frac{3kT}{m_v^*}} \tag{5.10}$$

We can once again model the evolution of the muon polarization in process 5.3 by a simple model, where the paramagnetic polarization is assumed to decay exponentially with time at rate ν_c:

$$p_0(t) = p_0^0 \exp(-\nu_c t) \tag{5.11}$$

and the diamagnetic polarization increasing correspondingly as:

$$p_d(t) = p_0^d + \nu_c \int_0^t p_0(\tau)d\tau = p_0^d + p_0^0\,(1 - \exp(-\nu_c t)) \tag{5.12}$$

The average diamagnetic polarization is observed in a RF-μSR experiment:

[4]Cf. p. 81, in the cited reference.

[5]Cf. eq. 7.10.16 of the cited reference.

$$\overline{p}_d = \nu_\mu \int_0^\infty p_d(t) \exp(-\nu_\mu t) dt = p_0^d + p_o \frac{\nu_c}{\nu_\mu + \nu_c} \tag{5.13}$$

We have fitted the data in fig. 5.16 with this model. In order to decrease the number of free parameters, and since the RF diamagnetic fraction is observed to recover to 100 %, we have forced the initial paramagnetic fraction p_0^0 to be $p_0^0 = 100\% - p_0^d$. The donor concentration parameter, initially released, was henceforth fixed to $N_d = 2.8 \times 10^{13}$ cm^{-3}, obtained from preliminary fitting, and which is a reasonably small number (the fit is nevertheless much insensitive to it). We have obtained, for the remainding free parameters, $E_a = 89 \pm 9$ meV, $N_a = (8 \pm 83) \times 10^{17}$ cm^{-3}, $\sigma = (90 \pm 5) \times 10^{-7}$ Å^2, $p_0^d = 4.9 \pm 0.4\%$, and show the corresponding fit in figure 5.16. The obtained acceptor energy E_a compares well with known acceptor energies for ZnTe (which vary between 58.3 meV for Li and 272 meV for Au [Mad82, Mag79]). Despite the acceptor concentration N_a being not known for this sample from Hall-effect measurements, the obtained value of N_a is also a sensible number, sufficiently large to justify the experimental impossibility to directly observe the paramagnetic muonium fraction, which is known to disappear as the metal limit is approached in materials.

5.2.3 High-temperature spectroscopic incursion

The inverse process to 5.3, where an electron from the valence band is thermally promoted to the muonium donor level, is expected to occur at much higher temperatures

$$Mu^+ + e^-_{VB} \rightarrow Mu^0 \tag{5.14}$$

This process is dependent on the Boltzmann factor $\exp\left(-E_{0/+}/kT\right)$ and the position of the donor level above the valence band (expected to be larger than 1.7 eV, even for an extremely deep donor). We have extended the transverse field measurements at PSI up to the highest possible temperature (760 K, at date) and verified that the diamagnetic fraction is quite stable with temperature (figure 5.17),

which further supports the identification of this state as a donor. Interestingly, a plateau at c. 27% is observed in these data, whose nature remains puzzling.

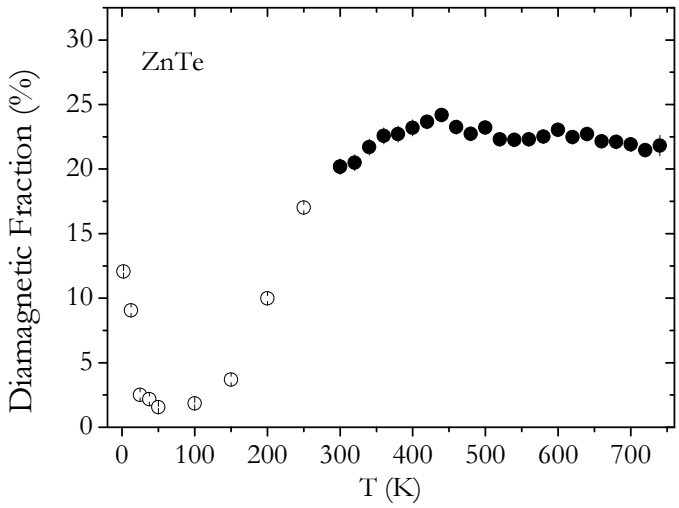

Figure 5.17: Temperature dependence, up to 760 K. of the diamagnetic fraction in ZnTe, as observed under an applied transverse magnetic field of 20 G. White circles correspond to measurements up to room temperature and black circles correspond to measurements above room temperature.

5.2.4 Probing Mu dynamics with LF

Despite its spectroscopical (TF) signature not being visible, the presence of paramagnetic muonium can nevertheless be inferred from longitudinal-field repolarization curves (see section 2.3.3). We have only began these studies at ISIS, where two repolarisation curves were obtained at 4 K and 100 K.

In Fig. 5.18, a representative time spectrum is shown, where there is no sign of relaxation, similarly to the transverse-field data. These spectra where hence fitted with a simple constant line, the value of the constant representing the time-averaged asymmetry. We represent the 4 K and the 100 K longitudinal-field dependence of this asymmetry in figures 5.19 and 5.20, respectively.

The maximum asymmetry in these experiments was determined from a 20 G transverse-field run on silver, yielding $A_{max} = 22.4$. No correction to the slight maximum asymmetry variation with applied field was taken.

Both curves show distinctive repolarization behaviour, again demonstrating the presence of strong, paramagnetic-like, interactions. This is much more pronounced at 100 K. Both curves were fitted with eq. 2.59, and hyperfine interactions of the order of 3000 MHz seem plausible, together with 10^7 MHz electron spin-flip rates in the first hundred nanoseconds.

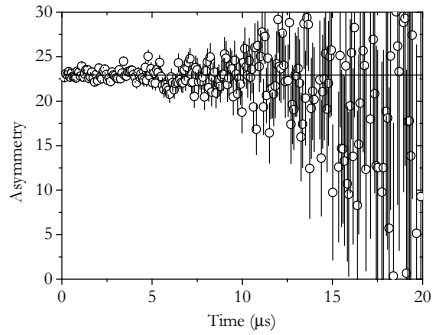

Figure 5.18: Asymmetry time spectrum obtained for a monocrystalline ZnTe sample on an applied longitudinal field LF=4500 G, at T=100 K. No significant relaxation is observed.

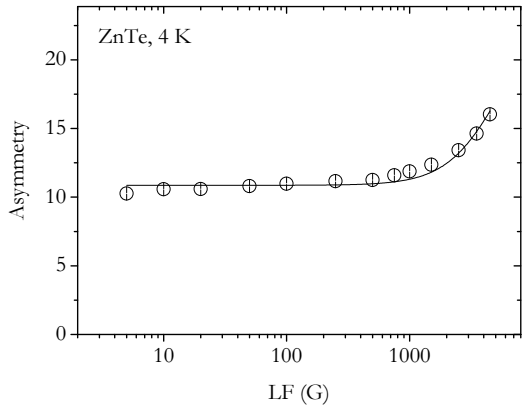

Figure 5.19: Longitudinal field repolarization of the muon spin for ZnTe at 4 K. The line is a fit with equation 2.59, with A=3.2(2.8) GHz, $\nu = 3.6(3.2) \times 10^7$ MHz and $\tau = 0.43(36)$ μs. However, the fit is rather poor and many other parameter combinations are possible.

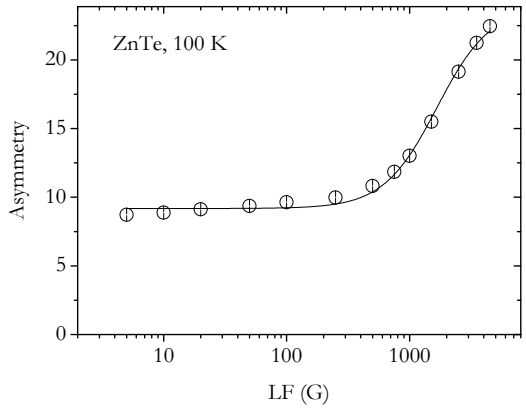

Figure 5.20: Longitudinal field repolarization of the muon spin for ZnTe at 100 K. The line is a fit with equation 2.59, with A=3.5(1.1) GHz, $\nu = 1.2(4) \times 10^7$ MHz and $\tau = 0.15(5)$ μs.

5.3 Conclusive remarks

The muon spin experiments for ZnS and ZnTe presented and discussed in this chapter highlight the expected similarities of n-type ZnS with ZnSe and the expected differences of p-type ZnTe. We now briefly present the essential results of these investigations. Again, some of these results have already been included in a number of publications [Cox03a, Vil05a, Vil06, Vil07a, Wei03a, Wei03b], whereas other aspects are presented here for the first time, the respective publication in peer-reviewed journals being currently (January/2007) in preparation [Vil07b].

In ZnS, our experimental data basically mimic what was presented in the previous chapter for ZnSe. An important difference is found at high-fields and low temperatures, where a single paramagnetic muonium state is found, assigned to an hyperfine interaction $A_{\rm iso} = 3545(1)$ MHz at $T = 0$ K, together with a substantial missing fraction. This state most likely corresponds to the $\rm Mu_{II}$ acceptor-like state in ZnSe, the missing fraction corresponding to highly-relaxing (therefore unobservable) $\rm Mu_{I}$. The temperature dependence of $A_{\rm iso}$ was fitted to the interaction with a local vibrational model with an oscillator energy of approximately 13 meV. A phase-shifted diamagnetic fraction is observed in low-transverse field experiments and is observed to correspond at 80 K to nearly 100% of the total fraction, in muon-spin resonance experiments. The temperature dependence of the diamagnetic fraction observed in these RF-μSR experiments has been analyzed assuming the same interpretation developed for ZnSe, i.e., second electron capture upon ionization of the donors in the material (occurring up to 80 K) and subsequent ionization to the conduction band of the second electron captured by muonium. An ionization energy of c. 250 meV has been fitted to this latter process. Again, evidence of additional muon-spin dynamics is present and is not fully understood.

The experimental data for ZnTe contrast strongly with those for ZnSe and ZnS in the sense that no paramagnetic state is directly observed, despite extensive searches. Only a phase-shifted diamagnetic fraction is observed, which corresponds to 100% of the total polarization at temperatures above 150 K, where the acceptors in the material are fully ionized. The data suggest that muonium in this compound may correspond to a deep donor.

Chapter 6

Conclusions and perspectives

Mas escuta! Onze horas! Onze horas ligeiras estão dançando, no meu velho relógio, o minuete de Gluck. Ora esta carta já vai, como a de Tibério, muito tremenda e verbosa, verbosa et tremenda epistola*; e eu tenho pressa de a findar, para ir, ainda antes do almoço, ler os meus jornais, com delícia.*[1]

Eça de Queiroz
Correspondência de Fradique Mendes, XV

6.1 Towards a final synthesis

In chapters 4 and 5 we have presented a detailed account of our experimental data on ZnSe, ZnS and ZnTe, together with the respective particular analysis and discussion. The essential conclusions of these particular studies have already been summarized in the end of chapters 4 and 5, in a rather focused way. We will now try a global synthesis, envisaging to draw some guidelines emerging from the current work, in the broader context of the physics of muonium/hydrogen in semiconductors.

Of course, the information on muonium states on semiconductors is significant *per se*. However, as stressed in chapter 1, it can become of much wider significance to the physics of semiconductors due to the muonium/hydrogen analogy.

[1]Free translation: *"But listen! Eleven o'clock! Eleven lively hours are dancing already, in my old clock, the Gluck's minuet. Yet this letter is by now, as that of Tiberius, too cumbersome and verbose,* verbosa et tremenda epistola*; and I'm hurrying to finish it, so that, even before lunch, I can read my newspapers, with delight."*

6.1.1 Configuration model

Hydrogen may be incorporated basically in two different ways in II-VI compounds (see Fig. 6.1, left side): (a) It may be bound to one of the negatively charged anions (e.g. to S^- in CdS), hydrogen itself having the character of a positively charged H^+ center, or (b) it may be embedded interstitially between four positively charged metal atoms, behaving like H^- in metal hydrides. We will limit the discussion to these two basic configurations, although other configurations (or variants of the above mentioned) can not be excluded completely on the basis of the present knowledge.

The geometrical configurations in Fig. 6.1 (left side) are associated with electronic configurations as shown in the right side of Fig. 6.1: a shallow donor +/0 level for the bonding configuration and a 0/- level for the interstitial incorporation.

As presented in chapter 1, a shallow donor state was identified in CdS by μSR. Similar shallow donor states were found as well in CdTe, CdSe and ZnO. The shallow donor behavior of this configuration can be understood qualitatively if one considers that the strongly bound anion-hydrogen "molecule" resembles in some respect an atom with an atomic number one higher than that of the anion (e.g. O-H resembles F in ZnO). Such atoms (with an extra unit charge) are typical donors in semiconductors and thus give a rationalization of the observed donor behavior. In ZnS, ZnTe and ZnSe, no state with the shallow donor characteristic was found in μSR, indicating that this configuration is not stable in the neutral electronic state. However, from the general considerations above, we would expect that these hypothetical conversion levels would also lie close to the conduction band in these materials.

In contrast, the character of the interstitially embedded muonium (Fig. 6.1 (b)) is that of an almost free muonium atom with a spherical and strong hyperfine interaction. In this work, such states were observed by μSR in ZnS and ZnSe. The corresponding 0/- acceptor levels are proposed to be placed c. 178 meV below the conduction band edge for ZnSe and c. 249 meV below the conduction band edge for ZnS.

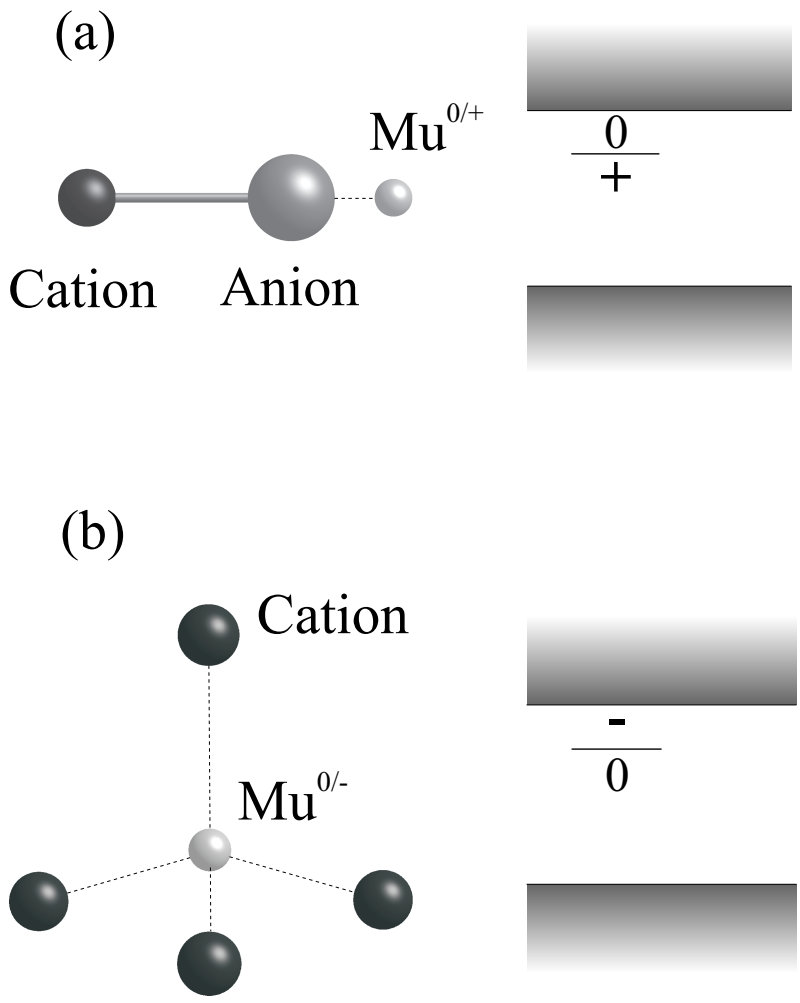

Figure 6.1: Basic configuration model for muonium/hydrogen in II-VI semiconductors: (a) muonium bonding to the anion, giving rise to a +/0 donor and (b) Mu at the cation cage, introducing a 0/- acceptor level.

6.1.2 Energy levels

A rationalization of the position of such deep levels across materials is best achieved by referring such levels to the vacuum state, and not only to the host material band edges [Cal84, Led82]. This requires knowledge about the position of the band edges with respect to vacuum, which can in principle be obtained experimentally by photoelectron emission spectroscopy measurements, the position of the conduction band edge corresponding to the electron affinity and the position of the valence band edge corresponding to the photothreshold energy [Yu99][2]. Although such measurements exist for the II–VI semiconductors [Swa67], it is not always clear how should surface effects be separated from bulk properties. In building a diagram of the position of the band edges for the II–VI semiconductors, we have thus followed the approach proposed by Cox [Cox03b], who used the valence band offsets for II–VI semiconductors, presented in ref. [Wei98], and the calculated position with respect to vacuum of the valence band of ZnO, presented in ref. [Kil02], in order to place the valence band edges. The position of the conduction band edges were then simply obtained by addition of the experimental bandgap, from ref. [Mad82].

The corresponding band scheme is shown in Fig. 6.2 and allows a very simple view on the hydrogen behavior in II-VI compounds. There, we also include the known experimental energies of the shallow donor levels in the cadmium chalcogenides and ZnO, together with the proposed acceptor energies in ZnSe and ZnS, obtained in this work.

The position of the bottom of the conduction band (the electron affinity of the material) with respect to vacuum seems to play an essential role in the formation of the shallow muonium state, associated with hydrogen behaviour uniquely as donor. A significant "(deep) muonium threshold" line is drawn just above the conduction band edge of CdTe. For compounds with larger electron affinity (CdS, CdSe, CdTe and ZnO), the shallow muonium is observed, whereas for compounds with lower electron affinity (ZnSe, ZnS and possibly ZnTe), the acceptor state is observed, which we take as a sign of amphoteric behaviour.

[2]Cf. p. 426 of the cited reference. In this context, it is also useful to define the work function, referring the position with respect to vacuum of the chemical potential (Fermi level).

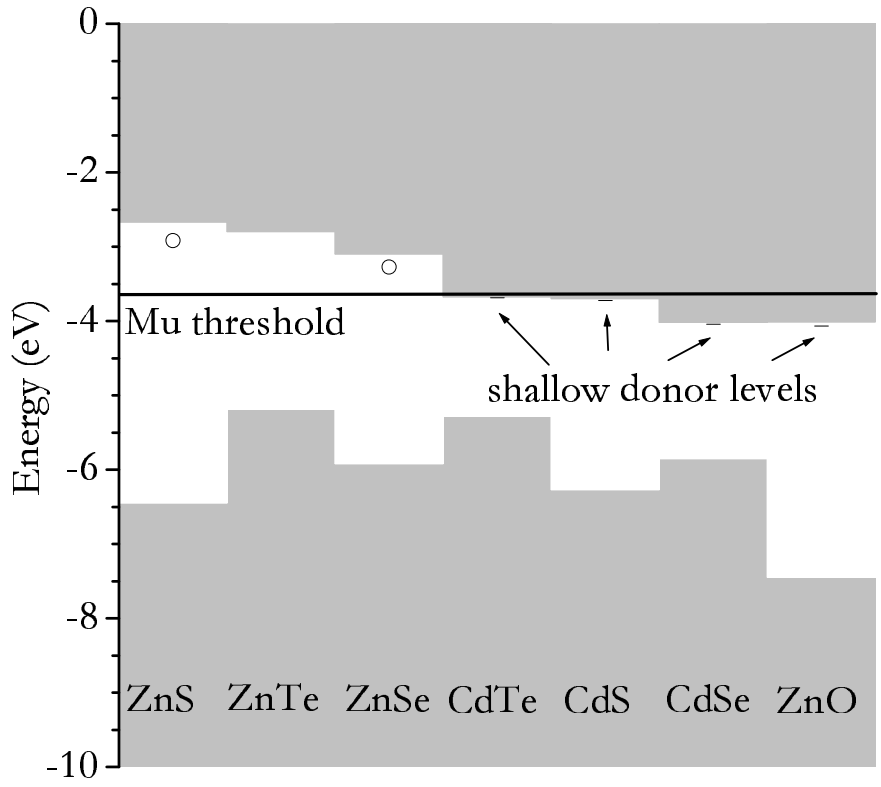

Figure 6.2: Band alignments for the Cd chalcogenides and the Zn chalcogenides and oxide. The Mu threshold level is plotted at 3.6 eV below the vacuum. Effective-mass donor levels determined experimentally are depicted (lines), together with the acceptor levels proposed in this work (open circles).

In the amphoteric behaviour case (ZnS, ZnSe and ZnTe), the two conversion levels lie in the band gap. If the Fermi level is close to the conduction band (n-type), the electron rich Mu^- state is formed, i.e. electrons are taken away from the conduction band and cannot contribute to conductivity. Similarly, if the Fermi level is close to the valence band (p-type), electrons from the Mu center fall to the Fermi level, therefore compensating the holes and thus reducing the conductivity. In the unique donor behaviour case (CdS, CdSe, CdTe and ZnO), only the donor state lies within the band gap, whereas the electron rich 0/- configuration is always unbound and thus is not formed.

The position of the deep acceptor level 0/- is possibly controlled by a vacuum pinning rule, such as that proposed in earlier studies of transition–metal impurities [Cal84, Led82]. Currently, such pinning rules have been proposed for hydrogen in semiconductors and oxides in at least three slightly different ways [Kil02, Rob03, VdW03]. The simplest possible way to address this question is the straightforward application to hydrogen of the spirit of the initial transition–metal pinning rules, and therefore consider that the binding energy of the second electron in H^-/Mu^- can be thought of as approximately constant with respect to vaccum in all materials. Such simple consideration does not necessarily stand over more detailed models such as those of references [Kil02, Rob03, VdW03] but it has nevertheless some heuristic value. With respect to the vacuum the binding energy of the second electron of Mu^- in ZnSe is approximately 3.4 eV, which may be compared with that of H^- in vacuum (E = 0.756 eV). The stronger binding of the embedded atom is reasonable since the positive cation environment provides some extra binding.

6.2 Future developments

The present investigation contains significant unresolved issues that require further clarification, either from the experimental point of view and/or from the theoretical side. It also touches upon other related unsolved problems in the field of hydrogen in semiconductors, whose investigation may gain from the insight of the present

work. In the following section, we will try to both summarize the former, giving possible directions to its clarification, and to point some of the latter.

6.2.1 Open questions

The synthesis presented in the last section also gives us the essential questions that should be clarified in order to allow a more conclusive contribution of the muonium investigations to the physics of hydrogen in the zinc-chalcogenide semiconductors. These points relate to the configuration of the muonium states, to the placement of the donor and acceptor levels, and to the rationalization of these levels in vacuum-pinning-levels.

Muonium configurations

Regarding the configuration assignment, we have assigned the deep muonium centres in ZnSe and ZnS to the cation tetrahedral cage based upon sensible arguments, but a direct identification is still missing. Also, most importantly, from this investigation we know nearly nothing about possible site-changes and diffusion processes. The use of the avoided-level-crossing technique [Cho98] can in principle elucidate about the position of the muonium atom, through the investigation of the interactions with nearby nuclear magnetic moments, but this is particularly difficult in these materials with a very low density of such magnetic moments.

Muonium levels

Similarly, the assignment of processes which allows to estimate the position of the levels in the bandgap requires further insight into the muon spin dynamics which is revealed particularly in the measurements on ZnSe and ZnS. At this point, we should remember that at present a satisfactory model is available only for silicon, and that this model was built after two decades of investigations on dozens of samples from extreme p-type to extreme n-type, which is, at least for the bulk, seemingly an impossible task in the current stage of sample preparation. It is doubtful that such advanced stage may ever be achieved for any of the II-

VI compounds. However, possible research directions (some of which are already making its way to new proposals in the muon facilities) include:

(i) detailed muon-spin relaxation measurements on longitudinal fields, at the relevant temperature ranges identified in the present work; these investigations may provide also more accurate measurements of the energy-levels from the field-dependent polarization and muon-spin relaxation, upon full adequate modelling [Cho94].

(ii) muon-spin-resonance measurements on the doped ZnSe samples (particularly *ZnSe:I*), in order to clarify the intriguing behaviour above 200 K;

(iii) extension of the ZnS and ZnTe research into both doping limits: (a) by using the current undoped samples, upon annealing in vacuum and/or in hydrogen atmosphere in order to increase compensation and reduce the concentration of free carriers; (b) by using other doped samples;

(iv) investigation of the paramagnetic state in ZnS by muon spin resonance (microwave) measurements; the question of the existence of a second paramagnetic state in highly-resistive samples should be taken into account, together with point (iii);

(v) further insight into the second electron capture and Mu^- formation in ZnSe and ZnS, by means of muon-spin investigations under applied electric fields [Sto97].

Testing "vacuum-pinning-levels"

Of course, the experimental test of any of the existing vacuum pinning models requires a thorough survey on many materials, such as those began by Lichti [Lic06] or Cox [Cox03b, Cox06a, Cox06b]. This is also hindered by the problem that the positions of the band edges with respect to vacuum are poorly known for many materials.

However, two possible directions seem plausible within the scope of II-VI semiconductors:

(i) investigation of the muonium configurations formed by varying the Fermi level position from extreme p-type to extreme n-type; the obvious candidate for this investigation is CdTe, the only II-VI semiconductor where both types of doping

can be achieved; interestingly, signs of the coexistence in this compound of deep and shallow muonium states have been found [Cor04, Gil01], which may be related to a particularly delicate balance of metastable states;

(ii) investigation of the muonium configurations in ternary compound series such as $Zn_xCd_{1-x}S$ with x varying between 0 and 1; this would allow to determine the x interval where the transition of the shallow state to the deep state occurs, and the corresponding position of the conduction band edge; of course, this investigation direction fights with the need of adequate high-resistive samples.

6.2.2 Related investigations

Theoretical digressions: H vs. Mu in the zinc chalcogenides

As mentioned in chapter 1, the existing theoretical calculations in the zinc chalcogenides are very incipient and mutually contradictory. A thorough calculation of the hydrogen and muonium configurations and transition levels in the zinc chalcogenides therefore appears as a most interesting and needed research work. The work now presented provides substantial amount of experimental information which was not previously available and which may work as a guide in the development and improvement in the corresponding theoretical work. For the interested theorist, the modelling of these deep compact states can also be undertaken as an easier preliminary step to address the extremely difficult problem of the theoretical modelling of shallow states in the cadmium chalcogenides counterparts.

Nitrogen-hydrogen interactions in MBE-grown ZnSe layers

Despite the fundamental interest of muonium/hydrogen behaviour in bulk semiconductors, which was pursued in this work for the II-VI zinc chalcogenides, the current technological applications of these materials relate essentially to thin-film structures. Up to now, the study of these two-dimensional systems was not available to μSR. As we have pointed out in chapter 2, the typical range of the implanted 4 MeV muon in a solid is above 100 μm, which precludes the investigation of lower dimension structures. However, a slow-muon facility has been developed in the

last few years at the muon-spectroscopy laboratory at the Paul Scherrer Institut [Bak04]. Muon implantation energies between 0 and 30 keV have been achieved with high intensities, allowing a controllable mean thermalization length between a fraction of a nm and a few hundred nanometers [Pra05, PSI07]. This facility has been opened to proposals by users in 2006.

This facility opens new and exciting research perspectives and some related results include the observation of conduction electron spin polarization in the non-magnetic spacer layer between two ferromagnets [Lue03] or the investigation of the spin-glass transition in a polimeric film [Pra05]. However, the research of semiconductor heterostructures with this technique is only giving its first steps.

Regarding the zinc chalcogenides in particular, the investigation of the role of hydrogen in MBE grown p-type films of ZnSe doped with nitrogen may be a particularly useful research direction. As mentioned in chapter 1, ZnSe is usually n-type and is not easily doped p-type. So, much excitement was created around p-type doping of ZnSe with nitrogen, achieving net acceptor densities of 10^{17} cm^{-3} [Par90]. This was accomplished on molecular-beam-epitaxy-grown (MBE) epitaxial layers. Nitrogen substituting on a selenium site introduces an acceptor level located 110 meV above the top of the valence band [Dea83]. However, the incorporation of hydrogen in the films was shown to increase dramatically the resistivity of the films [Ho95]. The acceptor compensation is most probably due to hydrogen passivation [Kam93], where hydrogen most likely sits at the bond-centre location in the H-N complex [Tor03].

In this context, μSR could shine much light on the microscopic details of the nitrogen-hydrogen interaction in ZnSe. In bulk samples, the trapping of hydrogen at defects has been observed for chalcopyrites [Vil02, Vil03a] and GaAs [Cho01].

Related II–VI materials for Blue/green light emitters - Be and Mg chalcogenides

The magnesium and beryllium II-VI chalcogenides seem to be emerging as promising candidates as base materials for blue and green light–emitting laser diodes, together with the respective alloys with the zinc chalcogenides [Has06, Nur97,

Seg03, Waa96]. Although this field remains very incipient, particularly with respect to the sample growth, it has already stimulated interesting experimental developments [Pla00, Pla03, Waa96]. The investigation of the beryllium and magnesium chalcogenides may provide a new field, up to now completely unexplored, for further experimental explorations of the vacuum-pinning level models. Calculations of the respective band offsets have already been published [Seg03, Wei98]. The beryllium chalcogenides also present an additional advantage: natural beryllium consists of a single isotope (^9Be) with nuclear spin 3/2 and a relatively large magnetic moment of -1.1779 μ_N [Web07], which allows a more direct localization of the Mu states, as well as other experimental studies such as the extraction of diffusion parameters.

Magnetic semiconductors for spintronics

As mentioned in chapter 1, both ZnSe [Edd06] and ZnTe [Oza06] are strong candidates for spintronics applications, upon doping with adequate ferromagnetic atoms. μSR can play a role in the elucidation of the eventual complexation of such impurities with the ubiquitous hydrogen atom. Also, the muon being a magnetic probe *par excellence*, it may become an extremely useful probe of the spin current in spintronics devices. This field, already far-off the main trend of this work, promises the most exciting developments, particularly if using the slow-muons facility in parallel with bulk techniques.

Appendix A

Calculation of resistivity in equation 3.17

As mentioned in chapter 3, the Van der Pauw theorem states that the resistivity ρ relates to the sample thickness d and to the characteristic resistances $R_{MN,OP}$ and $R_{NO,PM}$ by the equation (eq. 3.17):

$$\exp\Big(-\frac{\pi\, d}{\rho}\, R_{MN,OP}\Big) + \exp\Big(-\frac{\pi\, d}{\rho}\, R_{NO,PM}\Big) = 1$$

It is not possible to express ρ analytically from eq. 3.17, so it must be computed numerically. We have adopted the following algorithm, proposed by NIST [Nis06]:

- Initialization:

$$z_0 = \frac{2\ln 2}{\pi\,(R_{MN,OP} + R_{NO,PM})}$$

- Cycle to be repeated until $\delta = 0.0005$:

  1. i^{th} iteration of y:

$$y_i = \frac{1}{\exp(\pi\, z_{i-1}\, R_{MN,OP})} + \frac{1}{\exp(\pi\, z_{i-1}\, R_{NO,PM})}$$

2. i^{th} iteration of z:

$$z_i = z_{i-1} - \frac{\frac{(1-y_i)}{\pi}}{\frac{R_{MN,OP}}{\exp(\pi\, z_{i-1}\, R_{MN,OP})} + \frac{R_{NO,PM}}{\exp(\pi\, z_{i-1}\, R_{NO,PM})}}$$

3. Relative difference δ:

$$\delta = \frac{z_i - z_{i-1}}{z_{i-1}}$$

- The resistivity is

$$\rho = \frac{d}{z_i}$$

Bibliography

[Alb01] *Powder pattern hyperfine spectroscopy of shallow donor muonium centres*, H. V. Alberto, R. C. Vilão, J. Piroto Duarte, J. M. Gil, N. Ayres de Campos, R. L. Lichti, E. A. Davis, S. P. Cottrell, S. F. J. Cox, Hyp. Int. **136**, 471 (2001).

[All58] *Experimental results on charge-changing collisions of hydrogen and helium atoms and ions at kinetic energies above 0.2 keV*, S. K. Allison, Rev. Mod. Phys. **30**, 1137 (1958).

[Ama05] *GPS User Guide*, A. Amato, Laboratory for Muon Spectroscopy, Paul Scherrer Institut, Villigen, Switzerland (2005).

[And75] *Model for the electronic structure of amorphous semiconductors*, P. W. Anderson, Phys. Rev. Lett. **34**, 953 (1975).

[Ars84] *Muonium formation in vapors*, D. J. Arseneau, D. M. Garner, M. Senba, and D. G. Fleming, J. Phys. Chem. **88**, 3688 (1984).

[Ash76] *Solid state physics*, N. W. Ashcroft and N. D. Mermin, Saunders College Publishing, Fort Worth (1976).

[Ast00] *Standard Test Methods for Measuring Resistivity and Hall Coefficient and Determining Hall Mobility in Single-Crystal Semiconductors*, ASTM Designation F76, Annual Book of ASTM Standards, Vol. 10.05 (2000).

[Ave62] *Purification of II-VI compounds by solvent extraction*, M. Aven and H. H. Woodbury, App. Phys. Lett. **1**, 53 (1962).

[Ave63] *Carrier mobility and shallow impurity states in ZnSe and ZnTe*, M. Aven and B. Segall, Phys. Rev. **130**, 81 (1963).

[Ave65] *Electrical transport and contact properties of low resistivity n-type zinc sulfide crystals*, M. Aven and C. A. Mead, App. Phys. Lett. **7**, 8 (1965).

[Bai71] *Muonium. II. Observation of the muonium hyperfine-structure interval*, J. M. Bailey, W. E. Cleland, V. W. Hughes, R. Prepost, and K. Ziock, Phys. Rev. A **3**, 871 (1971).

[Bak04] *Generation and applications of slow polarized muons*, P. Bakule and E. Morenzoni, Contemporary Physics **45**, 203 (2004).

[Bar85] *Bistability and metastability of the gallium vacancy in GaAs: the actuator of EL2?*, G. A. Baraff and M. Schluter, Phys. Rev. Lett. **55**, 2340 (1985).

[Ber87] *Electronic structure of ZnS, ZnSe, ZnTe, and their pseudobinary alloys*, J. E. Bernard and A. Zunger, Phys. Rev. B **36**, 3199 (1987).

[Bhu98] *Photoluminescence and photoconductivity in hydrogen–passivated ZnTe*, S. Bhunia, D. Pal, and D. N. Bose, Semicond. Sci. Tech. **13**, 1434 (1998).

[Bir75] *Heat capacities of ZnS, ZnSe and CdTe below 25 K*, J. A. Birch, J. Phys. C: Solid State Phys. **8**, 2043 (1975).

[Bla62] *Semiconductor Statistics*, J. S. Blakemore, Pergamon Press, Oxford (1962).

[Bon99] *Bond-centered hydrogen in silicon studied by in situ deep-level transient spectroscopy*, K. Bonde Nielsen, B. Bech Nielsen, J. Hansen, E. Andersen, and J. U. Andersen, Phys. Rev. B **60**, 1716 (1999).

[Bon02] *Acceptor state of monoatomic hydrogen in silicon and the role of oxygen*, K. Bonde Nielsen, L. Dobaczewski, S. Søgård, and B. Bech Nielsen, Phys. Rev. B **65**, 075205 (2002).

[Bon03] *Bond-center hydrogen in dilute $Si_{1-x}Ge_x$ alloys: Laplace deep-level transient spectroscopy*, K. Bonde Nielsen, L. Dobaczewski, A. R. Peaker, and N. V. Abrosimov, Phys. Rev. B **68**, 045204 (2003).

[Bor00] *Negative ion formation in the scattering of atoms and ions from dielectric surfaces*, A. G. Borisov and V. A. Esaulov, J. Phys.: Cond. Matter **12**, R177 (2000).

[Bos99] *Steady-state and time-resolved phtoconductivity measurements of minority carrier lifetime in ZnTe*, D. N. Bose, R. K. Ahrenkiel, and S. Bhunia, J. Appl. Phys. **86**, 6599 (1999).

[Bot01] *Computacional study on the CVT of the ZnSe-I_2 material system*, K. Böttcher, H. Hartmann, D. Siche, J. Cryst. Grow. **224**, 195 (2001).

[Bou75] *Luminescence in highly conductive n-type ZnSe*, J. C. Bouley, P. Blanconnier, A. Herman, Ph. Ged, P. Henoc, and J. P. Noblanc, J. Appl. Phys. **46**, 3549 (1975).

[Bra04] *Passivation of Mn acceptors in GaMnAs*, M. S. Brandt, S. T. B. Goennenwein, T. A. Wassner, F. Kohl, A. Lehner, H. Huebl, T. Graf, M. Stutzmann, A. Koeder, W. Schoch, and A. Waag, Appl. Phys. Lett. **84**, 2277 (2004).

[Bra03] *Physics of atoms and molecules*, 2^{nd} edition, B. H. Bransden and C. J. Joachain, Prentice Hall, Harlow (2003).

[Bre31] *Measurement of nuclear spin*, G. Breit and I. I. Rabi, Phys. Rev. **38**, 2082 (1931).

[Bre73] *Anomalous μ^+ Precession in Silicon*, J. H. Brewer, K. M. Crowe, F. N. Gygax, R. F. Johnson, B. D. Patterson, D. G. Fleming, and A. Schenck, Phys. Rev .Lett. **31**, 143 (1973).

[Bre94] *Muon spin rotation/relaxation/resonance*, J. H. Brewer, Encyclopedia of Applied Physics **11**, 23 (1994).

[Bre99] *μSR: an introduction*, J. Brewer and R. Cywinski, in *Muon Science - Muons in Physics, Chemistry and Materials, Proceedings of the Fifty First Scottish Universities Summer School in Physics* (Eds. S L Lee, S H Kilcoyne e R Cywinski), IoP Publishing, Bristol (1999).

[Bud00] *Local vibrational modes of isolated hydrogen in germanium*, M. Budde, B. Bech Nielsen, C. Parks Cheney, N. H. Tolk, and L. C. Feldman, Phys. Rev. Lett. **85**, 2965 (2000).

[Cal84] *A universal trend in the binding energies of deep impurities in semiconductors*, M. J. Caldas, A. Fazzio, and A. Zunger, App. Phys. Lett. **45**, 671 (1984).

[Cel83] *Master–equation approach to muonium depolarization in solids*, M. Celio and P. F. Meier, Phys. Rev. B **28**, 39 (1983).

[Cha83] *Le muon sonde la matière*, J. Chappert and E. Karlsson, La Recherche **141**, 156 (1983).

[Cha94] *Doping in ZnSe, ZnTe, MgSe, and MgTe wide-band-gap semiconductors*, D. J. Chadi, Phys. Rev. Lett. **72**, 534 (1994).

[Che06] *Low specific contact resistance Ti/Au contacts on ZnO*, J.-J. Chen, S. Jang, T. J. Anderson, F. Ren, Y. Li, Hyun-Sik Kim, B. P. Gila, D. P. Norton, and S. J. Pearton, Appl. Phys. Lett. **88**, 122107 (2006).

[Chi83] *Electrical properties of n-type ZnSe:I and ZnSe:I:In single crystals*, D. M. Chiu, J. Phys. D: Appl. Phys. **16**, 2281 (1983).

[Cho93] *Muonium dynamics in Si at high temperatures*, K. H. Chow, R. F. Kiefl, J. W. Schneider, B. Hitti, T. L. Estle, R. L. Lichti, C. Schwab, R. C. DuVarney, S. R. Kreitzman, W. A. MacFarlane, and M. Senba, Phys. Rev. B **47**, 16004 (1993).

[Cho94] *Spin dynamics and electronic structure of muonium and its charged states in silicon and gallium arsenide*, K. H. Chow, PhD Thesis, Department of Physics, University of British Columbia (1994).

[Cho95] *Structure of negatively charged muonium in n-type GaAs*, K. H. Chow, R. F. Kiefl, W. A. MacFarlane, J. W. Schneider, D. W. Cooke, M. Leon, M.

Paciotti, T. L. Estle, B. Hitti, R. L. Lichti, S. F. J. Cox, C. Schwab, E. A. Davis, A. Morrobel-Sosa, and L. Zavieh, Phys. Rev. B **51**, 14762 (1995).

[Cho96] *Diffusion and charge dynamics of negatively charged muonium in n-type GaAs*, K. H. Chow, B. Hitti, R. F. Kiefl, S. R. Dunsinger, R. L. Lichti, and T. L. Estle, Phys. Rev. Lett. **76**, 3790 (1996).

[Cho98] *μSR on Muonium in Semiconductors and Its Relation to Hydrogen*, K. H. Chow, B. Hitti and R. F. Kiefl, in *Identification of Defects in Semiconductors*, edited by M. Stavola, Semiconductors and Semimetals Vol. 51A (Academic Press, San Diego, 1998), pp. 137-207, treatise edited by R. K. Willardson and E. R. Weber.

[Cho01] *Muonium analogue of Hydrogen Passivation: Observation of the Mu^+ - Zn^- Reaction in GaAs*, K. H. Chow, B. Hitti, R. F. Kiefl, R. L. Lichti, T. L. Estle, Phys. Rev. Lett. **87**, 216403 (2001).

[Cle72] *Muonium. III. Precision measurement of the muonium hyperfine-structure interval at strong magnetic field*, W. E. Cleland, J. M. Bailey, M. Eckhause, V. W. Hughes, R. Prepost, J. E. Rothberg, and R. M. Mobley, Phys. Rev. A **5**, 2338 (1972).

[Cle93] *Hydrogen-acceptor pairing in CdTe epitaxial layers grown by OMVPE*, B. Clerjaud, D. Côte, L. Svob, Y. Marfaing, and R. Druilhe, Solid State Comm. **85**, 167 (1993).

[Col68] *High resistivity Hall effect measurements*, D. Colman, Review of Scientific Instruments **39**, 1946 (1968).

[Cor04] *Dependence of the hydrogen spin dynamics on the conductivity type in CdTe as evidenced by its muonium analogue*, V. Corregidor, D. Martín y Marero, J. M. Gil and E. Diéguez, Europhysics Lett. **67**, 247 (2004).

[Cot00] *The commissioning of a spectrometer optimised for radio–frequency measurements at a pulsed muon source*, S.P. Cottrell, S.F.J. Cox, C. A. Scott, and J. S. Lord, Physica B **289-290**, 693 (2000).

[Cot03] *Radio-frequency techniques for muon charge state conversion measurements*, S. P. Cottrell, C. Johnson, S. F. J. Cox, and C. A. Scott, Physica B **326**, 248 (2003).

[Cox86] *Molecular radical models for the muonium centers in solids*, S. F. J. Cox and M. R. C. Symons, Chem. Phys. Lett. **126**, 516 (1986).

[Cox87] *Implanted muon studies in condensed matter science*, S. F. J. Cox, J. Phys. C: Solid State Phys. **20**, 3187 (1987).

[Cox01a] *Experimental Confirmation of the Predicted Shallow Donor Hydrogen State in Zinc Oxide*, S. F. J. Cox, E. A. Davis, S. P. Cottrell, P. J. C. King, J. S. Lord, J. M. Gil, H. V. Alberto, R. C. Vilão, J. Piroto Duarte, N. Ayres de Campos, A. Weidinger, R. L. Lichti, and S. J. C. Irvine, Phys. Rev. Lett. **86**, 2601 (2001).

[Cox01b] *Shallow versus deep hydrogen states in ZnO and HgO*, S. F. J. Cox, E. A. Davis, P. J. C. King, J. M. Gil, H. V. Alberto, R. C. Vilão, J. Piroto Duarte, N. Ayres de Campos, and R. L. Lichti, J. Phys.: Cond. Matter **13**, 9001 (2001).

[Cox03a] *Shallow donor states of hydrogen in II–VI oxide and chalcogenide semiconductors, modelled by muon spectroscopy*, S. F. J. Cox, S. P. Cottrell, P. J. C. King, J. S. Lord, H. V. Alberto, N. Ayres de Campos, J. M. Gil, J. Piroto Duarte, R. C. Vilão, E. A. Davis, D. Ellis, D. Lamb, R. L. Lichti, G. Celebi, and A. Weidinger, in *Physics of Semiconductors 2002*, J. H. Davies and A. R. Long (eds.), Institute of Physics Conference Series **171**, (2003).

[Cox03b] *The shallow-to-deep instability of hydrogen and muonium in II-VI and III-V semiconductors*, S. F. J. Cox, J. Phys.: Cond. Matter **15**, R1727 (2003).

[Cox06a] *Oxide muonics: I. Modelling the electrical activity of hydrogen in semiconducting oxides*, S.F.J. Cox, J.S. Lord, S.P. Cottrell, J.M. Gil, H.V. Alberto, A. Keren, D. Prabhakaran, R. Scheuermann, and A. Stoykov, J. Phys.: Cond. Matter **18**, 1061 (2006).

[Cox06b] *Oxide muonics: II. Modelling the electrical activity of hydrogen in wide-gap and high-permittivity dielectrics*, S. F. J. Cox, J. L. Gavartin, J. S. Lord, S. P. Cottrell, J. M. Gil, H. V. Alberto, J. Piroto Duarte, R. C. Vilão, N. Ayres de Campos, D. J. Keeble, E. A. Davis, M. Charlton, and D. P. Van der Werf, J. Phys.: Cond. Matter **18**, 1079 (2006).

[Cra86] *Mathematics of diffusion*, J. Crank, Clarendon Press, Oxford (1986).

[Dar98] *Recent developments and progress on electrical contacts to CdTe, CdS and ZnSe with special reference to barrier contacts to CdTe*, I. M. Dharmadasa, Prog. Crystal Growth and Charact. **36**, 249 (1998).

[Dav03] *Shallow donor state of hydrogen in indium nitride*, E. A. Davis, S. F. J. Cox, R. L. Lichti and C. G. Van de Walle, Appl. Phys. Lett. **82**, 592 (2003).

[Daw00] *Muonium transitions in n-type gallium nitride*, M. R. Dawdy, R. L. Lichti, S. F. J. Cox, T. L. Head, and C. Schwab, Physica B **289-290**, 546 (2000).

[Dea69] *Pair spectra and "edge emission" in zinc selenide*, P. J. Dean and J. L. Merz, Phys. Rev. **178**, 1310 (1969).

[Dea83] *Ionization energy of the shallow nitrogen acceptor in zinc selenide*, P. J. Dean, W. Stutius, G. F. Neumark, B. J. Fitzpatrick, R. N. Bhargava, Phys. Rev. B **27**, 2419 (1983).

[Des98] *Doping limits in II-VI compounds – challenges, problems and solutions*, U. V. Desnica, Prog. Crystal Growth and Charact. **36**, 291 (1998).

[Dev67] *Transport properties*, S. S. Devlin, in *Physics and Chemistry of II-VI Compounds*, edited by M. Aven and J. S. Prener (North-Holland Publishing Company, Amsterdam, 1967), p. 597.

[Dob04] *Donor level of bond-center hydrogen in germanium*, L.Dobaczewski, K. Bonde Nielsen, N. Zangenberg, B. Bech Nielsen, A. R. Peaker, and V. P. Markevich, Phys. Rev. B **69**, 245207 (2004).

[Dua03] *Estudo da difusão do muónio/hidrogénio em HgO utilizando técnicas de muões*, J. P. Piroto Duarte, Dissertação de Mestrado em Física, especialização em Física Experimental, Faculdade de Ciências e Tecnologia da Universidade de Coimbra (2003).

[Dua06] *Muonium diffusion dynamics in mercury oxide*, J. Piroto Duarte, J. M. Gil, H. V. Alberto, R. C. Vilão, A. Weidinger, N. Ayres de Campos, S. F. J. Cox, J. S. Lord, S. P. Cottrell, and E. A. Davis, Physica B **374-375**, 423 (2006).

[Dub70] *Alloyed ohmic contact to ZnSe*, K. K. Dubenskii, A. V. Rumyantseva and Yu. S. Ryzhkin, Instr. and Exper. Tech. (Pribory i Tekhnika Éksperimenta) **1**, 264 (1970).

[Eat99] *Muon production: past, present and future*, G. H. Eaton and S. H. Kilcoyne, in *Muon Science - Muons in Physics, Chemistry and Materials, Proceedings of the Fifty First Scottish Universities Summer School in Physics* , edited by S. L. Lee, S. H. Kilcoyne and R. Cywinski (IoP Publishing, Bristol, 1999), pp. 11-37.

[Edd06] *Interface bonding of a ferromagnetic/semiconductor junction: a photoemission study of Fe/ZnSe(001)*, M. Eddrief, M. Marangolo, V. H. Etgens, S. Ustaze, F. Sirotti, M. Mulazzi, G. Panaccione, D. H. Mosca, B. Lépine, and P. Schieffer, Phys. Rev. B **73**, 115315 (2006).

[EMU04] *The EMU user guide*, ISIS Facility, Rutherford Appleton Laboratory, Council for the Central Laboratory of the Research Councils (s.d. - 2004?).

[Esh03] *Excited muonium state in CdS*, D. G. Eshchenko, V. Storchak, S. P. Cottrell, and S. F. J. Cox, Phys. Rev. B **68**, 073201 (2003).

[Est87] *Bond-centered hydrogen or muonium in diamond: the explanation for anomalous muonium and an example of metastability*, T. L. Estle, S. Estreicher, and D. S. Marynick, Phys. Rev. Lett. **58**, 1547 (1987).

[Est95] *Hydrogen-related defects in crystalline semiconductors: a theorist's perspective*, S. K. Estreicher, Materials Science and Engineering **R14**, 319 (1995).

[Fel04] *Effect of lattice ionicity on hydrogen activity in IIVI materials containing isoelectronic oxygen impurities*, M. Felici, V. Cesari, A. Polimeni, A. Frova, M. Capizzi, Y.D. Choi, B. O, Y.-M. Yu, Y. Nabetani, Y. Ito, T. Okuno, T. Kato, T. Matsumoto, T. Hirai, I.K. Sou and W.K. Ge, IEE Proc.–Optoelectron. **151**, 465 (2004).

[Fer57] *Paschen–Back effect as a means of detecting muonium*, R. A. Ferrell and F. Chaos, Phys. Rev., **107**, 1322 (1957).

[Fer60] *Magnetic quenching of hyperfine depolarization of positive muons*, R. A. Ferrell, Y. C. Lee, and M. K. Pal, Phys. Rev., **118**, 317 (1960).

[Fle82] *μ^+ charge exchange and muonium formation in low–pressure gases*, D. G. Fleming, R. J. Mikula, and D. M. Garner, Phys. Rev. A, **26**, 2527 (1982).

[Fuk98] *Evidence for Oscillation of Atmospheric Neutrinos*, Y. Fukuda *et. al.* (Super-Kamiokande Collaboration), Phys. Rev. Lett., **81**, 1562 (1998).

[Gav03] *Polycrystalline zinc selenide for IR optical applications*, E. M. Gavrushchuk, Inorganic Materials **39**, 883 (2003).

[Geb02] *Identification and quantitative evaluation of compensating Zn-vacancy-donor complexes in ZnSe by positron annihilation*, J. Gebauer, R. Krause-Rehberg, M. Prokesch, and K. Irmscher, Phys. Rev. B **66**, 115206 (2002).

[Gha04] *Muonium formation as a probe of radiation chemistry in sub- and supercritical carbon dioxide*, K. Ghandi, M. D. Bridges, D. J. Arseneau, and D. G. Fleming, J. Phys. Chem. A **108**, 11613 (2004).

[Gil99] *Novel muonium state in CdS*, J. M. Gil, H. V. Alberto, R. C. Vilão, J. Piroto Duarte, P. J. Mendes, L. P. Ferreira, N. Ayres de Campos, A. Weidinger, J. Krauser, Ch. Niedermayer, and S. F. J. Cox, Phys. Rev. Lett. **83**, 5294 (1999).

[Gil00] *Shallow level muonium centre in CdS*, J. M. Gil, H. V. Alberto, R. C. Vilão, J. Piroto Duarte, P. J. Mendes, L. P. Ferreira, N. Ayres de Campos, A. Weidinger, J. Krauser, Ch. Niedermayer, and S. F. J. Cox, Physica B **289/290**, 564 (2000).

[Gil01] *Shallow donor muonium states in II-VI semiconductor compounds*, J. M. Gil, H. V. Alberto, R. C. Vilão, J. Piroto Duarte, N. Ayres de Campos, A. Weidinger, J. Krauser, E. A. Davis, S. P. Cottrell and S. F. J. Cox, Phys. Rev. B **64**, 075205 (2001).

[Gor87] *Electron-paramagnetic-resonance of Si-n centers in silicon*, Y. V. Gorelkinskii and N. N. Nevinnyi, Sov. Technol. Phys. Lett. **13**, 45 (1987).

[Gos03] *Theory of hydrogen in diamond*, J. P. Goss, J. Phys.: Condens. Matter **15**, R551 (2003).

[Gun97] *II–VI Blue–Green light emitters: device physics and epitaxial growth*, edited by R. L. Gunshor and A. V. Nurmikko, Semiconductors and Semimetals Vol. 44 (Academic Press, San Diego, 1999), treatise edited by R. K. Willardson, A. C. Beer and E. R. Weber.

[Hal80] *Acceptor complexes in germanium: systems with tunneling hydrogen*, E. E. Haller, B. Jos, and L. M. Falicov, Phys. Rev. B **21**, 4729 (1980).

[Har94] *ZnSe single crystal growth by the method of dissociative sublimation*, H. Hartmann and D. Siche, J. Cryst. Grow. **138**, 260 (1994).

[Has06] *Density functional study of* $Zn_{1-x}Mg_xSe_yTe_{1-y}$, F. E. H. Hassan, S. J. Hashemifar, and H. Akbarzadeh, Phys. Rev. B **73**, 195202 (2006).

[Hei59] *Electronic processes in zinc oxide*, G. Heiland, E. Mollwo, and F. Stöckmann, Solid State Physics **8**, 191 (1959).

[Hem73] *Measurement of high resistivity semiconductors using the van der Pauw method*, P. M. Hemenger, Rev. Sci. Instrum. **44**, 698 (1973).

[Hen71] *Self-diffusion of Zn and Se in ZnSe*, M. M. Henneberg and D. A. Stevenson, Phys. Stat. Sol. (b) **48**, 255 (1971).

[Her01] *Energy levels of isolated interstitial hydrogen in silicon*, C. Herring, N. M. Johnson, and C. G. Van de Walle, Phys. Rev. B **64**, 125209 (2001).

[Her06] *Hydrogen and muonium in diamond: a path–integral molecular dynamics simulation*, C. P. Herrero, R. Ramírez, and E. R. Hernández, Phys. Rev. B **73**, 245211 (2006).

[Heu92] *Reduced incorporation of unintentional impurities and intrisic defects in ZnSe and ZnS grown by MOVPE*, M. Heuken, J. Söllner, F. E. G. Guimarães, K. Marquardt, and K. Heime, J. Cryst. Grow. **117**, 336 (1992).

[Hit99] *Dynamics of negative muonium in n-type silicon*, B. Hitti, S. R. Kreitzmann, T. L. Estle, E. S. Bates, M. R. Dawdy, T. L. Head, and R. L. Lichti, Phys. Rev. B **59**, 4918 (1999).

[Ho95] *Hydrogen passivation in nitrogen and chlorine-doped ZnSe films grown by gas source molecular beam epitaxy*, E. Ho, P. A. Fisher, J. L. House, G. S. Petrich, L. A. Kolodziejski, J. Walker and N. M. Johnson, Appl. Phys. Lett. **66**, 1062 (1995).

[Ho97] *Gaseous source UHV epitaxy technologies for wide bandgap II–VI semiconductors*, E. Ho and L. A. Kolodziejski, in *II-VI blue-green light emitters: device physics and epitaxial growth*, edited by R. L. Gunshor and A. V. Nurmikko, Semiconductors and Semimetals Vol. 44 (Academic Press, San Diego, 1997), pp. 83-119, treatise edited by R. K. Willardson, A. C. Beer and E. R. Weber.

[Hof02] *Hydrogen: A Relevant Shallow Donor in Zinc Oxide*, D. M. Hofmann, A. Hofstaetter, F. Leiter, H. Zhou, F. Henecker, and B. K. Meyer, S. B. Orlinskii, J. Schmidt, P. G. Baranov, Phys. Rev. Lett. **88**, 045504 (2002).

[Hol91] *Deep state of hydrogen in crystalline silicon: evidence for metastability*, B. Holm, K. Bonde Nielsen, and B. Bech Nielsen, Phys. Rev. Lett. **66**, 2360 (1991).

[Hol03] *Two-photon photoconductive terahertz generation in ZnSe*, J. F. Holzman and A. Y. Elezzabi, Appl. Phys. Lett. **83**, 2967 (2003).

[Hu06] *Transparent indium zinc oxide ohmic contact to phosphor-doped n-type zinc oxide*, G. Hu, B. Kumar, H. Gong, E. F. Chor, and P. Wu, Appl. Phys. Lett. **88**, 101901 (2006).

[Hug60] *Formation of muonium and observation of its Larmor precession*, V. W. Hughes, D. W. McColm, K. Ziock, and R. Prepost, Phys. Rev. Lett. **5**, 63 (1960).

[Hug70a] *Muonium. I. Muonium formation and Larmor precession*, V. W. Hughes, D. W. McColm, K. Ziock, and R. Prepost, Phys. Rev. A **1**, 595 (1970).

[Hug70b] *Errata: Muonium. I. Muonium formation and Larmor precession*, V. W. Hughes, D. W. McColm, K. Ziock, and R. Prepost, Phys. Rev. A **2**, 551 (1970).

[Hug00] *Various researches in physics*, V. W. Hughes, Ann. Rev. Nucl. Part. Sci. **50**, i (2000).

[Irm01] *Spectroscopic evidence and control of compensating native defects in doped ZnSe*, K. Irmscher and M. Prokesch, Materials Science and Engineering B **80**, 168 (2001).

[ISI04] *The EMU User Guide*, ISIS Facility, Rutherford Appleton Laboratory, Council for the Research Laboratory of the Research Councils, Chilton, Didcot, United Kingdom (2004).

[ISI07] page of the ISIS Pulsed Muon Facility, Rutherford Appleton Laboratory, United Kingdom, in the Internet: http://www.isis.rl.ac.uk/muons (as in January/2007).

[Iss88] *The change in the photoluminescence spectra of Cu–doped ZnSe single crystals caused by heat treatment*, M. Isshiki and K. Masumoto, J. Phys. C: Solid State Phys. **21**, 2771 (1988).

[Iva68] *Theory of the muonium mechanism of depolarization of μ^+ mesons in media*, I. G. Ivanter and V. P. Smilga, Soviet Physics JETP **27**, 301 (1968).

[Iva71] *The theory of μ^+-meson depolarization with allowance for the process of charge exchange or formation of unstable chemical species*, I. G. Ivanter and V. P. Smilga, Soviet Physics JETP **33**, 1070 (1971).

[Jon94] *Experiment to demonstrate diffusion doping*, E. D. Jones, Am. J. Phys. **63**, 66 (1994).

[Jon04] *Radio frequency muon spin resonance: user guide*, version 0.2, C. Johnson, S. P. Cottrell, *et al.*, ISIS Facility, Rutherford Appleton Laboratory (s.d. 2004?).

[Jun99] *Aspects of fundamental muon physics*, K. P. Jungmann, in *Muon Science - Muons in Physics, Chemistry and Materials, Proceedings of the Fifty First Scottish Universities Summer School in Physics* , edited by S. L. Lee, S. H. Kilcoyne and R. Cywinski (IoP Publishing, Bristol, 1999), pp. 405-461.

[Kad07] *An era ended at KEK–MSL*, R. Kadono, International Society for μSR Spectroscopy Newsletter **5**, 4 (2007).

[Kam93] *Origin of the low doping efficiency of nitrogen acceptors in ZnSe grown by metalorganic chemical vapor deposition*, A. Kamata, H. Mitsuhashi, and H. Fujita, Appl. Phys. Lett. **63**, 3353 (1993).

[Kan06] *ITO/Ti/Au Ohmic contacts on n-type ZnO*, B. S. Kang, J. J. Chen, F. Ren, Y. Li, H.-S. Kim, D. P. Norton, and S. J. Pearton, Appl. Phys. Lett. **88**, 182101 (2006).

[Kau74] *Mechanism of formation of ohmic contacts to ZnSe, ZnS and mixed crystals ZnS_xSe_{1-x}*, R. Gilbert Kaufman and Peter Dowbor, J. Appl. Phys. **45**, 4487 (1974).

[KEK07] page of Muon Science Laboratory, KEK, Japan, in the Internet: http://msl-www.kek.jp (as in January/2007).

[Kie86] *Muonium centers in the cuprous halides*, R. F. Kiefl, W. Odermatt, Hp. Baumeler, J. Felber, H. Keller, W. Kündig, P. F. Meier, B. D. Patterson, J. W. Schneider, K. W. Blazey, T. L. Estle, C. Schwab, Phys. Rev. B **34**, 1474 (1986).

[Kie88] *SI-29 hyperfine structure of anomalous muonium in silicon - proof of the bond–centered model*, R. F. Kiefl, M. Celio, T. L. Estle, S. R. Kreitzman, G. M. Luke, T. M. Riseman, and E. J. Ansaldo, Phys. Rev. Lett. **60**, 224 (1988).

[Kil02] *n-type doping of oxides by hydrogen*, Ç. Kiliç and A. Zunger, Appl. Phys. Lett. **81**, 73 (2002).

[Kil03] *n-type doping and passivation of $CuInSe_2$ and $CuGaSe_2$ by hydrogen*, Ç. Kiliç and A. Zunger, Phys. Rev. B **68**, 075201 (2003).

[Kim93] S. L. Young-Dong Kim, S. L. Cooper, M. V. Klein, and R. T. Jonker, Appl. Phys. Lett. **62**, 2387 (1993).

[Kli86] *The quantized Hall effect*, K. v. Klitzing, Rev. Mod. Phys. **58**, 519 (1986).

[Kli05] *Terahertz modulation of the blue photoluminescence in ZnSe*, M. A. J. Klik, T. Gregorkiewicz, I. N. Yassievich, V. Yu. Ivanov, and M. Godlewski, Phys. Rev. B **72**, 125205 (2005).

[Kre90] *RF resonance techniques for continuous muon beams*, S. R. Kreitzman, Hyp. Int. **65**, 1055 (1990).

[Kre94] *A microwave μSR spectrometer*, S. R. Kreitzman, T. L. Estle, B. Hitti, J. W. Schneider, K. H. Chow, and R. L. Lichti, Hyp. Int. **87**, 1063 (1994).

[Kre95] *Muon-spin-resonance study of muonium dynamics in Si and its relevance to hydrogen*, S. R. Kreitzman, B. Hitti, R. L. Lichti, T. L. Estle, K. H. Chow, Phys. Rev. B **51**, 13117 (1995).

[Krö56] *Nature of an Ohmic Metal-Semiconductor Contact*, F. A. Kröger, G. Diemer, and H. A. Klasens, Phys. Rev. **103**, 279 (1956).

[Kua87] *First observation of the negative muonium ion produced by electron capture in a beam-foil experiment*, Y. Kuang, K.-P. Arnold, F. Chmely, M. Eckhause, V. W. Hughes, J. R. Kane, S. Kettell, D.-H. Kim, K. Kumar, D. C. Lu, B. Ni, B. Matthias, H. Orth, G. zu Putlitz, H. R. Schaefer, P. A. Souder, and K. Woodle, Phys. Rev. A **35**, 3172 (1987).

[Kua89] *Formation of negative muonium ion and charge-exchange processes for positive muons passing through thin metal foils*, Y. Kuang, K.-P. Arnold, F. Chmely, M. Eckhause, V. W. Hughes, J. R. Kane, S. Kettell, D.-H. Kim, K. Kumar, D. C. Lu, B. Matthias, B. Ni, H. Orth, G. zu Putlitz, H. R. Schaefer, P. A. Souder, and K. Woodle, Phys. Rev. A **39**, 6109 (1989).

[Lak91] *Role of native defects in wide–band–gap semiconductors*, D. B. Laks, C. G. Van de Walle, G. F. Neumark, and S. T. Pantelides, Phys. Rev. Lett. **66**, 648 (1991).

[Lak92] *Native defects and self–compensation in ZnSe*, D. B. Laks, C. G. Van de Walle, G. F. Neumark, P. E. Blöchl, and S. T. Pantelides, Phys. Rev. B **45**, 10965 (1992).

[Lan96] *Quantum Mechanics II*, R. H. Landau, John Wiley & Sons, Inc., New York (1996).

[Lau99] *Nobel lecture: fractional quantization*, R. B. Laughlin, Rev. Mod. Phys. **71**, 863 (1999).

[Lav02] *Hydrogen-related defects in ZnO studied by infrared absorption spectroscopy*, E. V. Lavrov, J. Weber, F. Börrnert, C. G. Van de Walle, and R. Helbig, Phys. Rev. B **66**, 165205 (2002).

[Led82] *On the position of energy levels related to transition–metal impurities in III–V semiconductors*, L.-Å. Ledebo and B. K. Ridley, J. Phys. C: Solid State Phys. **15**, L961 (1982).

[Leo94] *Techniques for nuclear and particle physics experiments*, 2nd edition, W. R. Leo, Springer-Verlag, New York (1994).

[Lic99a] *Dynamics of muonium diffusion, site changes, and charge-state transitions*, R. L. Lichti, in *Hydrogen in semiconductors II*, edited by N. Nickel, Semiconductors and Semimetals Vol. 61 (Academic Press, San Diego, 1999), treatise edited by R. K. Willardson and E. R. Weber.

[Lic03] *Sites and dynamics for muonium in III-V semiconductors*, R. L. Lichti, AIP Conf. Proc. **671**, 55 (2003).

[Lic04] *Hyperfine spectroscopy of muonium in 4H and 6H silicon carbide*, R. L. Lichti, W. A. Nussbaum, K. H. Chow, Phys. Rev. B **70**, 165204 (2004).

[Lic06] *Location of the H[+/-] level: Experimental limits for muonium*, R. L. Lichti, K. H. Chow, J. M. Gil, D. L. Stripe, R. C. Vilão, and S. F. J. Cox, Physica B **376-377**, 587 (2006).

[Liu99] *High Precision Measurements of the Ground State Hyperfine Structure Interval of Muonium and of the Muon Magnetic Moment*, W. Liu, M. G. Boshier, S. Dhawan, O. van Dyck, P. Egan, X. Fei, M. Grosse Perdekamp, V. W. Hughes, M. Janousch, K. Jungmann, D. Kawall, F. G. Mariam, C. Pillai, R. Prigl, G. zu Putlitz, I. Reinhard, W. Schwarz, P. A. Thompson, and K. A. Woodle, Phys. Rev. Lett. **82**, 711 (1999).

[Lor01] *Probing the shallow-donor muonium wave function in ZnO and CdS via transferred hyperfine interactions*, J.S. Lord, S.P. Cottrell, P.J.C. King, H.V. Alberto, N. Ayres de Campos, J.M. Gil, J. Piroto Duarte, R.C. Vilão, R.L. Lichti, S.K.L. Sjue, B.A. Bailey, A. Weidinger, E.A. Davis, and S.F.J. Cox, Physica B **308-310**, 920 (2001).

[Lor04] *Double-resonance determination of electron g-factors in muonium shallow-donor states*, J.S. Lord, S.F.J. Cox, H.V. Alberto, J. Piroto Duarte, and R.C. Vilão, J. Phys.: Cond. Matt. **16**, S4707 (2004).

[Lor06] *g-Sign determination with circularly polarised RF fields*, J.S. Lord, A. Keren, R.C. Vilão, Physica B **374-375**, 475 (2006).

[Lue03] *Observation of the Conduction Electron Spin Polarization in the Ag Spacer of a Fe/Ag/Fe Trilayer*, H. Luetkens, J. Korecki, E. Morenzoni, T. Prokscha, M. Birke, H. Glückler, R. Khasanov, H.-H. Klauss, T. Ślezak, A. Suter, E.M. Forgan, Ch. Niedermayer, and F. J. Litterst, Phys. Rev. Lett. **91**, 017204 (2003).

[Lug05a] *Charge exchange in 330 keV H^+ scattering off clean and AlF_3-covered Al(111) surfaces I. Experimental study*, J. O. Lugo, E. C. Goldberg, E. A. Sánchez, and O. Grizzi, Phys. Rev. B **72**, 035432 (2005).

[Lug05b] *Charge exchange in 330 keV H^+ scattering off clean and AlF_3-covered Al(111) surfaces II. Theoretical study*, J. O. Lugo, E. C. Goldberg, E. A. Sánchez, and O. Grizzi, Phys. Rev. B **72**, 035433 (2005).

[Mad82] *Landolt–Börnstein: Numerical data and functional relationships in Science and Technology, New Series* (Editor in Chief K.–H. Hellwege), Vol. 17: *Semiconductors* (edited by O. Madelung, M. Schulz and H. Weiss), subvolume b: *Physics of II–VI and I–VII Compounds, Semimagnetic Semiconductors* (edited by O. Madelung), Springer-Verlag, Berlin, 1982.

[Mag79] *Optical identification of substitutional acceptors in refined ZnTe*, Phys. Stat. Solidi (b) **94**, 627 (1979).

[Mai00] *Origin of Surface Conductivity in Diamond*, F. Maier, M. Riedel, B. Mantel, J. Ristein, and L. Ley, Phys. Rev. Lett. **85**, 3472 (2000).

[Mal88] *Polarization of luminescence of copper centers in ZnSe*, M. A. Maliński and F. Firszt, Acta Physica Polonica **A73**, 263 (1988).

[Mam99] *Shallow acceptor centres in silicon studied by means of spin rotation of negative muons*, T. N. Mamedov, I. L. Chaplygin, V. N. Duginov, V. N. Gorelkin, D. Herlach, J. Major, A. V. Stoykov, M. Schefzik, and U. Zimmermann, J. Phys. Cond. Matter **11**, 2849 (1999).

[Mam06] *Behaviour of shallow acceptor impurities in uniaxially stressed silicon and in synthetic diamon studied by μ^-SR*, T. N. Mamedov, D. Andreika, A. S. Baturin, D. Herlach, V. N. Gorelkin, K. I. Gritsaj, V. G. Ralchenko, A. V. Stoykov, V. A. Zhukov, and U. Zimmermann, Physica B **374-375**, 390 (2006).

[McC99] *Hydrogen in III–V and II–VI semiconductors*, M. D. McCluskey and E. E. Haller, in *Hydrogen in Semiconductors II*, edited by N. Nickel, Semiconductors and Semimetals Vol. 61 (Academic Press, San Diego, 1999), pp. 373-440, treatise edited by R. K. Willardson and E. R. Weber.

[McC02] *Infrared spectroscopy of hydrogen in ZnO*, M. D. McCluskey, S. J. Jokela, K. K. Zhuravlev, P. J. Simpson, and K. G. Lynn, Appl. Phys. Lett.**81**, 3807 (2002).

[Mei82] *Spin dynamics of transitions between muon states*, P. F. Meier, Phys. Rev. A **25**, 1287 (1982).

[Mil72] *Heterojunctions and metal-semiconductor junctions*, A. G. Milnes and D. L. Feucht, Academic Press, New York (1972).

[Mit49] *Electric Circuits: a first course in circuit analysis for electrical engineers*, by members of the staff of the Department of Electrical Engineering, Massachussets Institute of Technology, John Wiley & Sons, Inc., New York (1949), pp. 143-144.

[Miy06] *Status of J-PARC muon science facility at the year of 2005*, Y. Miyake, K. Nishiyama, N. Kawamura, S. Makimura, P. Strasser, K. Shimomura, J. L. Beveridge, R. Kadono, K. Fukuchi, N. Sato, K. Ueno, W. Higemoto, K. Ishida, T. Matsuzaki, I. Watanabe, Y. Matsuda, M. Iwasaki, S. N. Nakamura, J. Doornbos, and K. Nagamine, Physica B **374–375**, 484 (2006).

[Mol54] *Die Wirkung von Wasserstoff auf die Leitfähigkeit und Lumineszenz von Zinkoxydkristallen*, E. Mollwo, Zeitschrift für Physik, **138**, 478 (1954).

[Mon05] *Near-band-edge slow luminescence in nominally undoped bulk ZnO*, T. Monteiro, A. J. Neves, M. C. Carmo, M. J. Soares, M. Peres, J. Wang, E. Alves, E. Rita, and U. Wahl, J. App. Phys. **98**, 013502 (2005).

[Mor86] *Muonium to diamagnetic muon conversion in KCl and NaCl revealed by time–differential muon spin resonance*, Y. Morozumi, K. Nishiyama, and K. Nagamine, Phys. Lett. A **118**, 93 (1986).

[Mor94] *Temperature dependence of the proton hyperfine interaction in HC_{60} and the proton-muon hyperfine anomaly*, J. R. Morton, F. Negri, and K. F. Preston, Phys. Rev. B **49**, 12446 (1994).

[Mos83] *Muon trapping at monovacancies in iron*, A. Möslang, H. Graf, G. Balzer, E. Recknagel, A. Weidinger, Th. Wichert, R. I. Grynszpan, Phys. Rev. B **27**, 2674 (1983).

[Mye92] *Hydrogen interactions with defects in crystalline solids*, S. M. Myers, M. I. Baskes, H. K. Birnbaum, J. W. Corbett, G. G. DeLeo, S. K. Estreicher, E. E. Haller, P. Jena, N. M. Johnson, R. Kirchheim, S. J. Pearton, and M. J. Stavola, Rev. Mod. Phys. **64**, 559 (1992).

[Myn03] *Hydrogen in materials and vacuum systems*, edited by G. R. Myneni and S. Chattopadhyay, AIP Conference Proceedings **671** (Academic Press, San Diego, 1999).

[Nag99] K. Nagamine, *Exotic applications of muons: from fusion to the life sciences* in *Muon Science - Muons in Physics, Chemistry and Materials, Proceedings of the Fifty First Scottish Universities Summer School in Physics* (Eds. S. L. Lee, S. H. Kilcoyne e R. Cywinski), IoP Publishing, Bristol (1999)

[Nak97] *Characterization of ZnSe homo-interface grown by MBE*, F. Nakanishi, H. Doi, T. Yamada, T. Matsuoka, S. Nishine, K. Matsumoto, T. Shirakawa, Appl. Surf. Sci. **117/118**, 489 (1997).

[Nea97] *Semiconductor physics and devices: basic principles*, 2^{nd} edition, D. A. Neamen, Irwrin, Chicago (1997).

[Neu89] *Achievement of well conducting wide–band–gap semiconductors: role of solubility and noneuilibrium impurity incorporation*, G. F. Neumark, Phys. Rev. Lett. **62**, 9425 (1989).

[Neu95] *Hydrogen in GaN: novel aspects of a common impurity*, J. Neugebauer and C. G. Van de Walle, Phys. Rev. Lett. **75**, 4452 (1995).

[Nic98] *Hydrogen in Semiconductors and Metals*, edited by N. Nickel, W. B. Jackson, R. C. Bowman and R. G. Leisure, Materials Research Society: Symposium Proceedings Vol. 513 (Materials Research Society, Warrendale, 1998).

[Nic99a] *Hydrogen in Semiconductors II*, edited by N. Nickel, Semiconductors and Semimetals Vol. 61 (Academic Press, San Diego, 1999), treatise edited by R. K. Willardson and E. R. Weber.

[Nic99b] *Introduction to Hydrogen in Semiconductors II*, N. Nickel, in *Hydrogen in Semiconductors II*, edited by N. Nickel, Semiconductors and Semimetals Vol. 61 (Academic Press, San Diego, 1999), pp. 1-11, treatise edited by R. K. Willardson and E. R. Weber.

[Nis85] *Observation of "decoupled" diamagnetic muon states in alkali halides by muon spin resonance*, K. Nishiyama, Y. Morozumi, T. Suzuki, and K. Nagamine, Phys. Lett. **111**, 369 (1985).

[Nis06] *Hall effect measurements*, www.eeel.nist.gov/812/hall.html (March/2006).

[Nos63] *Depolarization of μ^+ mesons in solids*, V. G. Nosov and I. V. Yakovleva, Soviet Physics JETP **16**, 1236 (1963).

[Nur97] *II–VI diode lasers: a current view of device performance and issues*, A. V. Nurmikko and A. Ishibashi, in *II-VI blue-green light emitters: device physics and epitaxial growth*, edited by R. L. Gunshor and A. V. Nurmikko, Semiconductors and Semimetals Vol. 44 (Academic Press, San Diego, 1997), pp. 227–270, treatise edited by R. K. Willardson, A. C. Beer and E. R. Weber.

[Ohk91] *Doping of nitrogen acceptors into ZnSe using a radical beam during MBE growth*, K. Ohkawa, T. Karasawa, and T. Mitsuyu, J. Cryst. Grow. **111**, 797 (1991).

[Oza06] *Significant enhancement of ferromagnetism in $Zn_{1-x}Cr_xTe$ doped with iodine as an n-type dopant*, N. Ozaki, N. Nishizawa, S. Marcet, S. Kuroda, O. Eryu, and K. Takita, Phys. Rev. Lett. **97**, 037201 (2006).

[Pan78] *Photoluminescence recovery in rehydrogenated amorphous silicon*, J. I. Pankove, App. Phys. Lett. **32**, 812 (1978).

[Pan83] *Neutralization of shallow acceptor levels in silicon by atomic hydrogen*, J. I. Pankove, D. E. Carlson, J. E. Berkeyheiser, and R. O. Wance, Phys. Rev. Lett. **51**, 2224 (1983).

[Pan91] *Hydrogen in Semiconductors I*, edited by J. I. Pankove and N. M. Johnson, Semiconductors and Semimetals Vol. 34 (Academic Press, San Diego, 1991), treatise edited by R. K. Willardson and E. R. Weber.

[Par72] *Yellow–light–emitting ZnSe diode*, Y. S. Park, C. R. Geesner, and B. K. Shin, App. Phys. Lett. **21**, 567 (1972).

[Par90] *p-type ZnSe by nitrogen atom beam doping during molecular beam epitaxial growth*, R. M. Park, M. B. Troffer, C. M. Rouleau, J. M. DePuydt, and M. A. Haase App. Phys. Lett. **57**, 2127 (1990).

[Par99] *Ohmic contacts to n-type and p-type ZnSe*, M. R. Park, W. A. Anderson, M. Jeon, and H. Luo, Solid-State Electronics **43**, 113 (1999).

[Pas06] *The absolute neutrino mass scale, neutrino mass spectrum, Majorana CP-violation and neutrinoless double-beta decay*, S. Pascoli, S. T. Petcov, and T. Schwetz, Nuclear Physics B **734**, 24 (2006).

[Pat78] *Anomalous muonium in silicon*, B. D. Patterson, A. Hintermann, W. Kündig, P. F. Meier, F. Waldner, H. Graf, E. Recknagel, A. Weidinger, and Th. Wichert, Phys. Rev. Lett. **40**, 1347 (1978).

[Pat88] *Muonium states in semiconductors*, B. D. Patterson, Rev. Mod. Phys. **60**, 69 (1988).

[Pau76] *Doping, Schottky barrier and p–n junction formation in amorphous germanium and silicon by rf sputtering* , W. Paul, A. J. Lewis, G. A. N. Connell, and T. D. Moustakas, Solid-State Commun. **20**, 969 (1976).

[Pea94] *Hydrogen in Compound Semiconductors*, edited by S. J. Pearton, Materials Science Forum **148–149** (Trans Tech Publications, Aedermannsdorf, 1994).

[Pel98] *Neutralization of nitrogen acceptors in MBE-grown ZnTe by intentional diffusion of hydrogen*, H. Pelletier, B. Theys, A. Lusson, J. Chevallier, and N. Magnéa, J. Cryst. Grow. **184/185**, 419 (1998).

[Per78] *Radiolysis effects in muonium chemistry*, P. W. Percival, Chem. Phys. **32**, 353 (1978).

[Per82] *Spin depolarization in muonium by hydrated electrons*, P. W. Percival, J.-C. Brodovitch, and K. E. Newman, Chem. Phys. Lett. **91**, 1 (1982).

[Pif76] *A high stopping density μ^+ beam*, A. E. Pifer, T. Bowen, and K. R. Kendall, Nuc. Inst. Methods **135**, 39 (1976).

[Pla00] *Characterization of defects in (ZnMg)Se compounds by positron annihilation and photoluminescence*, F. Plazaola, K. Saarinen, L. Dobrzynski, H. Reniewicz, F. Firszt, J. Szatkowski, H. Meczynska, S. Legowski, and S. Chabik, J. Appl. Phys. **88**, 1325 (2000).

[Pla03] *Defect characterization of ZnBeSe solid solutions by means of positron annihilation and photoluminescence techniques*, F. Plazaola, J. Flyktman, K. Saarinen, L. Dobrzynski, F. Firszt, S. Legowski, H. Meczynska, W. Paszkowicz, H. Reniewicz, J. Appl. Phys. **94**, 1647 (2003).

[Pol04] *Temperature dependence and bowing of the abndgap in $ZnSe_{1-x}O_x$*, A. Polimeni, M. Capizzi, Y. Nabetani, Y. Ito, T. Okuno, T. Matsumoto, and T. Hirai, Appl. Phys. Lett. **84**, 3304 (2004).

[Pon58] *Mesonium and antimesonium*, B. Pontecorvo, Sov. Phys. JETP **6**, 429 (1958).

[Pra05] *Surface dynamics of a thin polystyrene film probed by low-energy muons*, F. L. Pratt, T. Lancaster, M. L. Brooks, S. J. Blundell, T. Prokscha, E. Morenzoni, A. Suter, H. Luetkens, R. Khasanov, R. Scheuermann, U. Zimmermann, K. Shinotsuka and H. E. Assender, Phys. Rev. B **72**, 121401 (2005).

[Pro00] *Reversible conductivity control and quantitative identification of compensating defects in ZnSe bulk crystals*, M. Prokesch, K. Irmscher, J. Gebauer, and R. Krause-Rehberg, J. Cryst. Grow. **214/215**, 988 (2000).

[Pro02] *Net acceptor concentration in ZnSe:Sb grown from vapor phase*, M. Prokesch, K. Irmscher, U. Rinas, H. Makino, and T. Yao, J. Cryst. Grow. **242**, 155 (2002).

[PSI07] page of the Laboratory for Muon Spin Spectroscopy, Paul Scherrer Institut, Switzerland, in the Internet: http://lmu.web.psi.ch/ (as in January/2007).

[Ray78] *The defect structure of pure and doped ZnSe*, A. K. Ray and F. A. Kröger, J. Electrochem. Soc. **125**, 1348 (1978).

[Rei65] *Fundamentals of statistical and thermal physics*, F. Reif, McGraw-Hill Inc., Singapore (1965).

[Rob03] *Doping and hydrogen in wide gap oxides*, J. Robertson and P. W. Peacock, Thin Solid Films **445**, 155 (2003).

[Rod95] *Isotope and temperature effects on the hyperfine interaction of atomic hydrogen in liquid water and in ice*, E. Roduner, P. W. Percival, P. Han, and D. Bartels, J. Chem Phys. **102**, 5989 (1995).

[Ron99] *Energy Loss of Low Energy Protons on LiF(100): Surface Excitation and H^- Mediated Electron Emission*, P. Roncin, J. Villette, J. P. Atanas, and H. Khemliche, Phys. Rev. Lett. **83**, 864 (1999).

[Sah83] *Deactivation of the boron acceptor in silicon by hydrogen*, C.–T. Sah, J. Y.–C. Sun, and J. J.–T. Tzou, App. Phys. Lett. **43**, 204 (1983).

[Sch85] *Muon Spin Rotation Spectroscopy: Principles and Applications in Solid State Physics*, A. Schenck, Adam Hilger Ltd, Bristol (1985).

[Sch86] *Muonium states in zincblende-structured compounds* J. W. Schneider, Hp. Baumeler, H. Keller, R. F. Kiefl, W. Kündig, W. Odermatt, B. D. Patterson, T. L. Estle, S. P. Rudaz, K. W. Blasey, C. Schwab, Hyperfine Interact. **32**, 607 (1986).

[Sch90] *Resolved nuclear hyperfine structure of muonium in CuCl by means of muon level-crossing resonance*, J. W. Schneider, H. Keller, W. Odermatt, B. Pümpin, I. M. Savic, H. Simmler, S. A. Dodds, T. L. Estle, R. C. DuVarney, K. Chow, R. Kadono, R. F. Kiefl, Q. Li, T. M. Riseman, H. Zhou, R. L. Lichti, C. Schwab, Hyp. Interactions **64**, 543 (1990).

[Sch92] *Local tunneling and metastability of muonium in CuCl*, J. W. Schneider, R. F. Kiefl, K. Chow, S. F. J. Cox, S. A. Dodds, R. C. DuVarney, T. L. Estle, R. Kadono, S. R. Kreitzman, R. L. Lichti, C. Schwab, Phys. Rev. Lett. **68**, 3196 (1992).

[Sch94] *Integrated heterostructure of Group II-VI semiconductor materials including epitaxial ohmic contact and method of fabricating same*, J. F. Schetzina, US Patent, PN/ 5294833, (1994).

[Sch05] *Nature of charged muonium in GaAs with an applied electric field*, B. E. Schultz, K. H. Chow, B. Hitti, Z. Salman, S. R. Kreitzman, R. F. Kiefl, and R. L. Lichti, Phys. Rev. B **72**, 033201 (2005).

[See82] *Semiconductor Physics: an introduction*, 2^{nd} edition, K. Seeger, Springer, Berlin (1982).

[Seg03] *Effects of covalency, p-d- coupling, and epitaxial strain on the band offsets of II-VI semiconductors*, D. Segev and S.-H. Wei, Phys. Rev. B **68**, 165336 (2003).

[Sen57] *Re-establishment of μ^+ polarization in depolarizing media by an external magnetic field*, J. C. Sens, R. A. Swanson, V. L. Telegdi, and D. D. Yovanovitch, Phys. Rev. **107**, 1465 (1957).

[Sen90] *Spin dynamics of positive muons during cyclic charge exchange and muon slowing down time*, M. Senba, J. Phys. B: At. Mol. Opt. Phys. **23**, 1545 (1990).

[Sen93] *Muonium spin exchange as a Poisoon process: magnetic field dependence in transverse fields*, M. Senba, J. Phys. B: At. Mol. Opt. Phys. **26**, 3213 (1993).

[Sen94] *Muonium spin exchange in spin–polarized media: spin–flip and -nonflip collisions*, M. Senba, Phys. Rev. A **50**, 214 (1994).

[Sen00] *Anisotropic muonium atoms: energy levels and electron spin exchange*, M. Senba, Phys. Rev. A **62**, 042505 (2000).

[Shi02] *Electronic Structure of the Muonium Center as a Shallow Donor in ZnO*, K. Shimomura, K. Nishiyama and R. Kadono, Phys. Rev. Lett. **89**, 255505 (2002).

[Shi04] *Muonium as a shallow center in GaN*, K. Shimomura, R. Kadono, K. Ohishi, M. Mizuta, M. Saito, K. H. Chow, B. Hitti, and R. L. Lichti, Phys. Rev. Lett. **92**, 135505 (2004).

[Šim66] *Temperature dependence of hyperfine coupling of s-state ions in cubic environment*, E. Šimanék and R. Orbach, Phys. Rev. **145**, 191 (1966).

[Smi55] *Properties of ohmic contacts to cadmium sulfide single crystals*, R. W. Smith, Phys. Rev. **97**, 1525 (1955).

[Smi94] *The muon methd in science*, V. P. Smilga and Yu. M. Belousov, Proceedings of the Lebedev Physics Institute, Academy of Sciences of Russia, volume 219, Nova Science Publishers, Inc., New Iork (1994).

[Sou99] *Low-energy reactive ion scattering as a probe of surface femtochemical reaction: H1 and H2 formation on ionic compound surfaces*, R. Souda, T. Suzuki, H. Kawanowa, and E. Asari, J. Chem. Phys. **110**, 2226 (1999).

[Sto97] *Muonium formation via charge transport in solids and liquids*, V. Storchak, J. H. Brewer, and S. F. J. Cox, Hyp. Int. **105**, 189 (1997).

[Sto99a] *Muonium formation via electron transport in solid nitrogen*, V. Storchak, J. H. Brewer, G. D. Morris, D. J. Arseneau, and M. Senba, Phys. Rev. B **59**, 10559 (1999).

[Sto99b] *Nobel Lecture: The fractional quantum Hall effect* , D. C. Tsui, Rev. Mod. Phys. **71**, 875 (1999).

[Sto01] *Landau diamagnetism of a weakly bound muonium atom*, V. Storchak, D. G. Eshchenko, S. P. Cottrell, S. F. J. Cox, E. Karlsson, R. Waeppling, and J. M. Gil, Phys. Lett. A **290**, 181 (2001).

[Sto03] *Weakly bound muonium state in GaP*, V. Storchak, D. G. Eshchenko, R. L. Lichti, and J. H. Brewer, Phys. Rev. B **67**, 121201(R) (2003).

[Sto04] *Formation and dynamics of muonium centres in semiconductors – a new approach*, V. Storchak, D. G. Eshchenko, and J. H. Brewer, J. Phys.: Cond. Matter **16**, S4761 (2004).

[Sto05] *Magnetic freezeout of electrons into muonium atoms in GaAs*, V. Storchak, D. G. Eshchenko, J. H. Brewer, B. Hitti, R. L. Lichti, and B. A. Aronzon, Phys. Rev. B **71**, 113202 (2005).

[Sto06] *Muonium in InSb: shallow acceptor versus deep trap or recombination center*, V. Storchak, D. G. Eshchenko, J. H. Brewer, S. P. Cottrell, and R. L. Lichti, Phys. Rev. B **73**, 081203 (2006).

[Str68] *Phtoelectronic properties of ZnSe crystals*, G. B. Stringfellow and R. H. Bube, Phys. Rev**171**, 903 (1968).

[Str04] *Surface transfer doping of diamond*, P. Strobel, M. Riedel, J. Ristein, and L. Ley, Nature **430**, 439 (2004).

[Su01] *Photoluminescence studies of ZnSe starting materials and vapor grown bulk crystals*, Ching–Hua Su, S. Feth, Ling Jun Wang, and S. L. Lehoczky, J. Cryst. Grow. **224**, 32 (2001).

[Swa58] *Depolarization of positive muons in condensed matter*, R. A. Swanson, Phys. Rev. **112**, 580 (1958).

[Swa67] *Surface properties of II–VI compounds*, R. K. Swank, Phys. Rev. **153**, 844 (1967).

[Swa69] *Barrier heights and contact properties of n-type ZnSe crystals*, R. K. Swank, M. Aven, and J. Z. Devine, J. App. Phys. **40**, 89 (1969).

[Sym84] *Chemical aspects of muon spin rotation*, M. R. C. Symons, Hyp. Int. **17-19**, 771 (1984).

[Sze81] *Physics of Semiconductor Devices, 2^{nd} edition*, S. M. Sze, John Wiley & Sons, Inc., New York (1981).

[Tak86] *Cathodoluminescence study on diffusion coefficients of Al, Ga and In in ZnSe*, H. Takenoshita, K. Kido, and K. Sawai, Jap. Jour. App. Phys. **25**, 1610 (1986).

[Tho73] *Muonium. IV. Precision measurement of the muonium hyperfine-structure interval at weak and very weak magnetic fields*, P. A. Thompson, P. Crane, T. Crane, J. J. Amato, V. W. Hughes, G. zu Putlitz, and J. E. Rothberg, Phys. Rev. A **8**, 86 (1973).

[Tol79] *The principles of statistical mechanics*, R. C. Tolman, Dover Publications, Inc., New York (1979).

[Tor03] *Ab initio modeling of NH, PH and AsH defects in ZnSe*, V. J. B. Torres, J. Coutinho, and P. R. Briddon, Physica B **340-342**, 272 (2003).

[Tou00] *Spectroscopy of the interaction between nitrogen and hydrogen in ZnSe epitaxial layers*, E. Tournié, G. Neu, M. Teisseire, J.–P. Faurie, H. Pelletier, and B. Theys, Phys. Rev. B **62**, 12868 (2000).

[Tri96] *Growth by solid phase recrystallization and assessment of large ZnSe crystals of high purity and structural perfection*, R. Triboulet, J.O. Ndap, A. Tromson-Carli, P. Lemasson, C. Morhain, and G. Neu, J. Cryst. Grow. **159**, 156 (1996).

[TRI07] page of the Centre for molecular and materials science, Tri-University Meson Facility (TRIUMF), Canada, in the Internet: http://cmms.triumf.ca/ (as in January/2007).

[Tsu99] *Nobel Lecture: Interplay of disorder and interaction in two-dimensional electron gas in intense magnetic fields* , D. C. Tsui, Rev. Mod. Phys. **71**, 891 (1999).

[Vaĭ60] *New experimental data on π and μ meson decays*, A. O. Vaĭsenberg, Soviet Physics Uspekhi **3**, 195 (1960).

[vdP58a] *A method of measuring specific resistivity and Hall effect of discs of arbitrary shape*, L. J. van der Pauw, Philips Res. Rep. **13**, 1 (1958).

[vdP58b] *A Method of measuring the resistivity and Hall coefficient on lamellae of arbitrary shape*, L. J. van der Pauw, Philips Tech. Rev. **20**, 220 (1958).

[VdW89] *Theory of hydrogen diffusion and reactions in crystalline silicon*, C. G. Van de Walle, P. J. H. Denteneer, Y. Bar-Yam, and S. T. Pantelides, Phys. Rev. B **39**, 10791 (1991).

[VdW93a] *First-principles calculations of hyperfine parameters*, C. G. Van de Walle, P. E. Blöchl, Phys. Rev. B **47**, 4244 (1993).

[VdW93b] *First–principles calculations of solubilities and doping limits: Li, Na and N in ZnSe*, C. G. Van de Walle, D. B. Laks, G. F. Neumark, S. T. Pantelides, Phys. Rev. B **47**, 9425 (1993).

[VdW00] *Hydrogen as a Cause of Doping in Zinc Oxide*, C. G. Van de Walle, Phys. Rev. Lett. **85**, 1012 (2000).

[VdW02] *Strategies for Controlling the Conductivity of Wide-Band-Gap Semiconductors*, C. G. Van de Walle, Phys. Stat. Sol. (b) **229**, 221 (2002).

[VdW03] *Universal alignment of hydrogen levels in semiconductors, insulators and solutions*, C. G. Van de Walle and J. Neugebauer, Nature **423**, 626 (2003).

[VdW05] *Hydrogen in materials*, C. G. Van de Walle, Lecture notes for course #288M, Materials Department, University of California at Santa Barbara (Spring 2005).

[VdW06] *Hydrogen in semiconductors*, C. G. Van de Walle and J. Neugebauer, Annu. Rev. Mater. Res. **36**, 179 (2006).

[Vil98] *Hidrogénio e muões em calcopirites usadas em células solares*, R. C. Vilão, Relatório de Seminário, Licenciatura em Física, Ramo Científico, Especialização em Física Experimental, Faculdade de Ciências e Tecnologia da Universidade de Coimbra (1998).

[Vil02] *Estudo das interacções do hidrogénio com defeitos estruturais em semiconductores do tipo calcopirite utilizando técnicas de muões*, R. C. Vilão, Dissertação de Mestrado em Física, Especialização em Física Experimental, Faculdade de Ciências e Tecnologia da Universidade de Coimbra (2002).

[Vil03a] *Muon diffusion and trapping in chalcopyrite semiconductors*, R. C. Vilão, J. M. Gil, H. V. Alberto, J. Piroto Duarte, N. Ayres de Campos, A. Weidinger, M. V. Yakushev, and S. F. J. Cox, Physica B **326**, 181 (2003).

[Vil03b] *Hydrogen states in $CuInSe_2$ a μSR study*, R. C. Vilão, H. V. Alberto, J. M. Gil, J. Piroto Duarte, N. Ayres de Campos, A. Weidinger, and M. V. Yakushev, Physica B **340**, 965 (2003).

[Vil05a] *Muonium In ZnTe As A Model For Isolated Hydrogen*, R. C. Vilão, J. M. Gil, H. V. Alberto, J. Piroto Duarte, N. Ayres de Campos, A. Weidinger, R. L. Lichti, K. H. Chow, and S. F. J. Cox, AIP Conference Proceedings **772**, 169 (2005).

[Vil05b] *Muonium spectroscopy in ZnSe: Metastability and conversion*, R. C. Vilão, H. V. Alberto, J. Piroto Duarte, J. M. Gil, N. Ayres de Campos, A. Weidinger, R. L. Lichti, K. H. Chow, and S. F. J. Cox, Phys. Rev. B **75**, 235203 (2005).

[Vil06] *Muonium states in II-VI zinc chalcogenide semiconductors*, R. C. Vilão, H. V. Alberto, J. Piroto Duarte, J. M. Gil, N. Ayres de Campos, A. Weidinger, R. L. Lichti, K. H. Chow, S. P. Cottrell, and S. F. J. Cox, Physica B **374-375**, 383 (2006).

[Vil07a] *Information on hydrogen states in II-VI semiconductor compounds from a study of their muonium analogues*, R. C. Vilão, J. M. Gil, A. Weidinger, H. V. Alberto, J. Piroto Duarte, N. Ayres de Campos, R. L. Lichti, K. H. Chow, and S. F. J. Cox, Nuc. Inst. Methods A (accepted for publication, January/2007).

[Vil07b] *Muonium acceptor level in ZnSe and ZnS*, R. C. Vilão, J. M. Gil, A. Weidinger, H. V. Alberto, J. Piroto Duarte, N. Ayres de Campos, R. L. Lichti, K. H. Chow, and S. F. J. Cox, Nuc. Inst. Methods A (in preparation, January/2007).

[Waa96] *Molecular–beam epitaxy of beryllium–chalcogenide–based thin films and quantum–well structures*, A. Waag, F. Fisher, H. J. Lugauer, Th. Litz, J. Laubender, U. Lunz, U. Zehnder, W. Ossau, T. Gerhardt, M. Möller, and G. Landwehr, J. Appl. Phys. **80**, 792 (1996).

[Wal83] *Muon and muonium chemistry*, D. C. Walker, Cambridge University Press, Cambridge (1983).

[Wan05] *Hydrogen induced metallicity on the ZnO*$(10\bar{1}0)$ *surface*, Y. Wang, B. Meyer, X. Yin, M. Kunat, D. Langenberg, F. Traeger, A. Birkner, and Ch. Wöll, Phys. Rev . Lett. **95**, 266104 (2005).

[Web07] Online periodical table: www.webelements.com (January/2007).

[Wei82] *Formation of negative–U centers in ionic crystals*, K. Weiser, Phys. Rev. B **25**, 1408 (1982).

[Wei98] *Calculated natural band offsets of all II–VI and III–V semiconductors: chemical trends and the role of cation d orbitals*, S.–H. Wei and A. Zunger, App. Phys. Lett. **72**, 2011 (1998).

[Wei03a] *Shallow donor versus deep acceptor state in II-VI semiconductor compounds*, A. Weidinger, J. M. Gil, H. V. Alberto, R. C. Vilão, J. P. Duarte, N. Ayres de Campos, and S. F. J. Cox, Physica B **326**, 124 (2003).

[Wei03b] *Muon and hydrogen states in II-VI semiconductor compounds. A μSR study*, A. Weidinger, H. V. Alberto, J. M. Gil, R. C. Vilão, J. P. Duarte, and N. Ayres de Campos, Phys. Stat. Sol. (c) **0**, 711 (2003).

[Wen99] *Homoepitaxial laser diodes grown on conducting and insulating ZnSe substrates*, H. Wenisch, M. Fehrer, M. Klude, A. Isemann, V. Grossmann, H. Heinke, K. Ohkawa, D. Hommel, M. Prokesch, U. Rinas, H. Hartmann, J. Cryst. Grow. **201/202**, 933 (1999).

[Yu99] *Fundamentals of semiconductors: physics and materials properties*, 2^{nd} edition, P. Y. Yu and M. Cardona, Springer, Berlin (1999).

[Zha98] *A phenomenological model for systematization and prediction of doping limits in II–VI and I–III–VI$_2$ compounds*, S. B. Zhang, S.–H- Wei, and A. Zunger, J. Appl. Phys. **83**, 3192 (1998).

[Zha02] *The microscopic origin of the doping limits in semiconductors and wide-gap materials and recent developments in overcoming these limits: a review*, S. B. Zhang, J. Phys.: Cond. Matter **14**, R881 (2002).